Neutrino Detection with the Surface Array of the Pierre Auger Observatory

Zur Erlangung des akademischen Grades eines
DOKTORS DER NATURWISSENSCHAFTEN
von der Fakultät für Physik der
Universität Karlsruhe (TH)

genehmigte

DISSERTATION

von

Alessio Tamburro
aus San Severo (Italien)

Tag der mündlichen Prüfung	19.12.2008
Referent	Prof. Dr. J. Blümer
Korreferent	Prof. Dr. M. Feindt
Betreuung	Dr. M. Roth

“To my wife Veronica, who supports me in all the important decisions, and to my family, who makes me feel at home wherever I am.”

Contents

List of Figures

List of Tables

Zusammenfassung

Diese Arbeit beschreibt eine Studie zu einer neuen Nachweistechnik für höchstenergetische astrophysikalische Neutrinos von mindenstens 10^{17} eV aus kosmischen Quellen am Pierre-Auger-Observatorium. Neutrinos stellen die Öffnung eines der letzten Beobachtungsfenster der Hochenergieastrophysik dar und lassen den Kosmos in "anderem Licht" betrachten.

Kosmische Objekte können mit einer Vielzahl theoretischer Modelle beschrieben werden. Der Nachweis weniger Teilchen mit Energien von mindestens 10^{20} eV - man geht davon aus, dass es sich um Protonen handelt - bedeutet, dass diese Teilchen mit diesen Energien auch direkt erzeugt werden müssen.

Folgende Modelle kann man klassifizieren: Erstens, Beschleunigungsmodelle ("Bottom-up" Modelle) beruhen auf dem Prinzip der Fermi-Bescheunigung in starken Magnetfeldern verbunden mit astrophysikalischen Objekten wie zum Beispiel Aktiven Galaktischen Kernen, und zweitens, Zerfallsmodelle ("Top-down" Modelle), die auf der Existenz massiver Relikte beruhen. Ein kosmisches Objekt, entweder ein Beschleuniger oder eine exotische Quelle, die Hadronen mit solch hohen Energien ausstoßen kann, muss auch eine Quelle höchstenergetischer Neutrinos sein. Neutrinos entstehen bei der Wechselwirkung der Protonen mit der Materie oder Strahlung in den Quellen, aus dem Zerfall geladener Pionen. Welches der beiden Szenarien, entweder Beschleunigungsmodell oder Zerfallsmodell, in der Natur realisiert ist lässt sich anhand der Stärke des Neutrinoflusses experimentell überprüfen. Eine dritte Quelle höchstenergetischer Neutrinos wird durch den Greisen-Zatsepin-Kuzmin-Effekt (GZK) vorhergesagt. Hierbei entstehen GZK-Neutrinos durch die Wechselwirkung hochenergetischer Teilchen mit der kosmischen Hintergrundstrahlung. Im Gegensatz zu Protonen enthalten diese Neutrinos eine Richtungs- und Energieinformation, weil sie keine Ablenkung in den intergalaktischen Magnetfeldern erfahren und keine Energie verlieren. Somit erreichen diese Neutrinos die Erde ungestört.

Der Nachweis von Neutrinos benötigt große Detektormassen wegen des sehr kleinen Neutrino-Nukleon-Wirkungsquerschnitts. Das Pierre-Auger-Observatorium ist sensitiv auf Neutrino-induzierten Luftschauern mit Energien von mindenstens 10^{17} eV.

Diese Arbeit enthält die Ergebnisse einer Monte-Carlo-Simulationstudie von Neutrino-induzierten Ereignissen am Oberflächendetektor des Observatoriums, der Messung ihrer erwarteten Detektionsraten und der Suche nach Signaturen von Neutrino-induzierten Luftschauern in den Daten. Der Oberflächendetektor setzt sich aus rund 1600 Wassertanks zusammen, die sich auf einem Areal der Größe von gut 3000 km^2 in einem Abstand von 1.5 km zueinender verteilen. Sekundärteilchen aus einem Luftschauer produzieren Cherenkov-Licht entlang der Bahnen durch die Wassertanks, wodurch der Luftschauer rekonstruiert werden kann. Ab Energien von 10^{15} eV nimmt die Transparenz der Erde gegenüber Neutrinos ab. Nur quasi-horizontale Neutrinos, die Luftschauer sehr nahe am Detektorfeld induzieren, oder die sogenannten "Earth-Skimming" ("up-going") Tau-Neutrinos, die bei Zenitwinkeln von 90° bis etwa 95° in die Erdkruste eintreten, haben gute Chancen beobachtet zu werden.

Eine andere Klasse von Neutrino-induzierten Luftschauern wird durch die Wechselwirkung von Elektron- und Tau-Neutrinos in der Atmosphäre bei Zenitwinkeln von 70° bis 90° ("down-going") definiert. Der Untergrund von kosmischen Hadronen und Photonen erzeugt jedoch die größte Begrenzung ihrer Identifikationseffizienz.

Die erwartete Detektionsrate der "Earth-Skimming" Neutrinos ist in etwa doppelt so hoch wie die Rate der quasi-horizontalen und abwärtsgehenden Neutrinos, aber Elektron- und Tau-Neutrinos bei Zenitwinkeln kleiner als 90° müssen berücksichtigt werden.

Unterschiedliche Typen von Luftschauern aus den relevanten Wechselwirkungskanälen wurden simuliert, und die Identifikationseffizienz wurde parametrisiert. Apertur, Akzeptanz, Ereignisraten und Flußobergrenze des Oberflächendetektors des Auger-Observatoriums gegenüber hochenergetischen Neutrinos wurden studiert. Die Abhängigkeit der Antwort des Oberflächendetektors von der systematischen Unsicherheit der verschiedenen Wechselwirkungsmodelle wurden berücksichtigt.

Unter Annahme des Waxmann-Bahcall-Flusses und den typischen Wechselwirkungsvoraussetzungen rechnet man mit nur einem gemessenen Neutrino in drei Jahren. Für die Zeit vom Januar 2004 bis zum Dezember 2007 wurde die Obergrenze des Neutrinoflusses berechnet. In den nächsten Jahren erlauben neue Daten die Flußobergrenze zu reduzieren, sodass das erste hochenergetische Neutrino erwartet werden.

Introduction

Searching for high-energy neutrinos (10^{18} eV or above) emitted from astrophysical objects is one of the most challenging fields of astroparticle physics.

The motivations for the search of high-energy astrophysical neutrinos can be summarized in three fundamental points:

- accessing a new observational channel, and thereby detecting new "messengers" from the universe;
- detecting particles which come from the most remote regions of the universe, which are not deflected by magnetic fields and are not significantly absorbed by traversing the matter and the background radiation on their way to the Earth (neutrino astronomy);
- studying the emission processes at the sources.

Many theoretical models predict that formation and evolution of astrophysical objects can be associated to the emission of a flux of particles, generally called cosmic rays, at macroscopic energies of about 10^{18} eV or larger along with gamma rays and neutrinos. However, the only direct observations of cosmic neutrinos are at low-energy (MeV range) from the Sun [1] and the Supernova SN1987A [2]. To fully explore the expected neutrino spectrum, more measurements are needed (Fig. 1). The main limit to the observation of clear signatures of high-energy astrophysical neutrinos with the current detectors is due to the associated background which is extremely huge compared to the expectation rates for neutrinos. Nevertheless, the increasing statistics of collected data and the improvements in the analysis techniques may allow in few years either the first detection of neutrino signatures or strong constraints on the prediction models.

Secondary particles, detected as air showers which are initiated by the interaction of primary cosmic rays in the atmosphere, are continuously detected on the ground by large arrays of detectors, which sample their lateral distribution, and/or fluorescence detectors,

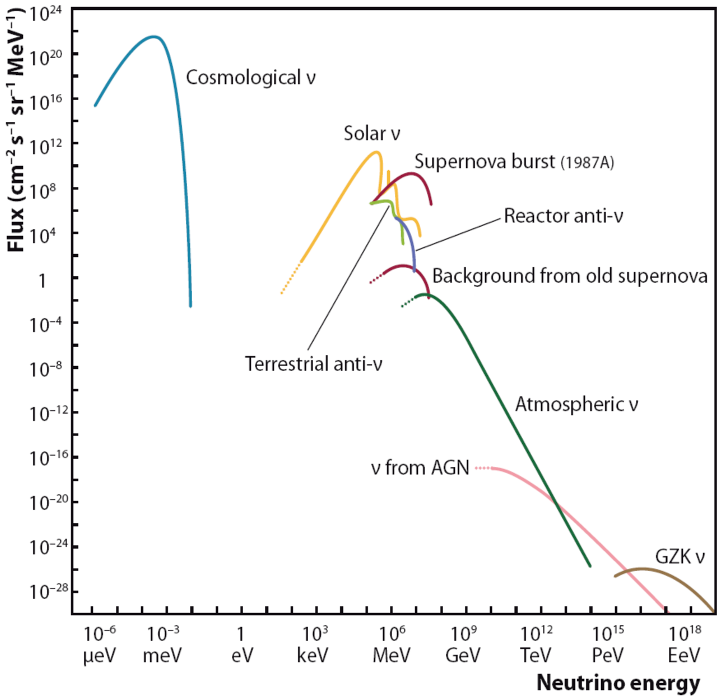

Figure 1: The *grand unified neutrino energy spectrum [3].*

which sense the ultraviolet radiation emitted by the excitation of nitrogen during the passage of particles in the atmosphere. The Pierre Auger Observatory combines the two detection methods in a hybrid technique, which allows for excellent event reconstruction quality and reduced systematic errors.

One of the observational windows opened by the Pierre Auger Observatory is the possibility to detect high-energy neutrinos. Due to the low neutrino cross-section and the corresponding requirement of large amount of matter for interaction, only inclined neutrinos are likely to induce showers close to the ground and might be detected by searching for the typical features of young showers as well as of elongated and asymmetric footprints. Down-going tau and electron neutrinos and up-going or earth-skimming tau neutrinos are expected to be revealed in the huge background of detected ordinary cosmic rays at large zenith angles (above 80°) by characteristic signatures of the showers they induce. In addition, the surrounding Andes mountains enhance the sensitivity of the Observatory to skimming tau-induced showers. Not only do the expected neutrino detection rates depend on the incoming flux, but also the neutrino-nucleon cross-section and the tau lepton energy loss at the highest energies (low Bjorken-x region, $x \lesssim 10^{-5}$) give an important contribution to the systematic uncertainty of calculated rates.

In this work a study of the possibility of detecting high-energy neutrinos with the surface array of the Pierre Auger Observatory is presented. After a short review on the recent discoveries from cosmic-ray detection and open questions addressed to the future increasing of collected data, expected neutrino fluxes and a way of detecting them will be introduced (Chap. 1). A general overview on the discriminating features of neutrino-induced extensive air showers will then be presented along with the experimental techniques developed to measure them (Chap. 2). A detailed description of the surface detector array of the Pierre Auger Observatory will be necessary to understand the techniques developed to analyze collected data (Chap. 3). A complete Monte Carlo chain was derived to simulated neutrino-induced showers at the surface detector array of the Observatory (Chap. 4). Simulations are needed to study the signatures expected from neutrino-induced air showers and to define suitable observables which allow one to identify them (Chap. 5). The same observables will then be used to analyze measured data. Analysis of measured data reveals on the one hand the possibility for future improvements in discrimination at lower zenith angles of incoming shower directions and on the other hand the certainty that in few years clear neutrino signatures are expected to be detected at large zenith angles (Chap. 6). An outlook to the future indicates that further studies on the method of including additional background from deep initiated showers, such as hard-muon induced showers, could help to improve the analysis techniques so that genuine signatures of neutrino-induced showers even at lower zenith angles (down to 60°–70°) might be achieved (Chap. 7).

1

Ultra-high energy cosmic rays

Cosmic rays are a source of ionizing radiation incident on the Earth's atmosphere. Their observed energy spectrum (Fig. 1.1) extends over 10 decades of energies, from 10^9 eV (1 GeV) to beyond 10^{20} eV (100 EeV), and their intensity varies with magnetic latitude,

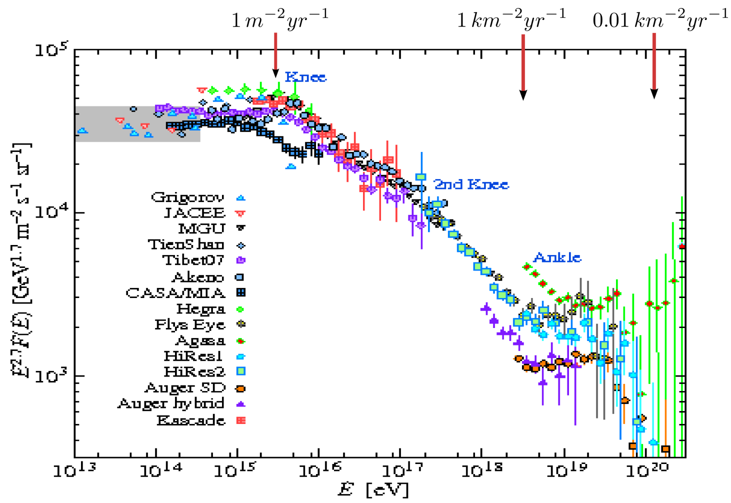

Figure 1.1: *Energy spectrum of cosmic rays as measured by several experiments. The main features of the spectrum are also marked (adapted from Ref. [4])*

with altitude, and with solar activity. Relatively little is known about the properties of the ultra-high energy cosmic rays because of their rarity above 10^{18} eV. As a matter of fact, while at energies below 10^{13} eV the flux of cosmic rays is large enough to be measured directly with high precision, the upper part of the cosmic ray energy spectrum (Fig. 1.2) can be measured only indirectly by observing secondary particles induced by the interaction of a primary cosmic ray in the top layers of the atmosphere and developing extensive air showers (Sec. 2.1). The energy spectrum can be well described by a broken power-law

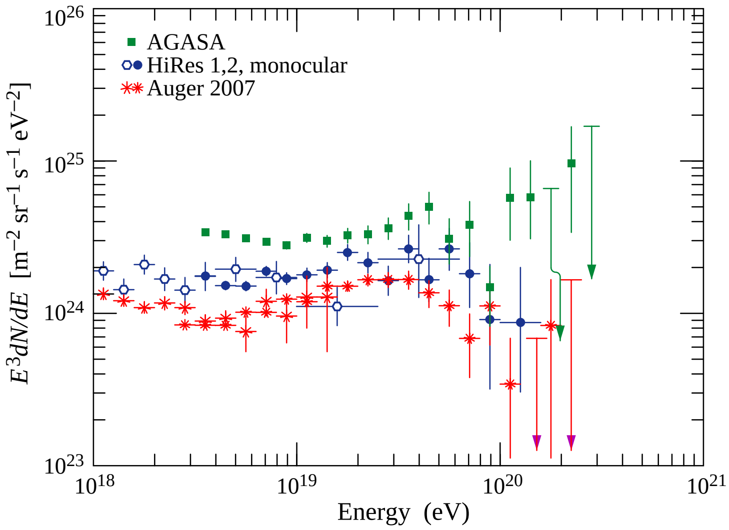

Figure 1.2: *Energy spectrum of ultra-high energy cosmic rays [4] measured at the three latest operating experiments, AGASA [5], HiRes [6] and the Pierre Auger Observatory [7].*

$$\frac{dN}{dE} \propto E^{-\gamma}, \tag{1.1}$$

with $\gamma \approx 2.7$ for energies below $E_{knee} = 10^{15.5} eV$, $\gamma \approx 3.0$ up to $E_{2nd\,knee} = 10^{19} eV$ and back to $\gamma \approx 2.7$ above $E_{ankle} = 3 \times 10^{19} eV$.

Despite the used term “cosmic ray”, which was commonly adopted since the first detection of relativistic particles of cosmic origin on board of balloons about a century ago (Chap. 2), cosmic rays comprise a complex chemical composition which, at low energy (below 2 GeV), consists of fully ionized atomic nuclei (Fig. 1.3).

A reasonable overall agreement of the interstellar galactic chemical composition with the chemical composition of the Solar System has been found at energies below 10^{14} eV [8], but the nature of the most energetic cosmic rays (above 10^{18} eV) remains one of the central enigmas of modern astroparticle physics. Their extreme rarity (1 particle/(km$^2 \cdot$ yr)) at the ultra-high energies needs large detectors on the ground to accumulate enough statistics. Thus, several open questions are awaiting an answer from the analysis of new data but also new interesting experimental results are motivating scientists to clarify the big mystery which involves the observation of very energetic cosmic rays (Sec. 1.1).

In addition, the ultra-high energy cosmic-ray enigma is increasing the attention of theoreticians who try to explain the production of such energetic cosmic rays (Sec. 1.2) in several models. Finally, the observation of very energetic cosmic rays implies the existence of a flux of high-energy neutrinos which might be detected on the ground (Sec. 1.3).

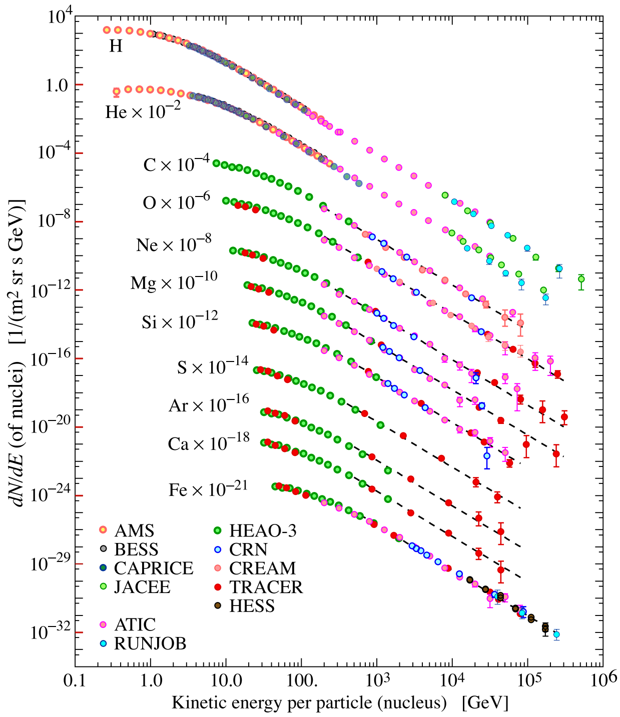

Figure 1.3: *Intensity of the main components of low-energy cosmic rays (below* 2 GeV*) detected on board of balloons, rocket or satellite detectors [4].*

1.1 Recent discoveries and open questions

The most recent breakthrough in cosmic-ray mystery was announced by the Pierre Auger Collaboration on November 8, 2007 [9]. Most of the ultra-high energy cosmic rays, which bombard the Earth's atmosphere, come from directions which are associated with near astrophysical sources, known as Active Galactic Nuclei (Fig. 1.4). The most important parameter in anisotropy studies is the angular accuracy of the detector used. The Pierre Auger Observatory has an angular accuracy better than $1.2°$ for energies larger than 10 EeV. The recent discovery provides indirect evidence for the existence of the expected so-called Greisen-Zatsepin-Kuzmin (GZK) cutoff [10, 11] in the energy spectrum of ultra-high energy cosmic rays. If cosmic rays at the highest energies are predominantly protons or nuclei, only sources closer than 200 Mpc from the Earth can contribute to the flux which is observed above $60 \cdot 10^{18}$ eV (60 EeV). Above this threshold protons or nuclei interact with the cosmic microwave background (CMB), leading to a strong attenuation of their flux before reaching the Earth (Fig. 1.5). The reactions involved are

$$p + \gamma_{2.7K} \rightarrow \Delta^+(1232) \rightarrow n + \pi^+ \tag{1.2}$$

or

$$p + \gamma_{2.7K} \rightarrow \Delta^+(1232) \rightarrow p + \pi^o. \tag{1.3}$$

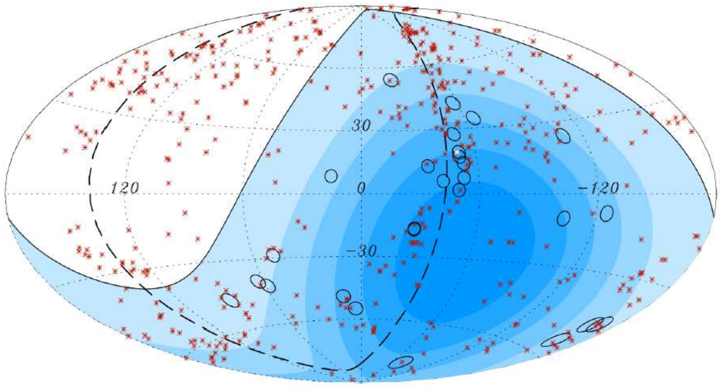

Figure 1.4: *Aitoff projection of the celestial sphere in galactic coordinates with circle of radius* 3.1° *centered at the arrival directions of 27 cosmic rays with ultra-high energy detected by the Pierre Auger Observatory [9]. Solid lines represent the border of the field of view of the Observatory for showers whose zenith angle is below* 60°. *Positions of Active Galactic Nuclei at distances smaller than* 75 Mpc *are marked in red. A darker sky color indicates larger relative exposure. One of the closest Active Galactic Nuclei, Centaurus A, is marked in white.*

If the sources of the highest energy cosmic rays are relatively near and not uniformly distributed, an anisotropic arrival direction distribution is expected.

Photon primaries are expected to dominate over nucleon primaries in non-acceleration models of ultra-high energy cosmic ray production, such as decay of heavy relics. An upper limit on the expected photon fraction was derived from measurements of depths of shower maxima (Sec. 2.1.1) of 29 good-quality events (Fig. 1.6). Above 10 EeV, the photon fraction is 16% at 95% confidence level [13].

Improvements in the detection of ultra-high energy cosmic rays lead to enhanced possibilities of detecting ultra-high energy neutrinos which are expected to be associated with the emission of cosmic rays at their sources (Sec. 1.3). An interesting window for observing possible neutrino-induced showers is a few degrees below the horizon where earth-skimming up-going tau neutrinos might produce a tau lepton just above the detector. The subsequent tau lepton decay in the Earth's atmosphere would produce clear signatures both for the surface detector array and for the fluorescence detector of the Pierre Auger Observatory [14, 15]. A limit on the expected number of observable up-going neutrino-induced events was derived. In the EeV range and for an injected flux of tau neutrinos $dN/dE = K \cdot E^{-2}$, the upper limit is $1.0^{+0.3}_{-0.5}10^{-7}\,\mathrm{GeV} \cdot \mathrm{cm}^{-2} \cdot \mathrm{s}^{-1} \cdot \mathrm{sr}^{-1}$ at 90% confidence level (C.L.) with the uncertainties due to systematic errors such as cross-section, energy losses, tau polarization, topography and extensive air shower simulations.

Although a suppression of the ultra-high energy cosmic ray spectrum above $60 \cdot 10^{18}$ eV can be inferred by the observation of anisotropy of arrival direction distribution of ultra-high energy cosmic rays, astrophysical acceleration processes for cosmic rays need to be pushed to very high energy of the order of 10^{20} eV to account for energies as high as the

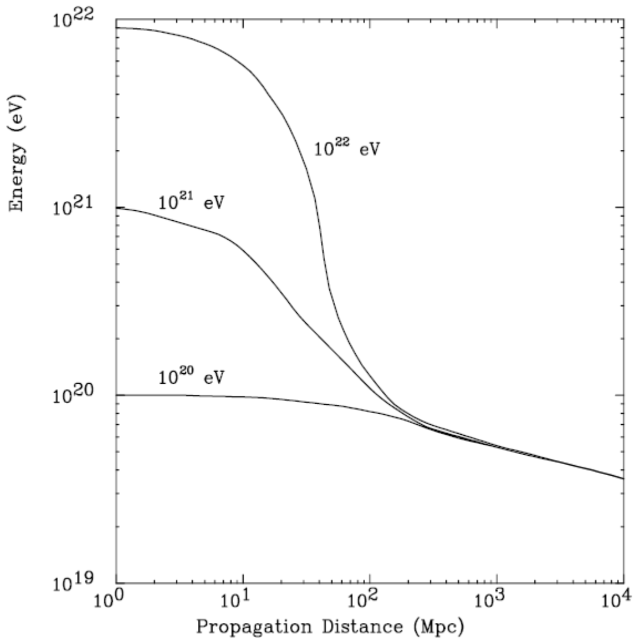

Figure 1.5: *Proton energy versus distance of propagation through the gamma ray background [12].*

ones which have been observed from the Earth. Such very energetic cosmic rays must be of extragalactic origin. An ideal separation between galactic and extragalactic cosmic rays can be indicated in the typical feature of the cosmic ray spectrum, so-called *ankle* (Fig. 1.1), at around 10^{18} eV where a steep *galactic spectrum* encounters the flat *extragalactic spectrum* (Hillas model [16]). The transition from galactic to extragalactic cosmic rays was inspired also by the KASCADE data [17] which showed how light nuclei gradually disappeared from the spectrum with increasing the energy. Basically, this transition occurs at crossing of proton and iron spectra (Berezinsky model [18]).

Many speculations on the possible sources which might produce the observed cosmic rays were done but only the accumulation of enough statistics could help to learn more about how particle acceleration works in extreme conditions and which sources are the most important candidates.

1.2 Two scenarios for the production: conventional sources and exotic models

Substantial progress has been made in understanding the cosmic-ray spectrum at relatively modest energy (10^{15} eV and beyond) and most of the investigations focus on supernova remnants as possible sources. Here acceleration is assumed to take place at the shock front associated with the supersonic motion of the expanding shell where particles are energized

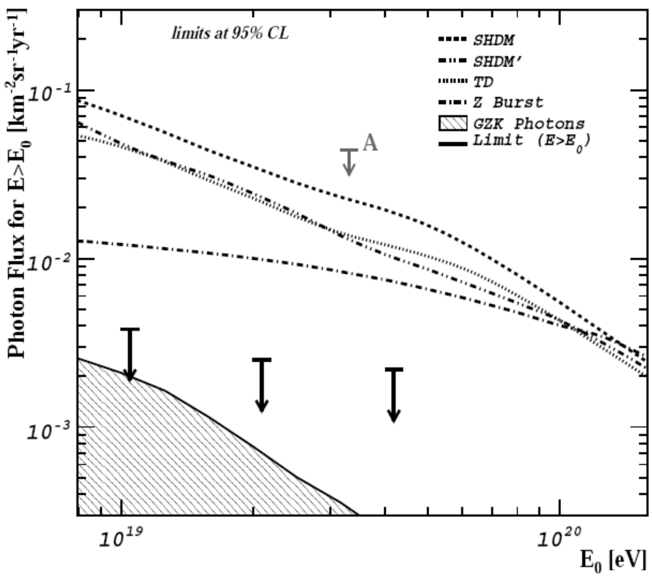

Figure 1.6: *The upper limits on the integral flux of photons (black thick arrows) along with the predictions from top-down models (SHDM, SHDM', TD and ZB) and GZK photon flux [13]. A flux limit derived indirectly by AGASA experiment (Sec. 2.3) and marked with "A" is shown for comparison.*

through Fermi acceleration [19] (the so-called "first-order Fermi process").

Models of acceleration of protons or nuclei to the extreme energies are difficult to construct and only few sufficiently energetic astrophysical environments can be identified as candidate sources which produce such an acceleration. If particle acceleration proceeds through relativistic Fermi shock-acceleration mechanism (the so-called "second-order Fermi process"), a more efficient version of the original Fermi mechanism [20, 21, 22], repeated interactions of particles with a magnetized moving plasma can reach a maximum energy, E_{max}, given by the relation

$$E_{max} \approx \beta c Z e B L, \tag{1.4}$$

where βc is the velocity of the shock associated with the moving plasma, B is the average magnetic field of this plasma in μG, L is the characteristic size of the acceleration region in kpc and Ze the charge of the accelerated particles. Repeated accelerations of the particles in the moving plasma from low energies up to high energies (beyond 10^{21} eV) constrain the so-called *bottom-up* models. A relationship between possible sources and corresponding attainable magnetic fields, able to produce energies according to Eq. 1.4, can be drawn in the so-called Hillas-plot (Fig. 1.7). Large structures, such as galaxies or cluster of galaxies, seem to have sufficient size and field strength to be considered the most likely sites for accelerating high-energy cosmic rays. However, when energy losses are properly treated, even such scenarios loose the necessary requisites to generate the highest energetic cosmic rays.

Several exotic explanations based on *top-down* models (see e.g. [24]) try to circumvent

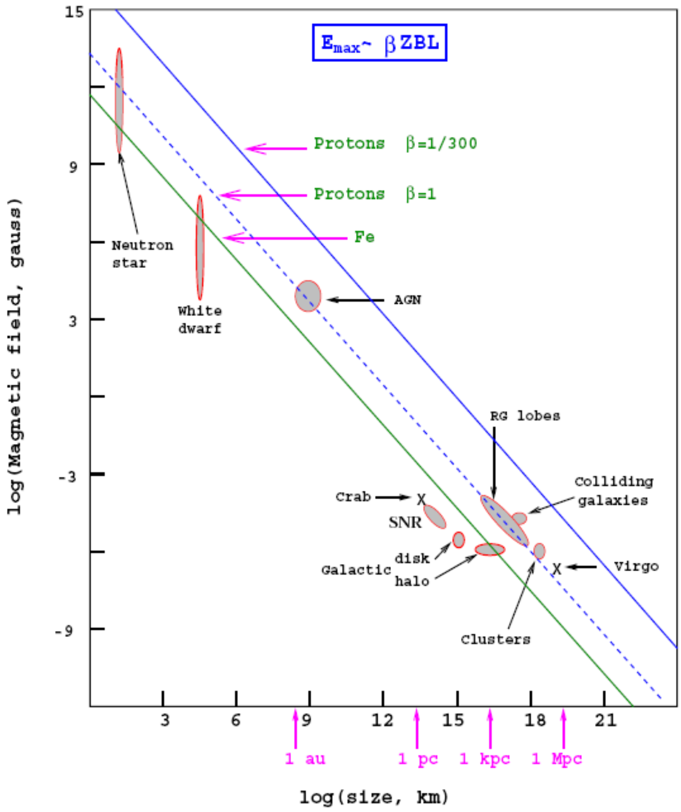

Figure 1.7: *Size and average magnetic fields of acceleration regions of typical astrophysical objects (adapted from Ref. [23]).*

the limitations of the bottom-up models by hypothesizing new physics, such as decay of super-heavy particles, collapse of cosmological defects, cosmic strings etc., which would add new *ingredients* at the possible sources of cosmic rays. The recent calculation of the upper limit on the photon flux (Sec. 1.1) constrains some of the proposed models which predict a high flux of photons associated with a high flux of neutrinos from the sources of cosmic rays.

Accumulation of enough statistics might allow tests of several modifications of the standard model of particle physics. Very massive particles, so-called X particles [25], which might have originated in the early universe or from decays of topological defects [26] are predicted to decay into quarks and leptons. Quarks can hadronize and produce hadrons which decay mainly to light mesons (pions). Pions produce photons, neutrinos and charged leptons in their decays and these particles have an energy which is of the same order as the X particle mass, larger than 10^{20} eV. The most important requirement for the products of X particles to survive without being completely absorbed in the background radiation is that their production must be within distances smaller than 100 Mpc.

1.3 A new window of observation: ultra-high energy neutrinos

Neutrinos offer a unique opportunity to open a new window of observation in astronomy, since they are only weakly interacting and neutral [27]. The first property allows neutrinos to travel cosmological distances without being perturbed, whereas the second property prevents them from being deflected in the interstellar medium. Neutrinos behave, therefore, as messengers of the most remote astrophysical sources which cannot be observed by other means or in other wavelengths. Nevertheless, the only direct observations of cosmic neutrinos are low-energy neutrinos (MeV range) from the Sun [1] and the Supernova SN1987A [2].

In the range $10^{10} - 10^{15}$ eV, astrophysical neutrinos of any flavor, ν_l, are expected to be observed by detecting the leptons, l, induced by Deep Inelastic Scattering (DIS) processes on nuclei, N, of the traversed matter, according to the reaction

$$\nu_l + N \rightarrow l + X, \tag{1.5}$$

where X represents the outgoing fragments of hadrons. The interaction in Eq. 1.5 is known as charged current interaction and it will be described in more detail in the next section. The favored process is the one with a muon as outgoing lepton because muons carry on average about 70% of neutrino energy and muon ranges can be larger than several kilometers, so that big interaction volumes can be reached. Underwater and ice telescopes are able to detect such neutrinos and, at the same time, are able to keep the background from atmospheric muons negligible, since they are placed several kilometers below the Earth's surface and detect up-going neutrinos. Neutrino astronomy is still possible because at such energies the outgoing muon direction is expected to be almost collinear to the interacting neutrino.

Experiments operating under ice are AMANDA [28] and its "successor" IceCube [29]. Another experiment currently taking data is ANTARES which operates under water [30]. An upcoming underwater experiment with an interaction volume comparable to the one expected for IceCube is NEMO [31] to be built in the Mediterranean Sea.

Above 10^{15} eV, the Earth starts becoming opaque to neutrinos and only down-going neutrinos (zenith angles smaller than or equal to 90°) or earth-skimming (zenith angles greater than 90°) tau neutrinos can be observed (Fig. 1.8). The background is due to the plethora of down-going cosmic rays and high-energy atmospheric muons.

In the next section a brief description of the detection possibility at the highest energies will be given. A discussion of theoretical models and expected fluxes will be given in Sec. 1.3.2

1.3.1 Detection of ultra-high energy neutrinos

Collision of astrophysical down-going neutrinos in the Earth's atmosphere are expected to produce different interactions: charged current (CC) interactions with atmospheric nuclei,

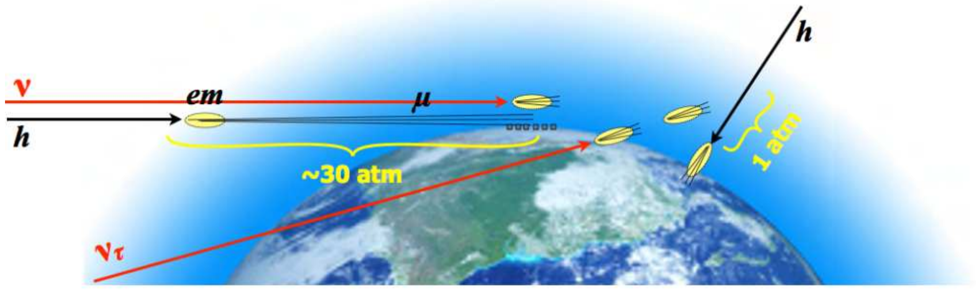

Figure 1.8: *Sketch of the different interactions which neutrinos can produce in the atmosphere. Down-going neutrinos are likely to interact deep in the atmosphere due to their small cross-sections (Sec. 1.3.1). Earth-skimming tau neutrinos produce tau leptons just above the Earth's surface. Down-going cosmic rays (h) and their interactions in the atmosphere are also shown.*

neutral current (NC) interactions and resonant interactions of $\overline{\nu}_e$ with atmospheric electrons (so-called Glashow resonance [32]). A CC interaction of a neutrino of any flavor, ν_l, with a nucleus, N, can be written with the reaction

$$\nu_l(\overline{\nu}_l) + N \to l^-(l^+) + X, \tag{1.6}$$

where the products are an outgoing lepton, l^-, or anti-lepton, l^+, and fragments of hadrons. A NC interaction can be written with the reaction

$$\nu_l(\overline{\nu}_l) + N \to \nu_l(\overline{\nu}_l) + X, \tag{1.7}$$

where the products are a neutrino of the same flavor as the parent neutrino and fragments of hadrons. The resonant interaction is

$$\overline{\nu}_e + e^- \to W^-, \tag{1.8}$$

where W^- is the W-boson of the electroweak interaction.

Neutrinos with energy E_ν such that $10^{16} < E_\nu < 10^{21}$ eV are predicted to have cross-sections, σ, which increase typically as $E_\nu^{1/3}$ [33]. In general, neutrino cross-section for CC or NC interactions can be written as

$$\frac{d^2\sigma}{dxdy} = \frac{KG_F^2 M E_\nu}{\pi} \cdot \left(\frac{M_b^2}{Q^2 + M_b^2}\right) \cdot \left[xq\left(x, Q^2\right) + x\overline{q}\left(x, Q^2\right)(1-y)^2\right], \tag{1.9}$$

where $K = 1/2$ for NC and $K = 2$ for CC interactions, $x = Q^2/2M\nu$ and $y = \nu/E_\nu$ are the Bjorken scaling variables, with $\nu = E_\nu - E_l$ the energy loss in the target frame, $-Q^2$ is the invariant momentum transfer between incident neutrino and outgoing lepton, M the nucleon mass, M_b the intermediate boson mass ($b = W^\pm$ for CC or $b = Z^0$ for NC interactions), $G_F = 1.16632 \cdot 10^{-5}\,\text{GeV}^{-2}$ the Fermi constant of electro-weak interactions and q

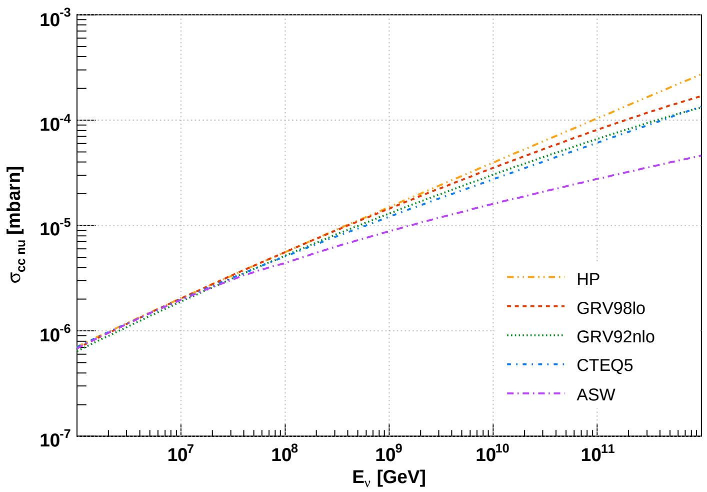

Figure 1.9: *Cross-sections of CC neutrino-nucleon interaction as a function of neutrino energy, obtained comparing different models at low x [34]. The resulting relative uncertainty ranges from 0.70 at* $E_\nu = 10^9\,\mathrm{GeV}$ *to 4.90 at* $E_\nu = 10^{12}\,\mathrm{GeV}$*.*

$(\overline{q})$ the quark (anti-quark) distribution functions which involve the so-called parton distribution functions (PDFs), which are different for CC and NC interactions. This modeling becomes singular at high energies or low x. Typically, experimental data allows evaluation of the parton distribution functions for $x \gtrsim 10^{-5}$. The region which extends below such a limit is unmeasured but it becomes important for neutrino energies $E_\nu \gtrsim 10^8\,\mathrm{GeV}$. Several extrapolations at low x are available in literature and involve different treatments of the nucleon structure functions in the context of Quantum Chromodynamics (QCD). For example, the models known as CTEQs (Coordinated Theoretical-Experimental project on QCD) tend to produce a gentler singularity which implies a smaller cross-section at the highest energies. For the purpose of the present work, a systematic study of the effect of different cross-sections and energy loss models on neutrino-induced showers was done (Sec. 5.9). A review with more detail can be found in Ref. [34]. In Fig. 1.9 cross-sections for CC interactions as a function of E_ν are shown for different models of the structure functions at low x. In particular, the more conventional cross-sections known as GRV98lo [35], GRV92nlo [36] and CTEQ5 [37] and the more extreme cross-sections known as HP [38, 39] and ASW [40] are displayed. The cross-section for NC neutrino-nucleon interaction is expected to be 1/3 smaller than the cross-section for CC interactions.

The resonant interaction is an exceptional case which can happen only in a narrow energy range.

The interaction length λ_{int} is defined as

$$\lambda_{int} = \frac{1}{\frac{N_A}{A} \cdot \rho \cdot \sigma}, \tag{1.10}$$

where A is the Avogadro number, N_A is the number of particles in a mole of traversed substance and ρ is the density of traversed substance. In Fig. 1.10 the dependence of λ_{int}

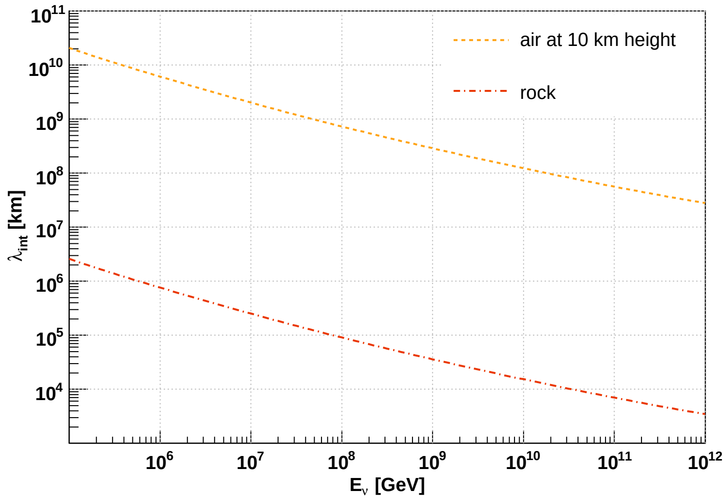

Figure 1.10: *Neutrino interaction length in rock ($\rho = 2.6\,\mathrm{g/cm^2}$) and air at an height of* $10\,\mathrm{km}$ *($\rho = 0.00043\,\mathrm{g/cm^2}$) [34]. The model GRV92nlo [36] was adopted.*

on the neutrino energy is shown. Typically, σ can reach values larger than $700\,\mathrm{pb}$[1]. Neutrino interaction lengths are much larger than Earth's atmospheric depth which reaches a maximum of 36000 km for horizontal incoming neutrinos. Thus, only deep interactions in the Earth's atmosphere might be detected as showers induced by the products of one of the three allowed channels[2]. Nevertheless, deep interactions may be produced by hard atmospheric muons through bremsstrahlung, pair production and nuclear interactions (Sec. 2.2.2 for details).

A shower induced by a CC interaction of an electron neutrino (anti-neutrino), ν_e ($\overline{\nu}_e$), consists of an electromagnetic sub-shower, initiated by the outgoing electron (positron) e^- (e^+), which carries 80% of the initial neutrino energy and a hadronic sub-shower initiated by the fragments X (see Eq. 1.6). A shower induced by a CC interaction of a muon neutrino (anti-neutrino), ν_μ ($\overline{\nu}_\mu$), consists of a low-energy purely hadronic shower, which carries 20% of the initial neutrino energy, and a muon (anti-muon), μ^- (μ^+) which only rarely produces detectable signals. A tau neutrino (anti-neutrino), ν_τ ($\overline{\nu}_\tau$), induces detectable showers only if the tau lepton (anti-lepton) produced, τ^- (τ^+), decays into particles (anti-particles) which can induce detectable showers. Depending on its decay length, a τ^- (τ^+) may also decay back to a ν_τ ($\overline{\nu}_\tau$) or decay to a ν_μ ($\overline{\nu}_\mu$) (regeneration).

Interactions in the NC channel induce only purely hadronic showers.

Resonant interactions (Eq. 1.8) are important only in a narrow energy range, around $E_{\overline{\nu}_e} = 6.4 \cdot 10^{15} eV$ [33]. The boson W^- decays into quarks $q\overline{q}$ may result in electromagnetic showers (induced by $e\overline{\nu}_e$ or 18% of times from $\tau\overline{\nu}_\tau$) or hadronic showers (64% of times from $\tau\overline{\nu}_\tau$).

[1] $1pb = 10^{-36}cm^{-2}$.

[2] A proton- or gamma-like shower has an interaction length which is roughly 0.01 km at 10^{19} eV. The probability for an ordinary shower to be initiated at large depth is about 10^{-9}.

A good window of observation for tau neutrinos is within few degrees below the horizon where the neutrinos skim the Earth's crust [41, 42, 43]. Tau neutrinos have interaction length of the order of 500000 km at 1 EeV and can undergo CC interactions into charged taus if they travel almost horizontally along a chord of the Earth's sphere. Tau leptons can escape from the Earth and emerge in the atmosphere as up-going particles which produce clear signals if they decay above the detector. As for most of tau-induced showers, 2/3 of the total tau energy produces an hadronic sub-shower. Earth-skimming electron neutrinos produce secondaries (e^+ or e^-) which are immediately absorbed inside the Earth, and muon neutrinos produce secondaries (μ^+ or μ^-) which can travel more than 10 km inside the Earth without suffering any interaction.

Finally, tau neutrinos can induce also a particular class of events, known as Double Bang (DB) events, already studied by underground experiments working at lower energies. These events can be described by the reaction

$$\begin{array}{lll} \nu_\tau + N & \rightarrow & \tau + X \\ & & \quad \searrow \\ & & \qquad h + \nu_\tau \end{array} \tag{1.11}$$

where h represents one of the allowed tau decay channels. Two down-going induced showers separated by a certain distance D are expected to be observed: a purely hadronic shower, induced by the outgoing fragments X, and a shower induced by the products h of tau decays. The distance D is roughly proportional to the tau energy E_τ, according to $D \sim 49\,\mathrm{km} \cdot \frac{E_\tau}{EeV}$, so that only at relatively low energies the double bang might be observed in the atmosphere. Fluorescence detectors (Sec. 2.3), which are able to follow the shower longitudinal development in the atmosphere, may observe such a signature [44, 45].

1.3.2 Theoretical models and expected fluxes

Several theoretical models predict a significant flux of high-energy neutrinos which are expected to be produced during the interaction of cosmic rays injected by astrophysical sources into the surrounding matter (gas of hadrons) or photon fields (UV or X-ray, e.g. from synchrotron radiation of electrons). In this so-called *beam dump* scenario, intermediate short-lived mesons, which decay into neutrinos, are produced according to the reactions

$$\begin{array}{l} p + X \rightarrow \pi^\pm + Y \\ \qquad\quad \searrow \\ \qquad\qquad \mu^\pm + \nu_\mu(\overline{\nu}_\mu) \\ \qquad\qquad\quad \searrow \\ \qquad\qquad\qquad e^\pm + \nu_e(\overline{\nu}_e) + \nu_\mu(\overline{\nu}_\mu) \end{array} \tag{1.12}$$

$$
\begin{aligned}
p + X \rightarrow & K^{\pm} + Y \\
& \searrow \\
& \quad \mu^{\pm} + \nu_{\mu}(\overline{\nu}_{\mu}) \\
& \quad \searrow \\
& \qquad e^{\pm} + \nu_e(\overline{\nu}_e) + \nu_{\mu}(\overline{\nu}_{\mu})
\end{aligned}
\tag{1.13}
$$

$$
\begin{aligned}
p + \gamma \rightarrow & \pi^{+} + n \\
& \searrow \\
& \quad \mu^{+} + \nu_{\mu} \\
& \quad \searrow \\
& \qquad e^{+} + \nu_e + \overline{\nu}_{\mu}
\end{aligned}
\tag{1.14}
$$

Neutral pion decays at the sources are also possible but they contribute to the spectrum of high energetic γ-rays emitted from the sources. The association of γ-ray emission and neutrino emission from astrophysical sources is, thus, expected.

The production mechanism constrains the expected flux ratio for the three different neutrino flavors (ν_e, ν_μ, ν_τ). The ratio can be predicted with small uncertainty, whereas the absolute expected flux depends on several parameters which define the astrophysical sources, such as size, thickness and magnetic field involved.

By assuming that the interaction length for mesons and muons are significantly larger than their decay length and counting the expected number N of emerging neutrinos from Eqs. 1.12– 1.14, the ratio is fixed to $N_{\nu_e} : N_{\nu_\mu} : N_{\nu_\tau} = 1 : 2 : 0$. The expected neutrino flux at different energies can be obtained by including the exact kinematics of the decays involved and the flux of the parent particles. In particular, a power-law spectrum for each parent particle is folded with its corresponding decay spectrum [46]. The resulting expected emerging neutrino flux from an astrophysical source, $\phi = dN/dE$, is distributed among the flavors according to the equation

$$\phi_{\nu_e} : \phi_{\nu_\mu} : \phi_{\nu_\tau} = 1 : 2 : 0 \tag{1.15}$$

for a large range of different spectra of parent particles.

Neutrino oscillations, confirmed by atmospheric and solar neutrino data [47, 48], modify the expected flavor ratio during the propagation from the sources to the observation point [49]. By combining atmospheric neutrino data with the constraints imposed on the neutrino oscillation parameters from reactor experiments, such as Chooz [50], the flavor ratio, after propagation to the Earth, becomes

$$\phi_{\nu_e} : \phi_{\nu_\mu} : \phi_{\nu_\tau} = 1 : 1 : 1. \tag{1.16}$$

This scenario might change drastically in case of unstable neutrinos [51, 52] and so-called exotic phenomena, i.e. processes beyond the standard model, such as Weakly Interacting

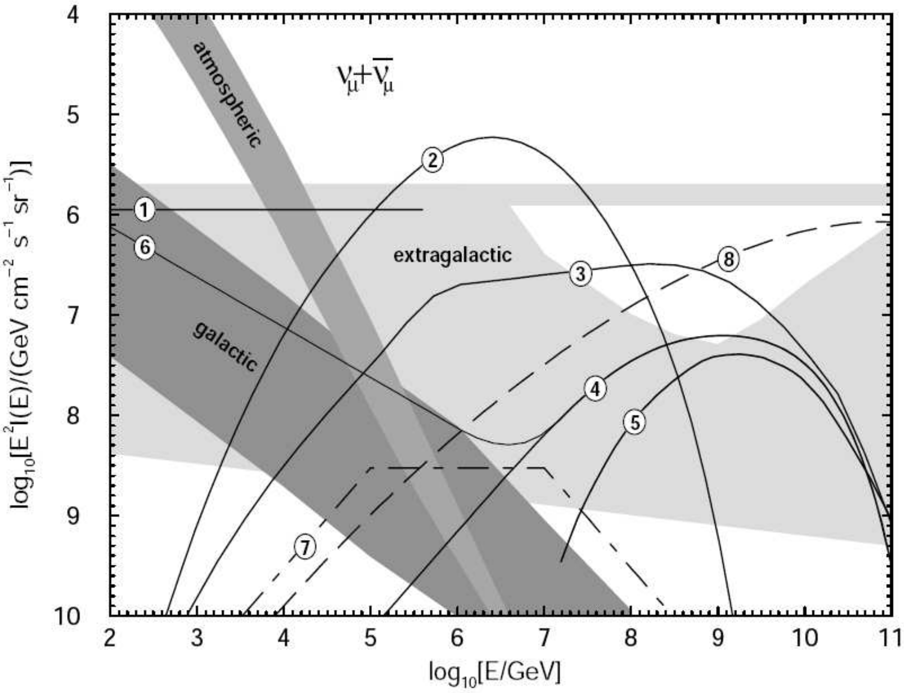

Figure 1.11: *Diffuse fluxes of $\nu_\mu + \overline{\nu}_\mu$ from several astrophysical sources, described in detail in Ref. [55] and references in there. The foreground shaded area represents neutrinos produced in the Earth's atmosphere. The intermediate shaded area represents neutrinos produced in the galactic disk. The background shaded area represents unresolved extragalactic sources. (1) neutrinos from pp interactions in the core of AGNs; (2) neutrinos from $p\gamma$ interactions in the core of AGNs; (3) neutrinos from $p\gamma$ interactions in extragalactic sources; (4) neutrinos from $p\gamma$ interactions in jets of blazars; (5) neutrinos from $p\gamma$ in radio galaxies; (6) neutrinos from pp interactions in hosts of blazar jets; (7) neutrinos from fireball GRB model; (8) neutrinos from decaying XY gauge boson created at topological defects.*

Massive Particle (WIMP) annihilation. In the latter case, neutrinos would be produced from the annihilation of neutralinos, the lightest stable super-symmetric particles, with the subsequent decay of the annihilation products, such as heavy leptons, quarks and gauge-bosons [53].

The predicted relation between cosmic-ray and gamma-ray production has the natural consequence that the most known sources of astrophysical high-energy neutrinos are the Active Galactic Nuclei (AGN), which are known to emit a large fraction of photons in the universe at all frequencies, from radio to TeV γ-rays, in very compact regions. Among AGN, BL Lacs and radio galaxies (grouped under the name of blazars) are a good field of investigations for theoretical speculations [54]. Other important gamma-ray sources are the objects associated with the emission of Gamma Ray Bursts (GRB), irregular hard γ-rays which are emitted during the expansion of a relativistic fireball. A few of GRBs have been associated to Supernova explosions.

A third important source of astrophysical neutrinos is predicted from the propagation of ultra-high energy cosmic rays in the interstellar medium, the so-called cosmogenic or GZK neutrinos [56]. In this scenario, neutrinos are expected to be produced by the interaction of primary cosmic rays with the cosmic microwave background through inverse photoproduction of a Δ^+ resonance, according to the reaction

$$\begin{array}{lcl} p + \gamma_{2.7K} \to \Delta^+(1232) & \to & n + \pi^+ \\ & & \downarrow \qquad \searrow \\ & & p e \overline{\nu}_e \qquad \mu \overline{\nu}_\mu \end{array} \tag{1.17}$$

Generally, diffuse fluxes of neutrinos, produced from several astrophysical sources, are used to evaluate and compare the sensitivity of a detector, which is expected to observe astrophysical neutrinos. A compilation of expected diffuse fluxes for $\nu_\mu + \overline{\nu}_\mu$ is presented in Fig. 1.11. The photon spectral shape of emitted gamma rays from the sources is fundamental to predict the kinematics of the photoproduction processes. Other important parameters which constrain the predicted fluxes are the optical depth for cosmic ray emission (also known as opacity) and the magnetic fields associated with the sources. Upper bounds on the expected flux of neutrinos emitted from the sources are usually used as a reference.

2

Detection of cosmic radiation on the ground

Since the discovery of cosmic radiation by Victor Hess on board of a balloon in 1912 [57], many investigations have been done in order to assign to this new source of energy the right place in the world of modern physics. From the assumption that the cosmic radiation consisted of only highly penetrating photons, ongoing increasing attention for this new phenomenon led to discovery that charged particles had to be present. This conclusion was driven by the observation that the intensity of the cosmic radiation varied with the magnetic field, first observed in detectors placed on a ship approaching the equator by Holland (1927) and late confirmed by the Geiger counters set by Bruno Rossi [58] in directional arrays (1930). The first photographic emulsion tracks produced by cosmic radiation were observed by using high-altitude balloons after the World War II. While the enrichment of the properties ascribed to the cosmic radiation was going on side by side with the development of new technologies, the evolution of the earliest concept of cosmic radiation involved many breakthroughs in the last century. Since the dawn of the space age, the main focus of cosmic radiation research has been more and more directed towards astrophysical investigations and the cosmic radiation has become the link between particle physics and astrophysics, contributing to the birth of astroparticle physics. Nowadays it is known that most galactic cosmic rays have energies between 100 MeV (corresponding to a velocity for protons of 43% of the speed of light) and 10 GeV (corresponding to 99.6% of the speed of light), but the number of cosmic rays with energies beyond 1 GeV decreases by about a factor of 50 for every factor of 10 increase in energy. The number of particles per $\mathrm{m}^2 \cdot \mathrm{sr} \cdot \mathrm{s}$ with energy greater than E (measured in GeV) is given approximately by $N(> E) = k(E + 1) - a$, where $k \sim 5000\,\mathrm{m}^{-2} \cdot \mathrm{sr}^{-1} \cdot \mathrm{s}^{-1}$ and $a \sim 1.6$. The highest energy cosmic rays currently measured have more than $10^{20}\,\mathrm{eV}$. Direct measurement at these energies is therefore not feasible due to the low flux. Direct measurement at lower energies do, however, provide useful information on the properties of cosmic radiation which has interacted in the Solar System, for example. Composition studies of the interstellar medium are, for instance, possible at lower energies. The less energetic cosmic radiation is absorbed by our atmosphere and only experiments on spacecrafts can detect it.

The idea to use the atmosphere as mean to indirectly measure the properties of primary radiation interacting at the top of the atmosphere, was developed by Pierre Auger in 1939 [59] by observing that the radiation on the ground could be associated to single events high in the atmosphere. The primary radiation able to produce such time coincidences on the ground was thought to have an energy of at least 10^{15} eV or 1 PeV.

Around such an energy and up to 10^{17} eV, small showers are produced by the interaction of a primary in the atmosphere and almost only Cherenkov radiation can reach the ground to be detected by radio telescope. The chance to observe the highest part of the energy spectrum of cosmic rays (above 10^{18} eV) lies on the possibility to build detectors on the ground which are large enough to detect the big showers produced by high-energy particle interactions in the atmosphere. Such showers are commonly called Extensive Air Showers (EAS). Cosmic ray ions at the top of their energy range produce in the atmosphere showers of many millions of fragments along with Cherenkov radiation, covering huge areas, and their more energetic fragments (mostly muons) are even registered in deep underground experiments. The existence of such energetic particles is a real riddle.

In the next sections the attention will be focused on the EAS production (Sec. 2.1), the composition of the primaries initiating EAS (Sec. 2.1.1) and the structure of the shower front (Sec. 2.1.2). The possibility to detect EAS initiated by neutrinos will be discussed more deeply in Sec. 2.2, in particular the possibility to identify neutrino showers among the very inclined EAS (Sec. 2.2.1) and how their features would display (Sec. 2.2.2). The most important historical experiments, built to study the cosmic radiation in the highest part of its spectrum, and the techniques related to the detection of EAS will be discussed briefly in Sec. 2.3. Finally, a description of the Pierre Auger Observatory which is currently using the new concept of hybrid technique to study the cosmic rays at the highest energies will be given in Sec. 2.4.

2.1 Extensive air showers

The atmosphere acts as a good amplifier for a primary cosmic particle. A primary particle, proton or nucleus, with an extremely high energy collides with a nucleus high in the atmosphere and the following hadronic interaction produces several energetic particles or secondaries which, on their part, collide with other air nuclei adding new energetic particles and developing a cascade or shower. The number of charged particles reaches a maximum, N_{max}, which is roughly proportional to the primary energy E and approximately equal to $E/(1.6\ GeV)$. Although such primaries are very rare (about $0.5\,\mathrm{particles}/(\mathrm{km}^2 \cdot \mathrm{sr} \cdot \mathrm{century})$), air shower detectors, covering areas of thousands square kilometers, are able to detect the particles produced by the shower development.

The cascade (mostly pions, 80%, and kaons) grows from the first primary hadronic interaction until the energy per pion falls to the level where pions are likely to decay before colliding. Neutral pions, which almost instantly decay to pairs of gamma rays, are also produced and take, on average, 1/3 of the parent particle energy. While the hadronic cascade continues its development, an electromagnetic sub-cascade dissipates almost all of the primary particle energy through ionization of atoms by means of $e^{\pm}$, which are

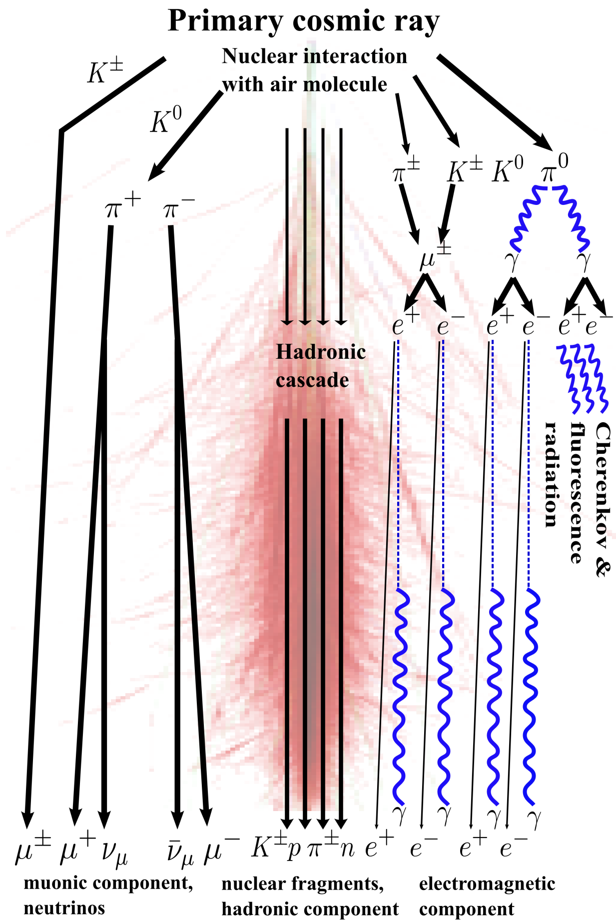

Figure 2.1: *Sketch of the processes involved in an EAS production in the atmosphere.*

produced by bremsstrahlung and pair production from γs. From charged pion decays, atmospheric muons are produced, according to the following reaction

$$\pi^\pm \rightarrow \mu^\pm + \nu_\mu \ (99.9\%). \tag{2.1}$$

Kaons decay according to the following reactions

$$K^\pm \rightarrow \mu^\pm + \nu_\mu \ (63.5\%) \tag{2.2}$$

$$K^\pm \rightarrow \pi^\pm + \pi^o \ (21.2\%) \tag{2.3}$$

and contribute to the number of shower muons. Neutrinos carry only 2% of the primary energy and weakly interact in the atmosphere. The number of shower muons depends on the amount of energy which is left in the hadronic cascade. Generally, if, after relatively few cascade generations, the pion energy is such that the pion decay is favored, a large number of muons is produced. Thus, while the number of muons $(1 - 10\,\mathrm{GeV})$ increases with little subsequent energy loss reaching a plateau, the number of electrons and positrons decreases rapidly after the shower maximum production of particles because of ionization

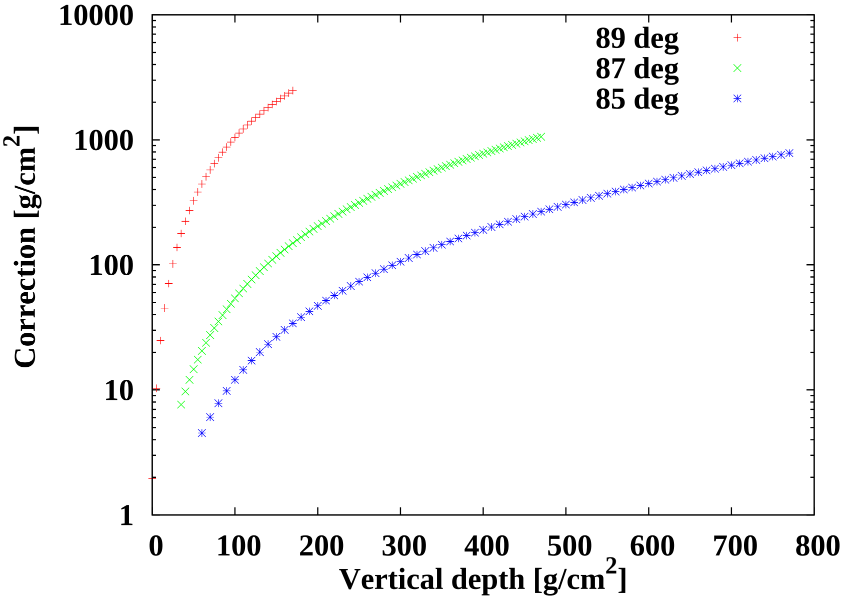

Figure 2.2: *Effect of the correction for the Earth's curvature to the slant depth in the approximation of flat geometry. Three very inclined directions are considered. Zero vertical depth corresponds to a reference depth of* $820\,\mathrm{gcm}^{-2}$ *(about* $1420\,\mathrm{m}$ *above sea level).*

processes. Muons, however, may decay in flight as their energy becomes as low as about $10\,\mathrm{GeV}$ according to the following reaction

$$\mu^{\pm} \rightarrow e^{\pm} + \nu_e(\overline{\nu}_e) + \nu_\mu(\overline{\nu}_\mu). \tag{2.4}$$

This produces a second source of atmospheric neutrinos.

Extensive air showers induced by γs behave differently in that the cascade of secondaries is purely electromagnetic and the dominant processes are pair production and bremsstrahlung. At very high energies ($10^{19}\,\mathrm{eV}$), the Landau-Pomeranchuk-Migdal (LPM) effect [60, 61, 62] becomes important and reduces the cross-section for pair-production and bremsstrahlung. In addition, photons interact high in the atmosphere with the geomagnetic field by pair production and reduce the particle energy for the subsequent interactions in the atmosphere.

In a nutshell, an extensive air shower, induced by a proton or a nucleus, consists of three main components, a hadronic, a muonic and an electromagnetic component, as sketched in Fig. 2.1, whereas an EAS induced by a γ possesses only an electromagnetic component which is quickly absorbed. Depending on the atmospheric depth X at which the primary interaction takes place, the contribution of one of the three components may be predominant in a hadronic EAS at a particular observing level. The atmospheric depth is measured from the top of the atmosphere in $\mathrm{g} \cdot \mathrm{cm}^{-2}$. A vertical depth X_v and a slant depth X_s are defined. The former is measured from the top of the atmosphere along the vertical direction towards the observation point and depends on the density profile of the

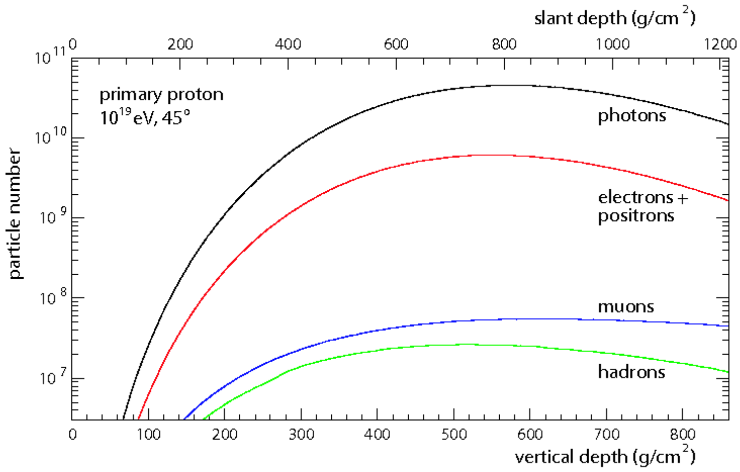

Figure 2.3: *Longitudinal development of the main components of a simulated EAS induced by a* 10^{19} eV *proton at* 45°.

atmosphere according to the equation

$$X_v = \int_h^\infty \rho(h')dh', \tag{2.5}$$

where $\rho(h)$ is the density of the atmosphere at the altitude h of the observation point. The latter is measured from the top of the atmosphere along the primary incoming direction towards the observation point according to the equation

$$X_s = \frac{X_v}{\cos\theta}, \tag{2.6}$$

where θ is the zenith angle of the primary incoming direction. Equation 2.6 is valid in the approximation of a flat geometry. For very inclined shower incoming directions (typically $\theta > 80°$), the Earth's curvature should be taken into account to calculate X_s. At large θ the correction for the curved geometry to Eq. 2.6 turns out to be quite important as it is shown in Fig. 2.2 for three directions. In Fig. 2.3 the longitudinal shower development of electrons and positrons, photons, hadrons and muons for a 10^{19} eV simulated proton shower at 45° is shown. The longitudinal development depends on the primary, its mass and type, its energy and its incoming direction and it can be used to infer indirectly the mass of the primary (Sec. 2.1.1). Basically, a deeply interacting primary will develop later than a shallow interacting primary. The former will produce a so-called *young* shower, i.e. a shower which can be detected with a large contribution of electromagnetic components, the latter will produce an *old* shower whose main component consists of muons. However, it is important to note that the primary incoming direction plays an important role in the absorption of the electromagnetic component of a developing shower. As a matter of fact, an inclined shower will loose most of its electromagnetic component faster than a vertical shower due to the larger amount of matter which it encounters during its development. This

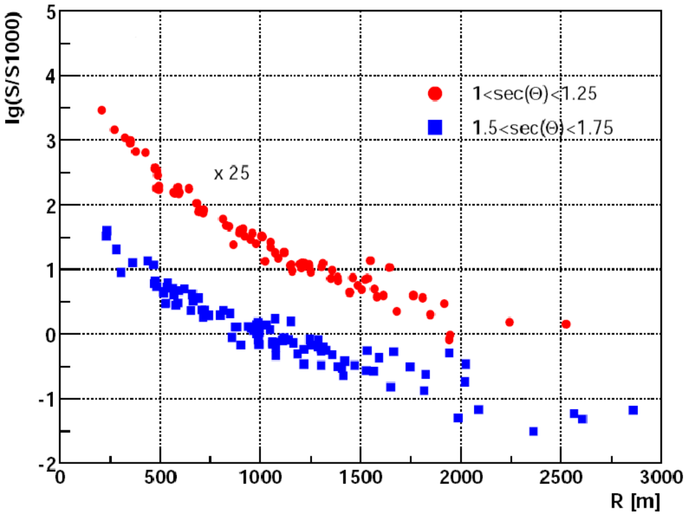

Figure 2.4: *Example of measured lateral development for 2 zenith angle bins. Data for* $1 < \sec(\theta) < 1.25$ *were shifted upwards for clarity [63].*

important feature of the inclined showers will be particularly interesting for the detection of neutrino-induced showers (Sec. 2.2).

Besides the longitudinal profile, the lateral distribution of the density of particles arriving at the ground is the second important feature to be used to study an EAS. A lateral distribution of densities (Fig. 2.4) can be measured to give an indirect estimate of the primary energy, whereas the timing information of the recorded particles allows reconstruction of the primary incoming direction (Sec. 2.1.2).

The plethora of processes and interactions taking place during the shower development gives, therefore, several opportunities for a shower to be detected. An EAS produces a large number of particles which can be sampled with an array of detectors deployed over an appropriate area to measure lateral distributions and time coincidences. In addition, air shower particles excite air molecules (mainly nitrogen) and the following de-excitation produces fluorescence light in the UV band ($300 - 400\,\mathrm{nm}$). Fluorescence light make it possible to follow the longitudinal development of a shower in the atmosphere. Moreover, since most of the particles travel at a relativistic regime, Cherenkov light is emitted along their paths in the atmosphere. Finally, charged particles in the geomagnetic field produce radio emission. In Sec. 2.3, a short review of the techniques deployed to detect EAS will be given.

2.1.1 Composition

The relation between the parameters which describe an EAS, such as the number of muons produced and the position of the shower maximum, depends on complex processes involved in subsequent interactions. Thus, the identification of the primary, which might have produced the detected shower, can be only inferred by measuring its mass A with the

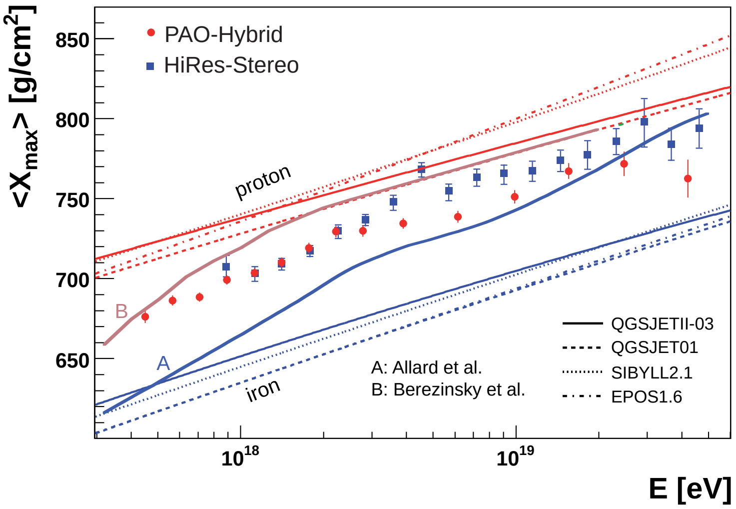

Figure 2.5: *Mean shower maximum depth of proton-induced showers (in blue) and iron-induced showers (in red) at different energies for several interaction models (lines) and inferred from data (points) of the Pierre Auger Observatory (PAO) [64] and HiRes [65]. The model "A" refers to Ref. [66], the model "B" refers to Ref. [18] (figure taken from Ref. [67]).*

help of Monte Carlo simulations [68, 69]. Interaction models at extremely high energies are uncertain and a more practical way of studying the mass composition of a primary cosmic ray is to use "indicators". An indicator of the mass composition is the depth of the shower maximum (Fig. 2.5), X_{max}, which is expected to change with energy E and mass [70, 71, 72, 73], according to

$$X_{max} \propto \log_{10} \frac{E}{A} \tag{2.7}$$

and which can be correlated with the rise time[1] of the signals detected in a surface detector, such as the surface detector array of the Pierre Auger Observatory (Sec. 2.4). In fact, X_{max} can be calibrated with the measurements of the average deviation of the rise time in an event [74, 75].

2.1.2 Spatial and temporal structure of the shower front

The development of EAS in the atmosphere produces secondary particles with different trajectories and velocities which delay them with respect to the shower axis during their travel to the ground. A spherical moving surface, expanding at the speed of light from the primary interaction, can be assumed as a reference shower front. The more the particles travel in straight lines, not suffering of scattering processes, the closer to this ideal front they

[1]Specifically, the rise time is defined as the time for an integrated signal to rise from 10% to 50% of its maximum.

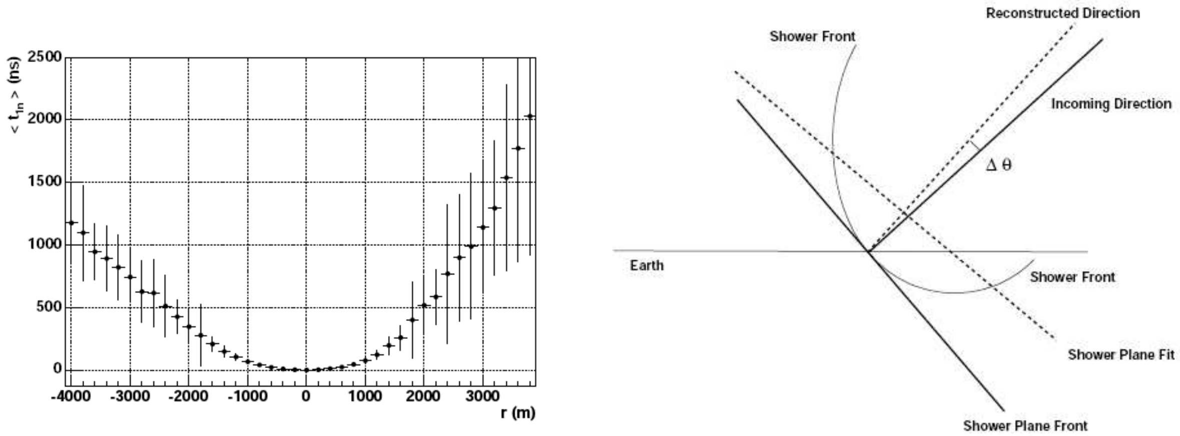

Figure 2.6: *(Left panel) Typical mean arrival time of first muons for* 10^{19} eV *showers at* 60° *zenith angle as a function of the distance from the shower core, r. Early region (positive r) and late region (negative r) show an asymmetry in their measured arrival times (text for details). Error bars show the RMS [76]. (Right panel) Sketch of the early-late asymmetry which can be observed in inclined showers [76].*

are expected to be. This circumstance is particularly true around the shower axis where the particles are more energetic, but in the regions which are further from the shower core particles accumulate more delay due to their sub-luminal velocities and angular deflections during their interaction with the traversed atmosphere.

Electrons have a larger cross-section than muons to multiple scattering processes and bremsstrahlung. In addition, muons are highly penetrating so that they are the earliest particles arriving at the ground and dominate the signal at large distances from the core.

Muons suffer several processes which contribute to complete the picture of a typical shower front: geometrical delay due to the path traveled by the parent pion before decaying, kinematical delay due to the fact that muons always propagate at velocities smaller than the speed of light, delay due to Coulomb scattering, and deviations produced by the geomagnetic field. In practice, however, only the first two processes assume a particular importance when studying the shower front time structure [77, 76]. Coulomb scattering is expected to be very small and can be neglected. Deflections due to the geomagnetic field is important only for very inclined showers.

In addition, an electromagnetic halo is produced by muons decaying to electrons along their paths. The energy transferred to a single electron is about 1/3 of the muon energy and is enough to produce sub-showers whose effects must be taken into account in detectors where the signal is proportional to the energy deposit, such as Cherenkov detectors.

A study of the arrival time of the first muons in detectors on the ground is important to correct uncertainties in the shower direction reconstruction (Sec. 3.4). In Fig. 2.6 (left panel) a typical measurement of arrival times of first muons for simulated showers in the surface detector array of the Pierre Auger Observatory is shown. An early-late asymmetry of the arrival time (Fig. 2.6, right panel) can be understood as a consequence of muons which have accumulated more delays in the early region with respect to the expected shower front due to a change of the production distance. As a consequence, the reconstructed direction has a slightly lower zenith angle.

The temporal structure which is recorded on the ground carries information on the shower arrival direction and hence on the primary direction. With an array of particle detectors, the direction of the primary cosmic ray is deduced from the relative arrival times of signals at a minimum of 3 non-collinear detectors.

Thickness and curvature of the shower front, arrival time distribution of signals, rise time of signals are the main features to study the shower front of EAS and help to identify the possible primary which has produced them.

2.2 The challenge: detection of neutrinos

Several theoretical models predict the production of ultra-high energy cosmic rays associated with emission of gamma rays and neutrinos at the sources. Neutrinos travel undisturbed, carrying information which can be used in constraining production models.

High-energy neutrinos may produce EAS which can be detected. The main challenge lies in separating showers initiated by neutrinos from showers initiated by ordinary cosmic rays. In the 1960s it was suggested that discrimination of cosmic-ray showers from neutrino-induced showers might be done at high zenith angles [56] where the large amount of atmosphere which an inclined primary encounters along its travel to the ground, might be enough to provide a suitable target to develop a neutrino-induced shower. Due to their large interaction cross-section, instead, protons, nuclei or photons initiate showers high in the atmosphere which are significantly absorbed before they reach the ground. The basic signature for neutrino events would be, therefore, inclined events interacting deeply in the atmosphere. Hard muons interacting deeply in the atmosphere may induce, however, showers which are background to the detection of neutrino showers [78].

When the Pierre Auger project was conceived as the largest and most accurate detector to study air showers, it became clear that it would achieve a competitive acceptance for inclined showers induced by neutrinos, compared to devoted neutrino experiments in construction [79]. One of the observations, made possible by the Pierre Auger Observatory, is the detection of high-energy neutrinos [80]. Up-going tau neutrinos have a chance to induce detectable EAS only if their incoming direction ranges up to few degrees below the horizon by scratching the Earth's crust (earth-skimming neutrinos) [41, 42]. Many studies have been led to evaluate the sensitivity of the Pierre Auger Observatory to up-going tau neutrino-induced showers [43, 14, 81] and it was clear that some observables could help in discrimination at large zenith [82, 83]. Moreover, the additional target offered by the Andes mountains surrounding the Pierre Auger Observatory enhances the sensitivity of the observatory to tau-induced showers [84, 85, 83]. A limit was put by the Pierre Auger Collaboration in case of up-going tau neutrinos [15].

Down-going neutrino-induced showers have a not negligible chance to be identified. In Chap. 5 and Chap. 6 the potentiality of the Pierre Auger Observatory to detect up- and down-going neutrino-induced showers will be presented.

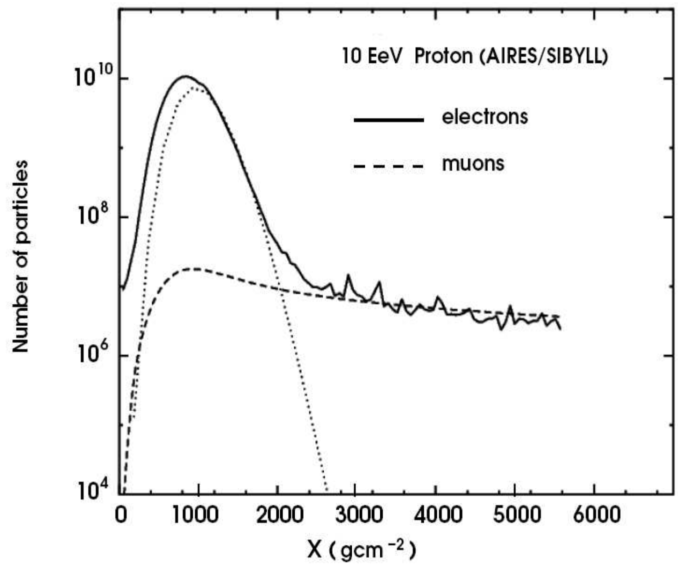

Figure 2.7: *Average longitudinal development of muons and electrons in extensive air showers, induced by more than 100 proton showers at* $10\,\mathrm{EeV}$*. At depths exceeding about* $2500\,\mathrm{g}\cdot\mathrm{cm}^{-2}$ *the electromagnetic component is mainly produced by hard muons. A depth of* $2500\,\mathrm{g}\cdot\mathrm{cm}^{-2}$ *corresponds to about* 60° *and is chosen as a threshold to distinguish very inclined from ordinary showers. The dotted line represents a theoretical prediction of purely electromagnetic development. The picture is taken from Ref. [93].*

2.2.1 Features of very inclined extensive air showers

Much of the relevance of very inclined air showers induced by cosmic rays is in the understanding of the background from which high-energy neutrino showers must be extracted. Very inclined air showers can be defined as extensive air showers, induced by primaries whose incoming directions have zenith angles above 60°. A sub-class of such showers consists of so-called horizontal air showers (HAS) whose zenith angle is about 90°. Very inclined air showers have been studied for many years for several different reasons [86, 87, 88, 89, 90, 91, 92], though, they are of great interest for two main reasons. Firstly, the acceptance of an air-shower array could be doubled if events above 60° can be adequately analyzed. Secondly, very inclined showers consist of surviving particles which are created very close to the shower core. The core of EAS comprises particles from the hadronic cascade (Fig. 2.1) and its study can help to constrain hadron interaction models at high energy. Moreover, understanding the azimuthal asymmetries at large zenith angles can lead to a significant improvement of ultra-high energy shower analysis at moderate zenith angles.

The substantial difference from vertical showers lies in the enhanced number of muons recorded on the ground (Fig. 2.7). At large zenith angles, cosmic rays (whether they are protons, heavier nuclei, or even photons) develop ordinary showers in the top layers of the atmosphere in a very similar way to the well understood vertical showers. Their elec-

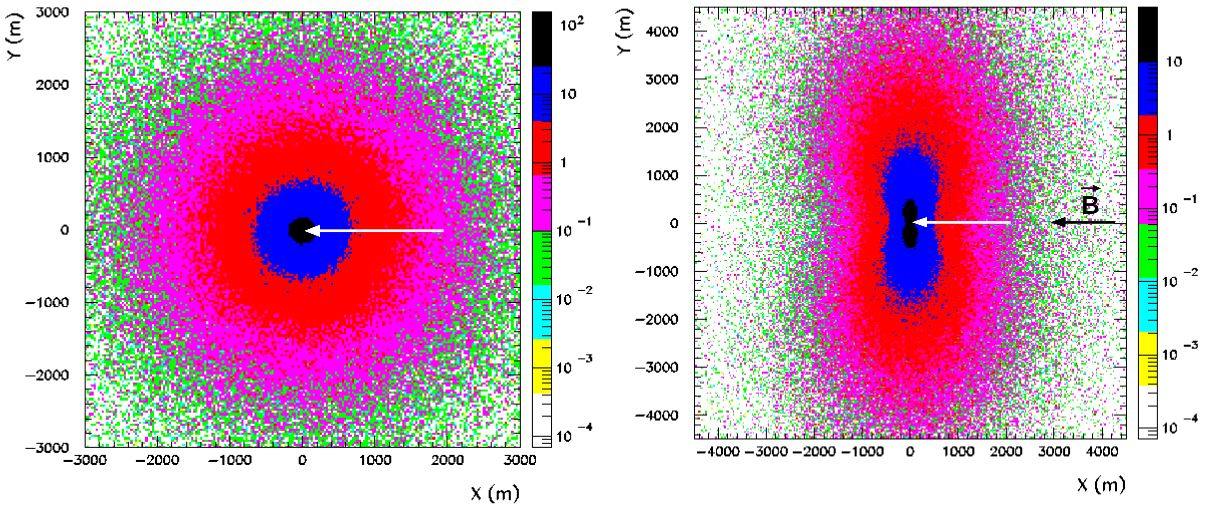

Figure 2.8: *Map of the muonic signal in the shower plane for a* 10 EeV *proton shower with a zenith angle of* 86° *and azimuth* 90°*. Left panel: map without the effect of the geomagnetic field. Right panel: map with the geomagnetic field. White arrows indicate the shower direction and black arrows the direction of the magnetic field [94].*

tromagnetic component is, however, almost completely absorbed by the greatly increased atmospheric slant depth. The atmosphere is about $1000\,\mathrm{g}\cdot\mathrm{cm}^{-2}$ deep for vertical showers, doubles to about $2000\,\mathrm{g}\cdot\mathrm{cm}^{-2}$ for 60° showers and becomes over 30 times deeper for HAS at sea level so that the electromagnetic component from neutral pion decays has no chance to survive with detectable signals on the ground. For inclined showers, the main sources of electrons and photons at the ground are the highly penetrating muons, which produce $e^{\pm}$ through decay, bremsstrahlung, and pair production. The number of electrons and photons follows closely the number of muons at every distance from the shower axis. The average length traversed by muons in very inclined showers from their production point to the ground ranges from about 10 km (at 60°) to 300 km (at 90°). Therefore, only muons produced with sufficiently high energy survive to the ground. The energy loss is well over 100 GeV for a completely horizontal shower, whereas it is only few GeV for the lowest energy muons in vertical showers. The average energy of muons detected on the ground shows a difference of 2 orders of magnitude between vertical and HAS.

The large paths traversed by muons in inclined and quasi-horizontal air showers makes it possible that μ^+ and μ^- are deflected in the geomagnetic field before reaching the ground level (Fig. 2.8). The deflections may become observable for very energetic showers, with a larger number of particles surviving, as two-lobe footprints on the ground.

2.2.2 Features of neutrino showers

Above 1 PeV the Earth becomes opaque to neutrinos and only down-going or Earth-skimming neutrinos may be detected. The challenge, as previously stated, lies in identifying these showers in the large background produced by down-going cosmic rays and

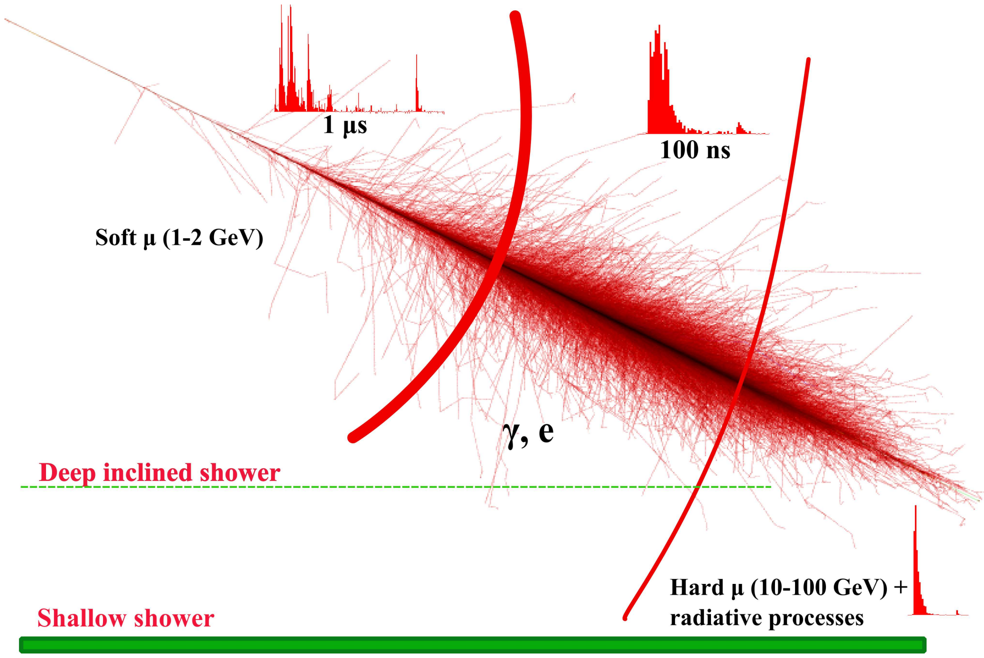

Figure 2.9: *Sketch of placement of an ultra-high energy neutrino-induced shower with respect to the ground and main expected features.*

atmospheric muons [95]. The main background is, however, mostly due to inclined showers induced by protons and nuclei so that in the present work the attention will be given to searching signatures which discriminate neutrino-induced showers from very inclined ordinary showers (Chap. 5).

In particular deeply inclined showers induced by neutrinos can develop close to the ground so that their shower front resembles that of typical vertical proton shower. Obtaining information on shower properties induced by deeply-interacting showers is crucial for searching discriminating signatures of neutrino-induced showers. The main difference between deeply-interacting neutrino showers and vertical showers lies in the fact that, for deeply-interacting neutrino showers, their complete development in the atmosphere can be measured, e.g. showers leave clear signatures of the stage of their development in the recorded signals of a surface detector. As a consequence, a neutrino shower front structure can be clearly distinguished, for instance, on the basis of its signal properties, such as rise and fall time, signal shapes etc. and on the basis of its incoming directions (Fig. 2.9). Particularly important is the type of detector which is used to record signals from extensive air showers. The surface array of the Pierre Auger Observatory (Chap. 3) offers the possibility of some differentiation between signals produced by muons from signals produced by electrons because it consists of an array of water Cherenkov detectors. Therefore, it allows to distinguish young and old showers.

Up-going neutrinos have a chance to induce detectable extensive air showers only if their incoming direction is less than few degrees below the horizon. In this case, the Earth offers a suitable target for a neutrino to initiate a shower just above the Earth's crust. Up-going neutrino showers can not be distinguished from down-going neutrino showers in surface detectors, since the reconstruction of their incoming directions relies only on the detected arrival times, but the expected features are similar to the ones associated to down-going neutrino-induced showers. Nevertheless, fluorescence detectors can, in principle, identify up-coming showers since they record development depths and depths of shower maxima. The duty cycle for observation limits, however, the expected detection event rates.

The second type of background to neutrino showers is due to production of showers from hard muon bremsstrahlung and plays an important role in limiting the detectability of down-going neutrino showers on the ground. As a matter of fact, although the atmospheric muon flux is very soft and at sufficiently high energy the expected rate for showers induced by hard muon processes is expected to be very small, the muon bremsstrahlung rate is subject to uncertainties due to production of prompt muons through charmed mesons. Studies to quantify such a limitation are currently underway.

2.3 The experimental techniques

Three methods are currently used to detect EAS. The most generic and oldest method consists in distributing several particle counters spread over a large area and detecting directly those particles surviving to the detection level [87]. The area required depends on the rate of events which are expected to be detected, and for ultra-high energy cosmic rays must be several square kilometers. The separation of the detectors is chosen to match the scale of the footprint of the showers and it is usually of the order of several hundred meters. Finally, the size of the detectors is chosen appropriately for the component to be studied and it is generally of the order of $10\,\mathrm{m}^2$ for charged particles but ideally larger for muons. An array of surface detectors sample the surviving particles on the ground and measure the arrival times at each detector. Lateral distributions of densities and relative arrival times of signals allow one to measure energy and arrival direction of EAS, respectively. The precision in the measure of the shower arrival direction is limited by the accuracy of the timing measurement, by the detector sampling area and by background. A surface array has also sensitivity to the primary mass through direct or indirect measurement of the muon and electromagnetic content of the shower and/or indirect measurement of the shower maximum.

A second method exploits the excitation of nitrogen molecules by the shower particles and the subsequent de-excitation with emission of fluorescence light in the $300 - 400\,\mathrm{nm}$ band (see e.g. [96]). Fluorescence light, emitted isotropically, can be detected in clear nights (average duty cycle 10%) with photomultipliers which collect it from focusing mirrors as a time sequence of light. The profile of the shower can be inferred rather directly. Fluorescence detectors follow the trajectory of an extensive air shower and measure the energy dissipated by shower particles in the atmosphere that acts as an air calorimeter of more than 10^{10} ton. Correlation between the light intensity and light arrival time detected provides unambiguous information on energy released and shower path in the atmosphere.

A third method is related to the possibility to detect radio emission from charged particles in the geomagnetic field [97, 98]. In particular, coherent emission from electron-positron pairs or charge excess in the shower may be detected as pulses of $10 - 100$ ns from emission of synchrotron radiation by gyration of electrons in the Earth's magnetic field [99].

Air Cherenkov detectors can be used at lower energies (below 10^{17} eV) to detect Cherenkov light emitted by shower particles before they are absorbed in the atmosphere (see e.g. [100] for a review).

The first giant array of surface detectors was constructed at Volcano Ranch, New Mexico, in 1961 and collected data yielding the first measurements of the energy spectrum of cosmic ray above 10^{18} eV [101].

A large array of water Cherenkov detectors was started at Haverah Park, United Kingdom, in 1967. The largest event was reconstructed as a $37°$ shower produced by a primary at 10^{20} eV [102].

The only giant array which operated in the Southern Hemisphere before the Pierre Auger Observatory was built by the University of Sydney at Narribri, New South Wales, Australia. The Sidney University Giant Air-Shower Recorder (SUGAR) was important because provided a unique set for arrival direction studies in the Southern Hemisphere. The main difference between the SUGAR array and the Haverah Park array was in the type of detectors used. The former used scintillators which are more sensitive to electrons and positrons of the electromagnetic component of showers, but its sensitivity is limited by statistical fluctuations of the signal. An array of water Cherenkov detectors is, instead, roughly equally sensitive to both muons and electromagnetic component. Since muons suffer less Coulomb scattering, they tend to arrive earlier than the electromagnetic component at large distances from the shower core. The most promising mass indicator is the time structure of the signal (Sec. 2.1.1), so that water Cherenkov arrays can be better adopted to estimate the mass composition.

The Yakutsk array, Siberia, Russia, was the most complex of the giant arrays ever built. The construction started in 1970 and after some improvements in 1995 it provided detailed studies of the shower structure near 10^{18} eV.

The two most important pre-Auger era cosmic-ray detectors are the Fly's Eye detector, located in the western desert of Utah, USA, and operating from 1981 to 1992, and the Akeno Giant Air-Shower Array (AGASA), in operation at Akeno, Japan, and operating from 1990 for about 10 years. The former was a fluorescence detector which allowed measurement of the maximum depth of showers directly on a shower-by-shower basis for the first time. The Fly's Eye detector was improved to obtain a higher resolution and became the HiRes detector.

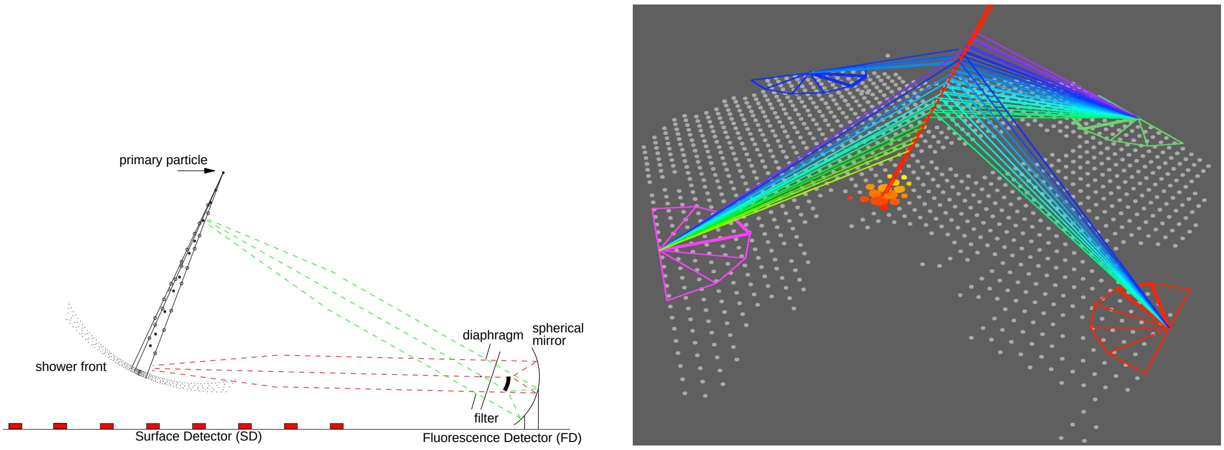

Figure 2.10: *(Left panel) Typical parameters characterizing the reconstruction of an EAS in hybrid mode (from Ref. [103]). (Right panel) Picture of detection of an EAS in the Pierre Auger Observatory.*

2.4 The hybrid technique: the Pierre Auger Observatory

The low event rate of the highest energy cosmic rays requires very large areas to gain good statistics in reasonable time. The Pierre Auger Observatory [7] combines the fluorescence detection technique with the surface counter technique in a hybrid detection technique (Fig. 2.10), which allows full characterization of the nature of EAS by improving the event reconstruction quality and reducing systematic errors. In addition, the independent measurements from both the detectors support important cross-checks and cross-calibrations. In particular, the shower energy can be obtained by determining the signal density at a particular distance from the estimated shower core (usually 1000 m) with the surface detector array. With the subset of events detected in hybrid mode, a nearly calorimetric energy determination, which is possible with the fluorescence detectors, can be used for an absolute calibration of the surface detector energy.

A first observatory is being completed in the Southern Hemisphere, in western side of Argentina, Province of Mendoza, while planning also to deploy a similar observatory in the Northern Hemisphere in Colorado, USA, so that a full-sky coverage can be achieved.

The Southern Site of the Pierre Auger Observatory covers an area of about 3000 km^2 with about 1600 water Cherenkov stations separated by a distance of 1500 m each other (Fig. 2.11, left) and arranged in a triangular grid. The aperture achieved until February 2007 for showers at zenith angle below 60° with such a detector is 7350 km$^2 \cdot$ sr. By adding events with zenith angle up to 80°, an increase of about 30% is obtained. The detectors are located in a large semi-desertic area at Malargüe, Argentina, at altitudes which range between 1340 and 1610 m above sea level, with an average altitude of 1420 m. At four different sites, on hills at the edges of the array, and overlooking it, four fluorescence detectors were built and operate during dark clear nights, working in coincidence with the ground

Figure 2.11: *(Left panel) Picture of a station of the surface array of the Pierre Auger Observatory with the Andes in the background. (Right panel) A fluorescence detector building [104].*

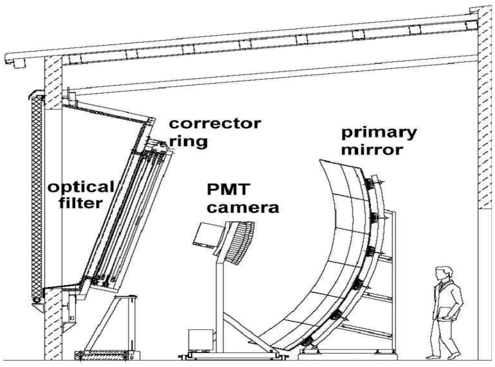

Figure 2.12: *Sketch of a fluorescence detector telescope.*

array. Each fluorescence detector (Fig. 2.11, right) consists of a building which houses 6 telescopes (eyes) with a $30^o \times 28.6^o$ viewing angle, leading to 180° azimuth angle coverage at each eye. The fluorescence light is focused through Schmidt-optics on spherical mirrors of about $11\,\mathrm{m}^2$ onto a camera consisting of 440 photomultipliers (Fig. 2.12). The signals are digitized with analog-to-digital converters at a frequency of 10 MHz leading to a pulse division of 100 ns. Two central laser facilities, located close to the center of the array, are used to fire laser shots into the sky to calibrate the response of the fluorescence detectors while operating. The largest uncertainties in the fluorescence detector measurements come from the precision of various atmospheric transmission, light multiple-scattering and cloud corrections. A program for atmosphere monitoring was undertaken to minimize these uncertainties. The Auger atmosphere monitoring program includes LIDAR stations (small receiver telescope and pulsed laser beam emitter) mounted at each fluorescence detector building which make routine surveys of the vertical profile of aerosols around the local fluorescence detector and, immediately after a shower detection, a scanning of the atmosphere to look for possible scattering inhomogeneities [105]. To complete the monitoring program, systems which monitor clouds, horizontal attenuation length, scattering phase function and meteorological situation were deployed on site [106].

An observatory campus is located in the town of Malargüe, at one edge of the array, with a data acquisition and storage station, office and assembly building.

In the next chapter more attention will be given to describing the surface detector array of the Pierre Auger Observatory, its properties and performances.

3

The Surface Detector Array of the Pierre Auger Observatory

Water Cherenkov detectors produce signals which can help to differentiate between muons and electrons in extensive air showers (see e.g. [107]). The relative numbers of muons and electrons is sensitive to the type of primary particle which has initiated a shower. Other experiments, such as Haverah Park (Sec. 2.3), successfully adopted such detectors [108]. A surface detector array (SD) consisting of several water Cherenkov detectors has a duty cycle of about 100% and allows coverage of areas whose dimension is roughly proportional to the energy of the cosmic-ray showers which are going to be detected. The Pierre Auger Observatory (Sec. 2.4) focuses its interest in the range of energies exceeding 10^{18} eV and comprises about 1600 water Cherenkov detectors covering a huge area of about $3000\,\mathrm{km}^2$ in the Southern Hemisphere (Fig. 3.1).

3.1 Design and properties

The surface detectors [7] of the Pierre Auger Observatory consist of cylindrical polyethylene plastic tanks with a circular base with a radius of 1.81 m and a height of 1.21 m (Fig. 3.2) filled with 12000 l of purified water (resistivity: $5-15\,\mathrm{M\Omega\cdot cm}$). A tank encloses a Tyvek liner for uniform reflection of the Cherenkov light produced by charged particles crossing its water at a speed larger than the speed of light in this medium. Two solar panels, mounted on its top surface, provide a power of 10 W for communication readout. The Global Positioning System (GPS) [109] provides a common time base for all of the tanks. Commercial GPS receivers (Motorola OnCore UT) emit 1 pulse per second and are used to synchronize a 100 MHz clock which serves to time-tag the local triggers. A IBM 403 PowerPC micro-controller is equipped for local data acquisition, detector monitoring, software trigger and memory for temporary data storage.

A fraction of the light produced by charged particles inside a station hits three 9" XP1805 photomultipliers (PMTs). The signal is read out from the anode and the last dynode of each PMT. The nominal amplification factor at the last dynode is 32, allowing a

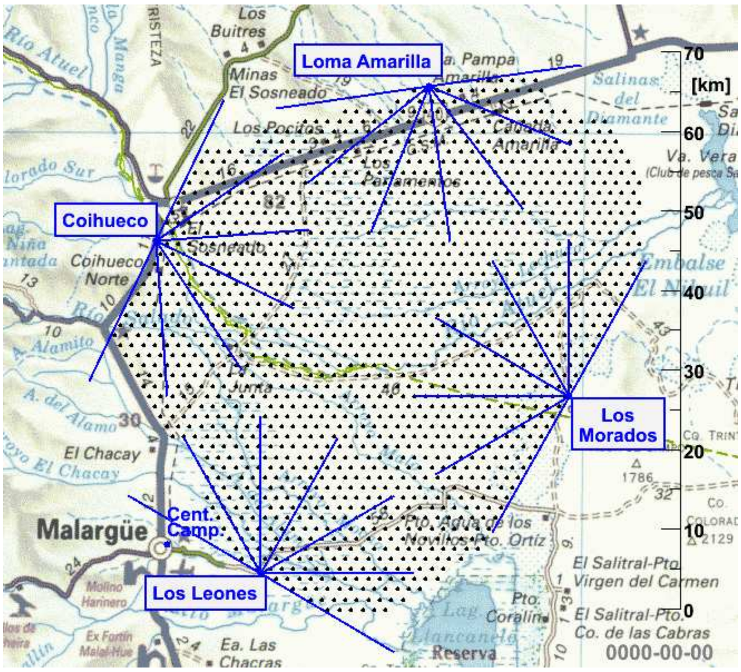

Figure 3.1: *View of the surface detector array of the Pierre Auger Observatory at its completion. The 4 telescope building sites, overlooking it, are also shown.*

dynamic range of 15 bits extending from a few to about 10^5 p.e. (1 p.e. = 1 photoelectron). The nominal operating gain of the PMTs is $2 \cdot 10^5$ and can be extended to 10^6. The photomultiplier signals are filtered and digitized in time slots of 25 ns by 10 bit flash-ADCs (FADCs) running at 40 MHz which returns signals in unit of channels with a range 0–1023 corresponding to $0 - 2\,\mathrm{V}$. A pedestal of 50 channels is added to the signal to observe possible fluctuation of its baseline. Finally, a programmable logic device (PLD), which reads from the FADC, implements a local trigger.

3.2 Calibration

The FADCs sample the current generated at the PMTs and return a measure of the light produced by particles crossing the water which fills a station. However, the Pierre Auger Observatory consists of several detectors whose properties, such as PMT gains, water quality, Tyvek reflectivity etc., do not guarantee equal counting in the corresponding FADCs. The signal detected at each station must refer, therefore, to a common calibration unit.

An automatic self-calibration procedure is required due to the remoteness and large number of detectors [110]. The calibration is based on the measurement of the charge collected by each PMT from the Cherenkov light produced by a vertical and central through-going (VCT) muon. At each detector the measurement is determined to 5–10% with a rate-based technique. A precision of 3% is obtained through the analysis of histograms of

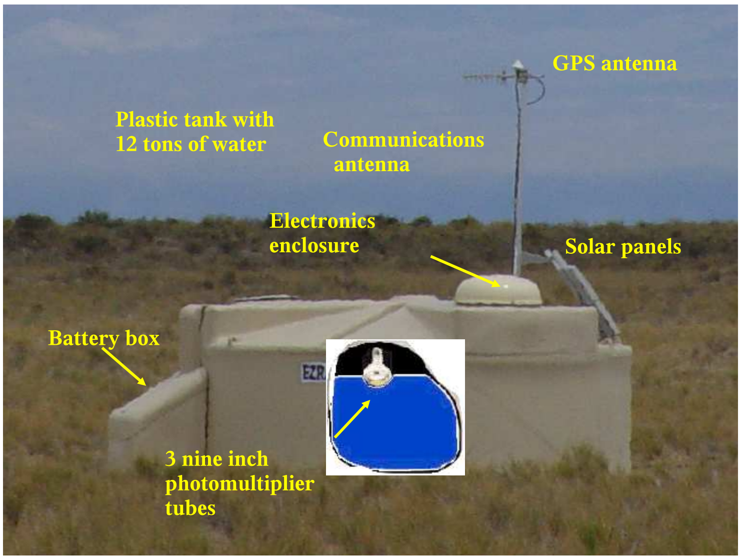

Figure 3.2: *Instrumentations mounted at an exemplary tank of the Pierre Auger Observatory.*

charge distribution.

A VCT muon produces light which is detected as collected charge and termed as vertical-equivalent muon (VEM) or Q^{peak}_{VEM}. This is the basic signal unit and provides a common reference level between stations. A surface detector can not discriminate between VCT muons and other inclined muons crossing it. However, a peak in the distribution of the charge can be related to the VEM unit. In particular, the sum of the signals produced in the three PMTs of a station produces a peak at about 1.09 VEM, whereas a value of 1.03 ± 0.02 VEM is measured for individual PMTs. The difference is due to the fact that a single PMT is sensitive only to the fraction of signal which is deposited in its proximity. A muon telescope of two centered scintillators, one above and the other underneath a tank, are typically used for laboratory measurements of the VEM unit. In Fig. 3.3, left panel, a typical charge histogram from a muon telescope and a station taking data is shown.

The peak produced in the charge histogram also produces a peak in the pulse height histogram and provides a common reference for the threshold levels of local triggers (Sec. 3.3). This peak is termed I^{peak}_{VEM}. In Fig. 3.3, right panel, a typical pulse height histogram from a muon telescope and a station taking data is shown.

Calibration task requires three principal studies to stabilize the VEM measurement. Specifically, one must set the gains of each of the three PMTs of a station to have I^{peak}_{VEM} at 50 channels, perform a local calibration to determine I^{peak}_{VEM} and compensate for the drifts occurring during the gain setting, and determine the peak from the charge histogram to obtain a high accuracy conversion factor from Q^{peak}_{VEM} to VEM. These steps must be carefully monitored to avoid systematic errors in the determination of signals. A detailed description of them can be found in Ref. [110] and will not be discussed further in this section.

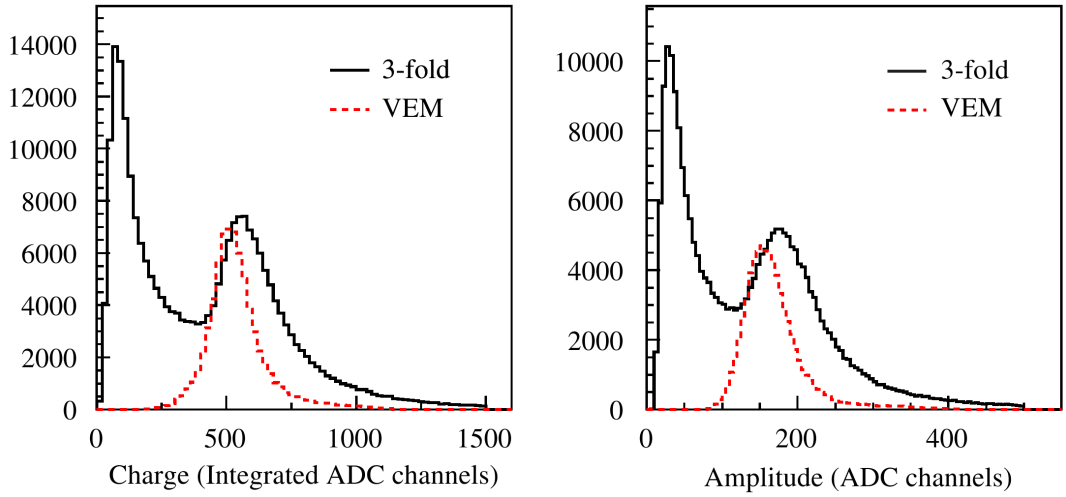

Figure 3.3: *Calibration histograms [110]. (Left panel) Charge histogram (3 PMTs summed) of light produced in a station crossed by atmospheric muons. The second peak in the 3-fold curve corresponds to the charge produced by single through-going muons. The dashed line correspond to events triggering a muon telescope (text for detail). (Right panel) Pulse height histogram.*

3.3 The hierarchy of the trigger system

The surface detector array triggering system [111] was designed as a hierarchy of three levels. From a local low-level trigger received from a single tank (T1 level), a station may be promoted to the set of second level trigger (T2) stations and finally be part of the multiplet of stations which form the highest level of hardware trigger (T3). An additional physics trigger (T4) was defined to select showers with energy above 10^{18} and incoming zenith angle directions below 60° [112] out of all the collected events.

A sketch of the level trigger thresholds implemented at each station is shown in Fig. 3.4. The T1 level trigger is evaluated by PLD units (Sec. 3.1) and aims to accept all of the signals which might be part of a physical shower. Two separate hardware triggers are implemented in each station to detect a T1 trigger: a simple threshold trigger (T1 Thr.) and a time-over-threshold trigger (T1 ToT). The T1 Thr. trigger requires a signal to be above $1.75\,\mathrm{I}_{\mathrm{VEM}}^{\mathrm{peak}}$ in at least 2 PMTs. The T1 Thr. trigger allows detection of very fast signals (100 Hz) which most of the time are produced by atmospheric muons[1]. A rate of 100 Hz per station is ensured by the calibration procedure. The nominal T1 ToT trigger requires the signal to be above $0.2\,\mathrm{I}_{\mathrm{VEM}}^{\mathrm{peak}}$ in at least 2 PMTs for a minimum of 13 bins (325 ns) within a sliding time window of 120 time bins ($3\,\mu$s). The ToT trigger appears to be the most powerful means to identify a stations belonging to a cosmic ray shower,

[1]It is not so rare to obtain a trigger with a peak of $1.75\,\mathrm{I}_{\mathrm{VEM}}^{\mathrm{peak}}$ and an area of $1\,\mathrm{Q}_{\mathrm{VEM}}$. It is even more possible in inclined events, where the signal is distinctly non-muon like due to direct light, i.e. light which hits the PMTS without suffering any reflection inside the station walls.

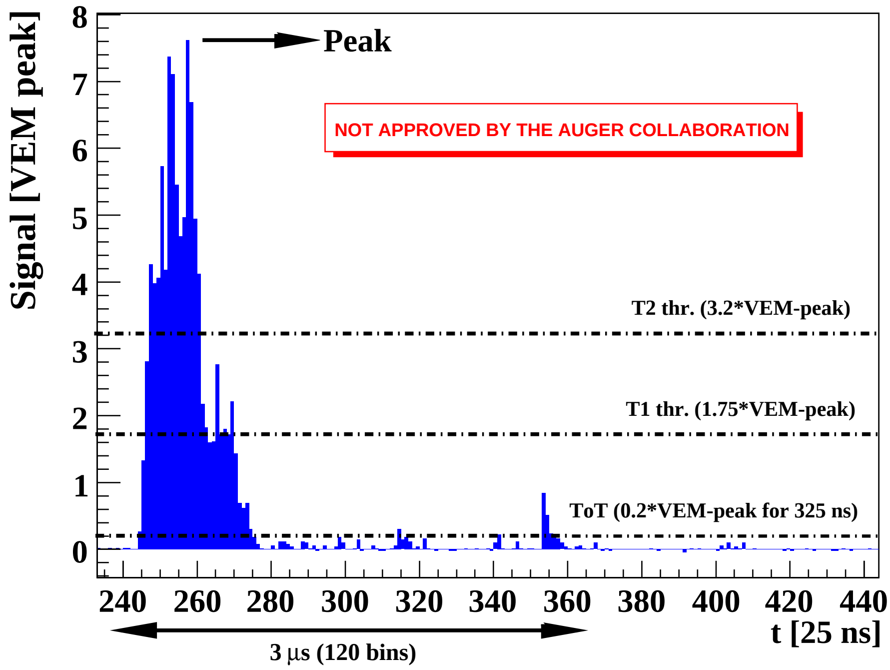

Figure 3.4: *Sketch of local trigger levels implemented at each station of the surface array of the Pierre Auger Observatory. The signal is in unit of I_{VEM}^{peak}. The peak is the maximum of the signal.*

and local stations marked as ToTs are directly promoted to the second level trigger (T2 ToT). The ToT rate per station is about 1.6 Hz. A T2 Thr. trigger was designed for the second level trigger along with the ToT trigger. Here the threshold is fixed to 3.2 $\mathrm{I}_{\mathrm{VEM}}^{\mathrm{peak}}$ and 3 PMTs in coincidence are required. The rate for such triggers is about 20 Hz. The intent of the T2 Thr. trigger is mostly to select the muonic component of horizontal showers. However, very energetic atmospheric muons, which form the background to the detection of cosmic rays (Sec. 4.2.2), may also satisfy the T2 level.

Stations marked as T2 may become part of the T3 decision, whereas T1 Thr. stations are included “a posteriori” in a multiplet of candidates identifying a shower only if their trigger times are in a time window of 60 μs around the central trigger time.

A central trigger (CT) algorithm [113] running at the Central Data Acquisition System (CDAS) of the Pierre Auger Observatory collects all the T2 triggering stations and identifies time coincidences between the collected station signals. The algorithm does not ensure that the selected stations are part of a real or physical event and a large number of accidental coincidences are expected to bias the decision due to low-energy showers and atmospheric muon background (Sec. 4.2.2).

Any time a station has a T2 trigger, it sends a signal to the CDAS with its trigger time (t_0). This station is considered as a central station. Other T2 triggers are searched in a time window of 50 μs with the requirement of satisfying one or more of the following

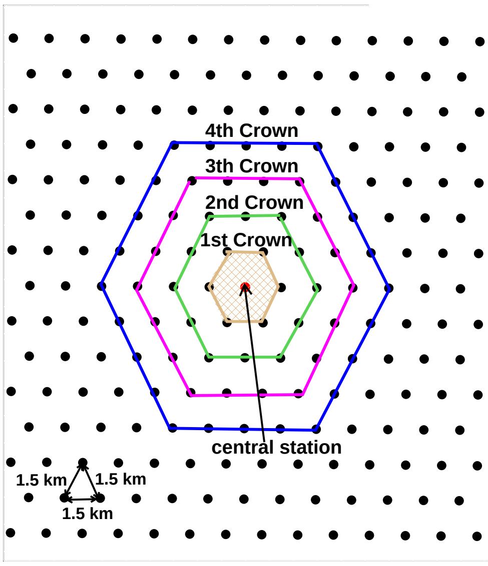

Figure 3.5: *Central station and scheme of the crowns around it.*

patterns:

- a 3-fold condition requiring the coincidence in time of 3 ToT stations within a time window which depends on their distance, according to the relation

$$t_i - t_0 < 5\mu s \times m + \Delta t, \tag{3.1}$$

  where t_i is the trigger time of the station i entering the condition, m the number of hexagonal crowns to be crossed to reach the station i from the central station (Fig. 3.5) and Δt is the GPS raw time uncertainty fixed to be 6 μs at the date. This condition allows a central station to have a neighboring station in the first crown and a second station within the first 2 crowns around the central one;

- a 4-fold condition requiring the coincidence of 4 stations passing the T2 level trigger within a time window which depends on their distance (Eq. 3.1). This condition allows a central station to have two stations inside the first 2 crowns and a further station within 4 crowns;

- a 3-fold condition requiring the coincidence of three aligned stations passing any of the T2 triggers;

- an external condition generated by the fluorescence detector.

A typical pattern for a possible physical shower which satisfies the CT algorithm may consist of a combination of successful conditions linked with the "&" symbol. The pattern 3ToT indicates that a multiplet of stations was selected as part of a physical shower, since it

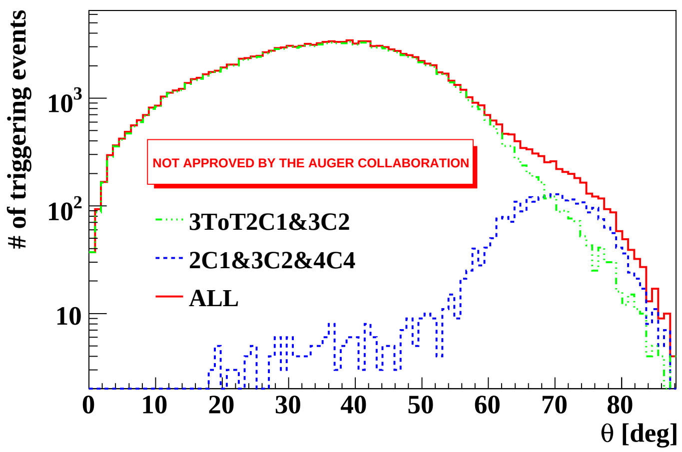

Figure 3.6: *Events triggering the surface detector array in 2005 versus reconstructed zenith angle. It is evident that the condition 2C1&3C2&4C4 is important to save more inclined events.*

passed the first of the 3-fold conditions above described, and the additional term $(n+1)Cm$, with $n+1$ the total number of triggers, 1 at the center of m hexagonal crowns and n around it, gives further information about the trigger type. In particular, the pattern allowed by the first condition is termed 3ToT2C1&3C2, whereas the 4-fold condition results in a pattern termed as 2C1&3C2&4C4. The trigger termed as 3ToT2C1&3C2 is very efficient for showers whose zenith angle is below 60°, and 90% of the events selected with this pattern are physical showers. Only 2% of the events selected with the second pattern are real showers. Nevertheless, such a trigger is needed for the detection of horizontal showers (Fig. 3.6). The trigger rate at CT input and output is limited to 32 kHz (20 Hz of local trigger rate times 1600 stations) and 0.2 Hz, respectively. The CT decision delay does not exceed about 1 second. These performances depend strongly on the minimal communication network bandwidth between local stations and the central station, and the local station event data buffer size. The set of triggering stations which pass the CT requirement is called *footprint*. A typical footprint for a shower with a zenith angle of 50°, azimuth angle of 141°, and energy $1.3 \cdot 10^{20}$ eV is shown in Fig. 3.7 (left panel).

The two highest level triggers implemented for the surface array of the Pierre Auger Observatory are the so-called *physics trigger* (T4) and the *quality trigger* (T5). Both are currently used to discriminate high quality showers from the bulk of all of the detected showers. The T4 trigger requires that an event has a station forming a triangle with 2 neighbors in its first crown (3ToT3C1, Fig. 3.8) or a compact configuration of type 4C1 (Fig. 3.9). This second configuration was added to save more horizontal events which present typically more aligned footprints on the ground. The T5 trigger selects only those events which can be reconstructed with a good angular accuracy after having passed the T4 condition. Events marked as T5 have also reconstructed energy. To the T5 conditions, an additional requirement is added in order to calculate the acceptance of the detector for

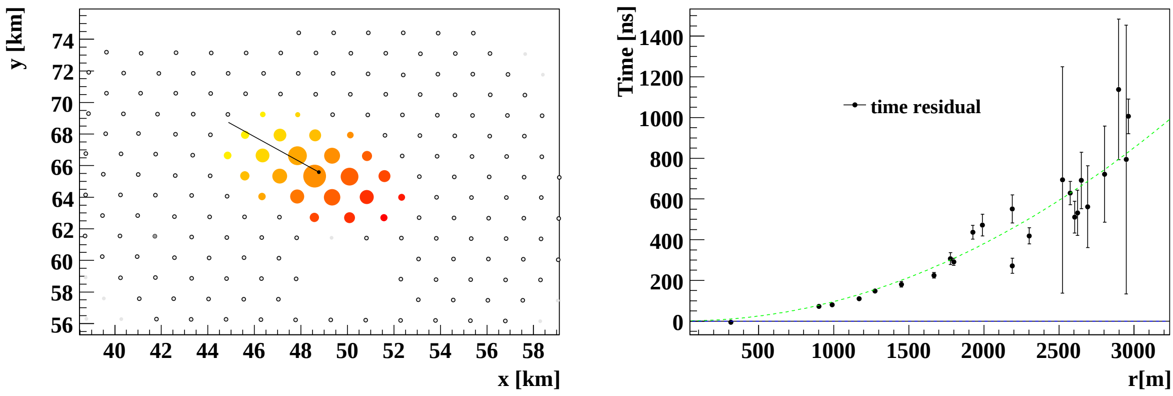

Figure 3.7: *(Left panel) Typical footprint of a triggering shower. The full colored circles represent the triggering stations which satisfy the CT requirement. The size of the circles is proportional to the energy released by the shower particles inside the corresponding station. The arrow points to the estimated core position. The arrow direction indicates the azimuth angle. (Right panel) Time residual of measured arrival times at the triggering stations with respect to the estimated arrival times from a plane fit for the reconstruction of the shower direction (Sec. 3.4). The time residual is plotted as a function of the distance of stations from the core.*

showers whose zenith angle is below 60°. The current condition for acceptance purposes requires that the station with the highest signal is surrounded by at least 6 working stations in the first crown. This allows for good shower reconstruction due to the fact that shower footprints with missing parts may give bad reconstructed shower parameters, such as the core position which is important for the energy reconstruction.

3.4 Selection of candidate stations and geometrical reconstruction

Stations which have passed the central trigger requirements are removed from an event in case of bad calibration and/or timing information. An additional station rejection is based on space-time compatibility of triggering stations in order to eliminate stations hit by atmospheric muons which might bias the following shower reconstruction. At the end, the stations which enter the reconstruction procedure are the ones which have passed the trigger condition and have been selected as *candidate* stations by a *selection* algorithm.

The current algorithm [114] is based on the selection of a *seed* of three stations which form the edges of an equilateral triangle (the basic component of the surface array) or a skewed isosceles triangle. A space compatibility is required at the beginning to clean the set of possible candidate stations from *isolated* (also called *lonely*) stations which might be produced by atmospheric muons. At this stage a station is marked as *accidental* if it does not have any neighbor within a distance of 1800 m or only one neighbor within 5000 m.

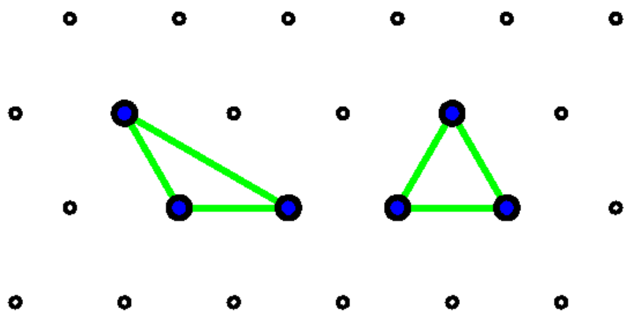

Figure 3.8: *Scheme of typical T4 triggers of type 3ToT3C1 [115].*

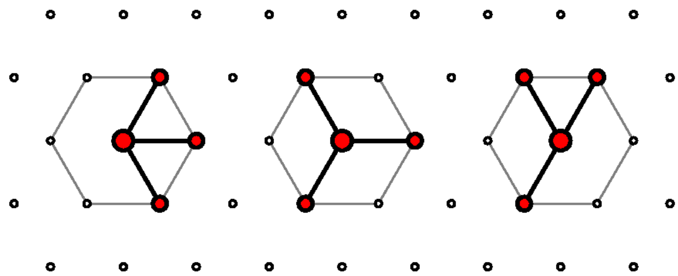

Figure 3.9: *Scheme of typical T4 triggers of type 4C1 [115].*

The seed is then identified among all the candidate stations which form a T4 pattern (Fig. 3.8 and Fig. 3.9) and maximize the sum of their signals. When the seed is found, it is considered as a compact starting point which allows selection of the candidate stations by means of a *bottom-up* procedure based on time compatibility of stations with the plane through the seed. For a station i to be selected, the allowed delay Δt_i with respect to the plane through the seed is given by the condition

$$-1000\,\mathrm{ns} < \Delta t_i < 2000\,\mathrm{ns}. \tag{3.2}$$

The asymmetry in the choice of values is due to the curvature of the shower front such that signals in stations with a lower density of particles are likely more delayed. More information on this topic will be given later in this section.

Finally the selected stations are marked as candidates and enter the reconstruction procedure. The current selection algorithm [115] works very well for showers whose axis has a zenith angle below 60° [112]. Above 60° the selection looses about 20% of events and marks a few good stations as *accidental* stations.

In particular, the selection presented here is not very effective for most of the events which show aligned footprints. In these cases, it is hard to find a seed through which a plane can be fit. Therefore, a different selection algorithm is adopted to clean events which are possibly induced by neutrinos (Chap. 5).

The geometrical reconstruction or angular reconstruction of an atmospheric shower is

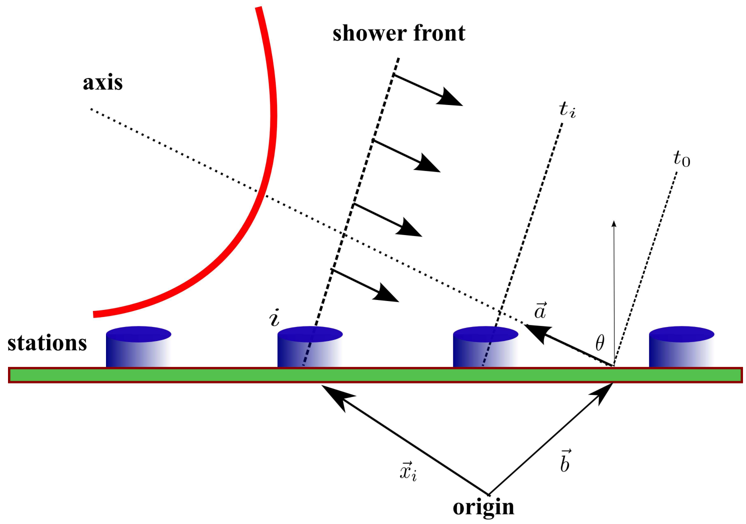

Figure 3.10: *Sketch of the angular reconstruction with the surface detector array. The vector $\vec{a}$ represents the shower axis with component (u, v, w), the vector $\vec{b}$ represents the position of the estimated core position in the site reference system.*

driven by the quality of the measurement of the arrival time of the first particles of the shower front in triggered stations. The time structure of the shower front relates to the shower geometry. Approximating the shower front with a plane moving at the speed of light c from the interaction point of a primary in the atmosphere (Fig. 3.10), the predicted arrival time t_i of the first particle at the station i is related to the components of the shower axis according to the following equation

$$t_i = T_0 - \frac{u\,(x_i - x_{core}) + v\,(y_i - y_{core}) + w\,(z_i - z_{core})}{c}, \tag{3.3}$$

where T_0 is the shower arrival time at the ground (event time) or core time, x_{core}, y_{core} and z_{core} the core position on the ground in the site reference system, x_i, y_i and z_i the position of the station i in the same reference system, and u, v and w the components of the vector of the expected shower axis pointing opposite to the arrival direction.

In order to reconstruct the shower arrival direction, an iterative minimization of the χ^2 [115], given by the following expression

$$\chi^2 = \sum_{i=0}^{n} \frac{\Delta T_i^2}{\sigma_i^2} = \sum_{i=1}^{n} \frac{(t_{i,meas} - t_i)^2}{\sigma_i^2}, \tag{3.4}$$

is used. In this equation $t_{i,meas}$ is the measured arrival time at the station i, i.e. the realization in the station i of the estimator of the predicted arrival time t_i (Eq. 3.3), σ_i is the uncertainty on $t_{i,meas}$ and the index i runs over stations which were selected as candidates to be reconstructed.

The core position as well as the event time which enter Eq. 3.3 are not crucial for the estimation of the axis direction. As a starting point and good estimation of the core position and event time, the reconstruction procedure takes respectively the barycenter of the stations, $\overrightarrow{b}$, defined as

$$\overrightarrow{b} = \frac{\sum_{i=1}^{n} w_i \overrightarrow{p_i}}{\sum_{i=1}^{n} w_i}, \tag{3.5}$$

and the barytime, b_t, defined as

$$b_t = \frac{\sum_{i=1}^{n} w_i \left(t_{i,meas} - T_t\right)}{\sum_{i=1}^{n} w_i}, \tag{3.6}$$

where $\overrightarrow{p_i}$ is the positional vector for the station i in the site reference system, T_t is the trigger time for the shower and w_i is a weight $\sqrt{S_i}$, where S_i is the integrated signal measured at the station i. The χ^2, expressed in Eq. 3.4, constrains a non-linear problem due to the condition

$$u^2 + v^2 + w^2 = 1 \tag{3.7}$$

which is implicitly involved. A first attempt to solve the problem lies in approximating z_i and, thus, $z_{core} \ll x_i, y_i$ such that u and w can be obtained by solving the linear equation in u^2 and v^2 [115]. The third component of the axis, w, is obtained from Eq. 3.7, if w^2 is physical, i.e. $w^2 \geq 0$.

It must be noticed that the uncertainty σ_i depends on the shower incoming direction and the fluctuations of the station signal. The first linear solution of the problem is obtained by fixing the maximum value of σ_i (for $w = 0$).

A second estimate of the shower incoming direction is done to improve the first solution with a new value for the uncertainty σ_i, obtained for the estimated w.

A non-linear fit is then obtained by minimizing the χ^2 with the help of MINUIT [116], a function minimization library. The linear approximation is used to provide initialization values. In Fig. 3.7 (right panel) an example of residual of fit after minimization is shown.

The two factors which affect mainly the minimization process of the χ^2 are the measured arrival time $t_{i,meas}$ and its error σ_i. From a physical point of view, the angular reconstruction accuracy depends substantially on:

- clock precision (GPS system and internal clock) and definition of measured arrival time;
- particle sampling;
- shower front definition (thickness of the shower front).

In order to make these points clear, it is useful to go deeper through them.

It is quite obvious that the accuracy with which one can measure the arrival time of the shower front in each station has an irreducible uncertainty. As a matter of fact, this uncertainty is related to the measure of the FADC traces of the photomultipliers and it is a discrete variable with steps of 25 ns[2]. The signal start time is defined as the time

[2]the maximum length of a trace is $19.2\,\mu$s.

slot when the integrated signal reaches a given threshold (in p.e.). The signal start time is chosen as measured arrival time. For this reason, the signal "start time" is commonly misunderstood as the arrival time of the first particle at a station. However, the arrival time may be delayed with respect to the signal start time[3] [117]. Therefore, in order to improve the measurement of the arrival time, one should add to the signal start time a factor which gets it closer to the physical arrival time. Moreover, one should take into account that electrons have a much larger cross-section than muons for multiple scattering and bremsstrahlung. As a result, muons are the earliest particles arriving at the ground because they undergo less deflection in their trajectories. In addition, muons are highly penetrating and dominate the signal. Therefore, a more precise model of the arrival time of the shower front at the ground is required in order to improve measurement [77].

The particle sampling effect is due to the decrease of the particle density observed as one measures signals in stations further and further away from the core. As a consequence, a flattening of the rise time of the signal is observed: the collection of particles in a station far from the core takes more time to pass due to the larger thickness of the shower front, but at the same time the particle density is low.

The front definition is related to the sampling effect. Away from the core the shower front does not present a well defined profile because of the lower particle density.

The latter two effects produce large fluctuations in the signal start time when distances from the core of the order of about 2000 m on the shower plane and beyond are considered. It is, thus, necessary to handle properly the large uncertainties in the signal start time for stations beyond about 2000 m from the core for accurate angular reconstructions.

In order to reproduce more realistically the structure of the shower front, a term involving its curvature can be added to Eq. 3.3. A first attempt to estimate the curvature can be done by using a parabolic analytical approximation for the shower front and expanding Eq. 3.3 to take into account such a term, as shown in the following equation

$$t_i = T_0 - \frac{u\,(x_i - x_{core}) + v\,(y_i - y_{core}) + w\,(z_i - z_{core})}{c} + \frac{\rho_i^2}{2R_c c}. \tag{3.8}$$

Here ρ_i represents the perpendicular distance of the station i from the axis and R_c the expected radius of curvature of the shower front. A different approach can be obtained by approximating the shower front as an expanding sphere from the primary interaction point in the atmosphere. Details of the calculations can be found in Ref. [115].

The curvature effect should be considered when one deals with vertical showers or in general with young showers, such as neutrino-induced showers. Electrons, which are copiously produced close to the shower maximum, suffer scattering processes which delay them from an ideal plane. In fact, starting from the first interaction point in the atmosphere, all of the secondary particles suffer deviations from the shower axis as the shower develops in the atmosphere. The larger is the deviation from the axis, the longer the particles travel until they arrive at the ground. The particles accumulate a geometrical

[3] a 1 MeV electron or photon may give no photoelectron at all and, if they are the first particles arriving at a station, they will not trigger it.

delay with respect to the shower plane: the result is an approximately spherical shower front. Three further mechanisms should be considered to better reproduce the physics of the shower front evolution: a contribution of the geomagnetic field, important for very inclined showers, the effect of Coulomb scattering in the atmosphere and the sub-luminal velocities. These effects give, however, only a small contribution to the overall curvature of the shower front and the main contribution is mostly due to the geometrical delay of particles respect to the shower plane (Sec. 2.1.2). Finally, another important effect which contributes to the distortion of the simplified spherical geometry of the shower front is the early-late asymmetry of the measured arrival times. The signals measured on the ground do not depend only on the perpendicular distance from the shower axis. In the case of inclined showers, due to the longitudinal development of the cascade in the atmosphere and the consequent attenuation, the geometry of the detector and the overall evolution of the shower, the particles which first hit the ground represent a different stage of the development of the cascade than the particles which arrive later [118, 119].

In the case of very inclined hadronic showers, the shower front consists mainly of muons which make the structure of the shower front appear flat, so that a plane fit gives a good approximation of the incoming direction.

3.5 The framework $\overline{\text{Off}}\underline{\text{line}}$ of the Pierre Auger Observatory

The $\overline{\text{Off}}\underline{\text{line}}$ software framework [120] of the Pierre Auger Observatory was designed to provide a flexible and robust infrastructure of classes and utilities to support the analysis of data from a large number of physicists developing a variety of applications over the projected 20-year lifetime of the experiment.

In particular, the $\overline{\text{Off}}\underline{\text{line}}$ framework includes the possibility to simulate and reconstruct events using surface, fluorescence and hybrid method. The algorithms which implement the physics code can be easily changed or modified to meet the requirements of specific analyses. The $\overline{\text{Off}}\underline{\text{line}}$ software consists of three principal parts:

- a collection of processing modules which can be sequenced through instructions provided in XML files;
- an event structure which allows storage of all simulation and reconstruction information;
- a detector description including the configuration and performance of the Observatory as well as atmospheric conditions as a function of time.

In the following sections a short description of typical simulation and reconstruction sequences used for surface events will be reviewed. Specifically, a short description of modifications adopted in order to study neutrino-induced showers will be given.

3.5.1 Simulation chain

Once an EAS has been simulated using one of the different simulation package formats supported (AIRES [121, 122], CORSIKA [123, 124] and CONEX [125]), $\overline{\text{Off}}\underline{\text{line}}$ can be used to reproduce the response of the surface array of the Pierre Auger Observatory through a set of input/output modules which are listed in App. A.1 for a typical sequence. The typical sequence presented there was slightly modified to meet the requirements of the present work. In particular, a modified version of the resampler, *CachedShowerRegeneratorAT*, was introduced (Sec. 4.2.1 and App. B) and a new module, *AccidentalInjectorAT*, was added to simulate the background from atmospheric muons (Sec. 4.2.2 and App. C).

3.5.2 Reconstruction chain

The event data structure of a simulated shower contains all calibrated and Monte Carlo data and it is ready to be analyzed by a sequence of modules implementing the desired physics applications. A real event presents the same structure.

A typical reconstruction module sequence includes the algorithms for the station selection, the geometrical reconstruction and the energy reconstruction, as reported in App. A.2.

The same module sequence was used both for Monte Carlo data (Chap. 5) and measured data analysis (Chap. 6).

4

Neutrino shower detection at the surface array

Studying the signatures expected from neutrino-induced showers at the surface array of the Pierre Auger Observatory involves a sequence of correlated steps which can not be based completely on deterministic input modeling. Once a flux of astrophysical neutrinos has been chosen, a set of coupled degrees of freedom, which arise from the use of different physical models, such as neutrino propagation, cross-section, energy loss, and lepton/hadron shower development in the atmosphere, makes it difficult to assign properly each uncertain variable. A semi-analytical or semi-deterministic approach was already proposed and results are available in Ref. [126, 127, 94]. In this work a complete Monte Carlo (MC) chain is adopted.

A MC approach was used to study sensitivity and event rates for up-going ν_τ-induced showers by including local-topography conditions [85]. The results were compared with the previous work of Refs. [81, 84] and showed a significant enhancement of the sensitivity due to the presence of the Andes mountains surrounding the Pierre Auger Observatory. An earlier estimate of the sensitivity and event rates for ν_τ-induced showers at the Pierre Auger Observatory based on a MC approach [14] was found to be in agreement with this work. A preliminary study for the fluorescence detector was also attempted and showed the promising results of this MC chain.

Recently many modifications and improvements were implemented, among which the possibility to study the impact of different interaction and cross-section models to evaluate the systematic uncertainties [34], and the implementation of a complete set of tools to reconstruct neutrino-induced shower simulations and to study the identification efficiency of the surface array. Many shower simulations were performed by scanning zenith angles of possible incoming directions both in the up-going ($90° - 95°$) and in the down-going ($60° - 90°$) range. Discrete energy bins above the detector threshold (10^{17} eV) and up to the highest value of 10^{21} eV were considered.

Still the huge amount of data can not be considered yet as an exhaustive library of neutrino shower simulations, but it allows the study of detection and identification efficiency and to place the basis of a serious procedure to discriminate expected ν-shower signatures in measured data and find possible neutrino candidates.

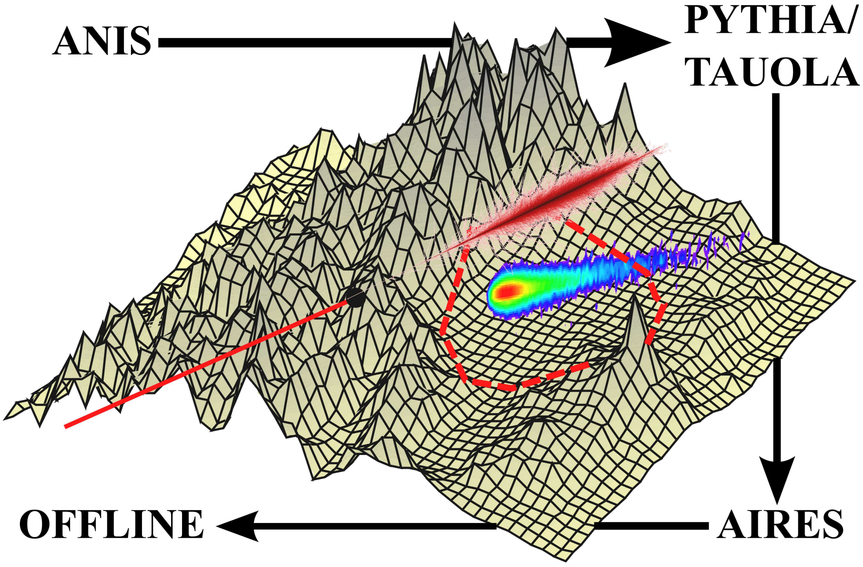

Figure 4.1: *Scheme of the MC chain set to simulate neutrino-induced showers at the Pierre Auger Observatory. A description of the programs, tools and results involved will be discussed in detail in this chapter.*

It is interesting to note that the MC chain was also used to study the sensitivity of the proposed Northern Observatory (Sec. 2.4) [128, 129].

In this chapter the attention will be focused on the simulation of neutrino-induced showers at the southern site of the Pierre Auger Observatory and the study of the detection efficiency of the surface array of the Observatory. In the next two chapters the reconstruction of simulated and measured data will be discussed.

The MC chain (Sec. 4.1) includes the simulation of the flux of leptons expected to produce a shower in the detector volume (Sec. 4.1.1), the simulation of extensive air showers (EAS), namely particle density distributions on the ground (Sec. 4.1.2), and the simulation of the detector response by including all the performances of the Surface Array (Sec. 4.2). A scheme which summarizes all the steps involved is shown in Fig. 4.1.

Modifications to the existing codes, which are normally used to handle vertical and horizontal ordinary showers, either hadrons or photons, were done. In particular, a modified resampling/un-thinning algorithm was adopted (Sec. 4.2.1) and the possibility to introduce stations with background signals, produced by atmospheric muons, was added (Sec. 4.2.2). Atmospheric muons produce signals which may bias the following shower reconstruction. The investigation of such signals can help to improve the current selection and geometrical reconstruction algorithms (Chap. 5).

Finally, the expected detection efficiencies at different neutrino energies, flavors and for up-going and down-going neutrinos are discussed in Sec. 4.3.

4.1 Simulating neutrino-induced showers

The starting point is the definition of the incoming isotropic flux of astrophysical neutrinos. The chosen reference flux is a power-law of type $\Phi(E_{\nu+\bar{\nu}}) \sim E^{-2}$.

It is important to model neutrino propagation and interaction in the medium around the detector. Therefore, Earth and atmosphere need also suitable modeling. Since, for the energies at which the detector is more sensible, the Earth is opaque to neutrinos, it turns out that only earth-skimming tau neutrinos and/or down-going electron neutrinos may initiate detectable showers in the atmosphere (Sec. 1.3). The former may produce τ leptons close to the detector surface after many regenerations in the Earth's crust. A τ lepton has an interaction length of a few kilometers at the energy of about 1 EeV and, therefore, it may emerge from the Earth's crust and decay just above the detector, initiating a potentially detectable shower. The latter may initiate electron showers which develop faster than hadronic showers in the atmosphere. As a matter of fact, since the electromagnetic component is more absorbed by the atmosphere than the other components of a shower, an incoming ν_e shower is expected to be initiated close to the detector and/or in a distance from the detector such that its energy is still able to produce a shower surviving the attenuation.

Up-going and down-going muon neutrinos have a lower probability to be detected but, yet, they have a not negligible chance to produce detectable showers and they are accounted for the evaluation of the detector sensitivity. Thus, although dedicated ν_μ-shower simulations were not performed, their contribution to the sensitivity and event rates can be included.

The production of EAS which are induced by neutrinos consists of three phases: the propagation and interaction inside the Earth and atmosphere to produce the primary able to initiate a potentially detectable shower in the atmosphere; the simulation of the initiated shower in the atmosphere and, finally, the simulation of the detector response.

In the following sections the three phases will be discussed in more detail.

4.1.1 Earth simulations and flux of emerging leptons

The initial flux of incoming neutrinos is propagated through matter (Earth, its atmosphere or both) until an interaction takes place. The interaction is modeled by an extended version of the code ANIS [130, 85].

First, for fixed neutrino energies, 10^6 events were generated with zenith angles in the range $[60°, 90°]$ (down-going showers) and $[90°, 95°]$ (up-going showers) and with azimuth angles in the range $[0°, 360°[$ on the top of the atmosphere. Then, neutrinos were propagated along their trajectories of length Δl from the generation point to the backside of the detector array (Fig. 4.2, left panel) in steps of $\Delta l/1000$ (≥ 6 km). At each step of propagation, the ν–nucleon interaction probability was calculated according to different parameterizations of its cross-section based on the chosen parton distribution function (Sec. 1.3.1). In particular, the propagation of τ leptons through the Earth was simulated with different energy loss models. Electrons were assumed to interact immediately with

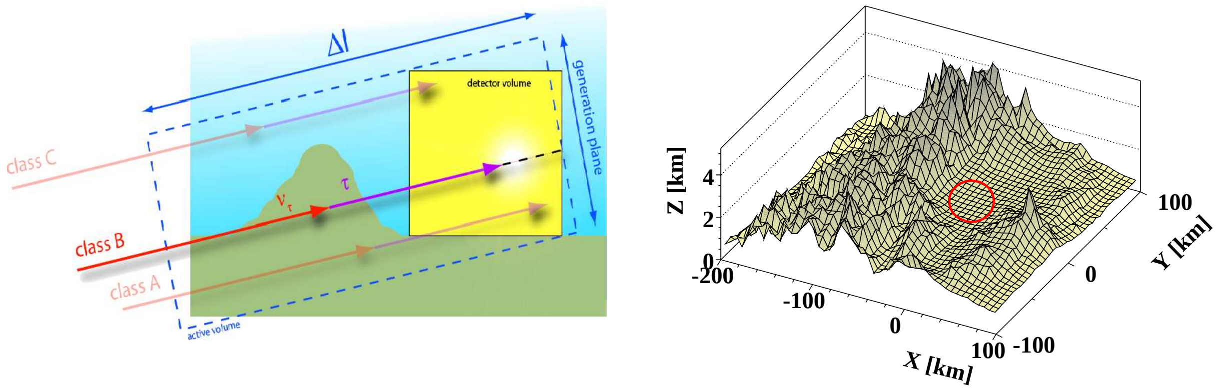

Figure 4.2: *Neutrino simulation of the southern site of the Observatory by using ANIS. (Left panel) Sketch of the geometry relevant for neutrino simulations in ANIS. The active volume describes the area, where a neutrino may undergo a potentially detectable interaction [85, 34]. (Right panel) Topography of the Southern site according to CGIAR-CSI data [131]. The center of the map corresponds to the center of the Auger array (latitude* $\phi_{SO} = 35.25°$ *S, longitude* $\lambda_{Auger\,center} = 69.25°$ *W). The Auger position is marked by a circle.*

the surrounding medium. If the interaction takes place in the atmosphere, an EAS is produced. A detailed study of the systematic uncertainties, derived by the use of different cross-section and interaction models, on the sensitivity and on the event rate calculations has been started with the work presented in Ref. [34]. In Sec. 5.9 the systematic effects on the event rates will be evaluated in more detail.

All the computations were done by using digital elevation maps (DEM) [131] and were repeated by using the spherical model of the Earth (SP), with its radius set to 6371 km (sea level). In Fig. 4.2 (right panel) the topography of the Southern site of the Pierre Auger Observatory is shown. The flux of the out-coming leptons as well as their energy and the decay vertex positions were calculated inside a defined detector volume. For the Southern Observatory, the geometrical size of the detector volume was set to $50 \times 60 \times 10\,\mathrm{km}^3$ and it contained the real shape of the Auger Observatory on the ground at its completion. The detector was positioned at 1430 m above sea level, which corresponds approximately to the average altitude of the array. In case of computations with the simple spherical model of the Earth, the same size of the detector volume was assumed, but the detector position was set at 10 m above the sea level.

The additional out-coming particle spectrum from deep inelastic NC and CC ν-nucleon interactions was simulated by using the event generator PYTHIA [132]. PYTHIA is an event generator for high-energy processes, with particular emphasis on detailed simulation of QCD parton showers, such as simulation of hadronic final states and internal jet structures. In Fig. 4.3 a typical out-coming spectrum of hadronic products from ν_e NC interactions is shown. In Fig. 4.4 the distribution of the inelasticity[1] of ν_e CC and NC

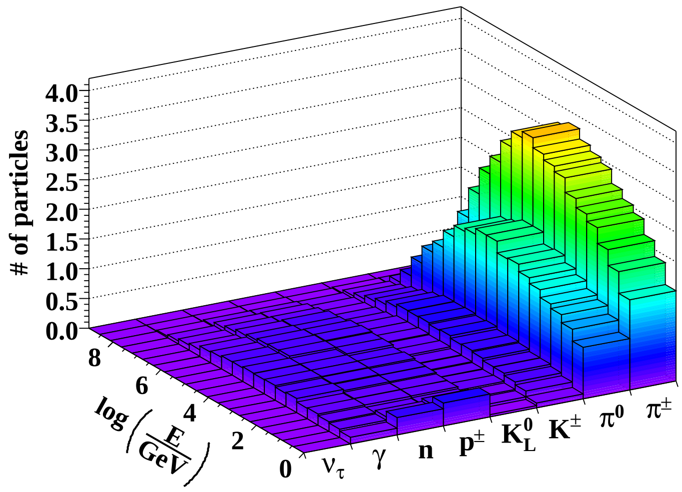

Figure 4.3: *Typical spectrum of hadronic products for ν_e NC interactions from the PYTHIA generator with the GRV98lo parton distribution [34].*

interactions is is given. Both the distributions show a similar behavior and the average values agree quite well with the canonical value of 0.2.

In case of ν_e CC interactions, the out-coming electrons are expected to induce electromagnetic showers at the same point where the hadronic products induce hadronic showers. In case of ν_τ CC interactions, the produced taus can travel some distance in the atmosphere and decay into particles which can induce a detectable shower. Thus, hadronic showers initiated by ν_τ are usually separated from the shower initiated by τ decay products by a certain distance (Sec. 1.3). In this particular case, τ decays were simulated by using the additional package TAUOLA [133].

Finally, the muons produced in ν_μ CC interactions are expected to induce showers which are generally weaker, with a smaller energy transfer to the EAS, and with a suppressed longitudinal profile and much fewer particles on the ground [134]. The detection probability is expected to be reduced.

Interactions in the NC channel induce only pure hadronic showers whose primaries are generated with PYTHIA.

4.1.2 Simulation of extensive air showers

To investigate the response of the Auger detector, 2-dimensional particle density distributions of secondaries were generated by using PYTHIA output as input for the EAS MC generator AIRES [121, 122]. In case of τ leptons, products from the TAUOLA generator were inputed to AIRES. The particle density distributions of secondaries produced by AIRES on the ground were stored. A special mode was used to inject simultaneously

[1]The inelasticity is defined as the fraction of energy which is carried away by the hadronic component.

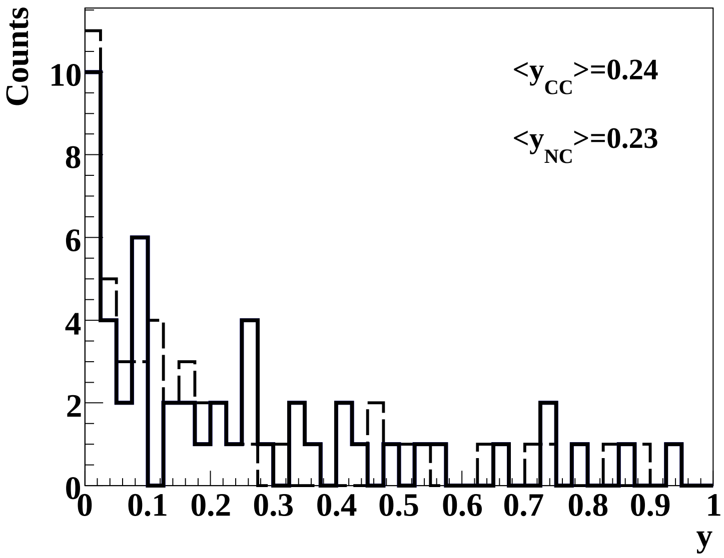

Figure 4.4: *The inelasticity distribution in CC (solid line) and NC (dashed line) interactions of 50 simulated events, as obtained from PYTHIA, at* $E_\nu = 10^{18}\,\mathrm{eV}$ *with the GRV98lo parton distribution.*

several particles or primaries (namely, the products of ν-nucleon interactions) at a given interaction point.

Showers induced by the products of up-going decaying τ leptons with energies from 0.1 EeV to 100 EeV at altitudes of decay points h from 0 to 3500 m above the ground level, in steps of 100 m, were simulated. At each altitude 40 events were generated to cover the τ decay channels implemented in ANIS (Tab. 4.1). In case of down-going showers, the decay altitudes were distributed from the ground level up to the altitude corresponding to the beginning of the atmosphere for a given zenith angle. For example, for down-going electrons, the particles produced by PYTHIA were inserted at different slant depths[2] measured from the ground up to 3000 g/cm^2 in steps of 200 g/cm^2. At zenith angles $\theta > 80°$, the simulations were done at slant depths, measured from the ground, starting from 50 g/cm^2 up to 8000 g/cm^2 in steps of 200 g/cm^2. Finally, a thinning algorithm [135] was selected, with a thinning level of 10^{-7} (Sec. 4.2.1). The kinetic energy thresholds for explicitly tracking particles were set to: 100 , 100 , 0.25 , 0.25 MeV for hadrons, muons, electrons and photons, respectively. In Tab. 4.2, a summary of the actual status of the performed neutrino simulations is reported. These simulations allow a study of the properties of neutrino-induced showers in the energy and angular observation window where the expected incoming flux gives the largest contribution to the event rates. More simulations were planned to be done in order to cover the left gaps in the angular window.

It has to be noted that not all of the combinations of interaction channels (NC or CC) with neutrino flavors (ν_e, ν_μ, ν_τ) are necessary to be simulated (see also Sec. 1.3.1).

[2]The Earth's curvature is taken into account to calculate the slant depth (Fig. 2.2 and Sec. 2.1).

Table 4.1: Tau decay channels implemented in ANIS [34]. The number of air showers which can be induced by a decay mode is shown in the last column.

Decay	Secondaries	Probability	Air-shower
$\tau \to \mu^- \bar{\nu}_\mu \nu_\tau$	μ^-	17.39 %	unobservable
$\tau \to e^- \bar{\nu}_e \nu_\tau$	e^-	17.85 %	1 e/m
$\tau \to \pi^- \nu_\tau$	π^-	11.08 %	1 hadr.
$\tau \to \pi^- \pi^0 \nu_\tau$	π^-, $\pi^0 \to 2\gamma$	25.37 %	1 hadr., 2 e/m
$\tau \to \pi^- \pi^0 \pi^0 \nu_\tau$	π^-, $2\pi^0 \to 4\gamma$	9.19 %	1 hadr., 4 e/m
$\tau \to \pi^- \pi^0 \pi^0 \pi^0 \nu_\tau$	π^-, $3\pi^0 \to 6\gamma$	1.08 %	1 hadr., 6 e/m
$\tau \to \pi^- \pi^- \pi^+ \nu_\tau$	$2\pi^-$, π^+	8.98 %	3 hadr.
$\tau \to \pi^- \pi^- \pi^+ \pi^0 \nu_\tau$	$2\pi^-$, π^+, $\pi^0 \to 2\gamma$	4.30 %	3 hadr., 2 e/m

Table 4.2: Summary of performed neutrino-induced shower simulations. X represents the outgoing fragments of hadrons.

Direction		ν flavor	Induced show.	Energy [EeV]						
Up/down	θ [deg]			0.1	0.3	1	3	10	30	100
down	87	CC, NC ν_e	$e + X$, X	•	•	•	•	•	•	•
	75			•	•	•	•	•	•	•
	65			•	•	•	•	•	•	•
down	87	CC ν_τ	τ_{dw}	•	•	•	•	•	•	•
	85			•	•	•	•	•	•	•
up	91	CC ν_τ	τ_{up}	•	•	•	•	•	•	•

First, NC interactions are mostly relevant for down-going neutrinos. An up-going ν_τ, which undergoes a NC interaction after emerging the Earth's crust, does not have high chances to suffer an interaction in the atmosphere and to produce a detectable shower close to the detector, even through regeneration $\nu_\tau \to \tau \to \nu_\tau$ in the Earth. Second, the primaries (fragments of hadrons) produced by NC interactions of down-going neutrinos are expected to be indistinguishable for all flavors. Finally, AIRES shower simulations of CC interactions for down-going ν_τ and up-going ν_τ consider only the products of the second interaction, i.e. the products from τ decays ("second bang"). The first shower (hadronic part) is discarded since it is expected to be weaker (inelasticity of the order of 20%). A special treatment should be studied and included during AIRES simulations in order to produce ground particle distributions which reflect the delayed double interaction with the two subsequent separated developments.

The background to neutrino detection is mainly due to showers induced by protons. An additional source of background might come from prompt atmospheric muons, depending on the assumption on their incoming flux (Sec. 2.2.2). In this work proton-induced showers, simulated with the code CORSIKA [123, 124] and considering the model QGSJET 01 [136] for interactions in the atmosphere, will be treated as the main background to the detection of neutrino showers in the surface array of the Pierre Auger Observatory.

4.2 Detector response to neutrino-induced showers

In this section the detector response to AIRES simulated EAS will be evaluated by retaining all the real performances of the surface array. Particular attention will be given to the description of the un-thinning algorithm (Sec. 4.2.1) and the procedure to include signals of atmospheric muons, which are expected to be the main background for the reconstruction of showers (Sec. 4.2.2). The surface detector array will be considered being fully efficient and complete. The showers will be simulated at the center of the array ("well-contained" events).

4.2.1 Resampling/Un-thinning

Due to the large number of particles created in an ultra-high energy cosmic-ray shower, it is computationally prohibitive to follow all of the generated particles in a Monte Carlo simulation. In order to simplify the problem and to reduce the computational time and memory needed to simulate cosmic-ray showers, the so-called thinning approximation [135] was applied in EAS Monte Carlo simulations. The method consists of tracking explicitly only a set of representative particles in a run. In particular, all the particles and their interaction products are tracked in the program until they reach a certain energy. For each subsequent interaction, which produces particles below this defined energy, a statistical method is used to determine the resulting particles to be tracked and a weight is assigned to each of these particles. At energies above 10^{17} eV, the number of particles of kinetic energy above 100 MeV at the ground level exceeds 10^8 with a disk space requirement of the order of 100 GB and a CPU time of the order of 15 days. In addition, thousands of simulated showers are needed for comparison with experimental data. On the other hand, the surface array of the Pierre Auger Observatory can detect only a small fraction of these particles and much of the information which is stored in a shower without thinning approximation would be redundant. Thinning allows an important reduction of the number of tracked particles and, at the same time, to keep the physical information carried by the initial interaction. Of course, the fact that not all of the particles are followed may result in artificial fluctuations of ground particle distributions, depending on the level of thinning applied.

A problem arising when one uses thinning is that the weights assigned to the particles may become extremely large as the primary energy gets larger and larger. This effect should be taken into account during detector simulations.

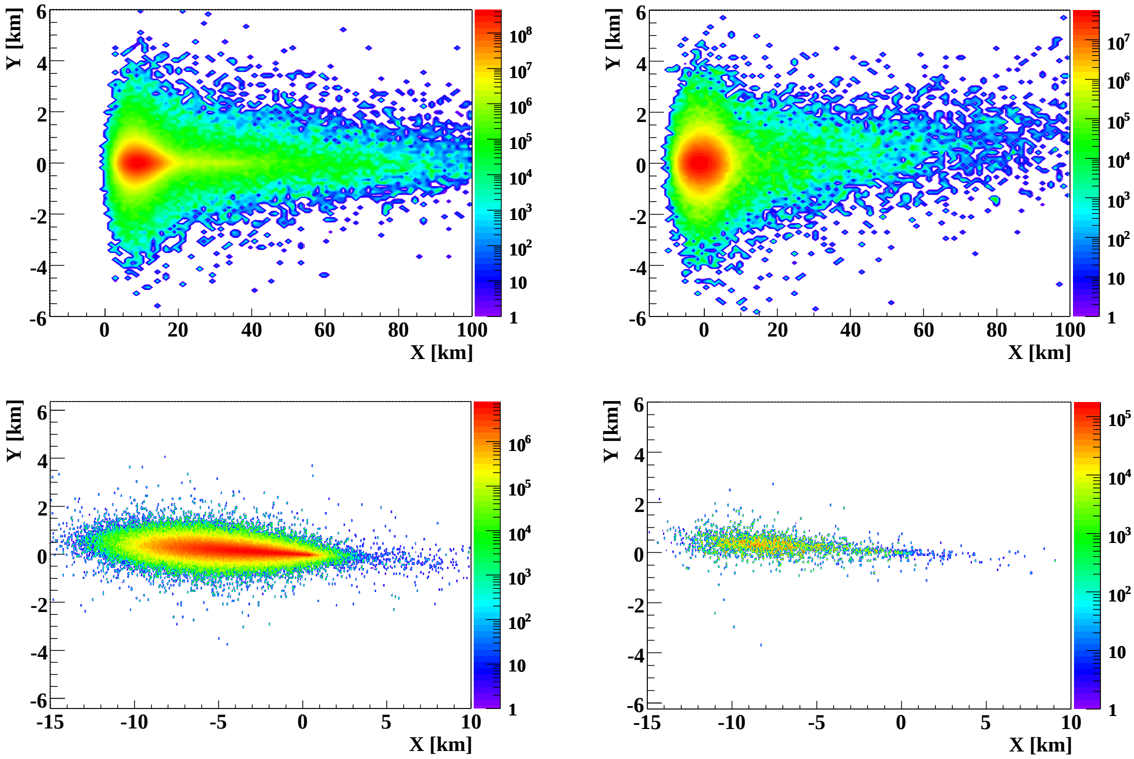

Figure 4.5: *Examples of ground particle density distributions of simulated neutrino-induced showers obtained with the AIRES program [121, 122]. The azimuth of their incoming directions is* 180° *(from the left to the right of the pictures) in the AIRES coordinate system. The z-axis corresponds to the weights assigned to the charged particles (electrons, gammas and muons) on the ground. In the upper-left panel:* τ *decay with* $E_\tau = 10\,\mathrm{EeV}$, $\theta = 89°$, $h = 500\,\mathrm{m}$*; In the upper-right panel:* τ *decay with* $E_\tau = 10\,\mathrm{EeV}$, $\theta = 91°$, $h = 500\,\mathrm{m}$*; In the lower-left panel: CC* $(\nu_e + N \to e + X)$ *interaction with* $E_{\nu_e} = 1\,\mathrm{EeV}$, $\theta = 87°$, $h = 850\,\mathrm{m}$*; In the lower-right panel: NC* $(\nu_e + N \to \nu_e + X)$ *with* $E_{\nu_e} = 1\,\mathrm{EeV}$, $\theta = 87\,\mathrm{deg}$, $h = 850\,\mathrm{m}$. *The two* τ *decay footprints will be discussed in more detail in App. B in order to explain the resampling procedure.*

Once a simulated shower has been stored with a certain thinning, an "un-thinning" algorithm must be applied during detector simulations in order to regenerate the particles entering the stations of the surface detector array and preserve the properties of the signal with its fluctuations. The general idea is not based on a parameterization of the multi-dimensional space of the parameters of the ground particles (e.g. weight, position, time, energy) but on a local sampling procedure. This idea, developed and optimized originally for vertical and inclined (up to 70°) hadronic showers [137, 138, 139], has been revised to better simulate the detector response to up-going and down-going neutrino showers in the $\overline{\mathrm{Off}}\underline{\mathrm{line}}$ framework [120]. Typical weight distributions for neutrino-induced shower footprints, as simulated with the AIRES program, are shown in Fig. 4.5. The elongation of

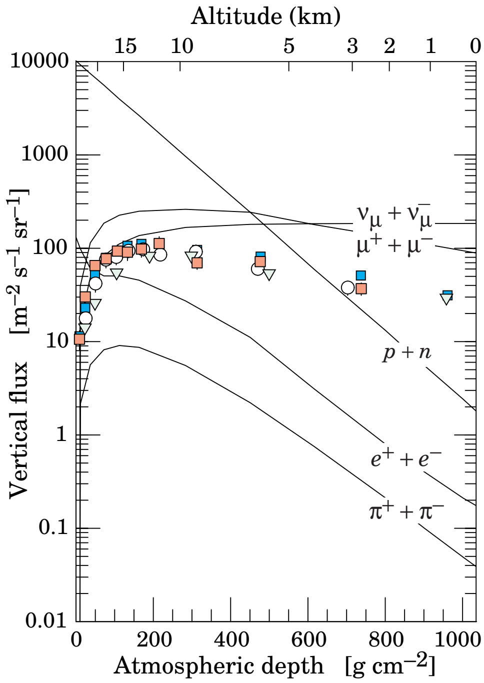

Figure 4.6: *Estimated vertical flux of cosmic rays with energies larger than* 1 GeV *in the atmosphere. Muons are the most numerous particles along with muon neutrinos at sea level and their flux increases at larger altitudes [4]. The points show measurements of negative muons with energy above* 1 GeV*.*

the two quasi-horizontal ν_τ shower (upper panels) footprints, which extends up to 100 km, and the thin muonic tail which is left in the latest regions (on the right part of the panels) is evident. The footprints relative to ν_e CC and NC interactions in the atmosphere (lower panels) present a poor muonic tail. In case of the ν_e NC interaction, an evident shortage of the electromagnetic core component is also present.

The peculiarities of neutrino-induced showers at large zenith angles is one of the reasons to extend the original algorithm. A detailed description of the modified algorithm is available in Ref. [140] and it is reported in App. B.

4.2.2 Including the background of atmospheric muons

Along with the secondary particles, produced by the interaction of a primary cosmic particle in the atmosphere and triggering the Pierre Auger surface detector array on the ground, a continuous flux of atmospheric muons and/or the occurrence of little showers developing close to the detector are expected to trigger some stations of the array. Muons are the most numerous charged particles at sea level (Fig. 4.6) and are produced mostly in the upper part of the atmosphere (around 15 km) from pion decays, losing about 2 GeV by ionization before reaching the ground. The mean muon energy at the ground is of the order of 4 GeV.

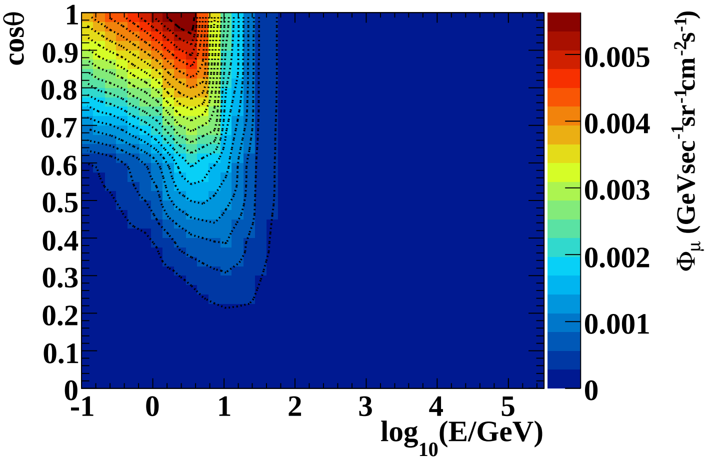

Figure 4.7: *Lipari flux of atmospheric muons at sea level [141].*

In general, their energy and angular distribution reflect the convolution of the production spectrum, the energy loss in the atmosphere, and the decay (see Fig. 4.7). Since pions with an energy larger than 115 GeV tend to interact before decaying, the energy spectrum steepens at the highest energies while it reflects the primary spectrum back up to 1 GeV.

Local showers are initiated by secondary particles, interacting with the atmosphere close to the detector array. They are able to produce small sets of little energetic particles and sometimes to trigger locally the detector array.

The expected rate per station (exposed area of about 18.4 m^2) for atmospheric muons at the altitude of the Pierre Auger Observatory is of the order of 3500 Hz [110]. Signals exhibited by atmospheric muons in the flash ADC traces (Sec. 3.1) consist of narrow peaks which, when they occur in a station already hit by shower particles, appear most of the times to be isolated and easily observable due to their random time occurrence.

Little local shower secondaries hit a single station producing either broader signals, which are below the trigger threshold (mostly electromagnetic secondaries), or larger and narrow signals, similar to the signals produced by energetic atmospheric muons, but their occurrence is less frequent than the occurrence of atmospheric muons. Atmospheric muons are, therefore, the main background to the detection of cosmic rays.

Although the Pierre Auger Observatory was designed to maximize the trigger efficiency for cosmic-ray showers with energy of 10^{18} eV or higher, stations hit by particles of the background may still give a contribution which in some cases distorts the shower reconstruction and in the worst case makes the reconstruction fail. For example, three important variables, e.g. the apparent velocity of showers on the ground, the rise time and fall time of stations, which are currently used for discriminating neutrino showers from hadronic showers [15] can be strongly biased by atmospheric muon background (Fig. 4.8). In App. C details on the procedure to include the background of atmospheric muons in

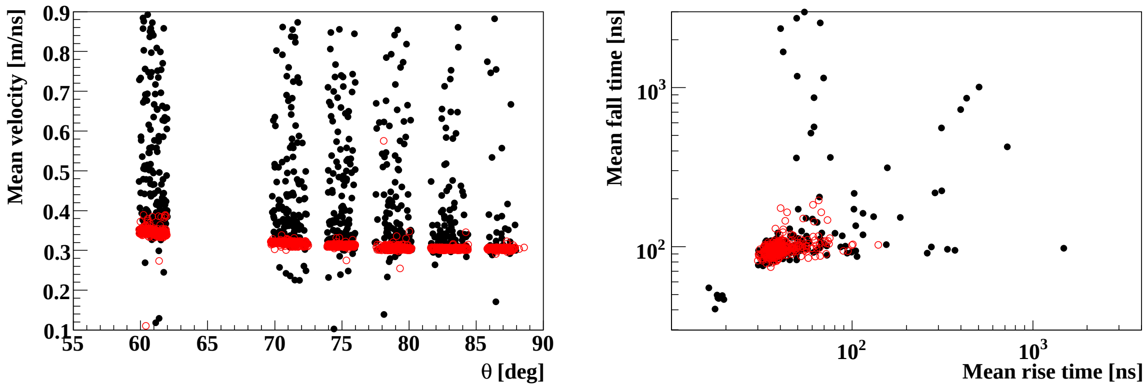

Figure 4.8: *Effects of the addition of atmospheric muon background in proton simulated showers. The red open circles represent simulation without addition of atmospheric muons; the black full circles represent simulation including atmospheric muons. In the left panel, apparent velocity of showers on the ground versus incoming zenith angle. In the right panel, mean rise time versus mean fall time of the two earliest triggering stations for zenith angles larger than* $80°$*. Three typical features, which can be observed also in measured data, are evident: the subset of points with mean fall time in the range* $50 \div 100\,\mathrm{ns}$*, the subset of points with mean rise time around* $100\,\mathrm{ns}$ *and the points with mean rise time and fall time concentrated at around* $20-30\,\mathrm{ns}$*. Most of these points will be removed during the selection and the trace cleaning before the reconstruction. The simulation used in these plots are the CORSIKA showers mentioned in Sec. 4.1.2.*

detector simulations will be discussed. The parameterization chosen for the flux Φ_μ of atmospheric muons at sea level is the Lipari parameterization [141] (Fig. 4.7). An example of a footprint with the addition of simulated atmospheric muons is shown in Fig. 4.9.

4.2.3 Detector response

The response of a surface detector to different particles (mainly electrons, muons, gammas) depends on the physics of interaction in water. Cherenkov light is emitted by charged particles traversing the cleaned water inside a tank and collected by the 3 PMTs. The amount of emitted light produced by muons is quite different from that produced by electrons. Gamma rays are particularly affected by the water absorption length. Simulation of the surface detector response shows that the number of photoelectrons (p.e.) emitted by muons is almost constant above $2\,\mathrm{GeV}$, whereas it increases with energy for electrons and gamma rays [142]. In Fig. 4.10 the footprint particle content for an up-going and a down-going simulated shower is shown. The long tail of the muonic component guarantees a large probability for a station to trigger even a single muon at large distance from the earliest region on the ground (left parts of Fig. 4.10). The average number of collected p.e. equivalent to $1\,\mathrm{I}_{\mathrm{VEM}}^{\mathrm{peak}}$ is 18.5. Above $1\,\mathrm{GeV}$, a single muon is expected to emit about $60\,\mathrm{p.e.}$ and above $2\,\mathrm{GeV}$ about $80\,\mathrm{p.e.}$ At large distance from the earliest point on the

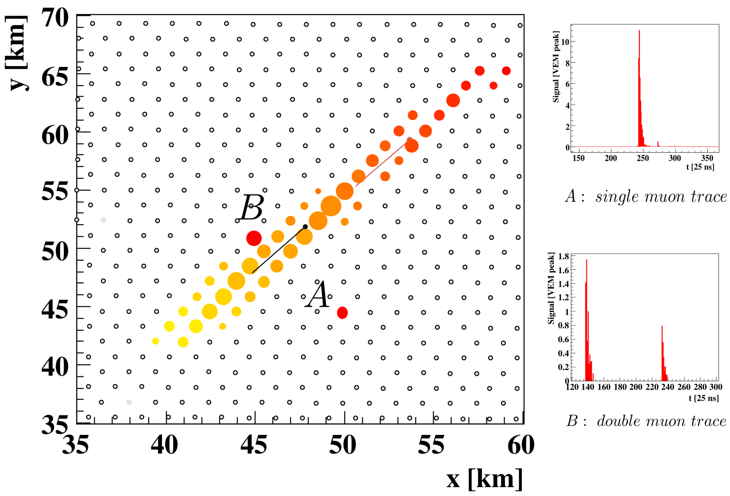

Figure 4.9: *Example of footprint with the addition of simulated atmospheric muons. The trace "A" is from an isolated station triggered by a single muon; the trace "B" shows the contribution of a second low-energy atmospheric muon to the signal of a station with triggering shower particles.*

ground, the average muon energy is above 2 GeV. Therefore, the latest part of a footprint is expected to trigger due to the penetrating muonic shower component. The earliest regions, instead, contain mostly soft muons but a large electromagnetic component. These regions are expected to trigger electrons and gamma rays whose average energy is around 200 MeV. Their expected number of emitted p.e. is about 60–80 whereas soft muons emit only 40–50 p.e.

4.3 Detection efficiency

With about 1 TByte of simulated data (20,000 up- and down-going τ-induced showers and 36,000 down-going electron-induced showers), distributed among different neutrino flavors, energy and angular bins, as described in Sec. 4.1.2 and Tab. 4.2, it was possible to study the detection or trigger efficiency of the surface array of the Pierre Auger Observatory. The detection efficiency $T_{eff}(E_i, \theta, h)$ is defined as the number of showers which pass the central trigger algorithm requirements (Sec. 3.3) over the number of simulated events for fixed zenith angle θ, energy E_i and decay altitude h of injected particles $i = e + X, X, \tau$, where X represents the out-coming fragments of hadrons.

As it is shown in Fig. 4.11, the detection efficiency for up-going showers induced by the products of τ lepton decays depends only on the τ lepton energy E_τ and the altitude above the ground, $h_{10\ km}$, which approximately corresponds to the position of the shower maximum, defined at 10 km from the decay point along the neutrino incoming direction. For this reason, the decay altitude of up-going neutrino showers will be measured conventionally with the parameter $h_{10\ km}$.

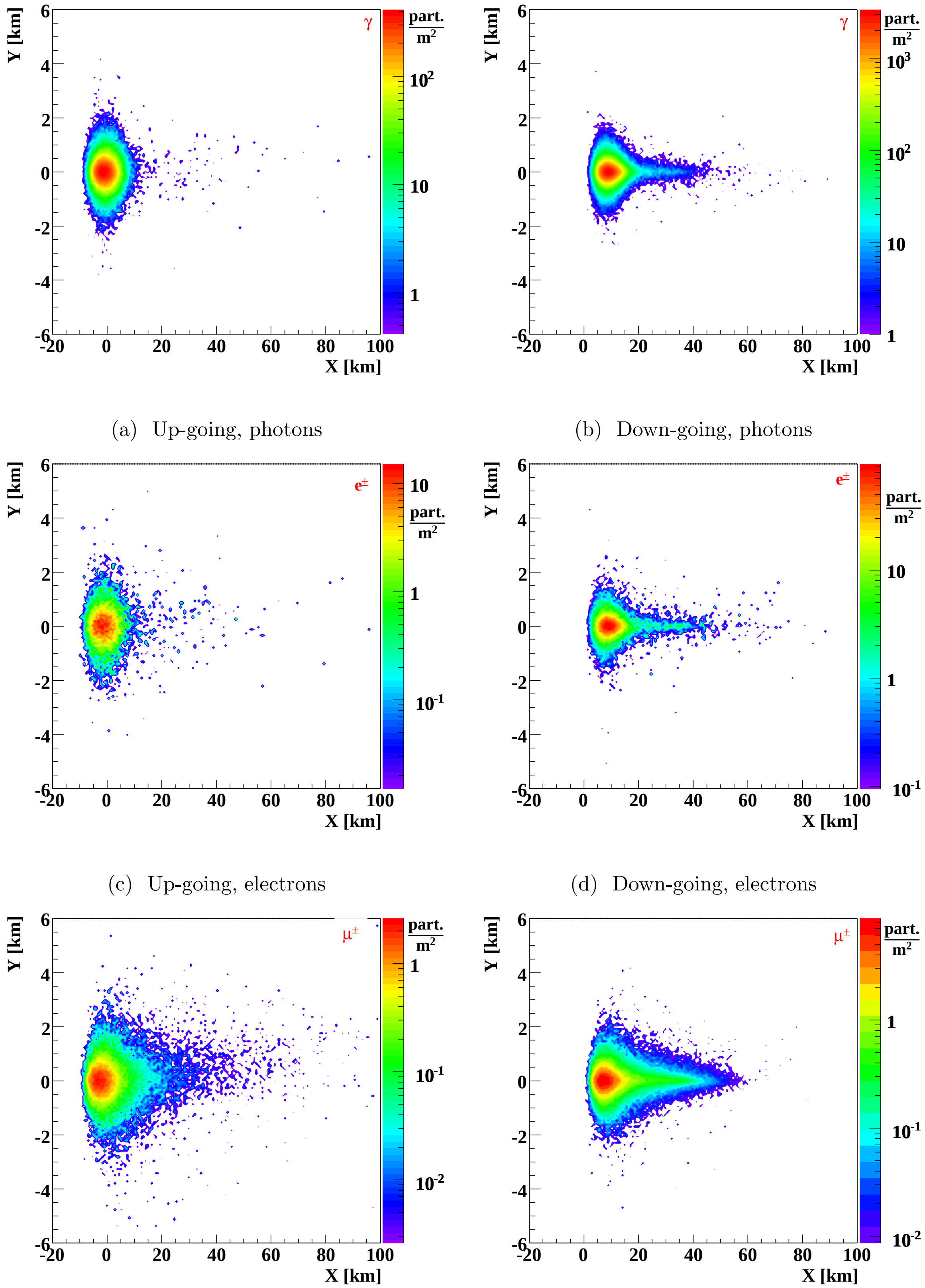

(a) Up-going, photons

(b) Down-going, photons

(c) Up-going, electrons

(d) Down-going, electrons

(e) Up-going, muons

(f) Down-going, muons

Figure 4.10: *Example of footprint particle content for an up-going (left panels) shower and a down-going (right panels) shower. The content is expressed in unit of* particles/m^2.

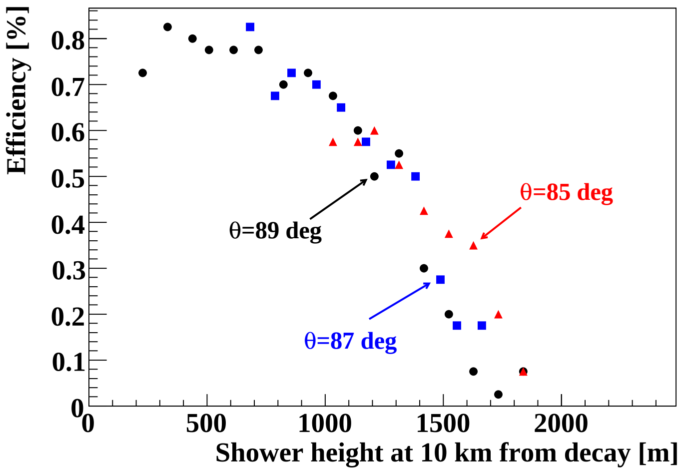

Figure 4.11: *Detection efficiency for up-going ν_τ at different zenith angles and energy of* 10 EeV *as a function of the parameter $h_{10\ km}$. It is evident that the efficiency does not depend on the zenith angle within the fluctuations imposed by the simulation process.*

In App. D a list of two dimensional maps of $T_{eff}(E_i, \theta, h)$, for different zenith angles and neutrino flavors, and a discussion on them is reported. The corresponding identification efficiency maps, which will be discussed in the next chapter (Sec. 5.4), are also shown for comparison.

4.4 Improvements in the detection

In this chapter a study of the detection efficiency of the surface array of the Pierre Auger Observatory, based on simulations performed with a suitable MC chain, was done.

The detection efficiency clearly depends on the physical trigger implemented and in use at the Observatory (Sec. 3.3). As long as the compactness of incoming showers is large enough, the central trigger requirements allow a full-efficient detection of ordinary cosmic-ray as well as neutrino-induced showers. A dedicated central trigger to detect neutrino-induced showers could be a useful starting point to improve the detection of neutrino-induced showers. In particular, at low energy and/or for high altitude of interaction point, more permissive trigger requirements on the compactness might allow an increase of the efficiency for young and aligned showers [143]. In this case, however, atmospheric muons, which trigger locally the surface detector array, may induce important errors during the shower reconstruction phase, mostly in events with low multiplicity of stations. Improvements to the selection algorithm, based on a better understanding of the background, should be done in this respect.

5 Identifying neutrino-induced showers

One of the main experimental challenges for the Pierre Auger Observatory is the identification of neutrino-induced showers from the background of showers initiated by ordinary cosmic rays (mainly protons). In principle, the concept of neutrino identification is simple. Whereas hadrons and photons interact shortly after having entered the atmosphere, neutrinos may penetrate, undisturbed, large amount of matter and induce showers close to the surface array (Sec. 5.1). The differences between showers developing close to the detector (*young*) and showers developing early in the atmosphere (*old*) become more enhanced when larger zenith angles are considered.

A suitable set of tools is necessary in order to analyze collected data and extract possible neutrino candidates (Sec. 5.2). Differences with the tools which are set to deal with ordinary cosmic rays are: a proper selection of stations to reduce the presence of signals from atmospheric muon background, the analysis of the parameters which can characterize the footprints expected for neutrino-induced showers in the surface array and some improvements adopted during the phase of geometrical reconstruction.

In this chapter, the reconstruction of simulated neutrino-induced showers (as from Chap. 4) will be discussed. Based on the results obtained, a set of observables which characterize neutrino showers can be chosen and, after optimization of cuts on these observables have been performed to reduce the effect of the background of proton showers (Sec. 5.3), the identification efficiency for the surface array of the Pierre Auger Observatory will be evaluated (Sec. 5.4). The efficiency will be necessary to calculate the acceptance (Sec. 5.6) and the expected event rates (Sec. 5.7) for neutrino-induced showers. A study of the contribution of individual neutrino flavors to the calculated acceptance and event rates will be also presented (Sec. 5.8) and a discussion on the systematic effects arising from the use of different cross-section and energy loss models will be done (Sec. 5.9). Finally, the sensitivity will be evaluated (Sec. 5.10).

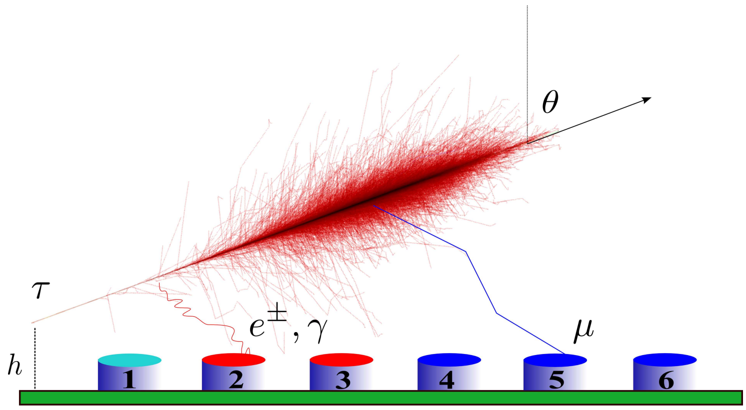

Figure 5.1: *Sketch of ν-induced shower (up-going) longitudinal development with zenith angle θ and altitude of the interaction point in the atmosphere h. The earliest stations (in red) are mostly triggered by electrons and γs while the latest stations are triggered by the muonic component of the shower.*

5.1 General properties of simulated neutrino-induced showers

In hadronic showers, which are expected to develop after few atmospheric depths, only high-energy muons can survive down to the ground. As a result, the detected showers have thin and flat fronts which lead to short and fast detected signals, lasting only few nanoseconds. In young ν-induced showers a significant electromagnetic component is present at the ground as well. The shower fronts, therefore, are curved and thick, and broad signals, lasting up to a few microseconds, are expected to be detected. As discussed in Sec. 4.2.2, atmospheric muons, which hit and trigger some of the stations of the surface array, may bias the analysis of collected data and should be removed.

In Fig. 5.1 a sketch of ν-induced shower development in the atmosphere is shown. An early bulk of particles which form the main electromagnetic component of the shower is expected to trigger the earliest stations as broad signals while, later along the footprint, narrower signals are expected (asymmetric signal duration). The attenuation in the atmosphere affects also the topology of the footprints such that a "broader" structure is present in the regions where a shower hits the ground level first, while a narrow structure can be observed in the latest regions (asymmetric footprint structure). In inclined hadronic showers hardly any evolution of the signal duration and asymmetry in their footprints can

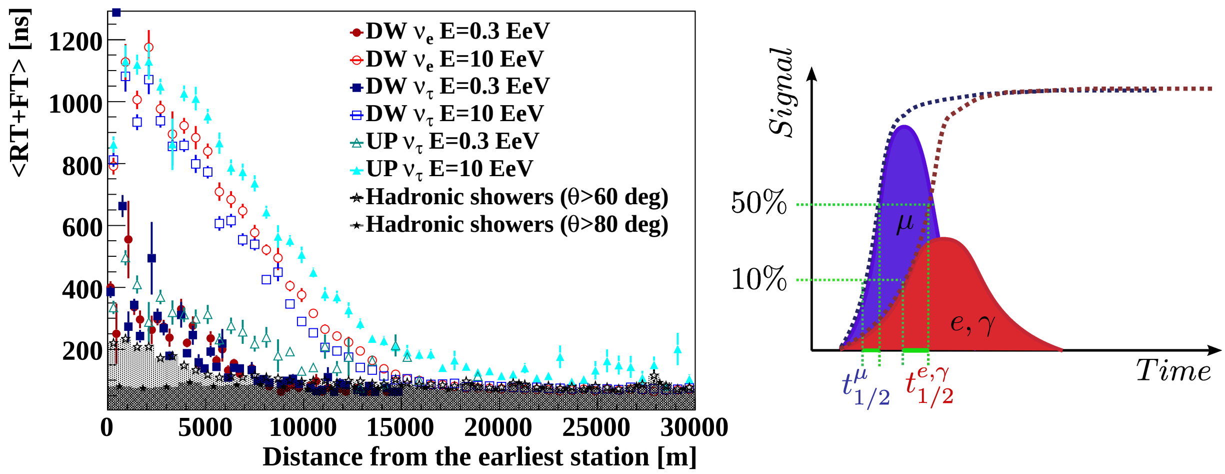

Figure 5.2: *(Left panel) Average of the sum of rise and fall time of station signals versus distance from the earliest triggering station. Quasi-horizontal up-going ν_τ-induced showers (labeled with "UP"), down-going ν_e-induced showers and down-going ν_τ-induced showers (labeled with "DW") at* 0.3 EeV *and* 10 EeV*, compared to inclined hadronic showers ($\theta >$ $60°$ and $\theta > 80°$) are shown. (Right panel) Sketch of determination of rise time for signals induced by muons and signals induced by electrons and gamma.*

be seen. In particular, the asymmetry in the signal rise and fall times, already presented in Ref. [94, 144], can be clearly seen in simulations of ν-induced showers (Fig. 5.2, left panel). The rise time is defined as the time for an integrated signal to rise from 10% to 50% of its maximum. The fall time is defined as the time for an integrated signal to decrease from 90% to 50% of its maximum. Electrons and gammas produce broader signals in a way that the rise and fall time present a longer duration (Fig. 5.2, right panel). The signal for neutrino showers is broader at around the position of the maximum of the shower development. At energies below 3 EeV broader signals can be observed in the two earliest triggering stations, while above 10 EeV, broader signals can be also observed in later stations since the complete ground shower development can be detected. The duration of broader signals is about 1000 ns, whereas it decreases to a value of about 150 ns in the latest stations which are hit by the muonic tail of the shower development. For hadronic showers, at zenith incoming directions larger than 80°, the expected duration of the signals is almost steady along the entire ground shower development and is of the order of 150 ns. At lower zenith angles a soft asymmetric signal duration can be also observed, but with a smaller number of stations (smaller footprint areas) with respect to ν-induced showers.

In the next section a description of the tools, developed to reconstruct and identify neutrino showers, and how well they can fit the signatures expected will be discussed.

5.2 Reconstruction of neutrino showers and identification observables

The removal of stations, which have been hit by atmospheric muons, is achieved by imposing some cuts on relative distances between the stations in order to identify isolated stations in a way similarly described for vertical showers in Sec. 3.4. With respect to the cuts used for vertical showers, a station is marked as accidental if it does not have any neighbor within a distance of 6000 m or only one neighbor in 10000 m. Larger distance gaps between candidate stations reflect the more elongated footprint structure with respect to the more compact footprints of vertical showers. The calibration of the signals, before any reconstruction has been performed, allows cleaning of the signal traces from additional spurious accidental peaks of atmospheric muons mixed with signals from shower particles. An additional station selection is performed later during the reconstruction phase after a preliminary analysis of the footprint topology has been performed.

The first step towards the identification of possible neutrino events is the discrimination of young inclined showers from old showers. The topology of the footprints expected for ν-induced showers at the surface array of the Pierre Auger Observatory constrains and identifies some featuring parameters which help to discriminate them from hadron-induced footprints. In particular, since ν-induced showers are expected in the range of zenith angles between 60 and 90° for down-going induced showers and in the range between 90° and 95° for up-going induced showers, the *elongation* of a footprint is a first sign to identify inclined showers. At this stage only small differences between ordinary hadronic inclined showers and ν-induced showers are expected to be seen since the elongation characterizes the declination of the incoming direction. However, it should be also noted that hadronic inclined showers present more elongated footprints whose triggering stations can be found mostly along the incoming direction, with only few stations in the transversal direction. A principal component analysis [145] is used to evaluate the length (L) over the width (W) of patterns on the ground. The positions of the stations are weighted by their signals. The elongation of a footprint is defined as L/W (Fig. 5.3). Due to the attenuation in the atmosphere, enhanced for more inclined incoming directions, whereas the electromagnetic component is quickly absorbed, the muonic component can survive longer. In inclined hadronic showers the muonic component covers almost all of the triggering stations and the elongation can be assumed to be more enhanced as the shower energy increases. In down-going ν_e-induced showers the hadronic fragments from CC or NC interactions take only 20% of the initial neutrino energy (Sec. 1.3.1) on average such that the electromagnetic component is more enhanced and covers most of the stations. In this case, the higher the energy, the broader is the footprint such that the elongation can be assumed to decrease with the increase of the shower energy. In down-going ν_τ-induced showers the additional hadronic channel from τ decays can again play an important role in the elongation of the footprints, but this effect is softened as the energy increases due to the predominant effect of the "youth" of such showers. In up-going ν_τ-induced showers the different geometry involved assumes the role to limit the earliest region assigned to the electromagnetic com-

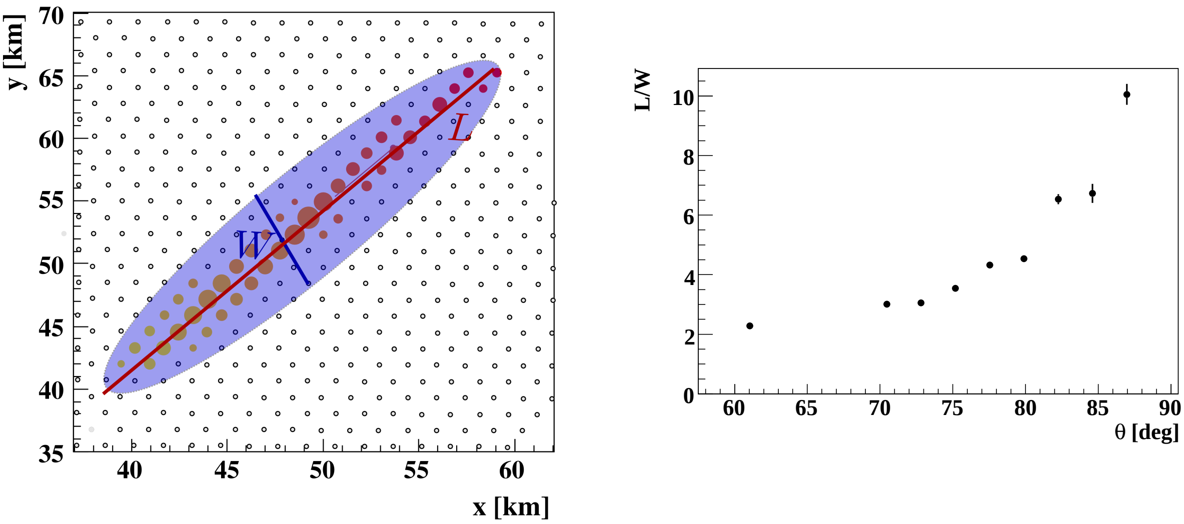

Figure 5.3: *(Left panel) Sketch of length and width determination of a footprint. Larger full circles represent larger station signals. Since the principal component analysis is performed by weighting the station positions with their signals, the picture appears to be asymmetric around the barycenter of the stations. (Right panel) Length over width as a function of the zenith angle. Results of proton shower simulations with energy between* 0.1 EeV *and* 100 EeV *are shown.*

ponent while the muonic component, which penetrates longer into the atmosphere, can enhance its effect in the elongation of the footprint. In Fig. 5.4 typical detected footprints for two types of ν-induced showers and for a proton-induced shower are shown. Differences in the elongation and attenuation of the signals can be appreciated.

A large value for the L/W of a footprint is not enough to establish whether the event, which has produced it, is inclined. Low-energy events (below 1 EeV), expected to have low multiplicity of stations, can still have quite a large L/W since the transversal development is not enough to trigger off-axis stations[1]. The same behavior is expected at high decay vertex altitudes due to the fact that the attenuation in the atmosphere allows trigger of only few stations. An additional parameter, which is taken into account to determine whether an event is inclined without reconstructing its direction, is the so-called *mean apparent velocity* of a shower on the ground, $\langle V \rangle$. The mean apparent velocity is defined by averaging the apparent velocity between couples of stations, defined as

$$v_{ij} = \frac{d_{ij}}{\Delta t_{ij}}, \tag{5.1}$$

where d_{ij} is the distance between the couples, projected onto the direction defined by the length of the footprint and Δt_{ij} the difference in their signal start times. Let $\vec{L}$ be the unit

[1]In addition, the inelasticity of the involved process can favor the hadronic channel so that the resulting footprint can be more elongated at the same altitude bin.

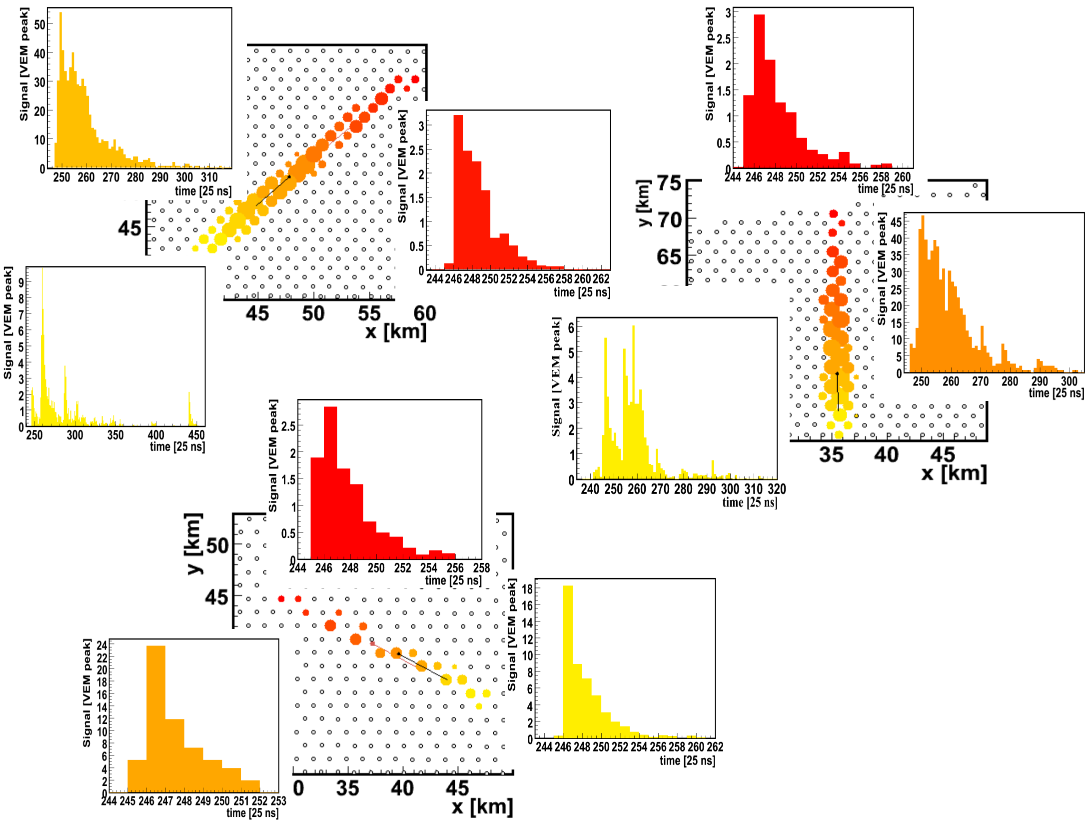

Figure 5.4: *Example of detected neutrino and proton footprints. The traces are colored as the corresponding triggering stations. (Upper-left) Down-going ν_e footprint from a shower initiated by a NC interaction of a ν_e with zenith angle of incoming direction at 87° and energy of* 1 EeV*. (Upper-right) Down-going ν_e footprint from a shower initiated by a CC interaction of a ν_e with zenith angle of incoming direction at 87° and energy of* 1 EeV*. (Bottom) Proton footprint produced by a shower with zenith angle of incoming direction at 87° and energy* 1 EeV*.*

vector along the main direction from the principal component analysis, D_{ij} the relative distance between the stations i and j of a couple, and $\vec{D}_{ij}$ the vector from i to j. The distance d_{ij} in Eq. 5.1 ca be written as

$$d_{ij} = \vec{D}_{ij} \cdot \vec{L} = D_{ij} \cos \delta_{ij}, \tag{5.2}$$

where δ_{ij} is the smallest angle between $\vec{D}_{ij}$ and $\vec{L}$. The mean apparent velocity results from the following equation

$$\langle V \rangle = \frac{\sum_i \sum_{j,j>i} v_{ij}}{C}, \tag{5.3}$$

where C is the total number of couples which are considered. The maximum number of

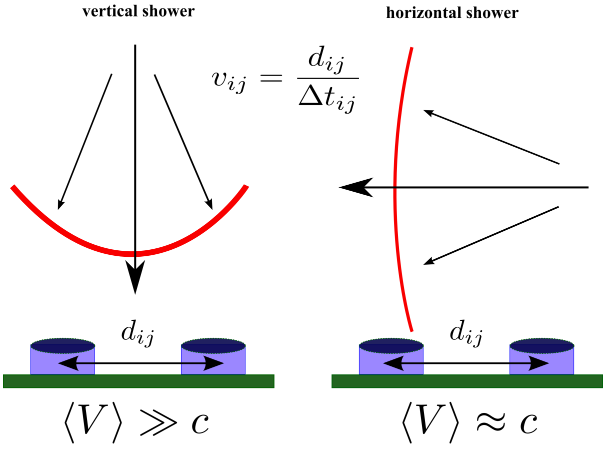

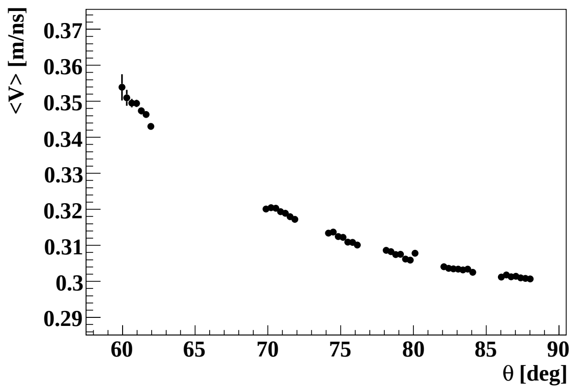

Figure 5.5: *(Left panel) Determination of the apparent velocity between couples of stations. (Right panel) Mean apparent velocity as a function of the zenith angle of shower incoming directions. Results of proton shower simulations with energy between* 0.1 EeV *and* 100 EeV *are shown.*

couples which are available to the computation of $\langle V \rangle$ can be expressed as

$$C = \frac{N(N-1)}{2}, \tag{5.4}$$

with N the number of stations. However, C is often reduced due to additional cuts which are placed to improve the estimate of $\langle V \rangle$. The mean apparent velocity is expected to be compatible with the speed of light for quasi-horizontal showers, within its statistical error (Fig. 5.5). Couples of stations which are situated perpendicularly to the incoming direction (the direction along the length, as from the principal component analysis) are expected to have Δt_{ij} of the order of zero within the signal start time resolution of 25 ns, while the distances d_{ij} are about zero. Such cases are avoided by placing cuts which require the distances to be at least 750 m or, in other words, the angle between the shower direction on the ground and the directions of the couples smaller than 45°. The determination of $\langle V \rangle$ is strictly related to the goodness of the principal component analysis. Broader footprints, typical of more energetic showers or less inclined showers, might produce large uncertainties in the estimate of the direction of the length and width. The requirement $L/W \geq 2$ is adopted to avoid too large uncertainties from the principal component analysis. Such a soft cut allows to keep all the footprints which are generated by shower incoming directions with zenith angles larger than about 60° (Fig. 5.3).

To summarize, mean apparent velocity and length over width of a footprint approximately constrain the shower incoming direction. However, the uncertainty in the principal component analysis can be large for broad footprints and cause large uncertainty in the estimate of the mean apparent velocity on the ground. In Fig. 5.6, this effect can be seen for ν_e-induced showers at 87°. The larger the energy, the broader are the footprints such that the L/W decreases whereas the mean apparent velocity shows more spread around the expected value of about 0.3 m/ns.

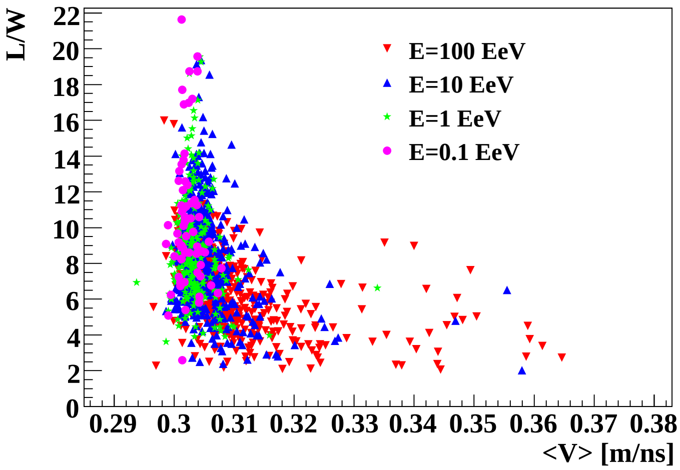

Figure 5.6: *Length over width of footprints of ν_e-induced showers at $87°$ and several energy bins. At higher energies the footprints are expected to be wider and the mean apparent velocity is expected to show more spread around the expected value of about* $0.3\,\mathrm{m/ns}$.

Before other parameters are considered, a station selection is performed. The selected stations are the largest subsample of the initial set of candidate stations whose calculated mean apparent velocity has an uncertainty smaller than 5%. The set, cleaned and selected, is ready to be analyzed further.

Once the shower incoming direction has been determined, the discrimination of young from old showers can be achieved by counting the number of stations whose signals are likely due to the electromagnetic component of the shower. Local time-over-threshold (ToT) trigger signals are clearly broad signals (Sec. 3.3) but, in order to assure that such signals are really produced by the electromagnetic component of the shower, signals triggering for at least 375 ns (equivalent to 15 time bins) were considered. In addition, to avoid that double muon signals or high energetic single muon signals might affect the set of selected ToT stations, the ratio of the integrated signal over their peak height was required to be larger than 1.4. The fraction of ToTs, fulfilling the conditions above reported, is, finally, the parameter which is considered to play an important role for a first discrimination of neutrino-like from hadronic footprints. This parameter will be called $TOTF$ (Time Over Threshold trigger Fraction) in the following discussion. A similar parameter was also used in Ref. [15] for analysis of up-going ν_τ-induced showers.

The additional condition is that the selected ToTs fulfill the central trigger requirements (Sec. 3.3). This condition is necessary to avoid configurations where ToTs are no clear evidence of young showers but they occur randomly along the footprint. In fact, the evolution of young showers along their footprints imposes that the young part of the footprint appears in the earliest triggering stations with compact configurations. Showers which do not fulfill such a condition are rejected. Simulations show that only a small fraction of events are rejected (below 5%) by using such a condition and these are mostly events generated at the highest altitudes and low energies where the attenuation in the atmosphere plays an important rule. Showers which are able to pass such a condition are marked with the label $IsStillT3$.

A final observation *criterium* to identify neutrino showers are broad signals in time in the earliest region of the shower development. As mentioned previously, the maximum of the shower development is well seen in case of ν-induced showers. Following this idea, the average rise time, $\langle RT_2 \rangle$, and the average fall time, $\langle FT_2 \rangle$, calculated for the 2 earliest triggered stations are used.

Several distributions for the parameters described above can be drawn to show the differences between hadronic induced showers and ν-induced showers. Such distributions only slightly depend on the initial neutrino, but are expected to be different for CC interactions and NC interactions. Differences are expected also between down-going and up-going ν_τ-induced showers due to the involved geometry. In the following discussion, distributions for up-going and down-going ν_τ-induced showers, and inclined horizontal proton-induced showers will be compared and distributions for down-going ν_e-induced showers produced in CC and NC interactions will be compared to nearly horizontal proton-induced showers.

In Fig. 5.7 (upper left panel) $TOTF$ as a function of L/W is shown. It can be seen that the fraction of young stations for hadronic showers decreases by increasing the zenith angle (the electromagnetic component is attenuated). For τ lepton showers, one expects that most of the stations have broad ToT signals along with elongated footprints. In Fig. 5.7 (upper right panel) the mean apparent velocity as a function of its standard deviation is shown. It can be seen that the velocity depends on the zenith angle of the shower (in hadronic simulations), and, for quasi-horizontal showers with zenith angle between 85° and 95°, it is tightly concentrated around the speed of light (range $0.30 \div 0.32\,\mathrm{m/ns}$) with an uncertainty below $0.02\,\mathrm{m/ns}$. As explained previously, the uncertainty in the mean apparent velocity strongly depends on the width of the footprints such that at lower zenith angles, or in other words for larger widths, the uncertainty in the estimate of $\langle V \rangle$ tends to larger values. In Fig. 5.7 (bottom panel) the average rise time, $\langle RT_2 \rangle$, versus the average fall time, $\langle FT_2 \rangle$, for the two earliest stations is shown. The separation is more enhanced in the region where the average rise time is larger than about 80 ns and the fall time is larger than 200 ns. In principle, such a large rise time and fall time can be also produced by hadronic showers with $\theta < 70°$ but in such a case the mean apparent velocity is expected to be larger than the speed of light and concentrated around $0.35\,\mathrm{m/ns}$. Thus, discrimination of neutrino showers from hadronic showers is still possible at lower zenith angles.

In Fig. 5.8 the same distributions for down-going ν_e-induced showers produced in CC and NC interactions compared to hadronic induced showers at zenith angles larger than 80° are shown. The overall difference between showers produced in CC and NC interactions is due to the large contribution from the electromagnetic component produced in the former with respect to the latter interactions. This is reflected in a slightly larger $TOTF$, smaller L/W and larger rise and fall time of the signals in the two earliest stations for showers induced in CC interactions with respect to the showers induced in NC interactions.

So far, no geometrical reconstruction of the incoming direction is needed. Nevertheless, in order to have an additional quality cut for neutrino identification, the requirement that

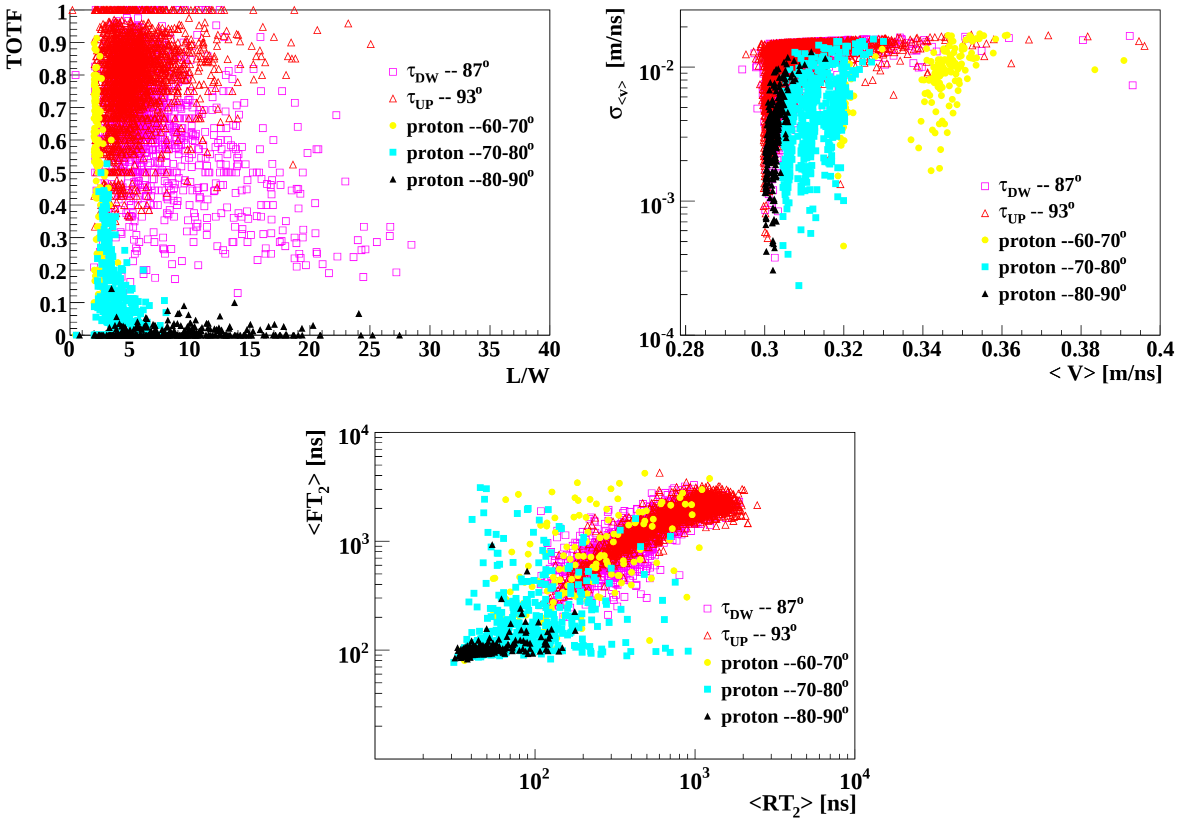

Figure 5.7: *Distributions of the parameters used to identify ν-induced showers for hadronic induced showers, up-going and down-going tau ν_τ-induced showers. (Upper left panel) Mean apparent velocity, $\langle V \rangle$, versus fraction of ToT stations, $TOTF$. (Upper right panel) Mean apparent velocity, $\langle V \rangle$, versus its statistical uncertainty, $\sigma_{\langle V \rangle}$. (Bottom panel) The average fall time $\langle FT_2 \rangle$ as a function of the average rise time, $\langle RT_2 \rangle$ calculated for the two earliest triggered stations.*

a shower can be reconstructed was considered as an optional choice. Modifications to the existing code to reconstruct the direction of completely aligned footprints, for which no plane can be fit to find the arrival direction (Sec. 3.4), were done. For these particular cases, the zenith angle is reconstructed by taking into account the mean apparent velocity, $\langle V \rangle$. In Fig. 5.9 a sketch of the determination of the zenith angle θ for aligned footprints is shown. By assuming that the main axis from the principal component analysis (the axis along the length, $\vec{L}$) can define a good estimate of the azimuth ϕ of the incoming direction, it results that θ can be obtained from the following equation

$$\sin\theta = \frac{c}{\langle V \rangle}, \tag{5.5}$$

where c is the speed of light. In general, if ϕ is undefined, Eq. 5.5 provides an estimate of the opening angle $\alpha = 90° - \theta$ of the cone defined by all the possible incoming directions with

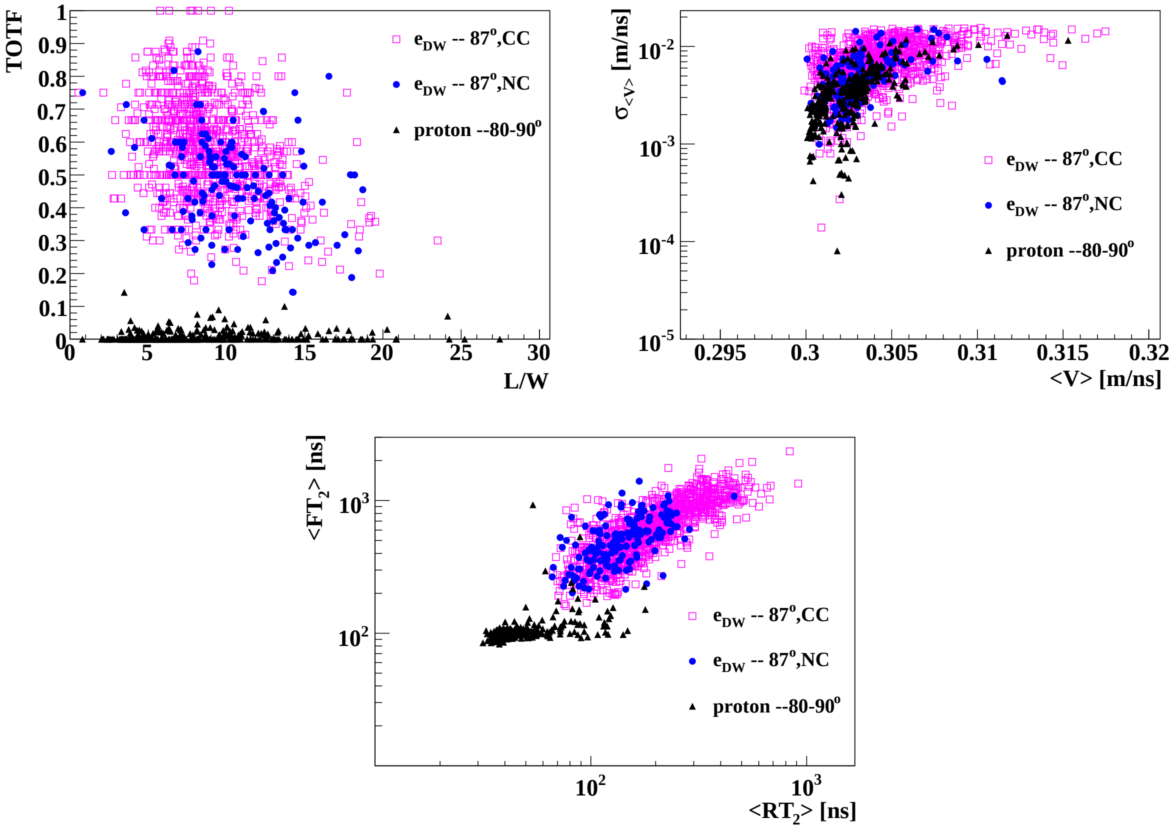

Figure 5.8: *Distributions of the parameters used to identify ν-induced showers for hadronic induced showers and down-going ν_e-induced showers produced in CC and NC interactions. (Upper left panel) Mean apparent velocity, $\langle V \rangle$, versus fraction of ToT stations, $TOTF$. (Upper right panel) Mean apparent velocity, $\langle V \rangle$, versus its statistical uncertainty, $\sigma_{\langle V \rangle}$. (Bottom panel) The average fall time $\langle FT_2 \rangle$ as a function of the average rise time, $\langle RT_2 \rangle$ calculated for the two earliest triggered stations.*

fixed $\langle V \rangle$. Distinction between up-going and down-going showers can not be achieved since the reconstruction deals only with positions and signal arrival times in triggering stations. Nearly aligned footprints can also cause the geometrical reconstruction to fail when low-multiplicity events are involved. In such a case, even a single station with a wrong estimate of the signal start time may result in a failure of the plane fit reconstruction. To recover some events, the condition which was chosen to identify aligned or nearly aligned footprints is $L/W > 10$. The condition on L/W involves a maximal range of allowed directions for the estimate of ϕ given by the following relation

$$|\Omega| \leq \arctan\left(\frac{W}{L}\right), \tag{5.6}$$

where Ω represents the maximal tilting angle with respect to the determined main axis $\vec{L}$. The condition $L/W > 10$ implies $|\Omega| \leq 0.0997 \approx 5.7°$. According to Fig. 5.9, let $\vec{L}'$

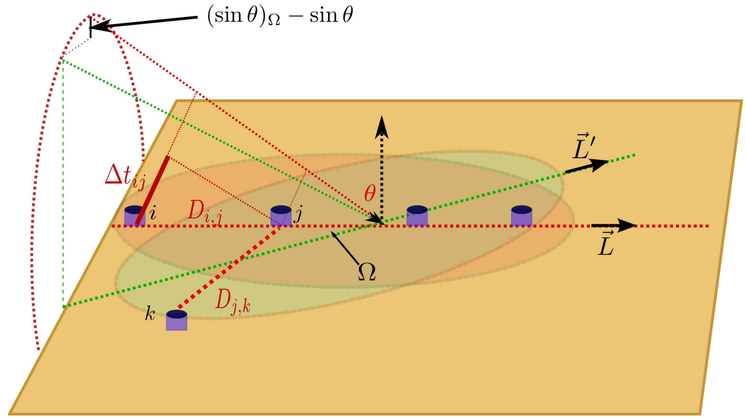

Figure 5.9: *Determination of zenith angle θ for aligned footprints. In red the shower direction for an aligned footprint of 4 stations is shown. The additional station, off axis, is representative for a possible outlier which may tilt the direction of the main axis of the principal component analysis, defined by the unit vector $\vec{L}$. In green the possible tilted main axis with unit vector $\vec{L}'$ is shown. The maximal tilting angle Ω can cause $\sin\theta$ (Eq. 5.5) to rise by $\cos\Omega + \sin\Omega$ due to the projection of relative distances of couple of stations onto the tilted axis (text for details). The calculated zenith angle θ is referred to the local reference system with its origin in the barycenter of the footprint.*

be the unit vector which defines the direction of the axis tilted of Ω with respect to the direction defined by $\vec{L}$. The unit vector $\vec{L}'$ can be decomposed onto $\vec{L}$ and the direction perpendicular to $\vec{L}$ with the equation

$$\vec{L}' = \vec{L}\cos\Omega + \vec{L}\sin\Omega. \tag{5.7}$$

Equation 5.2 becomes

$$d'_{ij} = \vec{D}_{ij} \cdot \vec{L}' = D_{ij}\cos\delta_{ij}\left(\cos\Omega + \sin\Omega\right). \tag{5.8}$$

Thus, if the main axis on the ground can be tilted of $|\Omega| \leq 5.7°$, the estimate for $\sin\theta$ can rise about 9.5% according to the following relation

$$\frac{(\sin\theta)_\Omega}{\sin\theta} \leq \cos\Omega + \sin\Omega, \tag{5.9}$$

where $(\sin\theta)_\Omega$ represents the evaluation of $\sin\theta$ based on the direction $\vec{L}'$.

An additional modification was considered for events with station multiplicity larger than 10. In particular, the direction was reconstructed with a "robust" procedure which was thought to avoid outliers which might bias the convergence of the fit. A preliminary linear fit uses all the selected N candidate stations of a footprint to give an estimate of $\cos\theta = w_{est}$. Each station k is assigned initially a score S_k equal to 0. Then, an iterative algorithm tries all the possible subsets of combinations of the initial set of candidates. At each step, w is evaluated and the degree of displacement $|w - w_{est}|/w_{est}$ was added to the

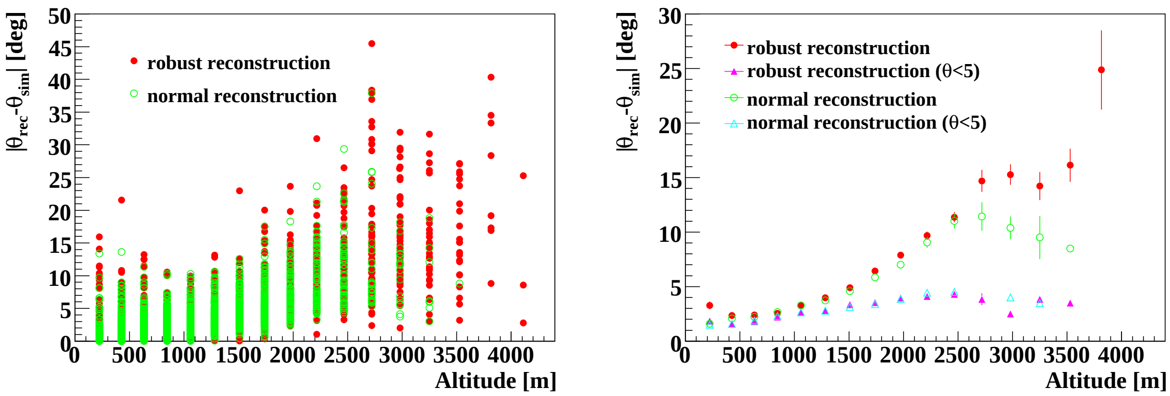

Figure 5.10: *Robust versus ordinary procedure to reconstruct shower directions. The absolute value of the difference between the reconstructed zenith angle θ_{rec} and the simulated zenith angle θ_{sim} for down-going ν_e showers at $87°$ is shown. The application of the robust procedure to reconstruct shower incoming zenith angles shows an overall increase in the number of reconstructed events.*

score S_k of each station which participated in the considered combination. The algorithm continues until a combination with at least 6 stations has been reached. For each station, the collected score is divided by the total number of combinations in which the station has taken part. The distribution of normalized scores is supposed to detect possible outliers or leverage stations, i.e. stations whose influence to the fit is too important. In particular, the median of the normalized scores and the stations whose normalized scores are at a distance larger than 1σ from the median are temporarily discarded.

After the evaluation of the direction, the removed stations are again introduced in the set of initial candidates but a definitive removal of outliers can be still allowed if some stations present a temporal distance from the reconstructed plane front outside the temporal window of $[-2000, 4000]$ ns. In Fig. 5.10, the difference between the reconstructed zenith angles of down-going ν_e showers at $87°$ by using the normal procedure and the robust procedure can be seen. The robust procedure is helpful at higher altitudes, where the attenuation of the atmosphere cause many stations to have scattered traces, and at lower altitudes, due to the large fluctuation of the signals produced by the electromagnetic component of the showers. An overall increase of about 30% in the number of reconstructed events can be observed. The precision of the algorithm might be even improved either by increasing the number of combinations allowed, i.e. by letting the algorithm processing the combinations until a set with less than 6 stations is reached, or by combining the reconstruction algorithm with a suitable selection of stations.

In conclusion, the geometrical reconstruction of ν-showers requires particular care and should not be adopted as additional cut for neutrino identification but rather as indication of possible sources of errors when discrepancies between results obtained with it and results obtained with $\langle V\rangle$ and L/W arise during the identification of inclined events. In other words, $\langle V\rangle$ and L/W remain the principal tools to discriminate vertical from inclined

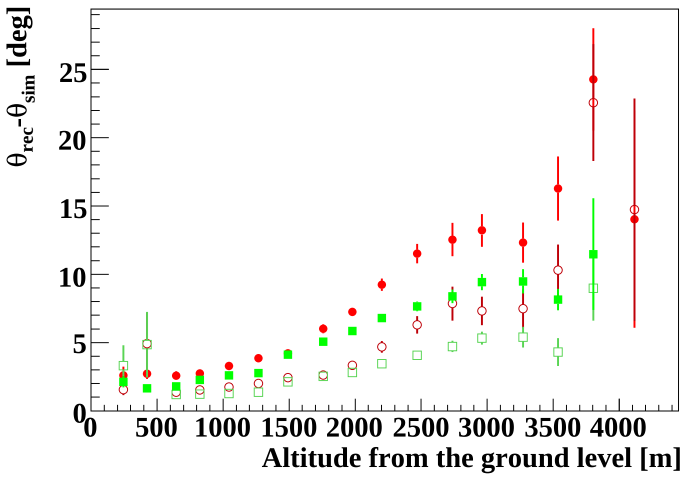

Figure 5.11: *Opening angle versus altitude for ν_e showers from CC (circles, red colors) and NC interactions (squares, green colors) at 87° in the atmosphere. The effect of the correction for the curvature is shown in dark colors (open markers).*

showers.

The curvature of the shower front affects the reconstructed direction of neutrino-induced showers. The simple parabolic analytical approximation for the shower front (Sec. 3.4, Eq. 3.8) can result in an improvement of the angular reconstruction of few degrees (Fig. 5.11). However, at the highest altitudes of decay points, the large fluctuations due to the atmospheric attenuation which affect the electromagnetic component of inclined and young events can lead to differences between expected and reconstructed zenith angle of about 20° or even larger. In Fig. 5.11 the difference between ν_e-induced showers from CC and NC interactions can be seen. In the latter case, the muonic component, more penetrating and with arrival times less affected by fluctuations, guarantees that some of the up-stream part of the shower front can be detected on the ground in a way that the reconstruction is less affected by the down-stream part which possesses a richer electromagnetic component. In the same figure it is also clear that a systematic discrepancy between expected and reconstructed zenith can not be lower than $2 - 5°$ due to the fact that the down-stream part is always predominant for young showers.

In Fig. 5.12 a scheme with the phases involved to identify neutrino events is shown. After the trace cleaning and signal calibration, a pre-selection of events is achieved through a pre-cleaning (rejection of events with less than 4 stations, removal of stations with no reconstructed data or with less than 3 working PMTs), a station selection (removal of isolated stations and top-down selection based on $\langle V \rangle$ and $\sigma_{\langle V \rangle}$) and an optional step of geometrical shower reconstruction. The next step is the reconstruction of the observables chosen to identify ν-induced showers.

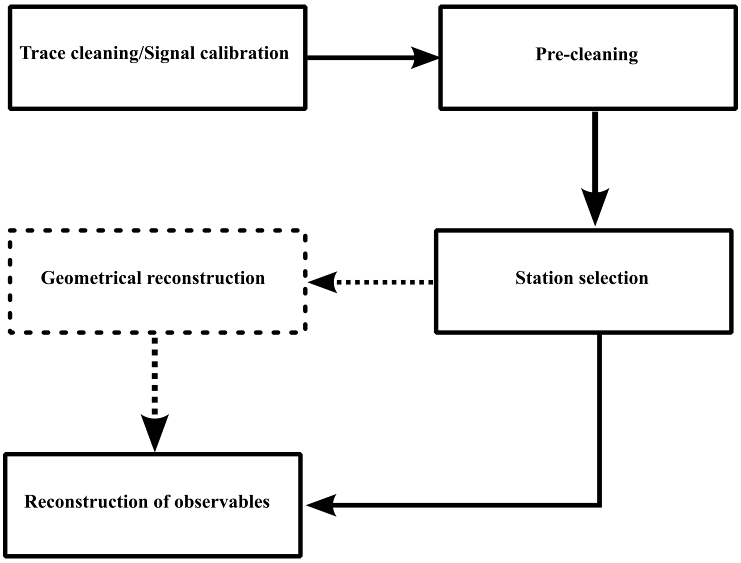

Figure 5.12: *Summary of the reconstruction phases which are applied to search for ν-showers (text for details).*

5.3 Background rejection and cut optimization

In order to evaluate the best set of cuts to identify neutrino showers, the program GARCON [146] was used. GARCON is based on genetic algorithms [147] to optimize cuts in a way that the signal passing rate is maximal while the background contamination minimal. GARCON can optimize multi-dimension phase space parameters within a reasonable time. In this work, the six parameter phase space $\vec{x} \equiv \{TOTF, L/W, \langle V\rangle, \sigma_{\langle V\rangle}, \langle RT_2\rangle, \langle FT_2\rangle\}$ is used to maximize the functional $F[S(\vec{x}^{cut}), B(\vec{x}^{cut})] = S(\vec{x}^{cut})/\sqrt{S(\vec{x}^{cut}) + B(\vec{x}^{cut})}$, where $S(\vec{x}^{cut})$ is the number of signal events passing after cuts and $B(\vec{x}^{cut})$ the number of remaining background events after cuts. The signal is represented by simulated neutrino showers with fixed energy (Sec. 4.1.2). The background is represented by the simulated proton showers mentioned in Sec. 4.1.2. Two approaches were used to optimize the cuts on the observables.

The first approach takes into account optimization in separate angular and energy bins for different types of neutrino simulations. The aim is to study the dependence of the cuts on the primary particle energy, since it might enable a further discrimination in future. The background was represented by all the CORSIKA showers with $\theta > 60°$. For down-going τ and electron-induced showers, due to the larger range of studied zenith angles, the signal was split into three angular bins: $[60°, 70°]$, $[70°, 80°]$, $[80°, 90°]$. Then, for each angular bin, the set of optimized cuts on the identification observables was calculated. In Tab. 5.1 a set of optimized cuts is listed for up-going and down-going showers in the angular range of zenith angle $\theta > 90°$ and $80° < \theta < 90°$, respectively. It can be well seen that the cuts depend on the injected particle energy, E_i. This is due to the fact that at higher primary energies, the width of patterns on the ground is larger than at lower energies. This leads

Table 5.1: Set of cuts for the identification observables obtained from GARCON optimization for down-going ν_τ and ν_e-induced showers with $80^\circ < \theta < 90^\circ$, and up-going ν_τ-induced showers with $\theta > 90^\circ$. E_i stands for initial injected particle energy.

i	E_i (EeV)	$(L/W)^{cut}$	$\langle V\rangle^{cut}$ (m/ns)	$\sigma^{cut}_{\langle V\rangle}$ (m/ns)	$\langle RT_2\rangle^{cut}$ (ns)	$\langle FT_2\rangle^{cut}$ (ns)	TOTF^{cut}
τ_{up}		>5.5		<0.010	>58	>144	>0.40
τ_{dw}	0.3	>3.5	0.30÷0.31	<0.016	>79	>242	>0.25
$e_{dw}+X$		>4.8		<0.004	>77	>160	>0.43
X		>3.2		<0.015	>66	>162	>0.21
τ_{up}		>3.3		<0.015	>49	>113	>0.3
τ_{dw}	1	>3.3	0.30÷0.31	<0.014	>49	>151	>0.2
$e_{dw}+X$		>3.6		<0.016	>67	>180	>0.2
X		>2.8		<0.015	>67	>175	>0.2
τ_{up}		>2.9		<0.016	>44	>118	>0.33
τ_{dw}	3	>3.2	0.30÷0.32	<0.016	>68	>253	>0.14
$e_{dw}+X$		>3.3		<0.017	>78	>197	>0.20
X		>2.7		<0.015	>71	>217	>0.14
τ_{up}		>2.0		<0.016	>48	>102	>0.30
τ_{dw}	10	>2.1	0.30÷0.33	<0.015	>56	>121	>0.10
$e_{dw}+X$		>2.4		<0.016	>70	>168	>0.18
X		>2.7		<0.015	>67	>177	>0.13
τ_{up}		>2.0		<0.017	>38	>87	>0.20
τ_{dw}	30	>2.1	0.29÷0.33	<0.017	>36	>93	>0.14
$e_{dw}+X$		>2.1		<0.017	>80	>218	>0.10
X		>2.3		<0.016	>70	>180	>0.10

to lower values of L/W. This is also the reason why for larger E_i the spread for the mean apparent velocity is larger (column 4 in Table 5.1). In addition, it is interesting to note that for down-going τ-induced shower at 0.3 EeV, for instance, $TOTF$ is small with respect to the corresponding energy bin for up-going τ-induced showers. This is due to the fact that the shower maximum position is usually closer to the ground level for up-going showers than for down-going showers. Differences of L/W and $TOTF$ in down-going and up-going τ-induced showers may be potential observables to discriminate the two classes of neutrino showers. The same tendency is also seen in Fig. 5.7.

The second approach takes into account the optimization of cuts without any restriction on the angular bin for the background and on the energy bin for neutrino events. In practice, searching for neutrino candidates in the huge amount of data collected with the

Table 5.2: Unique set of cuts for the identification observables as obtained from GARCON optimization. The underlying neutrino energy spectrum was assumed to be E^{-2} (text for details).

	$(L/W)^{cut}$ (m/ns)	$\langle V\rangle^{cut}$ (m/ns)	$\sigma^{cut}_{\langle V\rangle}$ (ns)	$\langle RT_2\rangle^{cut}$ (ns)	$\langle FT_2\rangle^{cut}$	TOTF^{cut}
τ_{up}	>4.0±0.6	0.299±0.001 0.309±0.002	<0.014±0.001	>63±8	>148±26	>0.38±0.03
τ_{dw}	>3.3±0.4	0.301±0.001 0.313±0.002	<0.0143±0.0005	>58±9	>147±12	>0.20±0.03
e_{dw}	>2.6±0.7	0.298±0.002 0.318±0.002	<0.0154±0.0004	>70±2	>178±14	>0.21±0.04
X	>2.9±0.4	0.298±0.001 0.314±0.002	<0.0149±0.0003	>66±1	>169±8	>0.18±0.03

Pierre Auger Observatory requires the use of a unique set of cuts which should not depend on energy and zenith angle but which should be related only to the neutrino type. The distribution of the variables $TOTF$, L/W, $\langle V\rangle$, $\sigma_{\langle V\rangle}$, $\langle RT_2\rangle$, and $\langle FT_2\rangle$, obtained for fixed energy and zenith angle, were weighted according to the expected distribution of leptons inside the Auger detector volume (Sec. 5.5) and their corresponding detection efficiency (Sec. 4.3). The incoming parent neutrinos were assumed to have a spectrum of type E^{-2}. The background of proton showers with energy between 0.1 EeV and 100 EeV was fully considered. The resulting sets of cuts depend only on the neutrino type. In Tab. 5.2 the sets of optimized unique cuts for different neutrino species and $\theta > 80°$ are listed.

The optimization of the cuts on the observables led to values for contamination of background of about 0% for all the examined zenith angles above 60° in the first approach and to values for the efficiency of about 100%. The second approach led to values of contamination smaller than 0.5% and selection efficiency larger than 98% for zenith angles above 80°. Even at smaller zenith angles the contamination did not exceed 1% and the efficiency remains above 97%.

Further discussion on efficiency and contamination in cut optimization will be done in the next chapter.

5.4 The identification efficiency

The unique set of cuts, calculated according to the description done in the previous section, is the necessary step to evaluate the neutrino identification efficiency, $T_{eff}(E_i, \theta, h)$, which is defined as the number of events triggering the detector and passing the cuts (N_{cut}) over the total number of simulated AIRES showers (N_{AIRES}). The efficiency was calculated for fixed zenith angle and energy of injected particles. As it was already shown in Sec. 4.3, the detection and the identification efficiency of up-going showers induced by the products of τ lepton decays, depend only on the τ lepton energy E_τ and the altitude above the ground, which approximately corresponds to the position of the shower maximum, $h_{10\ km}$, defined at 10 km from the decay point. In App. D a list of identification efficiency maps for different zenith angles and neutrino flavors is given. The corresponding detection efficiency maps, which were discussed in Sec. 4.3, are also shown for comparison. The detection efficiency is the maximum efficiency which can be achieved to detecting ν-induced showers.

It is worth mentioning that the application of cuts calculated according to the first approach described in the previous section leads to larger efficiency of about 8% on average. This is due to the fact that the first approach allows more permissive cuts.

5.5 Energy and angular range for neutrino detection

Two competing effects determine the most probable window for observing ν-induced showers at the surface array of the Pierre Auger Observatory. On the one hand, the probability to detect neutrinos increases with shower energy. On the other hand, the neutrino flux steeply falls with increasing energy. By assuming a power-law incoming flux E^{-2}, 10^6 events were generated with the neutrino generator ANIS (Sec. 4.1.1). The expected spectra for down-going and up-going τ leptons and down-going electrons at the site of the Auger detector (Fig. 5.13, left panel) were convoluted with the calculated detection efficiency. In Fig. 5.13 (right panel) the resulting spectra for down-going and up-going τ leptons and down-going electrons, as expected to be seen in the Auger detector, are shown. It is evident that the surface array of the Pierre Auger Observatory is expected to be more sensitive to neutrino events with energy below 10 EeV. Although the contribution of neutrino incoming directions with $\theta > 80°$ is larger, some dependence on the zenith angle can be observed also.

5.6 Aperture and acceptance of the surface array for well-contained events

The identification efficiency calculated in Sec. 5.4 can be applied to evaluate the sensitivity of the surface array of the Pierre Auger Observatory. In particular, the concept of aperture and acceptance of the surface array will be used.

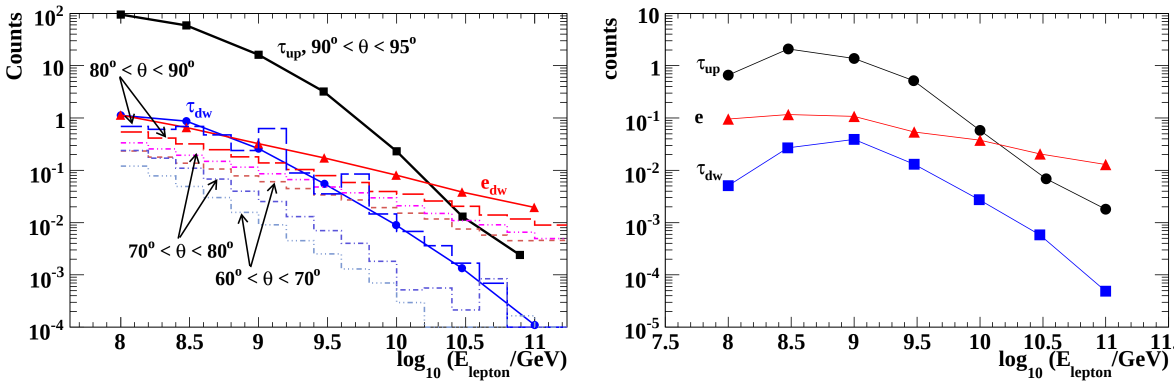

Figure 5.13: *(Left panel) Spectra of leptons expected at the site of the Pierre Auger Observatory. Some dependence on the zenith angle of incoming directions of down-going ν-induced showers can be observed. (Right panel) Convolution of expected lepton energy spectra with the detection efficiency as a function of the initial energy of leptons.*

In this work, the acceptance for a given initial neutrino energy E_ν is defined by the following equation

$$A(E_\nu) = N_{gen}^{-1} \times \sum_k \sum_{i=1}^{N_k} P_i(E_\nu, E_k, \theta) \times T_{eff,k}(E_k, \theta, h) \times A_i(\theta) \times \Delta\Omega, \qquad (5.10)$$

where N_{gen} is the number of generated neutrino events, N_k is the number of particles of type k (leptons/hadrons for CC/NC reactions)[2] with energy E_k larger than the threshold energy of the detector (E_{th}) and for which the decay vertex positions are above the ground and inside the detector volume, $P(E_\nu, E_k, \theta)$ is the probability that a neutrino with energy E_ν and crossing the distance ΔL would produce a particle with an energy E_k (this probability was used as "weight" of the event), $A_j(\theta)$ is the cross-sectional area of the detector volume seen by the neutrino, $\Delta\Omega$ is the solid angle. In case of aperture calculations, Eq. 5.10 was used with $T_{eff}(E_p, h, \theta)$ set to 1.

The aperture can be understood as the effective area which is seen by the incident cosmic neutrino flux Φ and can be calculated based on the output from ANIS. In other words, the aperture does not consider the detector identification efficiency. An energy threshold of 10^{17} eV was set to calculate the aperture since the Auger detector is not able to detect showers with smaller energy.

The acceptance is the convolution of the aperture with the detector identification efficiency calculated in Sec. 5.4.

It has to be noted that the simulated showers used for the calculation of the acceptance represents an ideal case of detection. Well-contained footprints were simulated in a fully efficient and complete detector. No edge effect and array evolution was considered so far so that the results presented here represent the best sensitivity which the Auger detector

[2] for ν_τ $k \in \{\tau, X_{CC}, X_{NC}\}$, for ν_e $k \in \{(e+X)_{CC}, X_{NC}\}$

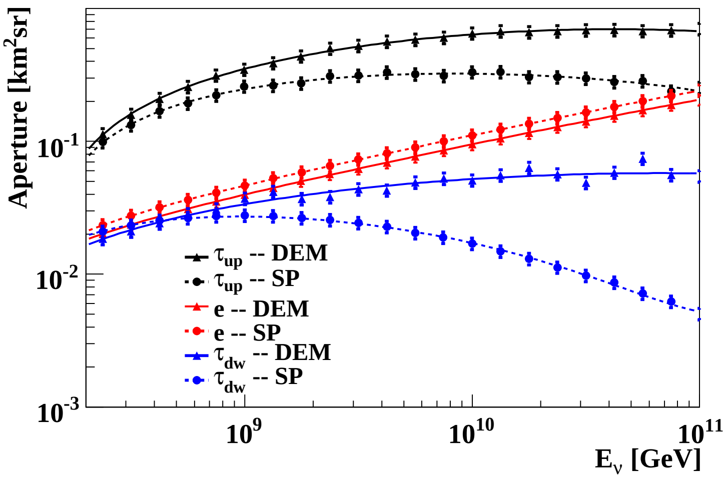

Figure 5.14: *The aperture for the surface array of the Pierre Auger Observatory. Here the computations including the topography of the Auger site (DEM) and with the simple spherical model of the Earth (SP) are shown. Results for up-going tau leptons are represented by the two grouped lines (black) in the top part of the picture, results for down-going electrons are represented by the two grouped lines (red) in the middle part of the picture and results for down-going tau leptons are represented by the two grouped lines (blue) in the bottom part of the picture.*

can achieve. It will be shown in the next chapter that the data collected from 1 January 2004 to 31 December 2007 correspond approximately to one year of fully efficient detector operation.

In Sec. 6.4 the calculation which takes into account the real time evolution of the detector configuration will be presented.

In Fig. 5.14 and Fig. 5.15 the aperture and acceptance for the surface array of the Pierre Auger Observatory are shown, respectively. The calculation adopted the GRV98lo cross-section model [35] (Sec. 1.3.1). The computations with the DEM and SP show significant differences especially for down-going τ-induced showers. For instance, at an energy of 0.3 EeV, the DEM calculations lead to an aperture of about 10% larger than the one obtained with the SP calculation. At energy of 10 EeV the DEM calculations lead to an aperture of about 3 times larger. The effect on the aperture is energy-dependent and it increases with increasing energy of the initial neutrino. The observed differences are due to the increase of the neutrino cross-section with the energy. The initial neutrino interacts with the mountains surrounding the Auger site and produces a τ lepton. For higher energies of the initial neutrino, the produced lepton in the mountains can reach the detector from larger distances.

In case of ν_e-induced showers, the aperture, calculated with DEM is slightly lower than the aperture with the SP computations. This is due to the larger amount of matter inside the detector volume which decreases the fiducial volume of the detector compared to the

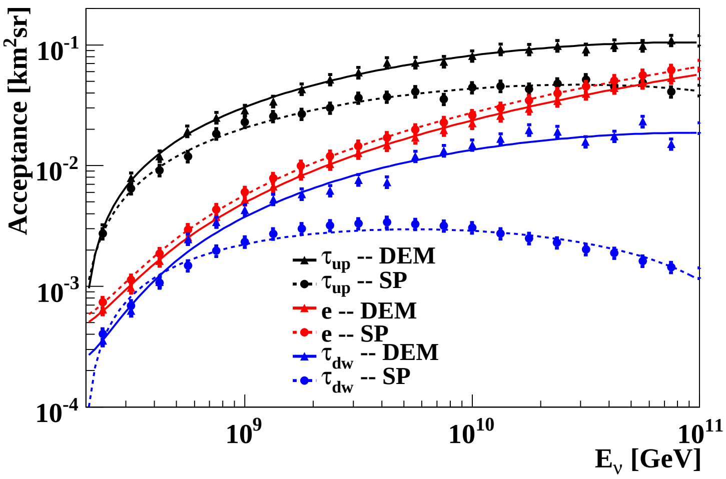

Figure 5.15: *The acceptance for the surface array of the Pierre Auger Observatory. Here the computations including the topography of the Auger site (DEM) and with the simple spherical model of the Earth (SP) are shown. Results for up-going tau leptons are represented by the two grouped lines (black) in the top part of the picture, results for down-going electrons are represented by the two grouped lines (red) in the middle part of the picture and results for down-going tau leptons are represented by the two grouped lines (blue) in the bottom part of the picture.*

fiducial volume used in the SP computations. In addition, one can observe an almost power-law like dependence of the calculated aperture on the neutrino energy. This effect is due to the increasing cross-section with the energy and the minor influence of energy loss processes for the propagated electron. In case of acceptance calculations the differences are even smaller.

5.7 Event rates

The total observable event rates (number of expected events per observation time unit) were calculated by using the following equation

$$N = \Delta T \times \int_{E_{th}}^{E_{max}} A(E_\nu) \times \Phi(E_\nu) \times dE, \tag{5.11}$$

where $\Phi(E_\nu)$ is the isotropic neutrino flux and ΔT the observation time.

In Tab. 5.3 the rate (number of events per year), for different injected neutrino fluxes, and based on the acceptance and aperture calculation shown in Sec. 5.6, are listed. The rates labeled with "WB" are obtained for the Waxman-Bahcall bound [148], $\Phi(E_{\nu_\tau+\bar{\nu}_\tau}) = 1\times10^{-8}E^{-2}\,\mathrm{GeVs^{-1}cm^{-2}sr^{-1}}$. Other rates are calculated for the GZK flux [149] and Topological Defects (TD) flux [150]. To quantify the influence of the topography of the Auger site on the calculated rate, the factor $k = (N_{DEM} - N_{SP})/N_{SP}$ was defined, where N_{DEM} is

Table 5.3: Expected event rates in (yr^{-1}) for the surface array of the Pierre Auger Observatory based on aperture (N_{Aper}) and acceptance (N_{Acc}) calculations. The values are calculated with the neutrino cross-section model GRV98lo [35]. The precision on the listed values is about 4%.

		WB			GZK			TD		
		N_{DEM} (yr^{-1})	N_{SP} (yr^{-1})	k (%)	N_{DEM} (yr^{-1})	N_{SP} (yr^{-1})	k (%)	N_{DEM} (yr^{-1})	N_{SP} (yr^{-1})	k (%)
N_{Aper}	τ_{up}	3.81	2.76	27.6	5.38	3.63	32.5	27.8	18.2	34.5
N_{Acc}		0.294	0.240	18.4	0.485	0.280	42.3	2.62	1.57	40.0
N_{Aper}	τ_{dw}	0.420	0.374	10.9	0.540	0.415	23.1	2.75	2.02	26.4
N_{Acc}		0.038	0.021	44.7	0.066	0.030	54.5	0.37	0.15	59.5
N_{Aper}	e_{dw}	0.513	0.600	-16.9	0.694	0.81	-16.7	3.79	4.43	-16.8
N_{Acc}		0.057	0.066	-15.8	0.101	0.12	-18.8	0.609	0.710	-16.6

the rate calculated with the DEM and N_{SP} the one calculated with the spherical model of the Earth. As one can see from Tab. 5.3, the rate of up-going τ-induced showers calculated with the DEM of the Auger site is about 30% larger in case of aperture calculations and about 18% larger in case of acceptance calculations with respect to the rate calculated with the simple spherical model of the Earth.

5.8 Contribution of individual neutrino flavors on the calculated acceptance and event rates

In Fig. 5.16 the effect of hadronic showers induced in NC and CC neutrino interactions on the calculated acceptance for down-going τ and electron-induced showers is shown.

Down-going ν_τ showers initiated by ν_τ CC interactions are spatially separated from showers induced in τ decays, resulting in additional triggers. The effect sums up to 60% at 3 EeV and is energy dependent since the separation distance depends on the incoming ν_τ energy. For instance, at an energy of 10 EeV the separation between the two showers is about 500 km. In this particular case the produced τ lepton can not decay before reaching the ground level, thus only the induced hadronic shower from ν_τ CC interactions can possibly be detected. In general, the higher the ν_τ energy, the larger is the separation distance and thus the contribution of hadronic showers induced by ν_τ becomes more important. In case of ν_e CC interactions, hadronic showers and showers induced by the electrons coincide since the production vertex for hadrons and electrons can be assumed to be at the same point. Therefore the active volume for ν_e CC interactions, defined as the volume around the detector which can contribute to the expected event rate, is much smaller than the

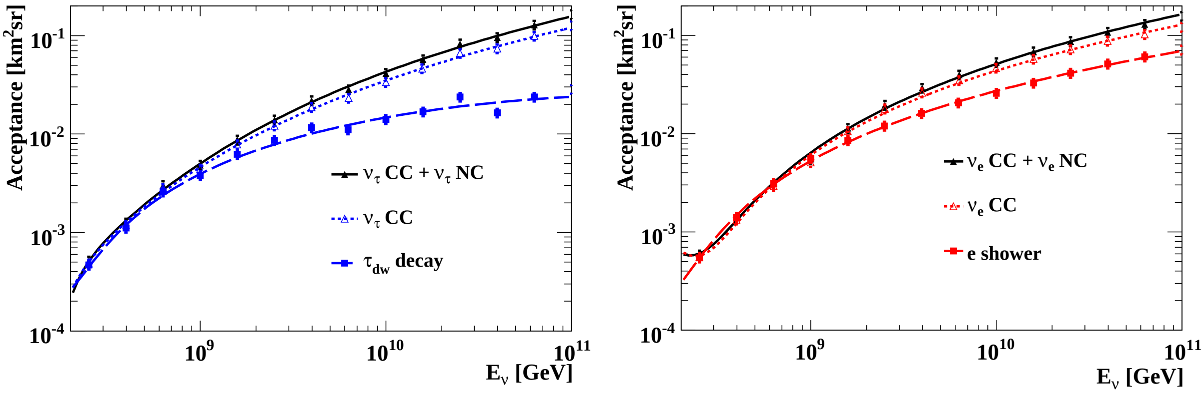

Figure 5.16: The acceptance for down-going showers induced by ν_τ (left panel) and ν_e (right panel) neutrinos. Here the contributions of hadronic showers induced from CC and NC ν interactions are shown.

Table 5.4: Relative contributions to the expected event rate for each neutrino flavor and weak interaction channel i in percent, with $N_{tot}^{DW} = 0.165\,\mathrm{yr}^{-1}$ and $N_{tot}^{UP} = 0.455\,\mathrm{yr}^{-1}$ for a WB flux.

interaction	channel	down going [%]			up and down going [%]		
		ν_e	ν_μ	ν_τ	ν_e	ν_μ	ν_τ
CC	l	34.5	0.0	23.0	12.5	0.0	72.1
	X	7.3	7.3	9.1	4.2	2.6	3.3
NC	X	6.1	6.1	6.7	2.4	2.2	2.4
Total		47.9	13.3	38.8	17.4	4.8	77.8

active volume for ν_τ-induced showers and the contribution of hadronic induced showers from ν_e CC interaction are thus smaller than ν_τ CC. In Fig. 5.16 also the contribution of ν NC for down-going electron and τ showers is shown. The calculated contribution is at the level of a few percent (below 10% for the studied energy range) and it is approximately the same for down-going ν_τ and ν_e. For up-going ν_τ showers (not shown in the Figure) the contribution of NC reactions and the contribution of hadronic states from CC are negligible, since these products are absorbed in the Earth during propagation to the detector.

It is interesting to study also the contribution of hadronic showers from CC and NC reactions at the level of the calculated event rates. In Tab. 5.4 the relative contribution to the expected event rate for each neutrino flavor and CC and NC interactions is listed. The relative contribution is shown for down-going showers with an expected rate of $N_{TOT} = 0.165\,\mathrm{yr}^{-1}$ and $N_{TOT} = 0.455\,\mathrm{yr}^{-1}$ for down-going and up-going showers together. Down-going ν_e showers dominate the calculated rates. However, also a significant ν_τ contribution comes from the enhanced τ lepton flux due to the topography surrounding the Pierre Auger Observatory and from the larger contribution of hadronic products for ν_τ CC interactions

Table 5.5: Total expected event rates (CC+NC) in (yr^{-1}) for the surface array of the Pierre Auger Observatory. The values are calculated with a digital elevation map and the ν cross-section model GRV98lo [35]. The precision on the listed values is about 4%

	WB (yr^{-1})	GZK (yr^{-1})	TD (yr^{-1})
ν_τ^{up}	0.294	0.485	2.620
ν_τ^{dw}	0.064	0.119	0.780
ν_e	0.079	0.150	0.977

than for ν_e CC interactions. The contribution of NC reactions to the calculated rates is about 6% for each flavor and is much smaller than the contribution of CC reactions. This is explained by the fact that the CC cross-section is roughly 3 times larger than the NC one. The ν_μ and ν_e channels contribute the same because they can be treated in an identical way in first approximation. Showers induced by ν_τ contribute at the level of about 78% to the total rate.

Finally, in Tab. 5.5 the total rates (CC + NC contribution) for different injected ν-fluxes are listed.

5.9 Systematic effects

The influence of the uncertainties is evaluated in terms of final event rates. Each class of events (τ and electron neutrino-induced showers) has its specific uncertainty. Nevertheless, a few sources of systematic uncertainties, such as the neutrino cross-section or uncertainties of the neutrino propagation in the atmosphere and the Earth affect all classes in the same manner. For τ-induced showers, also the uncertainties coming from the τ lepton energy loss and the τ lepton polarization are examined. The studied systematic effects are listed in Tab. 5.6 in case of the WB flux.

The systematic effects due to different neutrino-nucleon cross-sections are calculated using cross-sections given in Refs. [37, 35, 39]. The used cross-sections are given in Fig. 5.17 (left panel). They are different especially at the largest energies. This is due to different extrapolations of the probability density function (PDF) in the regions where the Bjorken-x and the squared 4-momentum transfer, Q^2, are not experimentally measured (low x and high Q^2). The neutrino cross-section from Ref. [35], GRV98lo, was used as a reference. This cross-section is extended to the extremely small-x region, $10^{-8} < x < 10^5$ (typically, CTEQ5 [37] and hard pomeron (HP) [39] cross sections are calculated above $x > 10^{-5}$) and it is evaluated on the basis of recent results from the HERA experiment [152]. The influence of different cross-sections on the calculated acceptance is given in Figure 5.18. For down-going electrons (upper-left panel) and down-going and up-going τ-induced showers (upper-

Table 5.6: Systematics due to cross-section, energy loss model, τ polarization and propagation are listed. The central value is computed by using GRV98lo cross-section as a reference and energy loss models are taken from Ref. [151] for $\Phi(E_{\nu_\tau+\bar{\nu}_\tau}) = 1 \times 10^{-8}E^{-2}$ (GeV s^{-1} cm^{-2} sr^{-1}).

flavor	N_{Acc}	cross-section	energy loss	polarization	propagation	sum
τ_{up}	0.290	$^{+10\%}_{-0.0\%}$	$^{+21\%}_{-29\%}$	-6%	8%	$0.290^{+25\%}_{-31\%}$
τ_{dw}	0.064	$^{+15\%}_{-22\%}$	$^{+3\%}_{-6\%}$	$+2\%$	8%	$0.064^{+17\%}_{-24\%}$
e_{dw}	0.079	$^{+12\%}_{-20\%}$			8%	$0.079^{+14\%}_{-22\%}$

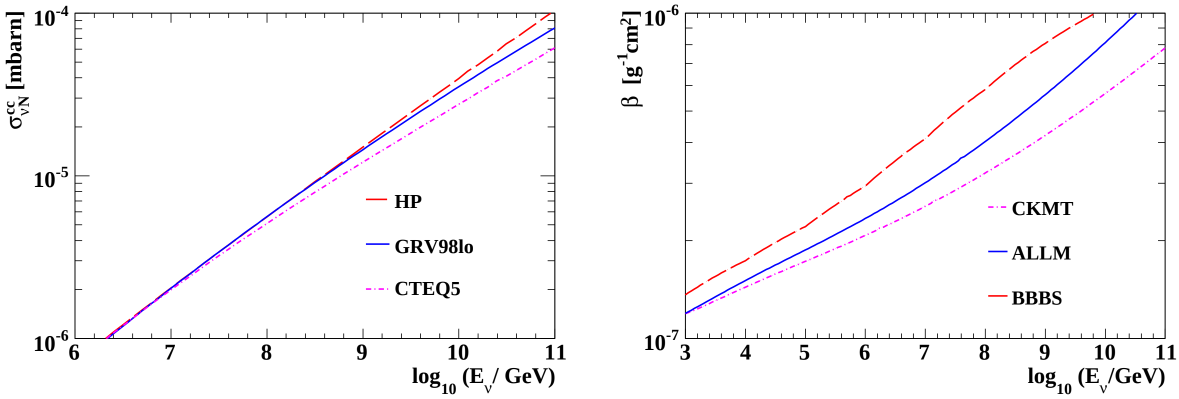

Figure 5.17: (Left panel) The ν-nucleon cross-section as a function of neutrino energy; (Right panel) The parameter beta as a function of the τ lepton energy.

right and bottom panel, respectively) the influence is energy dependent and differences are larger for down-going than for up-going showers.

Other sources of uncertainties are the different models of τ energy losses during propagation in atmosphere and Earth's crust. When a τ lepton is genereated, it looses energy due to ionisation and radiation processes (bremsstrahlung, pair production and photo-nuclear interaction). At the energy range of interest the photo-nuclear interactions are the main source of uncertainty. To calculate the nucleon cross-section, the proton structure function has to be used. This function is unknown in the the relevant energy range for the τ lepton at low Q^2 and low x and an extrapolation for $x < 10^{-6}$ is required. The proton structure function is evaluated applying the models ALLM [153], GVD (BBBS) [154] and CKMT model [155] respectively (see Refs. [156, 151] for more details reviewing the uncertainties). In Fig. 5.17 (right panel) the evaluated factor β, including contributions from bremsstrahlung, pair production and photo-nuclear interaction is displayed. The influence of the adopted energy loss model on the calculated acceptance is shown in Fig. 5.18 with

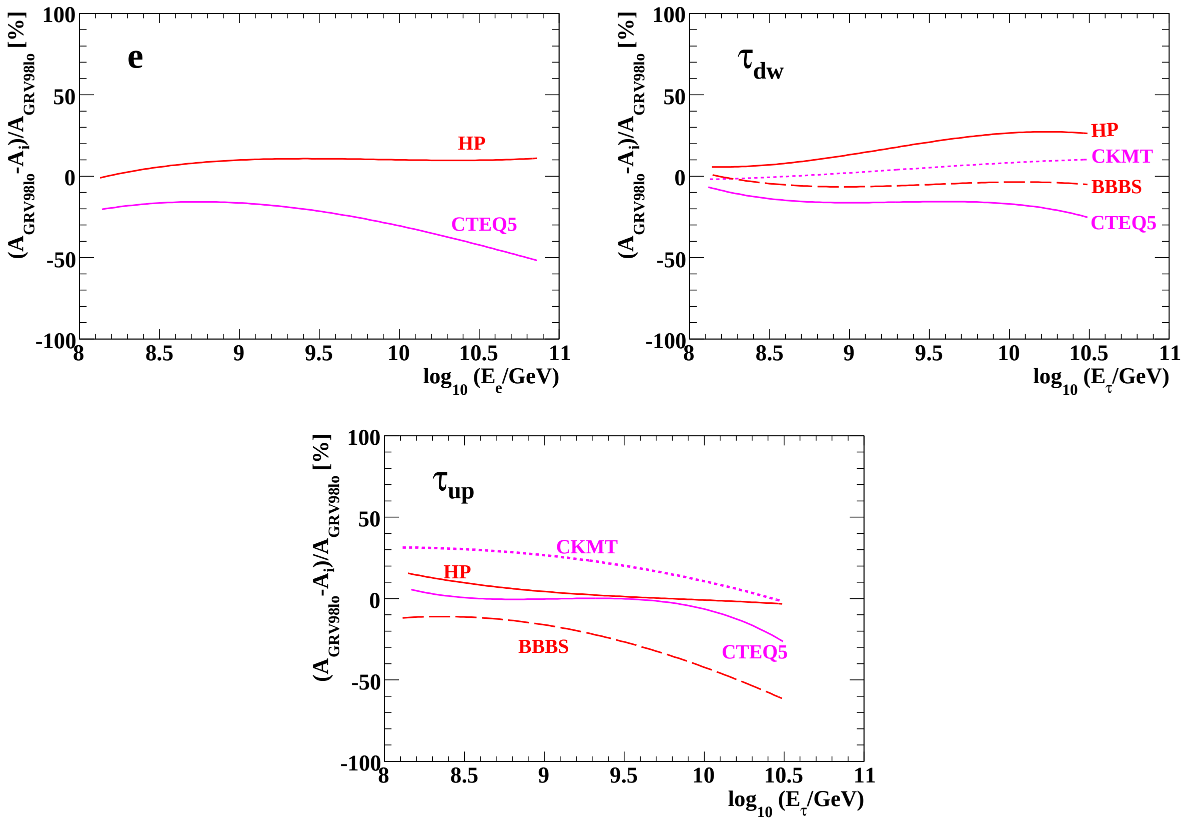

Figure 5.18: (Upper-left panel) Relative changes of calculated acceptances A_i with respect to GRV98lo cross-section for down-going electron induced shower; Relative changes of acceptance in case of down-going (upper-right panel) and up-going τ-induced showers (bottom panel) according to GRV98lo cross-section and the ALLM model of energy losses.

respect to a reference acceptance calculated within the ALLM model (GRV98lo is used as reference for the cross-section).

The uncertainty due to polarization of the τ lepton is also addressed. The τ lepton, produced from interaction of neutrinos or antineutrinos with matter, is expected to be polarized [157]. This effect is taken into account in the ANIS simulations, e.g. if the produced τ lepton is left-handed or right-handed, the different distributions of energy fraction (inelasticity distributions) in the laboratory frame for different decay products of the τ lepton are used. These distributions depend on the polarization of the τ lepton and are calculated using the generator TAUOLA. A conservative estimation of the systematics for a τ polarization equal to ± 1 leads to about 6% uncertainty. A total uncertainty of about 8% is quoted due to the Monte Carlo calculations of the emerging τ lepton flux and to the trigger efficiency, T_{eff}.

The systematic uncertainty added in quadrature sums up to $\binom{+25\%}{-31\%}$ for up-going τ leptons, $\binom{+17\%}{-24\%}$ for down-going τ leptons and $\binom{+14\%}{-22\%}$ for down-going electrons.

5.10 Sensitivity and upper limit to the neutrino flux

The calculation of the neutrino sensitivity can be started by requiring a fixed number of events N_{exp} within an observation time window ΔT with the assumption of a differential flux $f(E_\nu) = k\,E_\nu^{-2}$. From Eq. 5.11, one obtains

$$N_{exp} = \Delta T \int A(E_\nu)\; f(E_\nu)\; dE_\nu = k\;\Delta T \int A(E_\nu)\; E_\nu^{-2}\; dE_\nu = k\,\mathcal{N}\,. \tag{5.12}$$

The *integral* sensitivity can be calculated as

$$k = \frac{N_{exp}}{\Delta T\; \int A(E_\nu)\, E_\nu^{-2}\, dE_\nu} = \frac{N_{exp}}{\mathcal{N}}\;. \tag{5.13}$$

The *differential* format is obtained from Eq. (5.12) written as

$$N_{exp} = \Delta T \int A(E_\nu)\; f(E_\nu)\; E_\nu\; d\ln E_\nu\;. \tag{5.14}$$

By assuming that $f(E_\nu)$ can be approximated by a constant in an interval $\Delta \ln E_\nu$, the expected number of events is

$$N_{exp} = \Delta T\; A(E_\nu)\; f(E_\nu)\; E_\nu\; \Delta\ln E_\nu\;. \tag{5.15}$$

The differential sensitivity is given as

$$f(E_\nu) = \frac{N_{exp}}{E_\nu\; \Delta T\; A(E_\nu)\; \Delta \ln E_\nu}\;. \tag{5.16}$$

The assumptions for the calculation of the sensitivity are $N_{exp} = 1$ and $\Delta T = 1\,$year.

The integral and differential upper flux limit can be obtained similarly to the sensitivity described above, but with a different assumption on N_{exp}, as described in Ref. [158]. Under the assumption that all types of uncertainties and background signals can be neglected, at $(1-\alpha)\,100\%$ confidence level (C.L.) the upper limit can be found by solving the equation

$$p_0(k) = exp(-N_{exp}) = \alpha\;, \tag{5.17}$$

where p_0 is the Poisson probability of observing zero events when $N_{exp} = k\mathcal{N}$ events are expected. For a 90% C.L., this gives $N_{exp} = 2.3$.

The integral sensitivities to different neutrino species are

$$E_\nu^2 \Phi(E_\nu) < 7.8 \times 10^{-8} \left({}^{+25\%}_{-31\%}\right)\; \mathrm{GeV cm^{-2} s^{-1} sr^{-1}} \tag{5.18}$$

for up-going ν_τ,

$$E_\nu^2 \Phi(E_\nu) < 1.5 \times 10^{-7} \left({}^{+22\%}_{-33\%}\right)\; \mathrm{GeV cm^{-2} s^{-1} sr^{-1}} \tag{5.19}$$

for down-going $\nu_e + \nu_\tau + \nu_\mu$, and

$$E_\nu^2 \Phi(E_\nu) < 0.51 \times 10^{-7} \left({}^{+33\%}_{-45\%}\right)\; \mathrm{GeV cm^{-2} s^{-1} sr^{-1}} \tag{5.20}$$

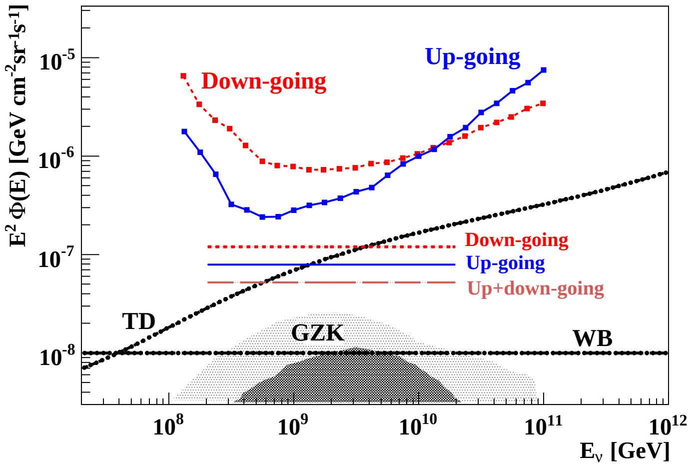

Figure 5.19: *Integral and differential sensitivity.*

for up-going and down-going neutrinos. It has to be noted that down-going ν_μ are expected to induce detectable showers only in the NC channel. The contribution of these showers to the total expected event rates is assumed to be the same as that of ν_e NC-induced showers (Sec. 4.1.2). The individual contributions of down-going ν_e, ν_τ, and ν_μ to the total sensitivity of Eq. 5.19 are

$$E^2_{\nu_e}\Phi(E_{\nu_e}) < 2.9\times 10^{-7}\left({}^{+14\%}_{-22\%}\right)\ \mathrm{GeVcm^{-2}s^{-1}sr^{-1}}, \tag{5.21}$$

$$E^2_{\nu_\tau}\Phi(E_{\nu_\tau}) < 3.6\times 10^{-7}\left({}^{+17\%}_{-24\%}\right)\ \mathrm{GeVcm^{-2}s^{-1}sr^{-1}}, \tag{5.22}$$

and

$$E^2_{\nu_\mu}\Phi(E_{\nu_\mu}) < 0.23\times 10^{-7}\left({}^{+14\%}_{-22\%}\right)\ \mathrm{GeVcm^{-2}s^{-1}sr^{-1}}, \tag{5.23}$$

respectively. These results are valid in the energy range $0.1-10$ EeV, where 90% of expected events can be located. The zenith angular range of validity is $60^\circ - 90^\circ$ for down-going neutrinos and $90^\circ - 95^\circ$ for up-going. In Fig. 5.19 the integral sensitivities are shown along with some typical spectra of astrophysical neutrinos. The differential sensitivities (defined as the inverse of the acceptance, namely $2.3/(E_\nu A^i(E_\nu)\Delta\ln(E_\nu))$ are also plotted. It is evident that the largest sensitivity is achieved at about 1 EeV. Moreover, the contribution of down-going showers is significant for the total expected sensitivity.

It is interesting to study also the sensitivities of the surface array to down-going neutrinos in the angular range $75^\circ - 90^\circ$. It will be shown in the next chapter that contamination of different sources of background at lower zenith angles, namely for $\theta \lesssim 75^\circ$, does not allow high-quality discrimination. The total sensitivity to $\nu_e + \nu_\tau + \nu_\mu$ is

$$E^2_{\nu}\Phi(E_{\nu}) < 2.76\times 10^{-7}\left({}^{+22\%}_{-33\%}\right)\ \mathrm{GeVcm^{-2}s^{-1}sr^{-1}}. \tag{5.24}$$

The individual contributions of down-going ν_e, ν_τ, and ν_μ to the total sensitivity of Eq. 5.24 are

$$E^2_{\nu_e}\Phi(E_{\nu_e}) < 5.3\times 10^{-7}\left({}^{+14\%}_{-22\%}\right)\ \mathrm{GeVcm^{-2}s^{-1}sr^{-1}}, \tag{5.25}$$

$$E^2_{\nu_\tau}\Phi(E_{\nu_\tau}) < 6.6 \times 10^{-7} \binom{+17\%}{-24\%} \ \mathrm{GeVcm^{-2}s^{-1}sr^{-1}}, \tag{5.26}$$

and

$$E^2_{\nu_\mu}\Phi(E_{\nu_\mu}) < 0.46 \times 10^{-7} \binom{+14\%}{-22\%} \ \mathrm{GeVcm^{-2}s^{-1}sr^{-1}}, \tag{5.27}$$

respectively.

6

Analysis of measured data

In the previous chapter, the analysis of neutrino-induced shower simulations and hadronic simulations showed that only few neutrino events are expected to be detected at the surface array of the Pierre Auger Observatory. Neutrino-induced showers are characterized by means of a set of parameters which allow their discrimination from proton showers even better as the zenith angle of incoming directions becomes larger. Optimization of the cuts to discriminate neutrino signatures from ordinary cosmic-ray signatures is the crucial step to evaluate the identification efficiency of the surface detector array and to calculate the expected event rates.

The negligible event rates, expected for neutrino-induced showers with respect to the huge amount of data collected with the surface array, allow to consider measured data as a new background for the analysis developed in the previous chapter in a way that hadronic simulations can be replaced with measured data and provide a real source of all the possible types of expected cosmic-ray primaries and instrumental background. The analysis of measured data, collected from January 2004 to August 2008, will be presented in Sec. 6.1. A new set of cuts for the identification observables is obtained (Sec. 6.2) and used for searching for neutrino candidates in measured data. No significant differences with the cuts obtained by using simulated hadronic showers are expected but the efficiency of identification is expected to be reduced at lower zenith angles. Some neutrino candidates will be presented and discussed in Sec. 6.3. Finally, the acceptance (Sec. 6.4), the expected event rates and upper bound to neutrino fluxes (Sec. 6.5) will be further discussed by including the real time evolution of the surface detector array.

6.1 Reconstruction of measured data

Measured data contain all the possible sources of background along with possible physical showers. Among the latter, only a negligible fraction of events is expected to belong to neutrino-induced showers. Therefore, the whole set of measured events can be considered as background to searching for neutrino events.

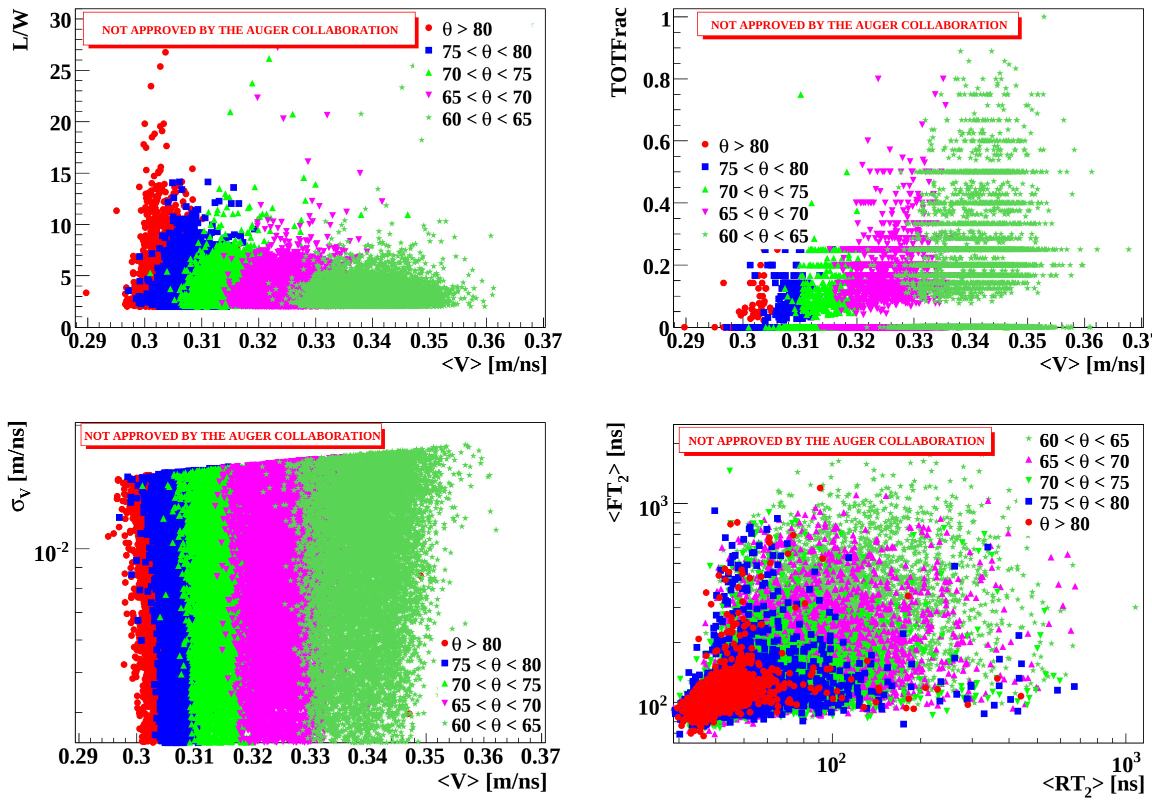

Figure 6.1: *Reconstructed observables, in different angular intervals, used to identify neutrino candidates in measured data. (Upper-left panel) Length over width versus mean apparent velocity; (Upper-right panel) Fraction of ToT stations versus mean apparent velocity; (Lower-left panel) Statistical uncertainty of mean apparent velocity versus mean apparent velocity; (Lower-right panel) Average fall time versus average rise time of the earliest two triggering stations.*

Nevertheless, the reconstruction of measured data returns an additional intrinsic source of uncertainty for the following analysis. It contains failures of the reconstruction and events whose traces are not fully cleaned from muon peaks during the calibration phase (Sec. 4.2.2). Such uncertainties are mostly evident for events with a low station multiplicity where even a single station may give its contribution in reconstructing an event.

The reconstruction of measured data is performed in the period from January 2004 to August 2008 with a total number of analyzed events of about 5×10^6. Neutrino events are expected to be young showers. Therefore, the smaller the zenith angle, the lower is the efficiency of discriminating neutrino events from the huge background of ordinary detected cosmic-ray showers.

As seen in Fig. 6.1, measured data in different angular intervals can be distinguished by means of observables both from footprint analysis, such as the length over width, L/W, and mean apparent velocity, $\langle V \rangle$, and from signal characteristics, such as the fraction of

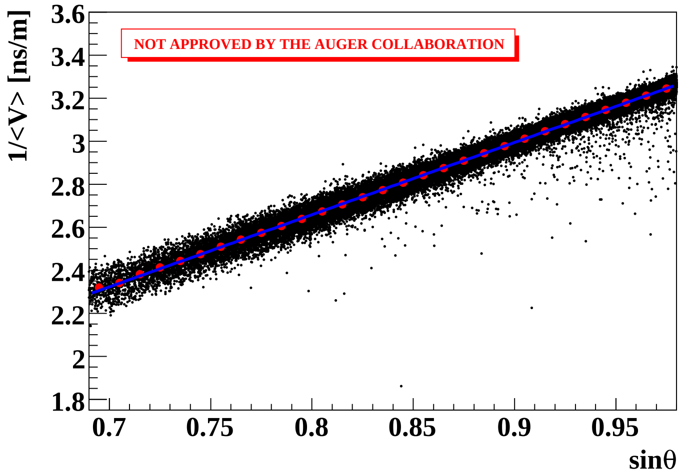

Figure 6.2: *Inverse of the mean apparent velocity as a function of sine of reconstructed zenith angle. The black points represent reconstructed measured data; the red full circles are a profile of data points; the blue line is the linear fit according to Eq. 6.1.*

ToT stations, $TOTF$, and the average of rise and fall time for the two earliest stations, $\langle RT_2 \rangle$ and $\langle FT_2 \rangle$.

At smaller and smaller zenith angles, although the observables which identify the incoming direction, L/W and $\langle V \rangle$, constrain less inclined events, the observables which correspond to the signal characteristics, $TOTF$, $\langle RT_2 \rangle$ and $\langle FT_2 \rangle$, are not enough to guarantee the identification of possible neutrino candidates by themselves. Only the combination of all the observables and the optimization of cuts on them can allow the background rejection at a satisfactory level.

The additional later requirement that the selected ToT stations obey the configurations which are given by the central trigger algorithm (Sec. 5.2) allows the reduction of the initial set of measured data and permits only showers with a compact young nucleus of ToT stations to be kept. This condition, called $IsStillT3$ in the following discussion, along with suitable cuts on the observables used to identify neutrino footprints is the final step to searching for neutrino candidates in measured data.

The huge statistics of measured data gives the possibility to study more carefully some characteristics which can be associated to different angular intervals. Particularly interesting is the search for additional quality cuts which might help to improve the selection of neutrino candidates. For example, the reconstructed zenith angle versus $\langle V \rangle$ is shown in Fig 6.2. By generalizing Eq. 5.5 to include less aligned events or events with $L/W > 2$, a linear dependence of $1/\langle V \rangle$ on $\sin\theta$ can be inferred with the following parameterization

$$\frac{1}{\langle V \rangle} = a \sin\theta + b. \tag{6.1}$$

According to the discussion of Sec. 5.2, an uncertainty smaller than about 25% can be associated to the zenith angle calculated with Eq. 6.1 in case of $L/W > 2$. A linear fit

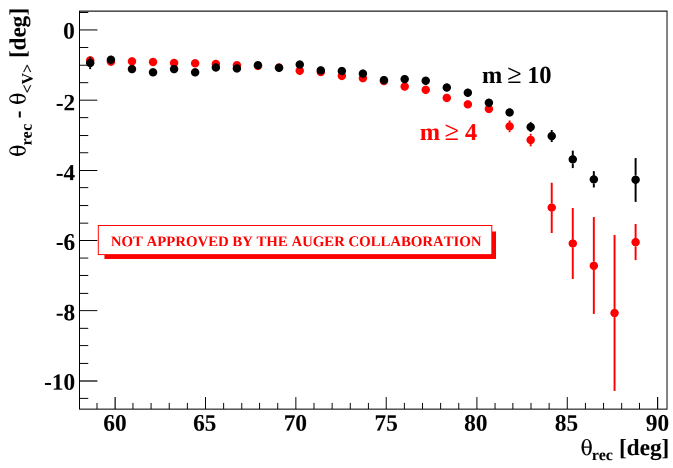

Figure 6.3: *Reconstructed zenith angle, θ_{rec} as from the modified plane fit, and expected zenith angle, $\theta_{\langle V\rangle}$ as from Eq. 6.1, are compared. The red full circles are for stations multiplicities larger than or equal to 4; the black full squares represent station multiplicities larger than or equal to 10.*

gives the following values for the parameters a and b of Eq. 6.1, and the uncertainty $\sigma_{1/\langle V\rangle}$: $a = 3.359 \pm 0.002\,\mathrm{ns/m}$, $b = -0.0030 \pm 0.0016\,\mathrm{ns/m}$ and $\sigma_{1/\langle V\rangle} = 0.24\,\mathrm{ns/m}$. The result can be used to identify different zenith angles of shower incoming directions without performing any shower geometrical reconstruction. The requirement that a geometrical reconstruction for a shower is possible can be considered as an optional quality cut. Basically, the reconstruction of the zenith angle can validate the possible discovery of a neutrino candidate. In Fig. 6.3 the expected zenith angle evaluated by using Eq. 6.1 and the calculated $\langle V\rangle$, $\theta_{\langle V\rangle}$, is compared with the reconstructed zenith angle, θ_{rec}, as from the modified plane fit. At larger zenith angles, more events are expected to be aligned and stations with traces which are not perfectly cleaned or stations which are not properly removed during the station selection may bias the principal component analysis especially for low multiplicity events by tilting the direction of the alignment on the ground. This is reflected in a biased $\langle V\rangle$ and $\theta_{\langle V\rangle}$ due to projection of distances of couples on a wrong evaluated direction (Sec. 5.2 and Fig. 5.9). At larger multiplicities the effect of bad stations is absorbed.

6.2 Optimization of cuts by using measured data

As it was already shown in Sec. 5.3, the program GARCON provides a set of tools which allow optimization of the multidimensional phase space $\vec{x} \equiv \{TOTF, L/W, \langle V\rangle, \sigma_{\langle V\rangle}, \langle RT_2\rangle, \langle FT_2\rangle\}$ by setting the signal events, represented by simulated neutrino showers, and the background events, represented now by measured data. Neutrino simulations were grouped into the intervals $[60°, 70°]$, $[70°, 80°]$, and $[80°, 90°]$ and distinguished in flavor. Measured data were considered as a whole. The geometrical reconstruction was adopted only to set

Table 6.1: Optimized cuts on the identification observables, $TOTF$, L/W, $\langle V \rangle$, $\sigma_{\langle V \rangle}$, $\langle RT_2 \rangle$ and $\langle FT_2 \rangle$, based on the analysis of measured data. The precision on the listed values is 5%. The efficiency of the procedure is also listed in the last column and it is indicated as "eff.".

ν-type	θ (deg)	$(L/W)^{cut}$	$\langle V \rangle^{cut}$ (m/ns)	$\sigma^{cut}_{\langle V \rangle}$ (m/ns)	$\langle RT_2 \rangle^{cut}$ (ns)	$\langle FT_2 \rangle^{cut}$ (ns)	TOTF^{cut}	eff.
	60–70	2.0	0.323÷0.352	0.022	88.2	170.8	0.48	50±12%
dw ν_e	70–80	2.5	0.315÷0.335	0.016	81.5	210.6	0.30	60±8%
	> 80	3.1	0.297÷0.319	0.015	70.6	160.0	0.19	82±10%
dw ν_τ	> 80	3.3	0.300÷0.313	0.014	58.0	145.0	0.31	87±10%
up ν_τ	> 80	3.8	0.298÷0.309	0.014	65.0	152.0	0.38	89±10%

a soft cut at 40° and avoid big sources of uncertainty in the procedure. A careful analysis of the results showed that, among all the observables in the adopted phase space, $TOTF$, RT and FT resulted to be the most important identification observables. The other two observables, L/W and $\langle V \rangle$ with its associated uncertainty $\sigma_{\langle V \rangle}$, depend on the considered angular bins. Since more young showers are expected to be detected at lower zenith angles, it is clear that a discrimination of ordinary cosmic rays from neutrino showers is not fully achievable unless additional observables are used. The final and strongest requirement is that the selected ToTs obey the central trigger requirements. This condition cleans the initial set of events from misleading young showers, such as ordinary cosmic-ray showers whose ToT stations do not form a compact nucleus as expected for neutrino showers.

The *contamination* of signal events (neutrino showers), defined as the number of surviving background events (measured data) in signal events, was found to be zero above 80°. In the range $70° - 80°$ the contamination increases to a value of 2% and below 70° the contamination is about 10%. At lower zenith angles it becomes harder and harder to distinguish the signatures produced by neutrino showers from the signatures expected from ordinary cosmic-ray showers and/or other instrumental and random sources of background. In other words, cut optimization can not provide a set of suitable values to separate background event distributions from signal event distributions.

In addition, the *efficiency* of the optimization, i.e. the number of surviving signal events over their total number, becomes lower as the zenith angle decreases. The optimization procedure tries to reach a compromise between rejection of background events and saving of signal events. Below 70° the application of the optimized cuts is not enough to guarantee high *purity* of the sample and high efficiency of rejection. In Tab. 6.1 the optimized cuts on the identification observables, based on the analysis of measured data, are listed. A comparison with the results reported in Tab. 5.2 shows that no important difference is obtained by replacing simulated showers with measured data. This is an indication that

Table 6.2: List of the number of neutrino candidates found after the application of the optimized cuts. The variable m indicates the multiplicity of candidate stations.

ν-type	θ [deg]	Candidates
	60–70	513 (133, $m > 10$)
dw ν_e	70–80	3
	> 80	0
dw ν_τ	> 80	0
up ν_τ	> 80	0

simulation can reproduce the characteristics expected for neutrino and proton-induced showers. On the other hand, the higher contamination and the lower efficiency show that more sources of background which are present in measured data are not contemplated in simulation. The additional condition $IsStillT3$ favors the increase of the purity by rejecting more background events (Sec. 6.3) but the increase of the efficiency can not be achieved unless a detailed study of the other sources of background is performed. If the features of the additional background are isolated and additional observables are introduced, an improvement in the efficiency can be expected.

6.3 Analysis of 3 selected events

The cuts on the identification observables, which were found in the previous section, were used to search for neutrino candidates in data collected at the surface array of the Pierre Auger Observatory. As it was discussed in the previous section and summarized in Tab. 6.1, the best angular range, where a good discrimination between ordinary cosmic ray showers and neutrino showers can be achieved, is above 80°. In this angular interval, no additional condition is required and the efficiency is between 77–99% for τ-induced showers and between 72–92% for electron-induced showers. No candidate of τ-induced or electron-induced showers was found. At zenith angles of shower incoming direction below 80°, few candidates were marked as neutrino candidates after the application of the additional condition $IsStillT3$ and required more careful analysis to eventually accept them definitively as candidates. In Tab. 6.2 the analysis for different neutrino flavors is shown. According to the discussion of the previous section, in the range $60° - 70°$ about 51 events out of 513 total candidates can be considered background due to the expected contamination of 10%. The remaining events can not be considered real candidates and there is no sense to analyze them further since discrimination from background events can not be achieved. In the range $70° - 80°$ a visual inspection of the selected candidates is required for a final decision.

In Tab. 6.3 results of the detailed analysis of surviving events after the application

Table 6.3: Detailed list of surviving events after cut application. The visual inspection is indicated with "eye".

Phase	Number of surviving events				
no cut	4280238				
pre-cleaning	3347054 (-21.8%)				
selection	74905 (-98.2%)				
reconstr. ($\theta > 40°$)	73647 (-98.3%)				
+Cuts	$60-70\,\mathrm{deg}$ ν_e	$70-80\,\mathrm{deg}$ ν_e	$> 80\,\mathrm{deg}$ ν_e	down ν_τ	up ν_τ
$\langle V\rangle + \sigma_{\langle V\rangle} + L/W$	24786	12631	15927	6954	50
$+TOTF$	3332	78	14	0	0
$+\langle RT_2\rangle + \langle FT_2\rangle$	2020	14	12	0	0
$+IsStillT3$	513	3	0	0	0
$+eye$	NA	1?	0	0	0

of the reconstruction procedure and optimized cuts step by step is shown. The analysis started with 4280238 triggering events among which only 3347054 were accepted to be reconstructed after a "pre-cleaning" procedure (no cut): at least 4 candidate stations with 2 or more working PMTs and no lightning phenomenon. The selection of stations is based on the procedure described in Sec. 5.2. The selection is optimized to search for inclined events ($\theta > 60°$) and, as expected, it rejects most of the triggering events. The modified plane fit reconstruction (Sec. 3.4 and Sec. 5.2) is used to set a soft cut at 40° and reduce misleading events. The plane fit reconstruction removes only a small fraction of events (0.1%). For each neutrino flavor, the corresponding cuts of Tab. 6.1 were then applied. As a final step, a visual inspection ("eye") was needed to validate the found candidates.

As it was already stated previously, searching for neutrino candidates at smaller zenith angles does not produce clear signatures ($\theta < 70°$). In other words, it is not possible to discriminate background events from neutrino events at a high confidence level.

The events 1605038 (2005/09/06), 2550163 (2006/08/13) and 4617571 (2008/03/03) passed the identification criteria for ν_e and were further analyzed to finally accept or reject them as neutrino candidates. In Tab. 6.4 a summary of their reconstructed observables is given. All these events were reconstructed with a zenith angle above 70° and are clear examples of young showers with elongated footprints. However, the procedure could not determine their origin. Further analysis of these events included the possibility that some stations could have been affected by accidental peaks which might have biased the reconstructed zenith angle. The constraints imposed by the robust linear fit (Sec. 5.2), however,

Table 6.4: Reconstructed observables for 3 selected events marked as neutrino candidates by the identification procedure.

Observables		Event identification number		
		1605038	2550163	4617571
θ	$[deg]$	70.1±0.6	71.4±0.5	71.1±0.6
ϕ	$[deg]$	137.9±0.7	241.6±0.5	-18.4±0.6
L/W		3.5	4.2	2.9
$\langle V \rangle$	$[m/ns]$	0.320±0.014	0.318±0.011	0.319±0.015
$\langle RT_2 \rangle$	$[ns]$	189.2	186.2	129.9
$\langle FT_2 \rangle$	$[ns]$	692.0	397.7	389.4
$TOTF$		0.32	0.33	0.32

imply that the reconstructed direction is not affected by outliers and that the associated error on the reconstructed parameters is a good estimate of the uncertainty.

A list of traces of the events 1605038, 2550163 and 4617571 can be found in App. E.

The event 1605038

According to the robust procedure described in Sec. 5.2, for the reconstruction of the event 1605038 (Fig. 6.4), the stations 584, 598, 617 and 619 were considered as leverage stations with a deviation of 5σ or larger from the median of scores but they were not removed because they were still in the allowed temporal window around the plane front. These stations are marked in Fig. 6.4 (left panel) with a red circle. The station 584 resulted to have only 2 working PMTs and the station 617 a double peak in its trace together with the station 619. It can be observed that $TOTF$ is almost at the limit allowed by the cut on its value and one of the stations having the $IsStillT3$ flag is a dubious station. This is the station 598 marked with a red circle and a black square. The removal of this station cause the central trigger to fail, e.g. no other pattern of remaining ToT stations is able to fulfill one of the central trigger requirements. In Fig. 6.4 (right panel) the evolution of the summed rise and fall time along the ground development is shown. A comparison with Fig. 5.2 shows that the average rise and fall time is expected to be above 150 ns for at least $6000-8000$ m of the footprint length. In conclusion, the event is a candidate at the border of the required conditions and can not represent a strong signature for a neutrino interaction in the atmosphere.

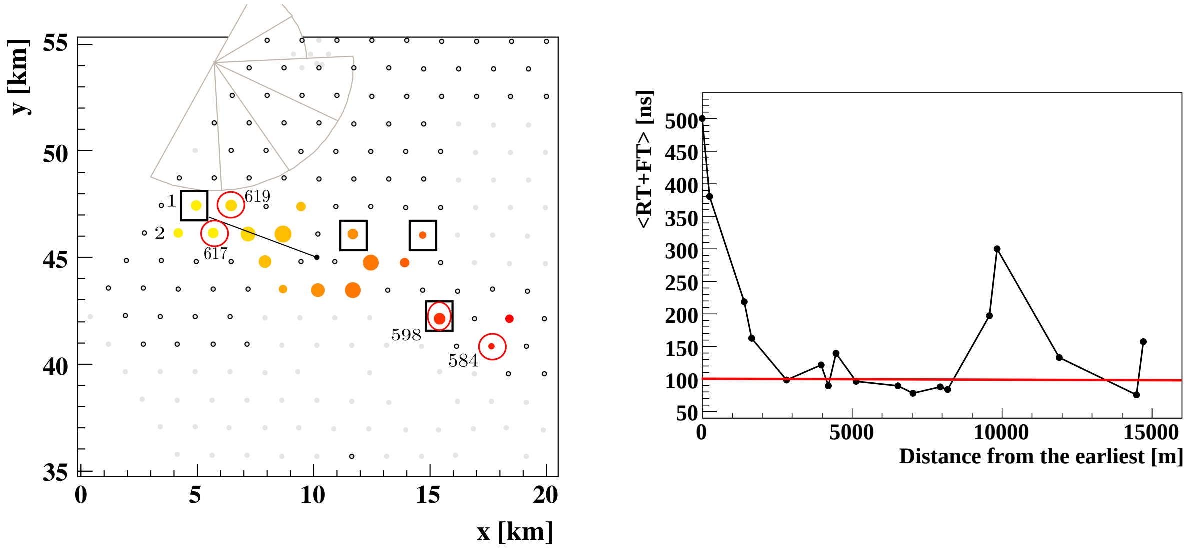

Figure 6.4: *The event 1605038. (Left panel) Footprint of triggered stations. Squares represent stations satisfying IsStillT3, circles represent stations marked as leverage stations during the direction reconstruction. The numbers 1 and 2 represent the first and second earliest stations. (Right panel) The summed rise and fall time evolution along its ground development. The steady red line represents an average evolution of ordinary cosmic ray showers.* **Disclaimer: The plots are not approved by the Auger Collaboration. Please do not use them.**

The event 2550163

The robust procedure for the reconstruction of the incoming direction (Sec. 5.2) of event 2550163 (Fig. 6.5, left panel) did not consider initially 10 stations with deviations larger than 1σ and up to 19σ from the median of scores but they were not removed because they were still in the allowed temporal window around the plane front. A visual inspection of the event showed that most of these stations had traces which were not perfectly cleaned during the calibration or difficult to clean. Only 4 stations, 684, 930, 619 and 1029, showed peculiar features which might have induced large scores. In particular, the station 684 (19σ) is a ToT station and apparently its trace does not show any peculiarity. A posteriori, however, it appears that the uncertainty on the signal start time is about 200 ns. The station 930 (6σ) has only 2 working PMTs. The station 619 (3σ) has two peaks. The station 1029 (3σ) is a T1 threshold trigger station. The use of these stations during the reconstruction would have not tilted the shower front zenith direction of 71.4°: the large multiplicity of stations allows to absorb the occurrence of a few bad stations. In Fig. 6.5 (right panel) the evolution of the summed rise and fall time along the ground development is shown. A clear evolution of a typical young shower is evident. The trend can be qualitatively compared to a typical average evolution for a low energetic neutrino shower (Fig. 5.2). Finally, the traces of the two earliest stations are shown in Fig. 6.6. It is clear that these traces are typical of the early stage evolution of a lower energy young shower. In Fig. 6.7 the expected

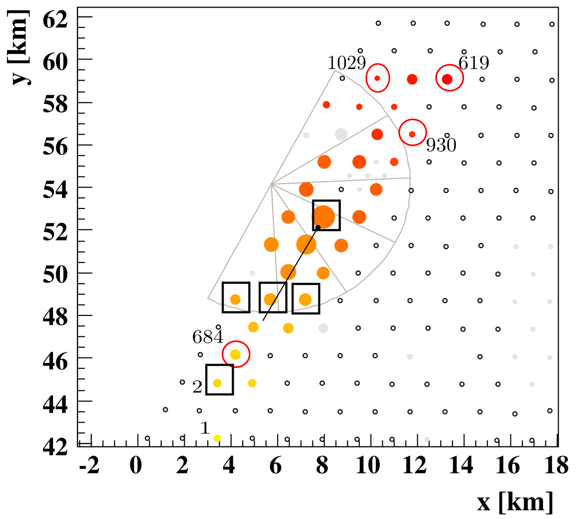

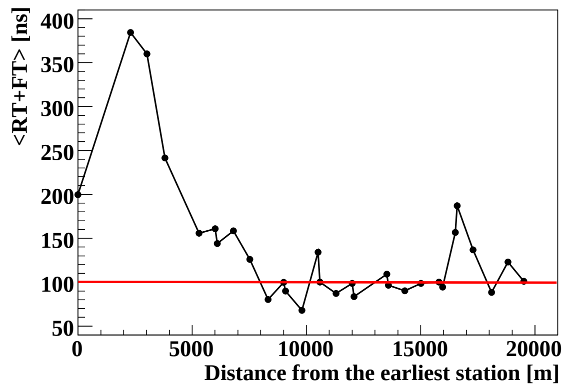

Figure 6.5: *The event 2550163. (Left panel) Footprint of triggered stations. Squares represent stations satisfying IsStillT3, circles represent stations marked as leverage stations during the direction reconstruction. The numbers 1 and 2 represent the first and second earliest stations. (Right panel) The summed rise and fall time evolution along its ground development. The steady red line represents an average evolution of ordinary cosmic ray showers.* **Disclaimer: The plots are not approved by the Auger Collaboration. Please do not use them.**

number of selected candidates at different angular bins for down-going electron neutrino simulated showers is shown. The range for the number of candidates at each energy bin reflects the inelasticity distribution of the involved processes. According to the number of selected stations in the event 2550163, a low energy neutrino shower is compatible with the observed average evolution of rise and fall time of Fig. 6.5 (right panel). In conclusion, the event 2550163 is a good neutrino candidate.

The event 4617571

The final event which is going to be discussed is the event 4617571 (Fig. 6.8, left panel). Here, as in the previous cases, the large multiplicity of stations is not affected by eventual outliers. The stations 849 (7σ), 1294 (7σ) and 1307 (3σ) did not affect the reconstruction at all. The evolution of the summed rise and fall time along the ground development is shown in Fig. 6.8 (upper-right panel). This definitively allows to reject the event 4617571 as a neutrino candidate. A peculiarity is the station 1296 which is not removed because in time, but clearly with rise and fall time outside the canonical evolution expected at such a position. The trace is shown in Fig. 6.8 (lower-right panel). This behavior was caused probably by an accidental muon with a time occurrence later with respect to the first triggering muon from the shower. The occurrence of a second muon increases the signal rise time.

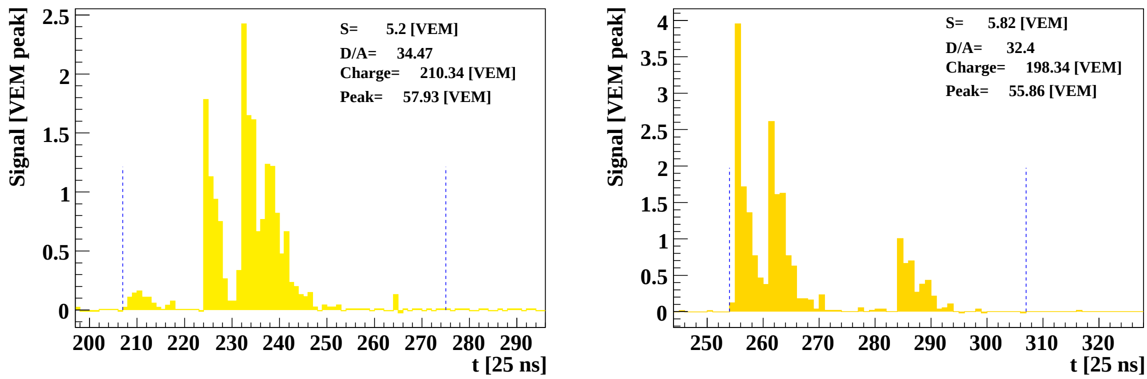

Figure 6.6: *Traces of the two earliest triggering stations of event 2550163.* **Disclaimer: not approved by the Auger Collaboration. Please do not use.**

Is there a neutrino candidate in measured data?

Among the 3 analyzed events, only the event 2550163 left some doubts on its origin. Further analysis included the simulations of proton-induced showers with the same incoming direction and energy (40 ± 4 EeV) as the event 2550163. By using AIRES 2.8.4a with the model QGSJETII for the high-energy interactions in the atmosphere, 100 proton-induced showers were simulated. The triggering showers (99 out of 100) were reconstructed and their properties evaluated. Out of 99 triggering showers, 95 showers were able to pass selection and reconstruction criteria. Only 1 event was able to pass the cuts for ν_e showers given in Tab. 6.1. The footprint is shown in Fig. 6.9 (left panel). The traces of the two earliest stations are shown in Fig. 6.9 (right panel). In Tab. 6.5 a summary is reported along with a comparison with the properties of the event 2550163. From the table, it is clear that, the proton-induced simulated showers can reproduce the features expected for the selected neutrino candidate event in 1% of cases. The single event left is deep enough to produce large rise and fall time and, thus, broad signals in most of the triggered stations.

The number of proton-induced showers N_p expected in the zenith angular range $70° - 80°$ and with energy 40 ± 4 EeV can be estimated from the measured cosmic-ray spectrum at the Pierre Auger Observatory (Chap. 1). By including the systematic uncertainty of about 22% [159],the number of expected proton-induced showers is $N_p = 69.1$ for the period January 2004 to August 2008. The number of proton-induced showers expected to pass the selection criteria is $N_b = 6.91$. The probability to measure $n = 0$ events from a background distribution with expected mean number of events $N_b = 6.91$ is given by

$$P(0|6.91) = exp(-6.91) \approx 0.5 \tag{6.2}$$

In conclusion, the hypothesis that the event 2550163 could be produced by a neutrino interaction has to be rejected. The purity and efficiency of the procedure can not guarantee discrimination of neutrino from proton-induced showers at zenith angles in the range of 70° and smaller.

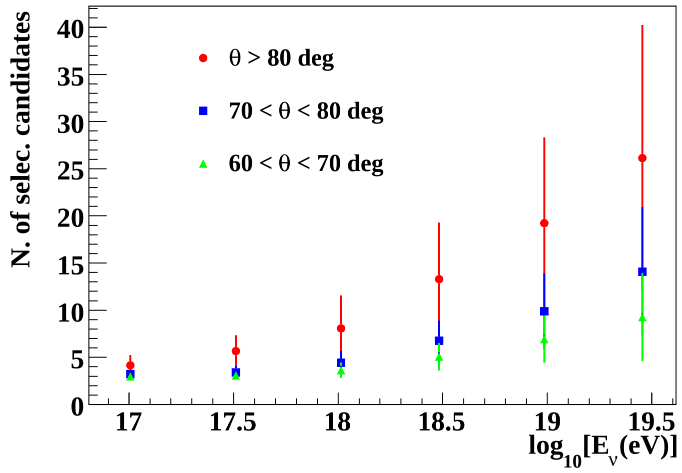

Figure 6.7: *Expected number of selected candidate stations for neutrino events in different angular and energy bins.*

6.4 Acceptance of the surface array

The calculations described in Sec. 5.6 considered a set of simulated neutrino-induced showers whose footprints were well-contained in an ideal configuration of the surface array of the Pierre Auger Observatory. In fact, the surface array has been growing in time since January 2004 and, moreover, it is also changing frequently its configuration in an irregular way due to stations which are temporarily not in acquisition, not transmitting etc. (Fig. 6.10). In addition, the efficiency for neutrino events depends not only on the shower energy and zenith angle but also on the depth at which the interaction takes place in the atmosphere. Finally, a *border effect* should be taken into account for showers whose footprints are partially cut when their development takes place close to the border of the surface array. In the latter case, a shower may not fulfill all the requirements imposed to identify a neutrino event or even it may not trigger the array at all.

The status of the surface array is monitored and stored 20 times per second of data acquisition in so-called T2-life activity files which contain information about the stations able to trigger as T2 (Sec. 3.3). Along with periods in which stations are not in acquisition, a list of "bad periods" is updated regularly to avoid array configurations in which no station sends T2 signals, stations send T2 signals but the Central Data Acquisition System (CDAS, Sec. 3.3) is off, stations send T2 signals and the CDAS is on but there is anomalous data taking.

To include the influence of the border effect on the identification efficiency, a circular area of radius 60 km centered at the surface array center was considered. The radius was optimized in such a way that also very elongated footprints from very energetic showers could be studied in all the possible positions with respect to the array: completely contained, semi-contained (or partially cut on the border of the array) and completely outside the array. This large area corresponds roughly to two times the surface array area.

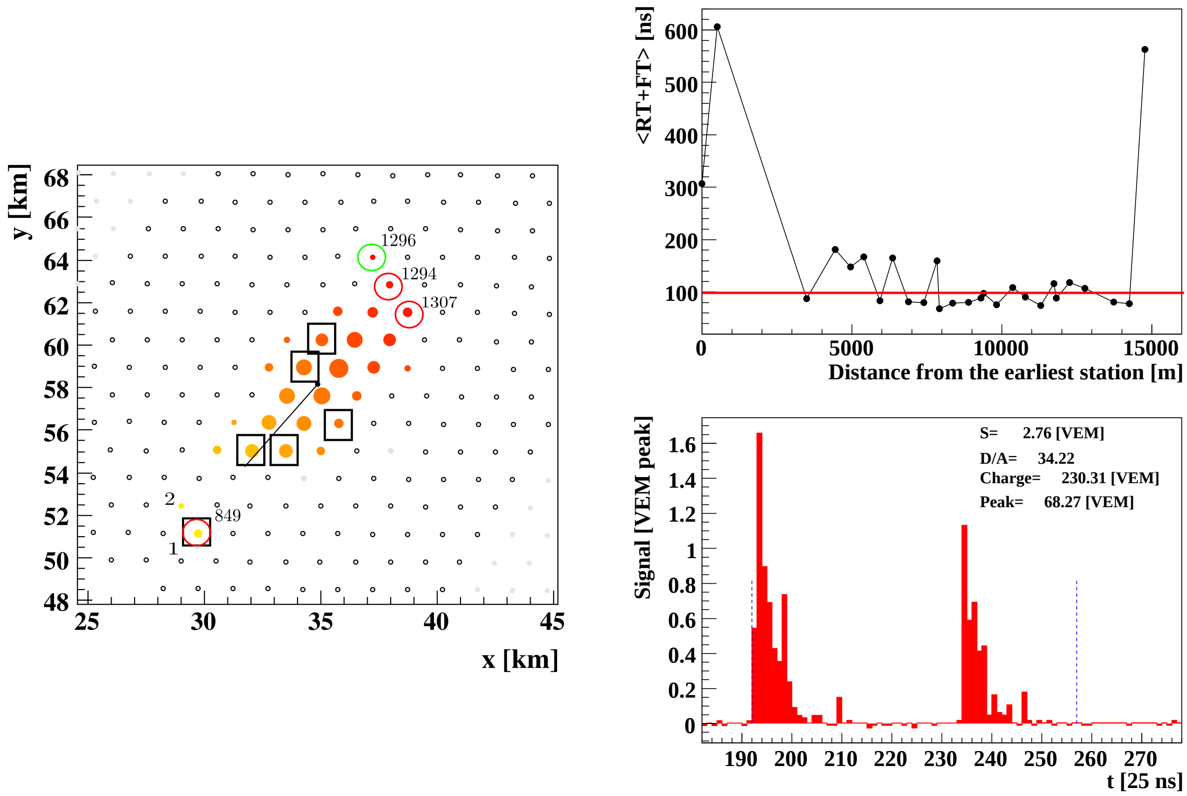

Figure 6.8: *The event 4617571. (Left panel) Footprint of triggered stations. Squares represent stations satisfying $IsStillT3$, circles represent stations marked as leverage stations during the direction reconstruction. The numbers 1 and 2 represent the first and second earliest stations. In light green, the particular station 1296 described in the text. (Upper-right panel) The summed rise and fall time evolution along its ground development. The red line represents an average evolution of ordinary cosmic ray showers. (Lower-right panel) The trace of the station 1296 for the event 4617571.* **Disclaimer: The plots are not approved by the Auger Collaboration. Please do not use them.**

The variation of the array configuration and, in particular, of the number of stations which are in acquisition can be significant, even on second-basis. In principle, the neutrino identification efficiency has to be calculated for each T2 lifetime interval but the acceptance would have to be evaluated with huge computational load. The final acceptance is the result of the integration over the all the periods considered. In particular, for each simulated neutrino shower and for each T2 lifetime interval, the position of the footprint should be chosen randomly across the large area and at each of such iterations the trigger and identification should be tested. A good randomization of footprint positions (uniform coverage of the whole area considered) can be usually achieved after thousands of iterations, depending mainly on the shower energy and, thus, on the number of triggering stations which are involved. Keeping in mind that such a procedure has to be repeated for each

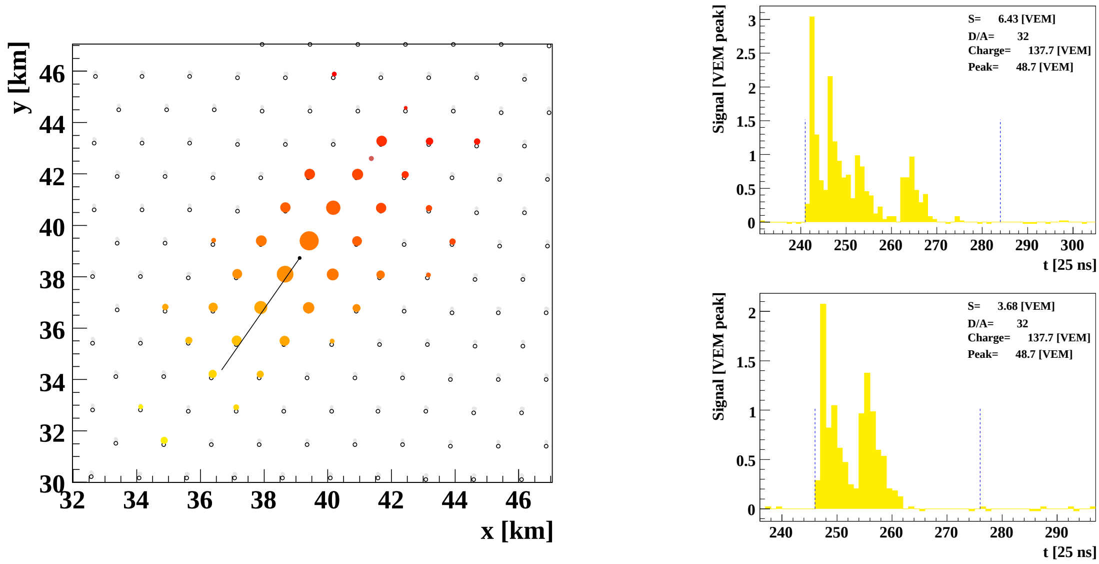

Figure 6.9: *Simulated proton-induced shower mimicking the neutrino candidate. The event was simulated at the center of an ideal array configuration. (Left panel) Footprint of triggering stations. (Right panel) Traces of the two earliest triggering stations.*

instant of time, a similar approach prevents one from obtaining feasible results in a realistic time scale.

In this work, a faster approach to calculate the acceptance, which takes into account the evolution of the array, was adopted. The aim is to calculate the acceptance which can be expressed as

$$A_{real}\left(E_\nu\right) = \frac{1}{t_1 - t_0}\int_{t_0}^{t_1} A\left(E_\nu, t\right) dt, \tag{6.3}$$

where t_0 corresponds to the time stamp of 1 January 2004, t_1 corresponds to the time stamp of 31 December 2007 and $A\left(E_\nu, t\right)$ is the acceptance calculated with the Eq. 5.10 at the time stamp t. First, the whole period from January 2004 to December 2007 was divided in 3-day periods in order to handle small sets of calculations. A total of 497 3-day periods was thus considered. For each angular bin and neutrino type, the set of footprints, which passed the identification criteria (Sec. 5.2) were separated in energy bins. In each 3-day period and for each set of selected monoenergetic neutrino footprints, an iterative procedure chooses randomly a footprint, a time stamp and a position within the large area. The random choice of a footprint is done according to the distribution of the identification efficiency for the particular energy bin considered. In principle, starting from EAS simulations, detector simulations should be performed many times for a single event by fixing footprint positions and array configuration. Nevertheless, detector simulations require much more computation time and disk space. The procedure uses the well-contained footprints which were simulated and stored in case of an ideal array (Sec. 4.1.2) and moves such footprints across an actual array configuration contained in the ideal array (Fig. 6.11, left panel). In other words, only the reconstructed showers were used and the core positions randomized

Table 6.5: Detailed analysis of event 2550163 with 100 simulated proton-induced showers which retain the same direction and energy of this event. The average reconstructed parameters of the triggering events, of the remaining event, and of the ν-candidate are given.

Observables		Reconstr. param.	Remaining event	Ev. 2550163
θ_{rec}	[deg]	70.8±0.6	70.8	71.41
$\delta\theta_{rec}$	[deg]	0.10±0.09	0.07	0.05
ϕ_{rec}	[deg]	241.5±0.8	241.6	241.6
$\delta\phi_{rec}$	[deg]	0.13±0.25	0.07	0.05
L/W		3.3±0.5	3.4	2.9
$\langle V \rangle$	[m/ns]	0.317±0.001	0.317	0.318
$\sigma_{\langle V \rangle}$	[m/ns]	0.001±0.003	0.001	0.001
$\langle RT_2 \rangle$	[ns]	160.5±211.0	128.5	186.2
$\langle FT_2 \rangle$	[ns]	262.5±319.5	260.5	397.7
$TOTF$		0.21±0.10	0.31	0.32

with significant saving of time and disk space. At each iteration, the identification can be tested by applying the reconstruction chain described in the previous chapter. A cumulative probability for the set of footprints, which were considered in each analyzed 3-day period, can be obtained. This probability is built as the ratio

$$R_\nu \left(n_p, E_\nu, \theta\right) = \frac{N_{id}}{N_{tot}}, \tag{6.4}$$

where n_p is the time period, E_ν the energy of the set of footprints considered, N_{id} the total number of events identified as neutrinos and N_{tot} the total number of iterations. The associated binomial uncertainty is given by

$$\sigma_{R_\nu} \left(n_p, E_\nu, \theta\right) = \sqrt{\frac{R_\nu \left(n_p, E_\nu, \theta\right) \left(R_\nu \left(n_p, E_\nu, \theta\right) - 1\right)}{N_{tot}}}. \tag{6.5}$$

The procedure is terminated successfully if $\sigma_{R_\nu}/R_\nu \leq 10\%$. In order to estimate correctly the statistical proportion R_ν, a cumulation of at least 10 failures and 10 successes was required or, in other words, $N_{id} \geq 10$ and $N_{tot} - N_{id} \geq 10$. The requirements are faster fulfilled for larger footprints and in periods when the array is closer to its completion (2006-2007). An example of the evolution of the ratio R_ν and its relative uncertainty σ_{R_ν}/R_ν

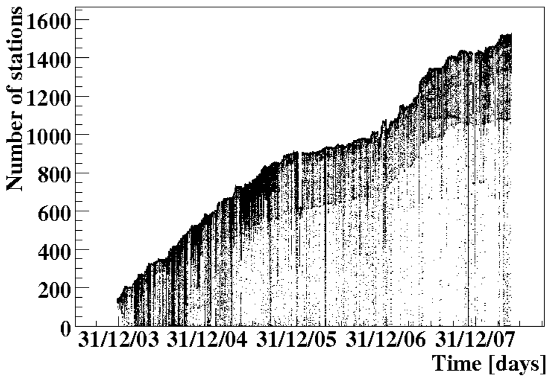

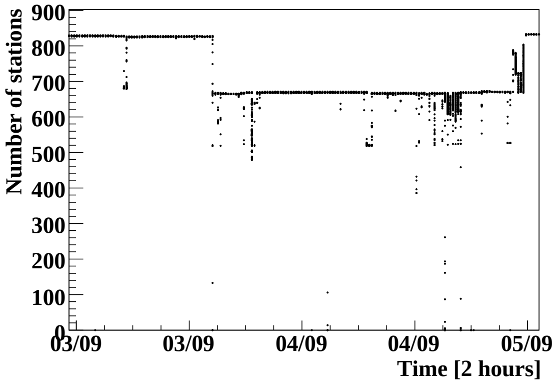

Figure 6.10: *(Left panel) Number of stations of the surface array of the Pierre Auger Observatory as a function of time. (Right panel) Variation of the number of stations in acquisition is shown for a period of 2 days.* **Disclaimer: The plots are not approved by the Auger Collaboration. Please do not use them.**

after 500 iterations in a fixed 3-day period for the set of down-going electron neutrinos from CC interactions at 1 EeV is shown in Fig. 6.11 (right panel). Usually, about 5000 iterations are necessary on average to reach 10% relative uncertainty. In some particular cases, when the variation in the array configuration is significant within the 3-day period, the fluctuations in R_ν are only slightly compensated by larger statistics and much more iterations are needed to decrease the uncertainty σ_{R_ν}. The ratio of Eq. 6.4 can be considered as a correction factor for the identification efficiency which was previously calculated for well-contained events. In particular, Eq. 5.10 can be re-written as

$$A(E_\nu) = N_{gen}^{-1} N_p^{-1} \times \sum_k \sum_{i=1}^{N_k} \sum_{n_p=1}^{N_p} P_i(E_\nu, E_k, \theta) \times T_{eff,k}(E_k, \theta, h) \times R_{i,k}(n_p, E_\nu, \theta) \times A_i(\theta) \times \Delta\Omega, \tag{6.6}$$

where R_ν is replace by $R_{i,k}(n_p, E_\nu, \theta)$ to indicate all the possible neutrino classes, N_p is the number of 3-day periods considered and $A_i(\theta)$ corresponds to the cross sectional area for the cylinder with base area of 60 km radius. An example of the evolution of the ratio, evaluated for the set of down-going electron neutrino simulations from CC and NC interactions at 87°, is shown in Fig. 6.12 (upper panels). By integrating over the whole considered 3-day periods, an integrated ratio $R_\nu(E_\nu, \theta)$ can be obtained from the following equation

$$R_\nu\,(E_\nu, \theta) = N_p^{-1} \sum_{n_p=1}^{N_p} R_\nu(n_p, E_\nu, \theta) \tag{6.7}$$

such that $R_\nu(E_\nu, \theta)$ can be considered as a correction factor for the efficiency $T_{eff,k}(E_p, \theta, h)$ in Eq. 6.6. The ratio $R_\nu(E_\nu, \theta)$ does not depend on neutrino type and shower incoming direction, or at least the dependence is absorbed by the fluctuations imposed by the array evolution, but it depends on neutrino energy and on the multiplicity of the stations. The

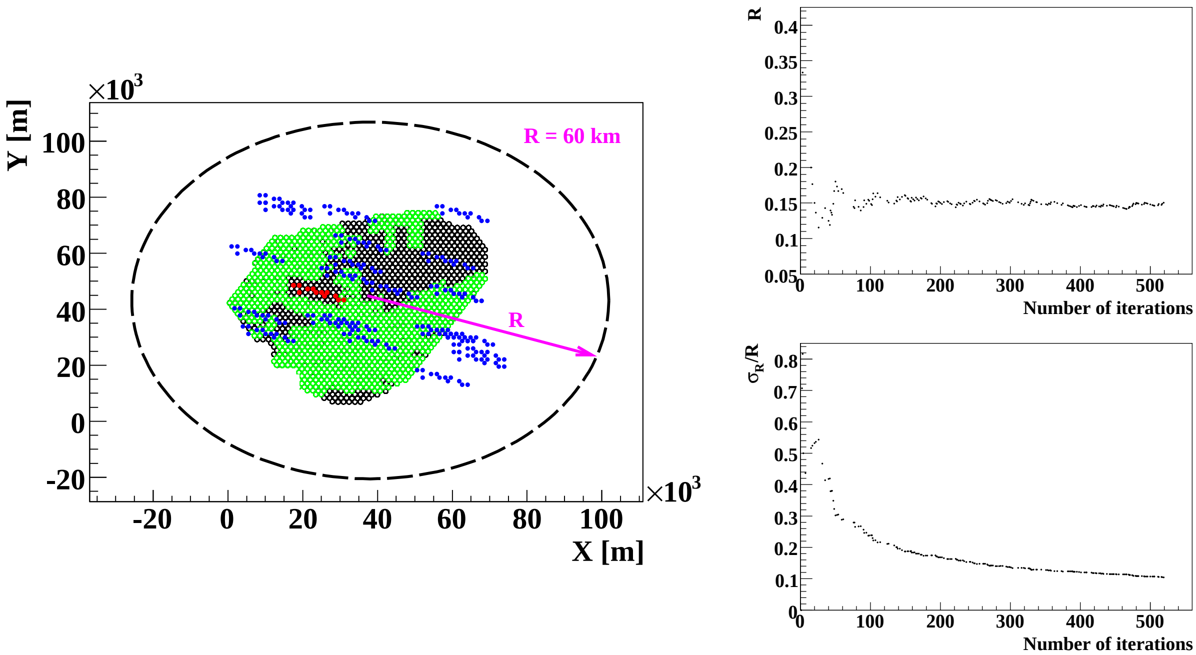

Figure 6.11: *(Left panel) Example of displacement of a well-contained simulated footprint in the area chosen to evaluate the acceptance. The red full circles represent the footprint before the displacements, the blue stars represent the footprint for 21 displacements, the green-marked area represents the status of the array at a chosen timestamp, the black-marked area is an ideal status of the array. (Right panel) Example of the evolution of the ratio R_ν (upper panel) and its relative uncertainty σ_{R_ν}/R_ν (lower panel) after 500 iterations. The set of down-going electron neutrinos from CC interactions at* 1 EeV *and in a fixed 3-day period is considered.* **Disclaimer: The plots are not approved by the Auger Collaboration. Please do not use them.**

integrated ratios $R_\nu(E_\nu, \theta)$ for different energies and neutrino simulations are shown in Tab. 6.6. The last row in the table shows the averaged $R_\nu(E_\nu, \theta)$ on different neutrino types and θ, $\langle R_\nu(E_\nu)\rangle$. In Fig. 6.12 (lower-right panel) $\langle R_\nu(E_\nu)\rangle$ as a function of neutrino energy is shown.

It is interesting to note from Fig. 6.12 (upper panels) that a dependence of the ratios at 0.1 , 0.3 , 1 , 3 , 10 EeV ($R_{E[EeV]}$) on the ratios at 30 EeV (R_{30EeV}) can be observed. As an example, in Fig. 6.12 (lower-left panel) the case of down-going electron neutrinos from CC interactions at 87° is shown. In Tab. 6.7 $\langle R_{E[EeV]}/R_{30EeV}\rangle$ as a function of neutrino energy is listed.

The acceptance, calculated by considering the real evolution and configuration of the surface array, is shown in Fig. 6.13 (upper panel) for down-going electrons and τ leptons in the range $60° - 90°$ and up-going τ leptons in the range $90° - 95°$. A comparison with the results obtained in Sec. 5.6 is also done.

In Sec. 5.6 it was stated that data collected from January 2004 to December 2007 repre-

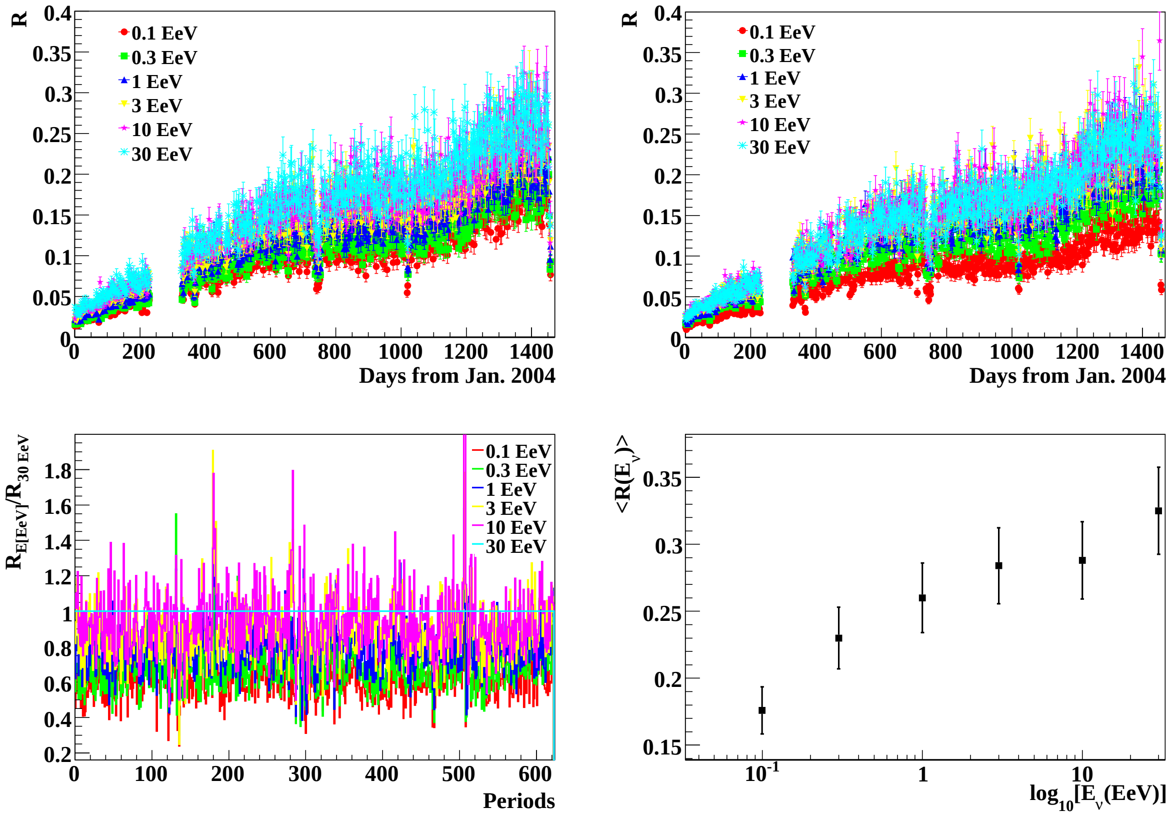

Figure 6.12: *(Upper panels) Evolution of the ratios evaluated for the set of down-going ν_e simulations from CC (left) and NC (right) interactions at 87°. On the x-axis the days starting on 1 January 2004 are shown. On the y-axis the ratio R_ν (Eq. 6.4) with its uncertainty σ_{R_ν} (Eq. 6.5) is shown. Larger fluctuations correspond to 3-day periods which include some bad periods. The empty area (August-October 2004) corresponds to a quite long bad period which was excluded from calculations. (Lower-left panel) Ratios at 0.1, 0.3, 1, 3, 10 EeV using the ratios at 30 EeV as a reference for down-going ν_e from CC interactions at 87°. The bad periods are excluded from the calculations. (Lower-right panel) Calculated $\langle R(E_\nu)\rangle$ for different neutrino simulations.* **Disclaimer: The plots are not approved by the Auger Collaboration. Please do not use them.**

sent approximately 1 year of fully efficient detector operation. A slightly larger acceptance (15–18%) at energies greater than about 3 EeV can be observed. One can expect a slightly larger period of fully efficient detector operation than 1 year.

The acceptance was calculated also in the angular range $75° - 90°$ for down-going neutrino showers and a comparison with the acceptance calculated in the range $60° - 90°$ is shown in Fig. 6.13 (lower panels).

Table 6.6: Integrated ratios. The uncertainty on the listed values is 10%.

Sim. ν footprints	Energy [EeV] 0.1	0.3	1	3	10	30	
ν_e, 87 deg, CC	0.165	0.221	0.269	0.268	0.274	0.307	
ν_e, 75 deg, CC	0.167	0.241	0.260	0.281	0.315	0.321	
ν_e, 65 deg, CC	0.187	0.205	0.273	0.276	0.264	0.299	
ν_e, 87 deg, NC	0.178	0.234	0.247	0.306	0.277	0.306	
ν_e, 75 deg, NC	0.164	0.244	0.269	0.265	0.297	0.352	
ν_e, 65 deg, NC	0.172	0.224	0.272	0.292	0.275	0.297	
ν_τ, 87 deg, CC	0.180	0.244	0.237	0.308	0.292	0.325	
ν_τ, 85 deg, CC	0.194	0.245	0.232	0.307	0.305	0.360	
ν_τ, 91 deg, CC	0.162	0.206	0.258	0.266	0.271	0.347	
	0.176	0.230	0.260	0.284	0.288	0.325	$\langle R_\nu(E_\nu)\rangle$

Table 6.7: $\langle R_{E[EeV]}/R_{30EeV}\rangle$ as a function of neutrino energy. The uncertainty on the listed values is 20%.

	E [EeV] 0.1	0.3	1	3	10
$\langle R_{E[EeV]}/R_{30EeV}\rangle$	0.541	0.708	0.800	0.873	0.886

6.5 Event rate calculation and upper limits

The total observable event rates were calculated based on Eq. 5.11 with the previously calculated acceptance. The assumption that at zenith angles lower than 75° discrimination of neutrino showers from the background can not be achieved was adopted. The results are listed in Tab. 6.8 for up-going τ-induced showers ($90° - 95°$) and down-going electron and τ-induced showers ($75° - 90°$). To quantify the difference with the calculations of Sec. 5.7, the factor $k = (N_{real} - N_{ideal})/N_{real}$ was introduced. The factor k includes the event rates calculated with the ideal configuration of the array, N_{ideal}, and the event rates in case of the real array configuration, N_{real}.

The integral upper flux limit to up-going ν_τ ($90° - 95°$) in the period between 1 January

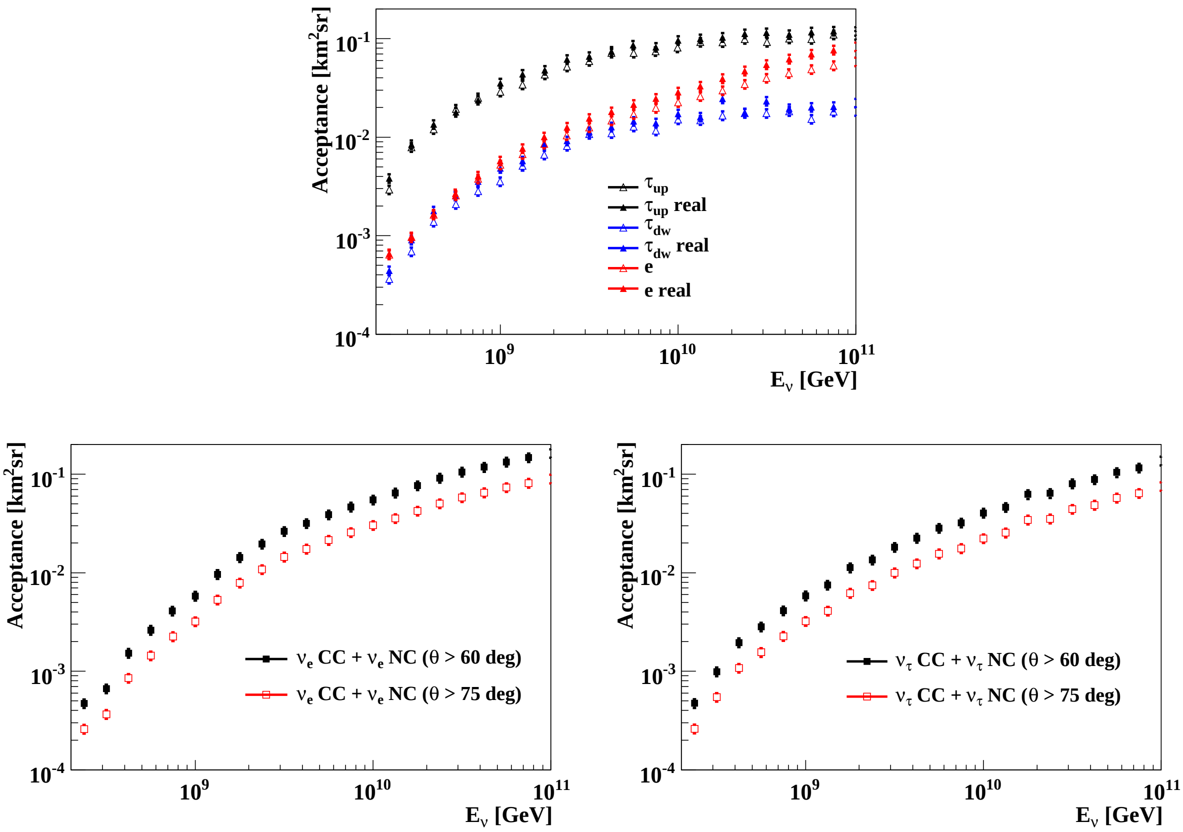

Figure 6.13: *Acceptance calculated by considering the real evolution of the surface array of the Pierre Auger Observatory in the period between 1 January 2004 and 31 December 2007. The effect of the mountains is included. (Upper panel) The acceptance calculated by considering the real evolution of the array (labeled with "real"), as from Eq. 6.6, is compared with the ideal case for down-going electrons and τ leptons in the range $60^\circ - 90^\circ$ and up-going τ leptons in the range $90^\circ - 95^\circ$. (Lower panels) Acceptance for down-going neutrino showers in the range $60^\circ - 90^\circ$ and $75^\circ - 90^\circ$. (Left panel) Acceptance for down-going ν_e. (Right panel) Acceptance for down-going ν_τ.* **Disclaimer: The plots are not approved by the Auger Collaboration. Please do not use them.**

2004 and 31 December 2007 is

$$E_\nu^2 \Phi(E_\nu) < 7.0 \times 10^{-8} \left(^{+25\%}_{-31\%} \right) \text{ GeVcm}^{-2}\text{s}^{-1}\text{sr}^{-1}. \tag{6.8}$$

This independent limit is in a quite good agreement with the upper limit presented by the Pierre Auger Collaboration [15]. The integral upper flux limits to down-going $\nu_e + \nu_\tau + \nu_\mu$ $(75^\circ - 90^\circ)$ is

$$E_\nu^2 \Phi(E_\nu) < 2.27 \times 10^{-7} \left(^{+22\%}_{-33\%} \right) \text{ GeVcm}^{-2}\text{s}^{-1}\text{sr}^{-1} \tag{6.9}$$

and the limit to up-going and down-going neutrinos is

$$E_\nu^2 \Phi(E_\nu) < 0.54 \times 10^{-7} \left(^{+33\%}_{-45\%} \right) \text{ GeVcm}^{-2}\text{s}^{-1}\text{sr}^{-1}. \tag{6.10}$$

Table 6.8: Expected event rates in (yr^{-1}) for the surface array of the Pierre Auger Observatory based on the acceptance calculated by considering the real evolution of the array in the period between 1 January 2004 and 31 December 2007 and zenith angles larger than 75°. The values are calculated with the cross-section model GRV98lo [35]. The precision on the listed values is about 4%.

	WB			GZK			TD		
	N_{ideal} (yr^{-1})	N_{real} (yr^{-1})	k (%)	N_{ideal} (yr^{-1})	N_{real} (yr^{-1})	k (%)	N_{ideal} (yr^{-1})	N_{real} (yr^{-1})	k (%)
τ_{up}	0.294	0.327	10.1%	0.485	0.542	10.5%	2.620	2.950	11.2%
τ_{dw}	0.032	0.037	13.5%	0.056	0.067	16.4%	0.340	0.416	18.3%
e_{dw}	0.021	0.027	22.2%	0.036	0.046	21.7%	0.205	0.258	20.5%

These results were obtained by assuming that no candidate has been observed in the angular range $75° - 90°$ for down-going and $90° - 95°$ for up-going neutrinos. The individual contributions of down-going ν_e, ν_τ, and ν_μ to the total sensitivity of Eq. 6.9 are

$$E^2_{\nu_e}\Phi(E_{\nu_e}) < 4.4 \times 10^{-7} \left({}^{+14\%}_{-22\%}\right) \text{ GeVcm}^{-2}\text{s}^{-1}\text{sr}^{-1}, \tag{6.11}$$

$$E^2_{\nu_\tau}\Phi(E_{\nu_\tau}) < 5.4 \times 10^{-7} \left({}^{+17\%}_{-24\%}\right) \text{ GeVcm}^{-2}\text{s}^{-1}\text{sr}^{-1}, \tag{6.12}$$

and

$$E^2_{\nu_\mu}\Phi(E_{\nu_\mu}) < 0.38 \times 10^{-7} \left({}^{+14\%}_{-22\%}\right) \text{ GeVcm}^{-2}\text{s}^{-1}\text{sr}^{-1}, \tag{6.13}$$

respectively. The expected event rates for down-going neutrinos in the angular range $75° - 90°$ are listed in Tab. 6.9. The integral and differential upper limits are shown in Fig. 6.14 along with some typical spectra of astrophysical neutrinos.

The surface detector array of the Pierre Auger Observatory is almost at its completion. The increasing amount of time in which the detector is fully efficient allows an increase of the effective acceptance to detect neutrino-induced showers. Even though the huge amount of data adds more background events to the detection of neutrino events, the discrimination at large zenith angles might allow identification of a clear signature of neutrino interaction within a few years. The expected differential upper limits have their minimum which peaks in the narrow energy range where GZK neutrinos are expected (Fig. 6.15), although theoretical predictions of GZK neutrino fluxes with lower order of magnitude could shift the expected time of detection ahead [66].

The calculations of upper bounds to neutrino fluxes is based on the assumption that no neutrino has been observed. Nevertheless, the identification of a possible candidate would shift the limits to lower values and closer to the predicted astrophysical neutrino fluxes. Only zenith angles above $70° - 75°$ can, however, guarantee a good discrimination level (high purity). At lower zenith angles, even though a neutrino produced a showers, at the

Table 6.9: Expected down-going neutrino event rates for zenith angles larger than 75° based on the updated acceptance. The values are calculated with the cross-section model GRV98lo [35]. The precision on the listed values is about 4%.

	WB	GZK	TD
	$N_{\theta>75^\circ}$ (yr^{-1})	$N_{\theta>75^\circ}$ (yr^{-1})	$N_{\theta>75^\circ}$ (yr^{-1})
ν_τ	0.043	0.080	0.524
ν_e	0.052	0.101	0.673
ν_μ (NC)	0.006	0.012	0.090

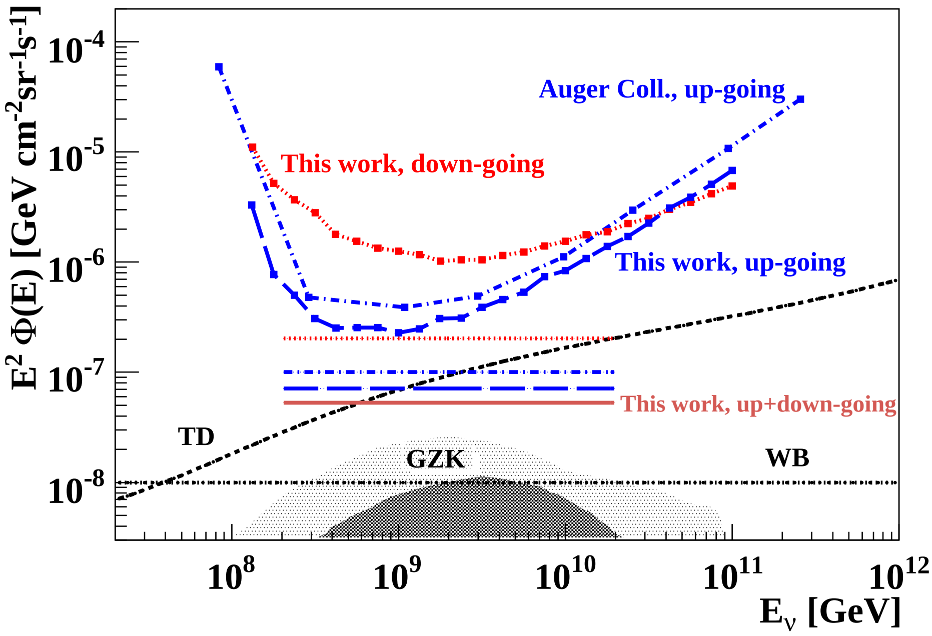

Figure 6.14: *Integral and differential upper flux limits based on the acceptance evaluated with the real evolution of the surface array in the period between 1 January 2004 and 31 December 2007. The results are valid in the angular range 75° − 90° for down-going neutrinos (red dotted lines) and in the angular range 90° − 95° for up-going neutrinos (blue dotted dashed lines). Dashed lines correspond to the results presented in Ref. [15].* **Disclaimer: The plot is not approved by the Auger Collaboration. Please do not use it.**

moment no discrimination technique would allow its identification with high confidence level.

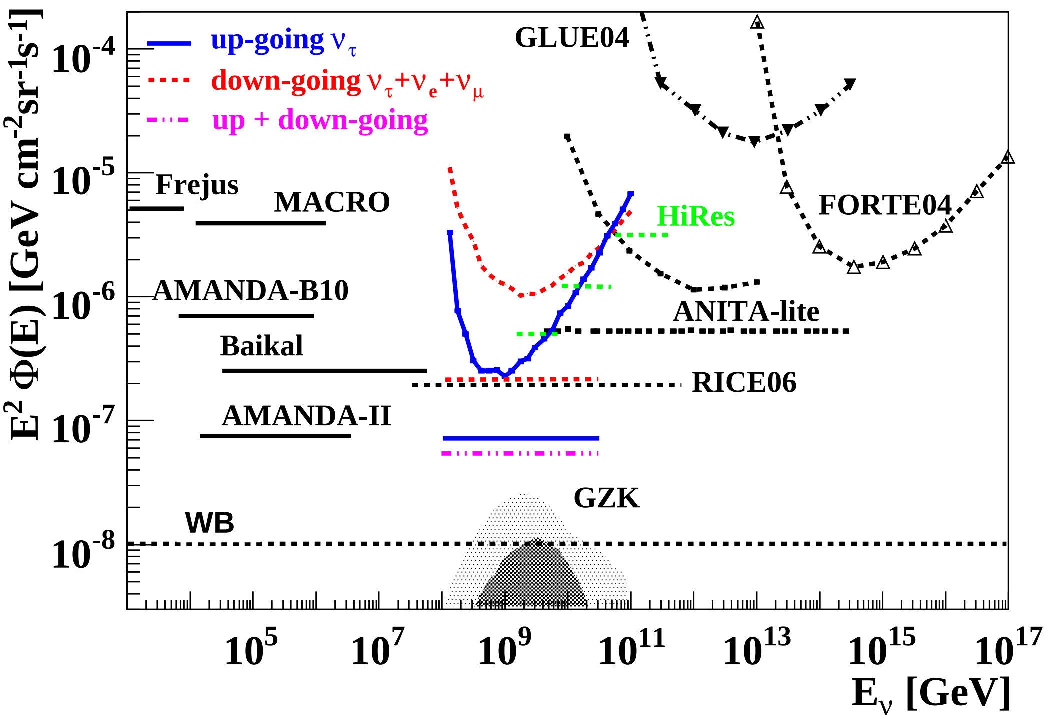

Figure 6.15: *Upper limits on the neutrino flux from sources with WB energy spectrum [148]. The Pierre Auger Observatory limits in their differential form are for up-going ν_τ and down-going $\nu_\tau + \nu_e + \nu_\mu$. Integral limits for up-going and down-going neutrino showers, and the sum of their contribution are also shown. Results from other neutrino experiments are also shown (MACRO [160], Frejus [161], AMANDA-II and AMANDA-B10 [162], HiRes [163], Baikal [164], RICE [165], ANITA [166], GLUE [167], FORTE [168]).* **Disclaimer: The plot is not approved by the Auger Collaboration. Please do not use it.**

Finally, other sources of background may bias the present analysis and should be studied carefully to exclude the possibility that their expected fluxes might produce signatures which can be mixed with neutrino signatures.

In Fig. 6.16 (left panel) a prediction on the time development of the upper limit to ν-induced showers at the surface array of the Pierre Auger Observatory is shown. By considering the real evolution of the array, the WB bound for all ν-flavors is expected to be crossed after about 1.2 years of effective data taking which roughly correspond to 3 years of real time (Fig. 6.16, right panel).

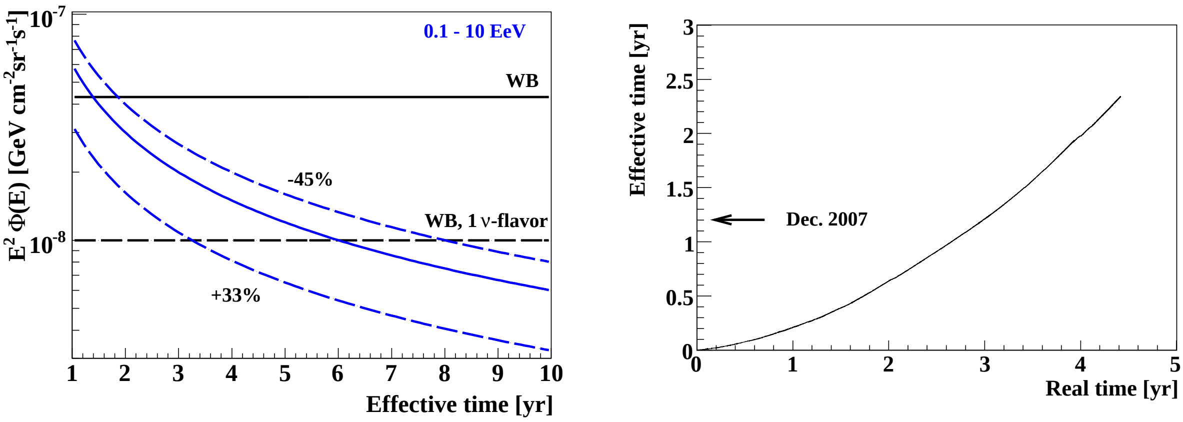

Figure 6.16: *(Left panel) Prediction on the time development of the upper limit to ν-induced showers at the surface array of the Pierre Auger Observatory. The Waxman-Bahcall bound [148] for a single flavor and for all neutrino flavors is also shown for comparison. (Right panel) Effective time versus real time for the surface array.* **Disclaimer: The plots are not approved by the Auger Collaboration. Please do not use them.**

7 Conclusions

A complete Monte Carlo chain to study the possibility of detecting up-going and down-going neutrino-induced showers with the surface detector array of the Pierre Auger Observatory has been presented. The systematic effects arising from the use of different interaction models were investigated to evaluate their impact in the expected neutrino event rates.

Detection of high-energy neutrino-induced showers is possible at the surface array of the Pierre Auger Observatory. Simulations of spectra of leptons induced at the site of the Observatory and expected detection efficiency of the surface array to initiated showers show that the detector is more sensitive to neutrino events in the energy range between 0.1 EeV and 10 EeV, and with zenith angle of incoming directions larger than 80°. Monte Carlo simulations were performed by using a chain of different subsequent packages. The chain includes a modified version of the neutrino generator ANIS, the event generators PYTHIA, which simulates the outgoing hadronic part of neutrino-nucleon interactions, and TAUOLA, which simulates tau decays, the extensive air shower generator AIRES, and the $\overline{\text{Off}}\underline{\text{line}}$ framework, which simulates the detector response and allows reconstruction of showers.

The crucial point for the identification of neutrino-induced showers in collected data is the definition and choice of the observables which select young and inclined showers and furthermore the correct definition and treatment of the background. In this work two approaches were adopted.

First, a purely simulation-based approach was considered. It was assumed that the largest contribution to the background is due to ordinary hadronic cosmic-ray showers. Simulations of proton-induced showers in the energy range $0.1-100$ EeV and zenith angular range $60° - 90°$ were performed. A set of observables was defined and an optimization of the cuts for these observables was performed. Contamination of background events in the sample of neutrino showers was observed to be low enough to guarantee discrimination even at zenith angles below 70°. A list of maps of identification efficiencies for different neutrino flavors was prepared and the sensitivity and the subsequent event rates were evaluated. For the Waxmann-Bahcall flux, the sensitivity of the detector for down-going neutrino-induced showers in the angular range $60^\circ - 90^\circ$ and up-going neutrino-induced showers in the angular range $90^\circ - 95^\circ$ resulted to be

$$E_\nu^2 \Phi(E_\nu) < 0.51 \times 10^{-7} \left({}^{+33\%}_{-45\%}\right) \ GeV cm^{-2} s^{-1} sr^{-1}. \tag{7.1}$$

About 1 event in 3 years is expected. Up-going tau-induced showers give the largest contribution to the expected rate with respect to down-going neutrino showers (1.7:1), but the rate for down-going neutrino showers can not be neglected.

Second, measured data were assumed to be the background to the detection and identification of neutrino-induced showers. It was found that the set of observables chosen could still allow discrimination from the given background, but the analysis of measured data revealed also a larger contamination from background events in the angular range $60^\circ - 70^\circ$. The huge amount of collected data hides additional sources of background to the identification of young and inclined showers at lower zenith angles. Simulations are not able to reproduce all of the sources of background recorded in measured data, although they included one of the most important source of background due to atmospheric muons which were proved to give significant background signal in triggering stations. Among the possible sources of background, instrumental anomalies and events with a low multiplicity of triggering stations (5 or less) can still make the reconstruction chain fail. Even a single station in a small sample can produce bad results when large zenith angles are investigated. In this sense, further improvements to the trace cleaning, to the selection and reconstruction algorithms are needed. Several other physical processes might induce signatures very similar to that of neutrino-induced showers. Although deep-proton inclined showers have a probability of the order of 10^{-9} to be initiated and can still be neglected, high-energy photon showers, initiated through muon bremsstrahlung in the earliest development of hadronic showers, may fulfill the neutrino identification criteria. In conclusion, in order to obtain more realistic results, the assumption that the whole set of measured data is the background for neutrino identification have to be favored due to the fact that the collected data include all the triggering sources of background which at the moment can not be fully reproduced in simulations. Therefore, the assumption of discrimination down to 60° for down-going neutrino showers could not be kept and a restriction to the angular range $75^\circ - 90^\circ$ was adopted. The real time evolution of the growing surface array was considered and it resulted that in the period from January 1, 2004 to December 31, 2007 the array ran at its full efficiency for an amount of time equivalent to 1 year + about 15% at its completion. The integral upper flux limit to up-going and down-going neutrinos resulted

$$E_\nu^2 \Phi(E_\nu) < 0.54 \times 10^{-7} \left({}^{+33\%}_{-45\%}\right) \ GeV cm^{-2} s^{-1} sr^{-1}. \tag{7.2}$$

Due to the largest contribution of up-going neutrino-induced showers to the upper limit, no significant difference with the previous estimate was observed, even though the expected ratio of up-going to down-going neutrinos changed to 3:1. Still, the contribution of down-going neutrino showers to the total expected event rate for neutrino-induced showers remains important.

The expected differential upper flux limits have their minima which peaks in the narrow energy range where GZK neutrinos are predicted (around 3−10 EeV). Although systematic uncertainty and more restrictive theoretical predictions may shift the expected date of the first neutrino detection ahead in time, the Pierre Auger Observatory is sensitive to neutrino-induced showers and one can be confident that a decade of data taking can be sufficient to clearly identify a neutrino candidate. On the other hand, should no candidate be observed, important constraints on high-energy interaction models can be made.

A

Simulation and reconstruction chain

In this chapter a typical simulation chain (Sec. A.1) and reconstruction chain (Sec. A.2) used in the $\overline{\text{Off}}\underline{\text{line}}$ framework are given.

A.1 Simulation chain

A typical simulation chain running in the $\overline{\text{Off}}\underline{\text{line}}$ framework is listed below:

```
<sequenceFile>
<enableTiming/>
<moduleControl>

  <loop numTimes="unbounded" pushEventToStack="yes">
    <module> EventFileReaderOG </module>
    <loop numTimes="1" pushEventToStack="yes">
      <module> EventGeneratorOG </module>
      <loop numTimes="unbounded" pushEventToStack="no">
        <module> CachedShowerRegeneratorOG </module>
        <module> G4TankSimulatorOG         </module>
      </loop>
      <module> SdSimulationCalibrationFillerOG </module>
      <module> SdPMTSimulatorOG                </module>
      <module> SdFilterFADCSimulatorMTU        </module>
      <module> SdBaselineSimulatorOG           </module>
      <module> TankTriggerSimulatorOG          </module>
      <module> TankGPSSimulatorOG              </module>
      <module> CentralTriggerSimulatorXb       </module>
      <module> CentralTriggerEventBuilderOG    </module>
      <module> EventBuilderOG                  </module>
      <module> EventFileExporterOG             </module>
```

```
      </loop>
    </loop>

  </moduleControl>
</sequenceFile>
```

The event (shower footprint) is read by the module *EventFileReaderOG* and held in memory until all the following processing modules do not return a terminating signal ("unbounded" loop mode). A shower is generated in the surface detector of the Pierre Auger Observatory with the module *EventGeneratorOG* by placing its core position and defining its core arrival time. The following modules *CachedShowerRegeneratorOG* and *G4TankSimulatorOG* are necessary to generate and track the particles in each station of the surface detector and simulate the response of the station to such particles. In particular, *CachedShowerRegeneratorOG* takes weighted particles from the read footprint, regenerates them with unity weight, and injects them into stations for simulation. In order to avoid excessive memory consumption in cases where the shower core is very close to a tank or a shower is developing very close to the ground, the module supports a limit on the maximum number of particles, which can be simulated in one pass. The event is updated with the wanted maximum number of new particles at each pass and continues processing from that point onward.

The module *G4TankSimulatorOG* is an interface of the package Geant4 [169] and allows to track the photons emitted by particles along their passage through the water of a station.

The signal given by *Geant4* is in photoelectrons (p.e.) and it must be converted into VEM units (Sec. 3.2). The assignment of the tank calibration constants is done by the module *SdSimulationCalibrationFillerOG*. In this work, the value of 1 VEM corresponds to the energy released by vertical and centered muons of 1.05 GeV, so that 1 VEM is equivalent to 89.53 ± 9.06 p.e..

The three following modules, *SdPMTSimulatorOG*, *SdFilterFADCSimulatorMTU* and *SdBaselineSimulatorOG*, simulate the traces with their baselines in the PMTs of each station.

Once the signal has been simulated, the local trigger simulation is done by *TankTriggerSimulatorOG* which implements the features of the real local trigger (Sec. 3.3). Timing of stations marked as triggering is provided by *TankGPSSimulatorOG* which reproduces the GPS system implemented at each station (Sec. 3.1).

The module CentralTriggerSimulatorXb implements the real algorithm used to decide whether a multiplet of triggering stations is part of a physical shower and the module *CentralTriggerEventBuilderOG* allows to store all the information regarding the eventual central trigger (Sec. 3.3). If the generated shower has passed all the modules until here described, a fixed data structure is built up by the module *EventBuilderOG* and then exported in a file by the module *EventFileExporterOG*. The event representation in memory is decoupled from the representation on disk. Serialization is currently implemented using the ROOT toolkit [170, 171], though the design is intended to allow for relatively straightforward changes of serialization machinery.

The new module, *AccidentalInjectorAT*, to add atmospheric muon signals in detector simulations (Sec. 4.2.2 and App. C) requires the chain to slightly change by introducing it in between *CachedShowerRegeneratorOG* and *G4TankSimulatorOG*. The modifications to the module *CachedShowerRegeneratorOG* (Sec. 4.2.1 and App. B) were implemented in a module called *CachedShowerRegeneratorAT* which replaces *CachedShowerRegeneratorOG* in the chain listed previously.

A.2 Reconstruction chain

A typical reconstruction chain running in the Offline framework is listed below:

```
<sequenceFile>
<moduleControl>

    <loop numTimes="unbounded">
      <module> EventFileReaderOG </module>
      <module> EventCheckerOG </module>
      <module> SdCalibratorOG </module>
      <loop numTimes="1">
         <module> SdEventSelectorOG </module>
         <module> SdPlaneFitOG </module>
         <module> LDFFinderOG </module>
      </loop>

</moduleControl>
</sequenceFile>
```

The module *EventFileReaderOG*, already mentioned in the previous section, is used here to read a different format of data which can be either Monte Carlo data or raw real data. Until all of the events are not read and a terminating signal is sent by this module, the sequence continues processing data ("unbounded" loop mode). The module *SdCalibratorOG* allows to retrieve the calibration constants, reconstruct the signal properties (integrated signal, signal start time, rise time, fall time, ...) and clean the signal traces from eventual spurious peaks produced by several sources of background such as atmospheric muons, lightning, etc. The module *SdEventSelectorOG* implements the station selection and the decision on the T4 trigger for the event considered. The module *SdPlaneFitOG* and *LDFFinderOG* perform the angular reconstruction and the energy reconstruction of the event considered, respectively.

The case of neutrino showers requires a specific treatment and the reconstruction module sequence, as presented here, was modified to match this assignment. A module, called *NeutrinoReconstructionAT*, was created to contain all the utilities which were developed to reconstruct neutrino showers at the Pierre Auger Observatory: station selection, geometry reconstruction, identification parameters (Sec. 5.2). The energy reconstruction for neutrino showers is not possible and it will not be considered at all.

$\mathcal{B}$

The modified un-thinning algorithm

In this section a detailed description of the un-thinning algorithm, modified to better simulate the detector response to up-going and down-going neutrino showers in the $\overline{\text{Off}}\underline{\text{line}}$ framework [120], is given. The report was submitted as a technical note and it is available for the Pierre Auger Collaboration [140]. The algorithm was implemented in a module called *CachedShowerRegeneratorAT*. The module can run in $\overline{\text{Off}}\underline{\text{line}}$ by using a suitable module chain. An example is reported in App. A.

Basically, the definition of the "resampling area" (following discussion for detail) was changed with respect to the original code and it is now calculated directly on the ground without implying the exploding factor $1/\cos\theta$, with θ the zenith angle of the shower.

The reason to improve the existing code is related to a fundamental point: being able to resample also horizontal and up-going simulated showers. The algorithm needs the coordinates of the primary interaction (the decay point for neutrino showers) which can be set by the user. Differently from the original algorithm, no core position is needed. On the other hand, a direct dependence of the resampling procedure on the core position is even not possible for very horizontal up- and down-going neutrino showers, where the core position may not be within the array. Once the interaction point is known, the procedure tries to retain the geometry of the shower footprint. A sketch of the geometry involved in the algorithm is given in Fig. B.1. The plane perpendicular to the shower axis and through the earliest position on the ground is determined and a circular grid on it is built. In particular, the algorithm allows to fix the optimal size of the cells of this grid by choosing a radial step ΔR on the ground and an angular step $\Delta\phi$ on the grid. Since the length of the footprint of the shower is known, ΔR defines the number of steps in which the total length is divided. The reference points of each step are then projected back to the plane of the grid towards the interaction point and rotated in angular steps of $\Delta\phi$. A non-equally spaced grid is obtained and a map of the cells on it is determined (Fig. B.1). The reason to divide the length of the footprint in linear steps will be clear in the following description.

To each cell of the map, a station of the array can be associated and the area of the cell around the station on the ground can be determined also. This particular area will be called *resampling area* ΔA_i associated to the station i. The choice of $\Delta\phi$ and ΔR should

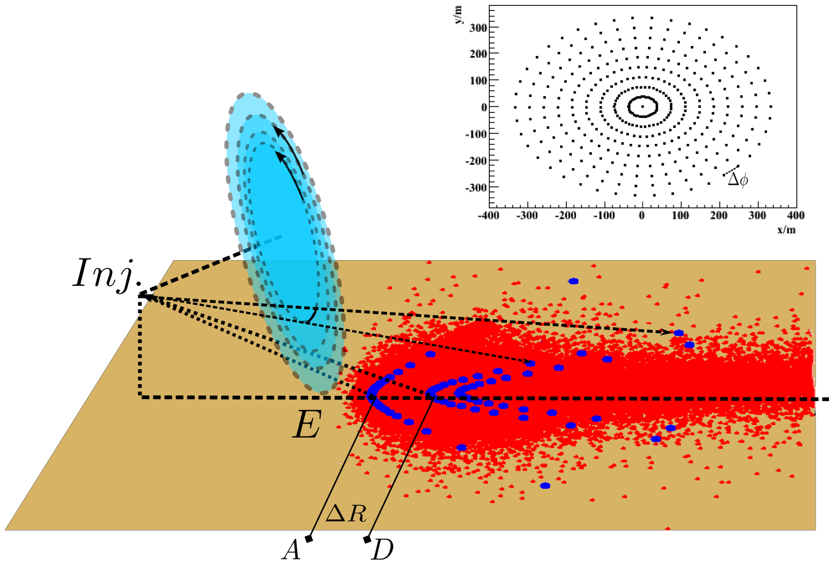

Figure B.1: *Sketch of the geometry involved in the revised resampling algorithm. Here an up-going neutrino shower is shown as an example. In the upper inset the typical structure of non-equally spaced grid for this particular shower is shown. A non-equally spaced grid on the shower plane is due to the used linear spacing on the ground (text for details).*

be done in a way that one station is associated to one cell.

In Fig. B.2 the typical shape of lines limiting resampling areas on the ground for a down-going and an up-going neutrino shower is shown. The shape is strictly related to the shower development and reproduces the expected shower iso-density lines [118].

All of the ground particles inside the area around a station are considered to belong to that station. Thus, from the set of ground particles around a station, an unbiased set of particles to be injected in the station is defined. The weight of each particle of the set considered allows to determine the density of the particle in the resampling area, defined as

$$\delta p_{ip} = \frac{w_{ip}}{\Delta A_i}, \tag{B.1}$$

where w_{ip} is the weight associated to the particle p. A particle can be resampled and results in a number of clone particles which enter the detector from its top side and/or from its wall. If a particle p has a direction whose zenith angle in the reference system of the station i is θ_p^{stat}, the effective area seen by this particle is defined as

$$A_{ip}^{eff} = \pi R_i^2 \frac{\cos\theta_p^{stat}}{\cos\theta_p} + 2\pi R_i H_i \frac{\sin\theta_p^{stat}}{\cos\theta_p}, \tag{B.2}$$

where θ_p is the zenith angle of the particle p in the ground particle reference system, R_i and H_i the radius and the height of the station i, respectively. The first contribution to the effective area comes from the top area of the station i. The ratio $\frac{\cos\theta_p^{stat}}{\cos\theta_p}$ includes possible

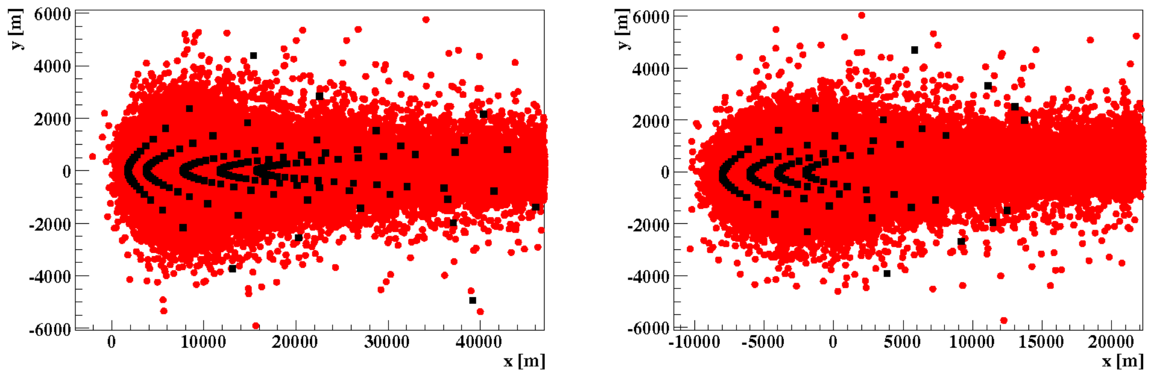

Figure B.2: *Typical shape of lines limiting resampling areas on the ground for a down-going shower (left panel) at* 89° *and an up-going shower (right panel) at* 91°. *Only few lines were drawn for sake of simplicity of the picture. The actual step size used is instead* 200 m.

tilting between the station reference system and the ground particle reference system and it is nearly 1 for small resampling areas. The second contribution comes from the station wall area. The full effective area can be seen as the shadow of the station produced by a beam of light coming with the same direction of the particle considered and projected onto a plane parallel to the ground. The projection of the shadow might produce very large values for the effective area when one considers horizontal or nearly horizontal particles. As a matter of fact $\cos\theta_p^{stat}$ tends to be zero in this condition. Typical values for the shadow area and effective area at different incoming zenith angles of particles can be observed in Fig. B.3. A limitation on the allowed zenith angle of a particle can be set as close as possible to the asymptotical point at 90°.

Once the effective area of the station i seen by a particle p is determined, n-clones with weight 1 are generated with n following a Poisson distribution with mean given by

$$\langle n_{ip}\rangle = \delta p_{ip} A_{eff}. \tag{B.3}$$

Positions of the n-clones on the station surface are randomly generated in the part of surface which can be seen by the arriving particle (Fig. B.4). In order to restore the time structure of the particle distribution, the arrival times are set such that the shower front propagation across the sampling zone is taken into account. In particular, if t_{ip} is the ground time of the particle p in the resampling area around the station i and Δd_{ip} its distance to the injection position of one of its clones on the station surface and projected onto the shower direction, the corrected time for the clone k is given by

$$t_{ip}^k = t_{ip} - \frac{\Delta d_{ip}}{c}, \tag{B.4}$$

assuming front propagation at the speed of light, c. A sketch of the arrival time correction is shown in Fig. B.5.

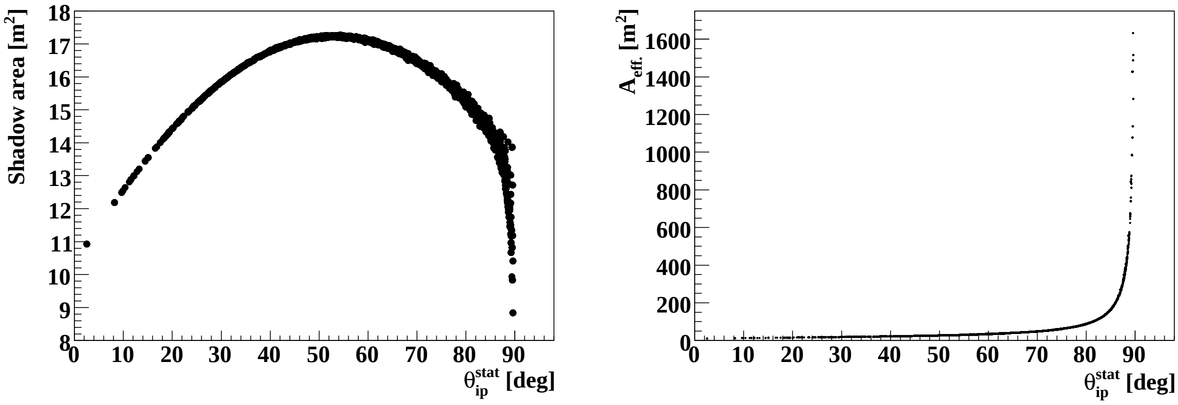

Figure B.3: *Typical trend of the shadow area and effective area with the particle zenith angle. In the left inset, shadow area of a station versus particle zenith angle. In the right inset, projected shadow area on the ground or effective area seen by a particle at several incoming zenith angles.*

In case of many clones generated, accumulation of particles with the same arrival time would produce unphysical saturated station signals. More realistically, to each generated clone, an arrival time, randomly generated from a gaussian with average value given by Eq. B.4 and variance $0.1 - 0.2\,\mathrm{ns}$, was already proposed in the existing procedure.

The problems which one encounters when one wants to optimize the resampling procedure lie mostly on the definition of the size of the cells containing each station. The cells should be chosen small enough to reproduce the local properties but also large enough to avoid artificial statistical fluctuations. The latter means that one might deal with unrealistic large numbers of clones due to large weights and small resampling areas. Moreover, the particles generated by the algorithm should form an unbiased set of particles entering the detector. Finally the assumption of circular symmetry on the propagation plane derives from the assumption that the space density of the particles depends strongly on the distance from the shower axis without any azimuthal asymmetry. From the previous considerations, it is evident why a linear division of the length of the footprint in steps of ΔR was chosen to resample neutrino showers. When one deals with young and quasi-horizontal showers, as one expects for most of neutrino candidates, the "compression" of iso-lines in the down-stream part of the footprint and the large weights expected in these regions may originate large and unrealistic numbers of generated clones. A solution can be achieved by adjusting the radial step in the shower plane. However, when one considers quasi-horizontal neutrino showers, setting the radial step on the shower plane too large may not help and even worsen the resampling procedure. As a matter of fact, in regions far from the earliest position on the ground (Fig. B.6, for example) the iso-lines will increase their spacing nearly exponentially with the result to have too large resampling areas with only few low weight particles. This effect produces bad resampling of the furthest regions of the footprint. In addition, two or more stations may happen in a single resampling area. Regions closer to the highest weight part of showers will present, instead, small resampling

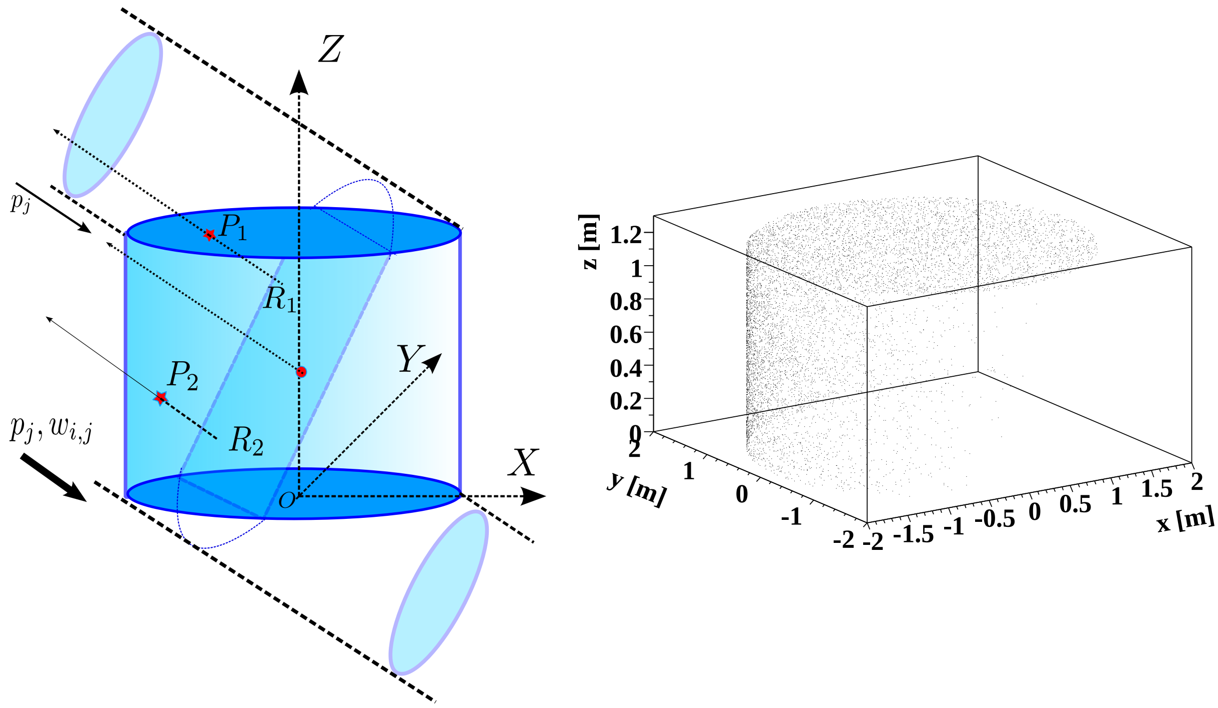

Figure B.4: *Random generation of clone positions on the area effectively seen by a particle (left inset). A red arrow represent the particle on the ground with its weight. The generation is firstly done on the big ellipse in the center of the station on a plane perpendicular to the incoming particle direction and then projected backwards until it crosses the station surface. In the right inset, example of generation of clone positions for a particle direction with* $\theta_p^{stat} > 45°$ *and* $\phi_p^{stat} \in [90°, 180°]$ *in the station coordinate system.*

areas with the result to have often large numbers of clones.

The existing algorithm, used to resample vertical and inclined showers, defines the size of the cells of the grid directly in the shower plane so that the grid consists of equally spaced circular lines. The resampling areas are, however, calculated analytically, implying a factor $1/\cos\theta$ which explodes for horizontal showers.

After several scannings of many footprints, it turned out that a good choice of ΔR on the ground is between 200 m and 750 m with no important difference in the general properties of resampled showers, whereas the choice for $\Delta\phi$ depends on the lateral development of the footprint with respect to its development along the main direction on the ground. In fact, the development of horizontal or quasi-horizontal neutrino showers on the ground results in elongated patterns so that a change in the angular step is not the main issue. In general, the choice of the two steps should give at the end a mean number of clones (Eq. B.3) which is not too large (typically, $\langle n_{ip}\rangle$, from Eq. B.3, around 1 or smaller) to

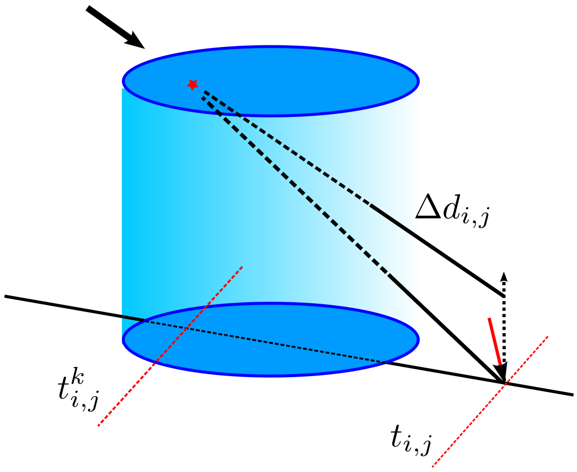

Figure B.5: *Sketch of the procedure to correct the clone arrival time for its position on the station surface. Red dotted lines represent the projected propagation of the shower plane front. The incoming direction of the shower is represented by a black arrow. A red thick arrow represents the shower particle p with weight w_{ip}. Its direction may be different from the shower incoming direction due to multiple scattering processes, for example, and in general to effects which sum up to give the shower front curvature. The clone k is represented on the station surface by a red star.*

avoid artificial fluctuations. Values for $\Delta\phi$ in the range $0.1 \div 0.15$ rad resulted to be a good choice with no big fluctuations in the number of generated clones per shower particle.

These values for $\Delta\phi$ are also chosen in the existing algorithm and one should expect a convergence of results when vertical and inclined showers are resampled with the revised algorithm, but optimization in this sense is still to be done.

Typical values for the size of resampling areas are of the order $10^3 - 10^4\,\mathrm{m}^2$. The distribution of the particle weights on the ground depends on the type of primary which is considered and on its energy. Both for down-going neutrino showers and for up-going neutrino showers (Fig. B.6), the weight distribution is related to the shower development which can be followed very well in all of its stages for such young showers, resulting in very elongated footprints. The highest weights are closer to the earliest position on the ground with respect to normal hadronic showers where the highest weights lie mostly around the core position. The number of clones generated for each particle depends on the particle weight, on the effective area and on the resampling area. As the geometry of the resampling algorithm has been fixed, one should consider the dependence of the average number of clones (Eq. B.3) on the weights as a sort of calibration curve to adjust the steps ΔR and $\Delta\phi$ and avoid too large fluctuations. Examples of such a curve for the down-going and up-going neutrino shower shown in Fig. B.6 are in Fig. B.7. By comparing the result of the down-going shower to the result of the up-going shower, the average number of clones generated for a fixed particle weight in the case of the up-going shower is reduced approximately by a factor 2. The reason is mostly related to the geometry involved and

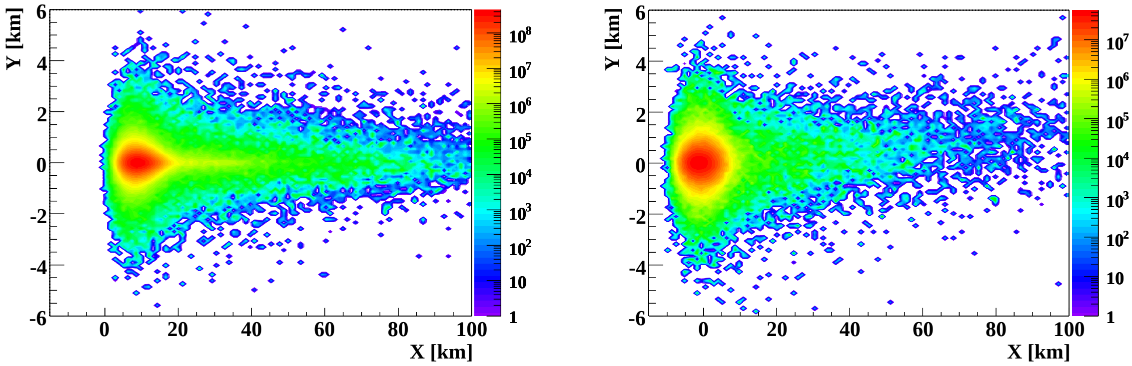

Figure B.6: *Distribution of weights for a down-going tau neutrino shower with the primary at* 89° *and energy* 10 EeV *(left panel) and an up-going neutrino shower with the primary at* 91° *and energy* 10 EeV *(right panel). The injection point for both the showers is at* 500 m *from the ground. In color, weights of particles.*

then to fact that an up-going shower develops from the lower part of the atmosphere and touches the ground only with part of its shower cone. The large weights carried by the large electromagnetic component associated to down-going shower and the cumulation of particles with such high weights give an important contribution to the increase of the number of generated clones. The same behavior can be observed in regions of normal hadronic shower footprints close to the core and resampled with the existing algorithm: average numbers of generated particles of the order of 50 are expected. These regions are limited around the core for normal showers, they extend to larger areas for young showers with a strong electromagnetic component.

Further improvements of the algorithm should be considered by taking into account the signals produced by resampled particles in the stations [172]. Moreover, a bias due to the curvature of the shower front for young showers might be corrected by correcting for the local curvature at each station with a suitable parameterization. Finally, a bias due to attenuation, important for inclined showers with a large electromagnetic component, should be corrected in order to avoid additional fluctuations in the station signal. All these corrections can improve the approach described in this work and further studies are necessary in this respect [137]. The purpose of introducing some changes to the existing algorithm was to implement a new idea of resampling thinned up-going and down-going Monte Carlo showers based on their geometry. No restriction on the conventional parameters of a shower, such as the core position and incoming direction of showers, has to be assumed. Comparisons of results produced with the existing code and with the modified code are shown in Fig B.8. Here the trigger efficiency (Sec. 4.3) was used as a preliminary parameter to compare the two algorithms. No dependence on the thinning within the allowed fluctuations is visible and indicates that the algorithm is quite reliable. Deeper studies are, however, necessary and further improvements in this respect can be foreseen.

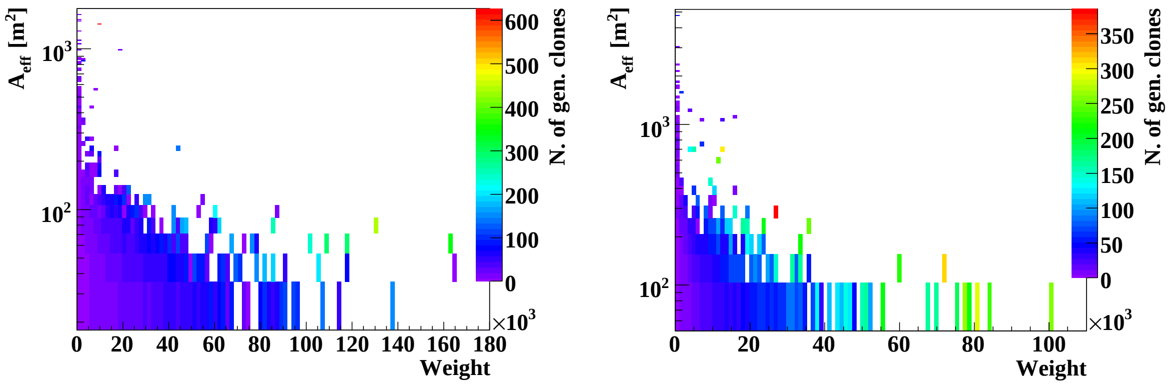

Figure B.7: *Average number of generated clones versus weights of particles and effective area for the down-going shower in the upper inset of Fig. B.6 (left inset) and for the up-going shower in the lower inset of Fig. B.6 (right inset).*

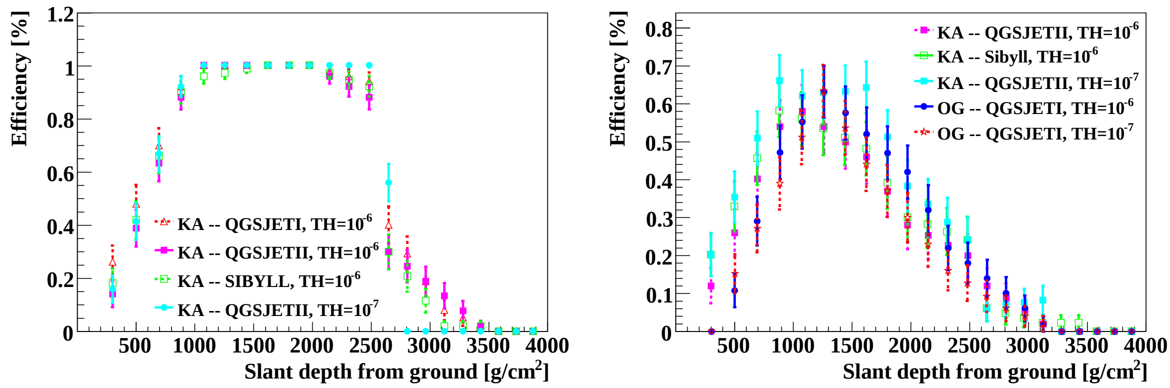

Figure B.8: *Comparisons of trigger efficiency for down-going electron neutrino showers at* 1 EeV *and zenith angle* 87°. *In the upper panel, charge-current interactions are shown. In the lower panel, neutral-current interactions are shown. Different thinning approximations and interaction models were used. The points labeled with "KA" represent detector simulations done with the modified resampling algorithm, and points labeled with "OG" represent detector simulations done with the existing algorithm. The existing algorithm could not be used with charge-current interaction simulations due to many crashed events caused by the high weights associated with such showers. No strong dependence among the different interaction models and thinning approximations is visible within the fluctuations.*

C

Atmospheric muons in detector simulation

In this section a detailed description of the algorithm developed to introduce atmospheric muon signals in extensive air shower simulations will be discussed. The procedure, implemented in the module called *AccidentalInjectorAT*, can run in the $\overline{\text{Off}}\underline{\text{line}}$ framework [120]. A complete report was submitted as a technical note and it is available for the Pierre Auger Collaboration [173].

The background simulation is done station by station in a way that atmospheric muons may or may not be injected into each single station according to a procedure which is going to be described below. The module creates the particles, i.e. the muons, from an expected flux of atmospheric muons and tries to inject them into the stations of the surface array by assigning them energy, direction and position on the surface of the station considered. The detector response is accomplished by the currently-used module sequence implemented in $\overline{\text{Off}}\underline{\text{line}}$ (App. A).

The random time of occurrence of atmospheric muons, their spatial distribution on the surface of a single station and the time window during which the station is able to store signals can be considered the driving features of the background simulation and, in principle, they should be considered the parameters to which the simulation is most sensitive.

The time of occurrence of a muon is directly related to the possibility that the signal produced may be detected. The spatial occurrence, which implies the arrival direction and position on the surface of a station, is related to the possibility to create a signal able to pass the local trigger condition. The best chance for a muon to be detected happens when it crosses the station along one of its diagonals. The time window to inject muons is fixed to 60 μsec around the central trigger time.

The parameterization chosen for the flux Φ_μ of atmospheric muons is the Lipari parameterization [141], but the user can choose a different parameterization to be used. This point-like flux, in $\mathrm{GeV}^{-1}\mathrm{sec}^{-1}\mathrm{cm}^{-2}\mathrm{sr}^{-1}$, at sea level is stored in a two dimensional histogram as a function of the muon energy E_μ, ranging from 0.1 GeV to 10^6 GeV, and of its incoming direction θ_μ, ranging from 0 to 90°.

The azimuthal dependence is not considered. In addition, although $\overline{\text{Off}}\underline{\text{line}}$ allows to distinguish between μ^+ and μ^-, such a distinction will not be considered in this work.

The flux of atmospheric muons depends, however, also on the altitude and geomagnetic latitude at which the detector is placed. The dependence on the second variable is neglected, although it should not be neglected for a more accurate study, whereas an approximation of the effect of the first variable is considered because it can give an important effect to the flux. For the purpose of the current work, in order to normalize the flux to take into account the altitude effect at the Pierre Auger Observatory site, a rough estimate of the background from atmospheric muons at Malargüe site was considered. It is usually assumed to be about 3500 Hz per station [110]. By integrating the expected flux at sea level over the effective area A_{eff}, seen by a muon with incoming direction θ, and over the complete range of energy, an integrated rate of 2900 Hz is obtained. The normalization factor results, then, 1.2[1]. The effective area A_{eff} depends on θ_μ according to the following equation

$$A_{eff}\left(\theta_\mu\right) = \pi R^2 \cos\left(\theta_\mu\right) + 2\pi R H \sin\left(\theta_\mu\right), \tag{C.1}$$

where R is the radius of the station and H its height. This area can be seen as the shadow produced by a station on the ground when it is "illuminated" by a beam of muons with a certain direction. The largest contribution to the integrated flux comes from the more vertical directions ($\cos\theta_\mu \approx 1$) and from the less energetic muons (E_μ around 1 GeV). We can extract an additional estimate of the normalization factor at Malargüe altitude from Fig. 4.6 and it results about 1.1 in agreement with the previous estimate.

The duration of the injection time window was fixed to $\Delta T = 60\mu sec$ around a central time T_{CT} estimated as the median of the arrival times of the shower particles on the ground [2]. The median was here considered to better treat the skewed time distributions given by very inclined showers. The expected average number of muons, $\langle n_\mu \rangle$, arriving at a single station, is obtained by multiplying the integrated flux times ΔT. For $\Delta T = 60\mu sec$, $\langle n_\mu \rangle \approx 0.2$. The number of expected muons is randomly generated from a Poisson distribution with mean $\langle n_\mu \rangle$. The following equation gives the probability P_n that n muons are generated

$$P_n = \frac{e^{-\langle n_\mu \rangle} \langle n_\mu \rangle^n}{n!}. \tag{C.2}$$

The probability for no muon to be generated is about 0.82, for 1 muon about 0.16, for 2 muons 0.016. If at least a single muon is generated, the time, the direction, the energy and the position on the surface of the station are generated. The time is uniformly randomized in ΔT centered at T_{CT}. The zenith of the direction and the energy are randomly generated from the bidimensional histogram of the flux. The azimuth is uniformly between 0 and 360°. The hitting position on the surface of the station is randomly generated by taking into account the effective area seen by the generated direction (Fig. C.1, left panel). Hence, if θ_μ and ϕ_μ define the generated arrival direction of a muon, the hitting position is obtained

[1] The normalization factor depends also on the arrival direction but at the date no direct and precise measurement of the atmospheric muon flux at Malargüe site has been done.

[2] An estimation of the central trigger time is necessary, since the muon injection is done at the beginning of the detector response simulation.

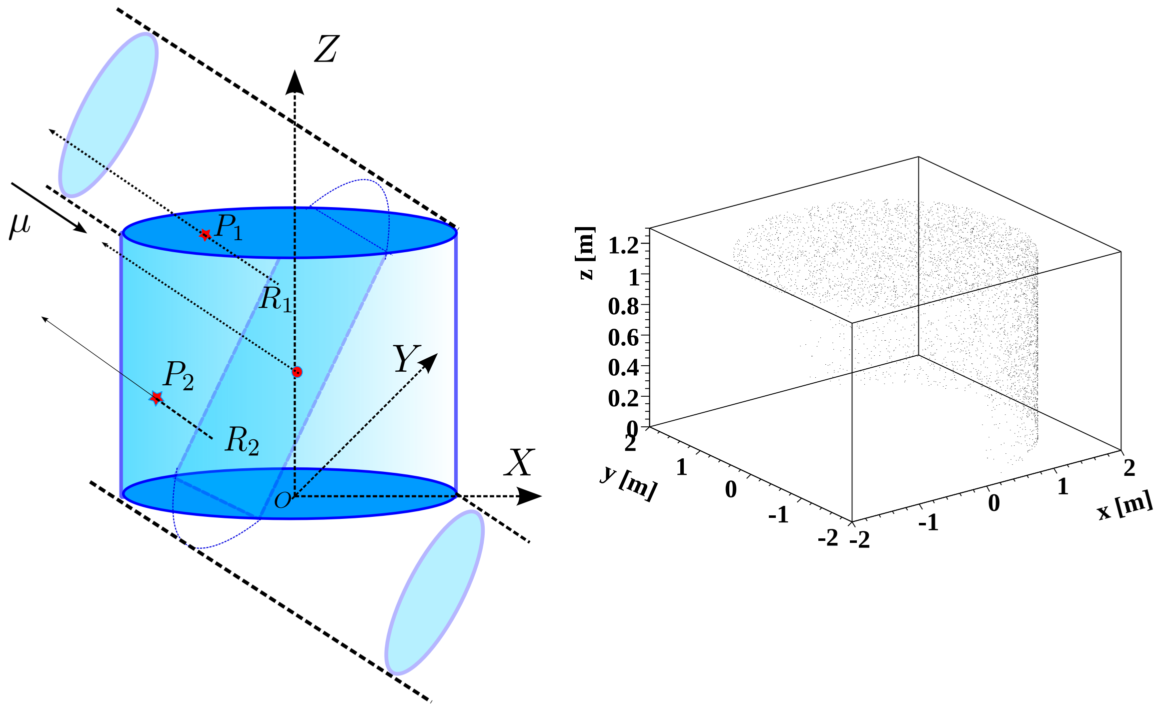

Figure C.1: *(Left panel) Effective area seen by a beam of muons with fixed direction. The two small ellipses are used to generate hits on the surface of the stations. The point R_1 and R_2 are example of generated position on the surface which is the projected cylinder on the plane perpendicular to the arrival direction of a muon. The point P_1 and P_2 are the projection of R_1 and R_2 back to the station surface along the opposite direction to the arrival direction. (Right panel) Distribution of injected position on a station surface by fixing the incoming direction. Here $\phi = 0$ and θ is along the diagonal.*

by randomly generating first a position on the surface representing the projection of the cylinder on a plane perpendicular to the arrival direction, then by projecting this position back to the cylinder surface along the direction opposite to the arrival direction. In other words, only the part of the surface seen by an arriving muon is taken into account for the random generation. An example of distribution of generated positions on a station surface for a fixed incoming direction is shown in Fig. C.1 (right panel). The trigger rates for single muons, arriving at a rate of $R_{1\mu}$, can be calculated by injecting a single muon into a single station $N_{1\mu,inj.}$ times and collecting the number of triggering muons $N_{1\mu,trig.type}$, according to the following equation

$$R_{1\mu,trig.type} = \frac{N_{1\mu,trig.type}}{N_{1\mu,inj.}} R_{1\mu} P_1, \tag{C.3}$$

where $P_1 \approx 0.16$ is the probability of having a single muon, according to Eq. C.2. In

Table C.1: Trigger rates for single muons, distinguished for the three trigger types.

	Trigger type		
	ToT	T1 thr.	T2 thr.
$R_{1\mu,trig.type}$ [Hz]	0.22	3	1.2
$\frac{N_{1\mu,trig.type}}{N_{1\mu,ToT}+N_{1\mu,T1}+N_{1\mu,T2}}$	5%	69%	26%

Table C.2: Trigger rates for double muons, distinguished for the three trigger types.

	Trigger type		
	ToT	T1 thr.	T2 thr.
$R_{2\mu,trig.type}$ [Hz]	1.28	0.6	0.2
$\frac{N_{2\mu,trig.type}}{N_{2\mu,ToT}+N_{2\mu,T1}+N_{2\mu,T2}}$	61%	30%	9%

Tab. C.1 the trigger rates for single muons are reported. Single muons are likely to trigger as T1 and T2 threshold trigger.

Double muons happening in the time window allowed by the ToT local trigger, may result in a background which is not negligible. The probability for a single muon to happen in a time window of 3 μsec (120 bins) is $P_{1\mu,3\mu sec} = R_{1\mu} \times 3\mu sec \simeq 0.01$. If one considers, then, that the probability for a bunch of 2 muons to happen in the same time window is $P_{2\mu,3\mu sec} \sim 5 \times 10^{-5}$ (Eq. C.2 with $\langle n_\mu \rangle = 0.01$), the rate for two muons in $3\mu sec$ is

$$R_{2\mu,3\mu sec} = \frac{P_{2\mu,3\mu sec}}{3\mu sec} \tag{C.4}$$

and it is of the order of 16.5 Hz. Of course, not all of these double muons will trigger stations as ToTs, but part of them will give an important contribution to the total background from atmospheric muons. As a matter of fact, Eq. C.3 for double muon injections becomes

$$R_{2\mu,trig.type} = \frac{N_{2\mu,trig.type}}{N_{2\mu,inj.}} R_{2\mu} P_2. \tag{C.5}$$

In Tab. C.2 the trigger rates for double muons are reported. Therefore, the contribution from double muons to the muonic background for the surface array is mostly due to double muons triggering the stations as ToT. Depending on the number of bins above the threshold which one chooses to mark a station as ToT triggering station, however, the rate for ToT triggering muons varies. The ideal rate seems to be the one currently coming from the choice of 13 bins for the minimal time window of the ToT trigger [174].

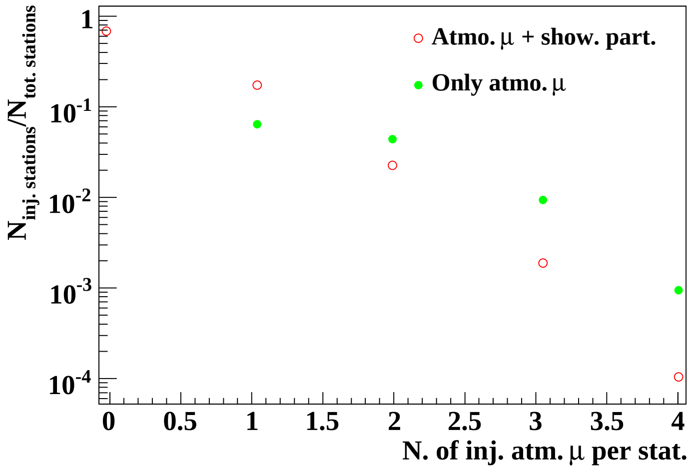

Figure C.2: *Fraction of stations into which atmospheric muons are injected versus number of injected atmospheric muons per station. The green full circles represent the stations injected with only atmospheric muons; the red open circles represent the stations where also shower particles are present.*

Since the probability to have three muons from the expected flux is negligible (1.6%), the expected rate for three muons to produce local triggers is also negligible. In conclusion, most of the background from atmospheric muons is expected to be due to single muons triggering as T1 and T2 and double muons triggering as ToT.

C.1 Comparison of simulated rates with real rates

For a full-array working (about 1600 stations), the average number of expected stations into which single muons are injected with a rate $R_{1\mu} = 3500Hz$ is 336 ± 18 or 20% of the total number of stations, 68% is expected not to be injected by atmospheric muons at all and the rest is expected to be injected with bunches of 2, 3 or more muons (Fig. C.2). Yet, depending on the shower energy and, thus, on the number of stations which are triggered by shower particles, some stations will present only atmospheric muons and the others will present muons along with shower particles. In the present work CORSIKA simulations of proton showers with energy distributed according their expected spectrum in the range $10^{18} - 10^{20}$ GeV and zenith angle in the range $60° - 90°$ were used. One expects, then, that only atmospheric muons are injected into 16% of the stations and the remaining 16% contains muons and shower particles. Therefore, at the end one may be left with stations triggering only by muonic background, stations triggering by shower particles, stations triggering by shower particles with a contribution from the muonic background and stations triggering by muonic background but with a contribution from shower particles.

The latter case is, obviously, the least probable. The first case is mostly driven by the probability that muons from the background produce either a first level threshold trigger, i.e. stations are triggered as T1 thr. by single muons, or a ToT trigger, which is always promoted to a second level trigger. In particular, the number of T1 threshold triggers expected from single muons is $3Hz \times 60\mu sec \times 1600 \approx 0.3$, i.e. 1 station per 3 events, whereas the number of stations into which double muons are injected and which triggers as T1 thr. is 0.06. The number of stations triggering as ToT because of single muon injections is 0.022 and it is 0.13 due to double muon injections. For T2 thr., the number of stations is 0.12 and 0.02 for single and double muon injections, respectively. In total, we expect a minimum of 3 stations per 2 events triggered by atmospheric muons.

The third case is related to the trace length stored when a local trigger is recognized. If a set of shower particles is able to trigger a station, after a local trigger has been recognized, 19.2 μsec around the station local trigger time are stored. This time interval corresponds to 768 time bins. In particular 256 pre-trigger bins and 512 post-trigger bins are stored. Muon signals may, therefore, affect the trace not directly, i.e. responsible for a local trigger, but in any case they may be part of a trace and distort the total signal, the signal start time and then the following reconstruction. The task of the trace cleaning [120, 115] is the removal of accidental peaks form these muonic signals.

In order to check whether the rate of injected atmospheric muons matches the observed rate in real data, the set of real events from January 2006 to December 2006 was considered. The possible stations into which real atmospheric muons are injected were selected as the ones which the SdEventSelector module marked as accidental and whose distances from the barycenter of the candidate stations on the shower plane was larger than the maximum distance, on the same plane, at which a candidate station could be found. In such a way an external area to the bulk of possible stations, into which mostly shower particles were injected, was built. The accidental stations, however, may include here also stations hit by little local showers and the result for real data might be considered an upper limit to the number of accidental stations due to the only contribution of atmospheric muons. Finally the result for real data might be biased by other random effects such as raining PMTs and failures of the selector.

By counting the total number of working stations in the external area considered for each triggering shower in real data, $N_{total,ext.}$ and the number of accidental stations, $N_{inj.,ext.}$, in the same area, a rough estimate of the rate of accidental stations, which possibly include atmospheric muons, in real data is given by the ratio $N_{inj.,ext.}/N_{total,ext.}$.

CORSIKA simulations with the addition of simulated atmospheric muons were treated the same way. In simulations the number of stations including the background, $N_{inj.}$, can be known exactly and one can count them over the number of total stations, N_{total} (1600).

The distributions of the total rates for accidental stations of type T1 thr., T2 thr. and ToT in real data and simulations are shown in Fig. C.3. The mean values for the trigger rates of ToT and T2 local triggers in real data and simulations are compatible, whereas the rate for T1 in real data has a value which is about 3 times larger. In fact, one should notice that the T1 thr. trigger has a rate of the order of 100 Hz whereas the expected rates for single and double muon injections is well below such a value. Therefore, other random effects are expected to be included during data acquisition along with atmospheric muons.

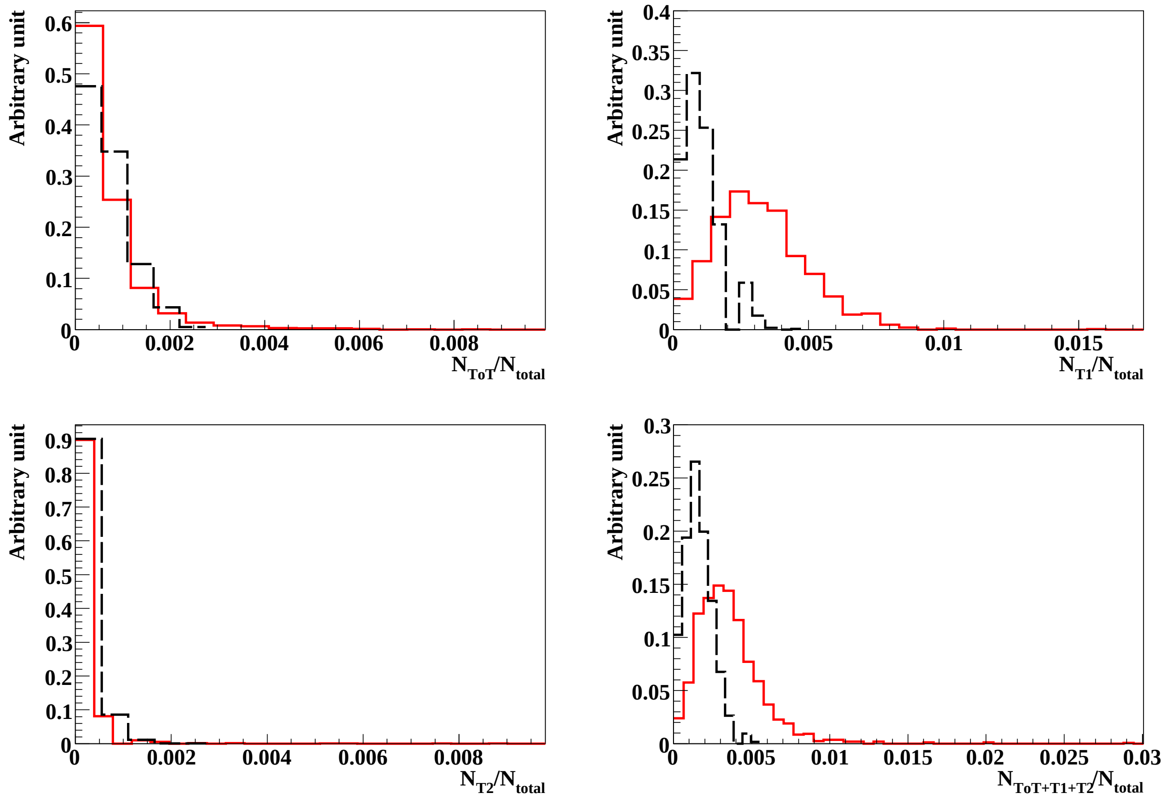

Figure C.3: *Comparisons of expected trigger rates (black dashed lines) with real trigger rates (red full lines), calculated according the procedure described in Sec. C.1. In the upper-left panel ToT trigger rates; in the upper-right panel T1 threshold trigger rates; in the lower-left panel T2 threshold trigger rates; in the lower-right panel total trigger rates.* **Disclaimer: The plots are not approved by the Auger Collaboration. Please do not use them.**

In other words, the safety area chosen can not guarantee the presence of only candidate stations and stations triggered by atmospheric muons at the level of T1 thr. trigger. A more precise work should scan the other unknown sources of random occurrences in T1 thr. trigger stations in real data and try to simulate them.

C.2 Identifying atmospheric muon signals

The addition of atmospheric muons during detector simulations is helpful to understand how to avoid or limit the influence of such background during shower reconstruction.

The signals and the spatial distribution of stations including muons from the background will be considered in this section as an example to study the impact of injected background during detector simulations. The CORSIKA simulations used in Sec. C.1 will be considered as a starting point for a future study. In particular, one can build the distri-

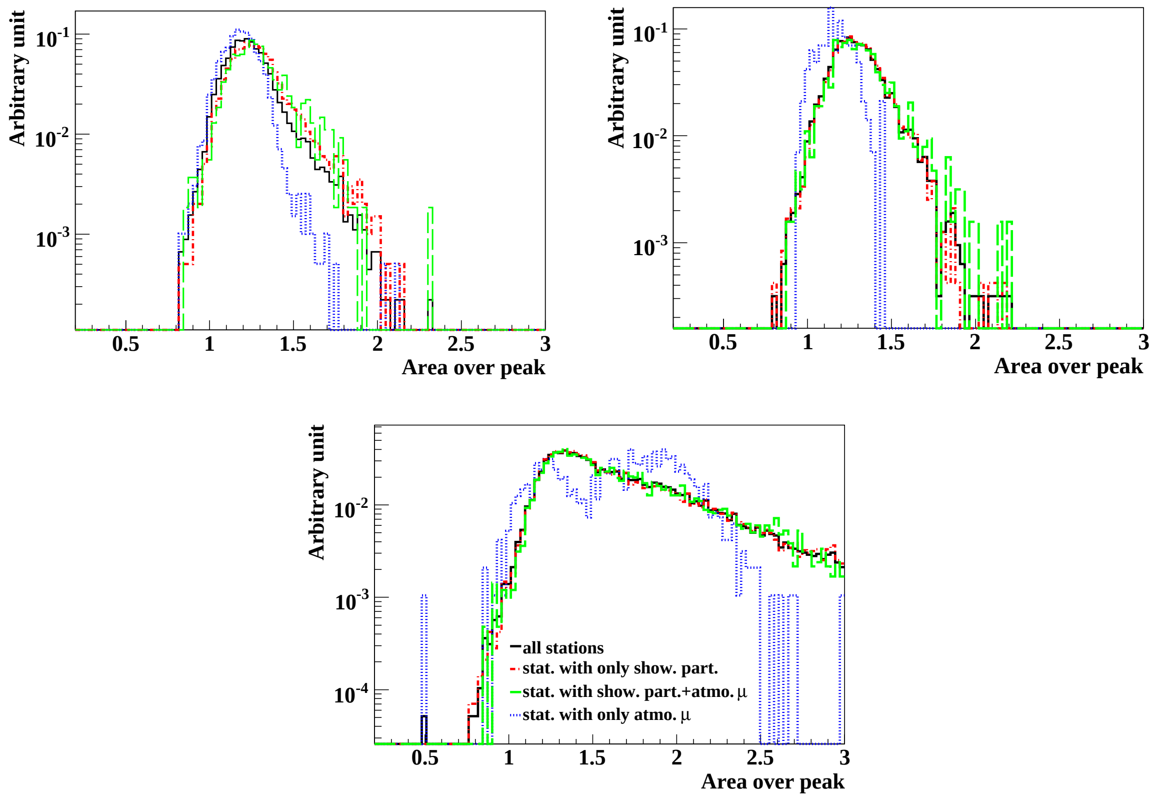

Figure C.4: *Area over peak for stations triggered by only atmospheric muons (blue dotted lines), stations triggered by only shower particles (red dotted dashed lines), stations with shower particles and atmospheric muons (green dashed lines) and stations with no distinction on the injected particles (black full lines). In the upper-left panel T1 trigger stations; in the upper-right panel T2 trigger stations; in the lower panel ToT trigger stations. The contribution from single and double muon injections in the area over peak for ToT trigger stations is evident.*

bution of the expected "area-over-peak" for stations triggered only by injected atmospheric muons and stations triggered only by shower particles (Fig. C.4), and the distribution of the distances of stations triggered by only atmospheric muons from the closest station with no atmospheric muon (Fig. C.5). The area-over-peak for stations triggered by single muons is of the order of 1.2–1.3 whereas stations triggered by double muons are expected to have values around 1.9–2. In T2 thr. trigger stations, including only atmospheric muons, a narrow distribution of the area-over-peak reflects the fact that the rate for two or more atmospheric muons to produce a T2 trigger is suppressed (Tab. C.2). In such cases, stations with area-over-peak larger than 1.5 and triggering as T2 thr. are expected not to be triggered by atmospheric muons. In T1 thr. trigger stations the contribution from double or more atmospheric muons is possible. The area-over-peak presents values larger than 1.5 for such cases (upper-right panel in Fig. C.4). In ToT trigger stations contributions from

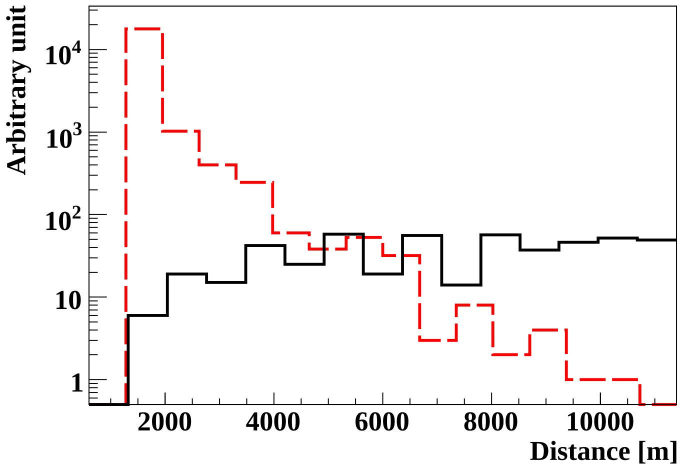

Figure C.5: *Distribution of distances of stations triggered by only atmospheric muons from the closest station with no atmospheric muon (black full line) and distribution of distances of stations triggered by only shower particles from the closest station with no atmospheric muon (red dashed line). Due to the random occurrence of atmospheric muons in the array of stations, the former distribution shows a uniform distribution. The latter distribution reflects the typical dimension of shower footprints.*

single or more atmospheric muons are expected.

On the basis of the distribution of Fig. C.5 it is also evident that it is possible to define a distance for which an isolated station may include atmospheric muons. Isolated stations are removed during shower reconstruction to safely avoid the presence of background which might distort the reconstruction of some variables.

$\mathcal{D}$

Detection and identification efficiency maps

In this section the list of calculated trigger and identification efficiency maps, shown in Fig. D.1–Fig. D.3, will be shown. The definition of trigger and identification efficiency can be found in Sec. 4.3 and Sec. 5.4, respectively. The number of triggering stations is larger or equal to 4 in the following.

In the left panels of the following figures, the detection efficiency for up-going and down-going ν_τ-induced showers (Fig. D.1), ν_e CC-induced showers (Fig. D.2) and ν_e NC-induced showers (Fig. D.3) is shown. In the right panels of the same figures, the corresponding identification efficiency is displayed.

In Fig. D.1 (upper panels) the calculated trigger and identification efficiency for up-going tau-induced showers in the range between $90° - 95°$ is shown. It can be observed that the efficiency increases with energy and reaches its maximum of about 0.82[1] for an initial tau lepton energy E_τ larger than 3 EeV and $h_{10\ km}$ larger than 200 m above the ground level. At higher altitudes, the trigger and the identification efficiency drop. In addition, at the highest energies (above 10 EeV) only tau-induced showers with the parameter $h_{10\ km}$ not larger than about 3000 m above the ground level can trigger the surface detector array.

For down-going tau-induced showers (Fig. D.1, middle and lower panels), the maps of efficiencies appear slightly different. A trend which is similar to up-going tau-induced showers can be observed at the highest altitudes, but below 500 m the detection and identification efficiency show that down-going showers induced by tau-neutrinos do not spread out sufficiently in the lateral plane to trigger the detector.

The same behavior can be observed for ν_e CC-induced showers. In Fig D.2 their identification efficiency as a function of the initial particle energies and injection slant depths from the ground is shown. For showers induced close to the ground level, the identification efficiency drops since the shower does not cross enough grammage to produce particles which can trigger more than 4 stations. It is also clearly seen that the efficiency as well as the range of slant depths, in which neutrino identification is possible, grows as the zenith angle increases. In Fig. D.3 the calculated efficiencies for simulated ν_e NC-induced showers

[1]The efficiency can reach a maximum value of 82.6% due to taus which decay into muons. Muons have a low probability to produce detectable showers.

are shown. The efficiency is quite similar to the efficiency shown in Fig. D.2. Slightly larger differences can be observed for the lowest depths due to the fact that in ν NC interactions the number of low-energy showers which can trigger the detector is larger than in CC interactions. In conclusion, trigger and identification efficiency depend mainly on the geometry associated to the showers and only slightly on the type of primary particle.

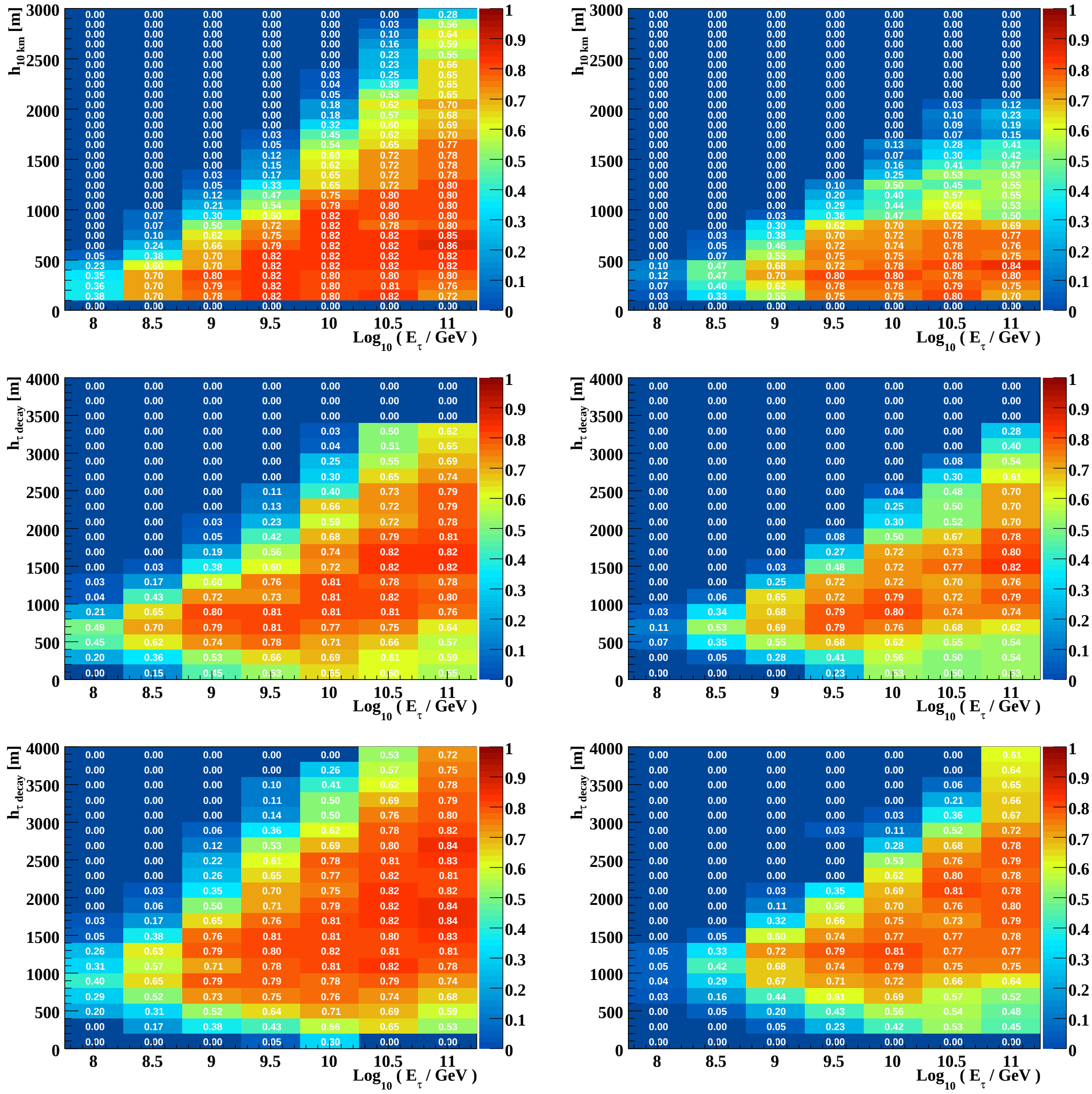

Figure D.1: *Detection (left panels) and identification (right panels) efficiency for CC ν_τ-induced showers at the surface array of the Pierre Auger Observatory. Showers with 4 or more triggering stations (4-fold events) are considered. (Upper panels) Detection and identification efficiency for up-going ν_τ at 91°. (Middle panels) Detection and identification efficiency for down-going ν_τ at 87°. (Lower panels) Detection and identification efficiency for down-going ν_τ at 85°.*

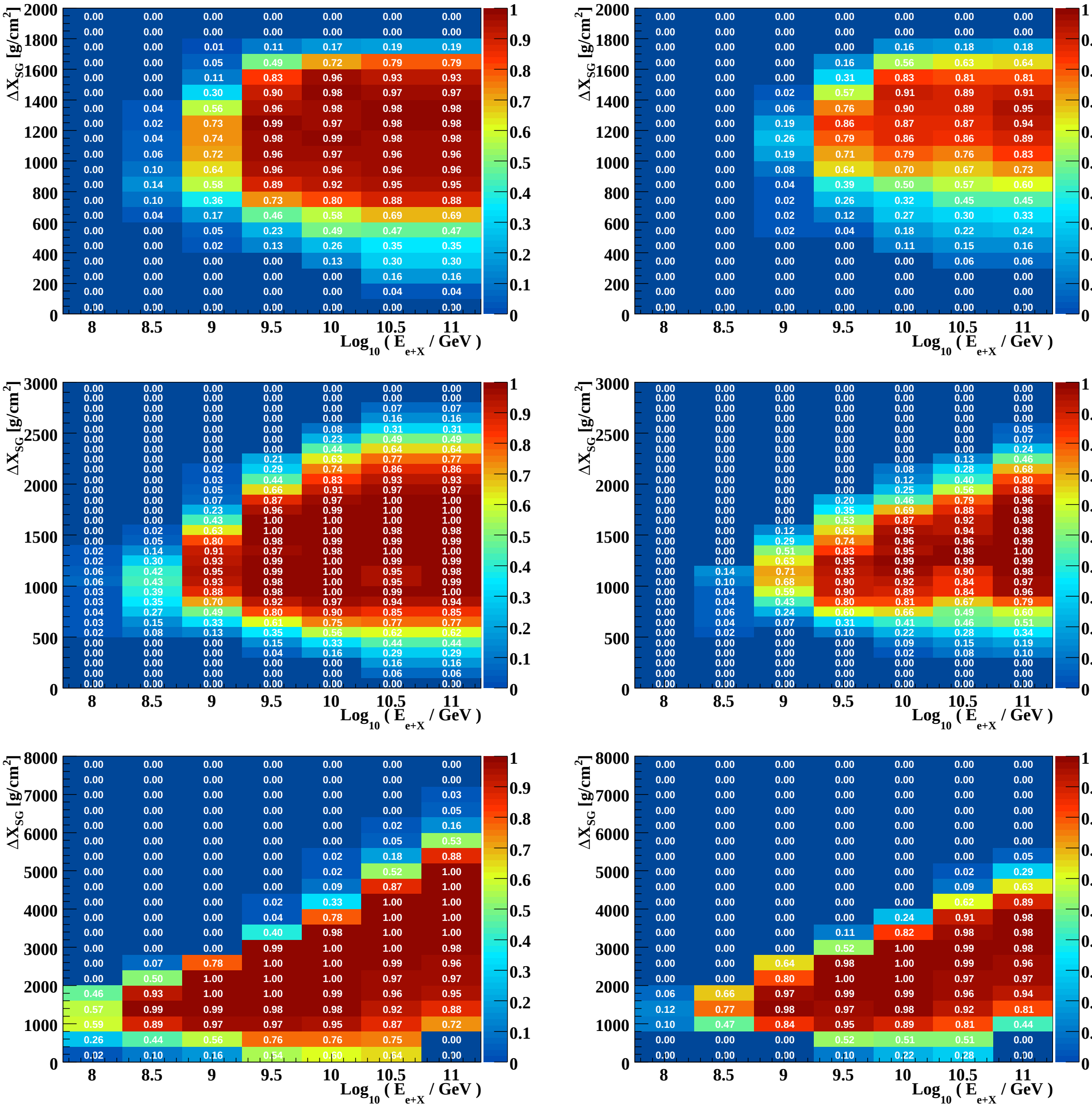

Figure D.2: *Detection (left panels) and identification (right panels) efficiency for down-going CC ν_e-induced showers at the surface array of the Pierre Auger Observatory as a function of the injection slant depth measured from the ground. Showers with 4 or more triggering stations (4-fold events) are considered. (Upper panels) Detection and identification efficiency for showers at 65°. (Middle panels) Detection and identification efficiency for showers at 75°. (Lower panels) Detection and identification efficiency for showers at 87°.*

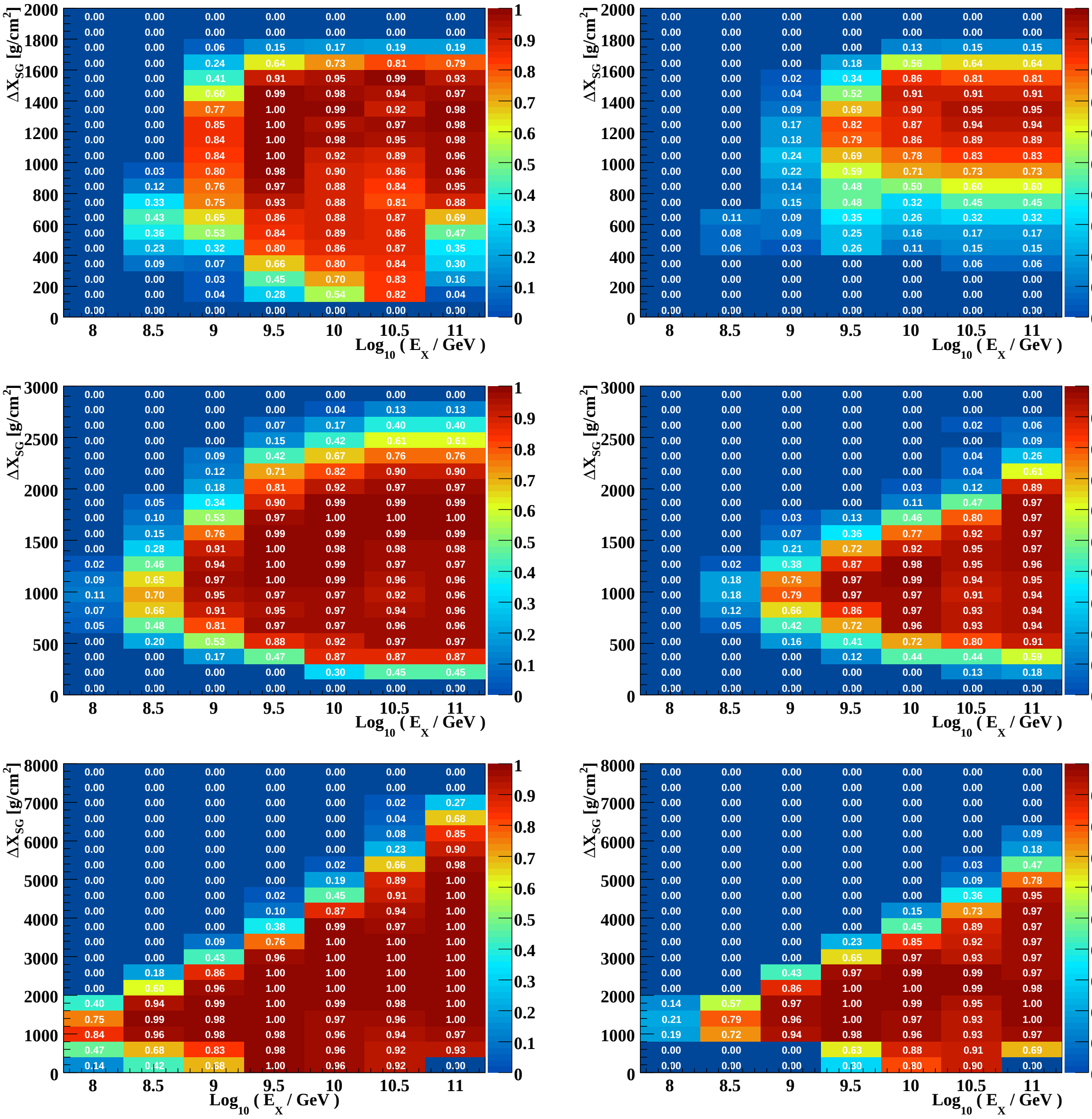

Figure D.3: *Detection (left panels) and identification (right panels) efficiency for down-going NC ν_e-induced showers at the surface array of the Pierre Auger Observatory as a function of the injection slant depth measured from the ground. Showers with 4 or more triggering stations (4-fold events) are considered. (Upper panels) Detection and identification efficiency for showers at 65°. (Middle panels) Detection and identification efficiency for showers at 75°. (Lower panels) Detection and identification efficiency for showers at 87°.*

E Traces of neutrino candidates

Disclaimer: The traces listed in this chapter are not approved by the Auger Collaboration. Please do not use them.

E.1 Event 1605038

In this section the traces for the candidate stations of event 1605038 are listed in decreasing order of signal.

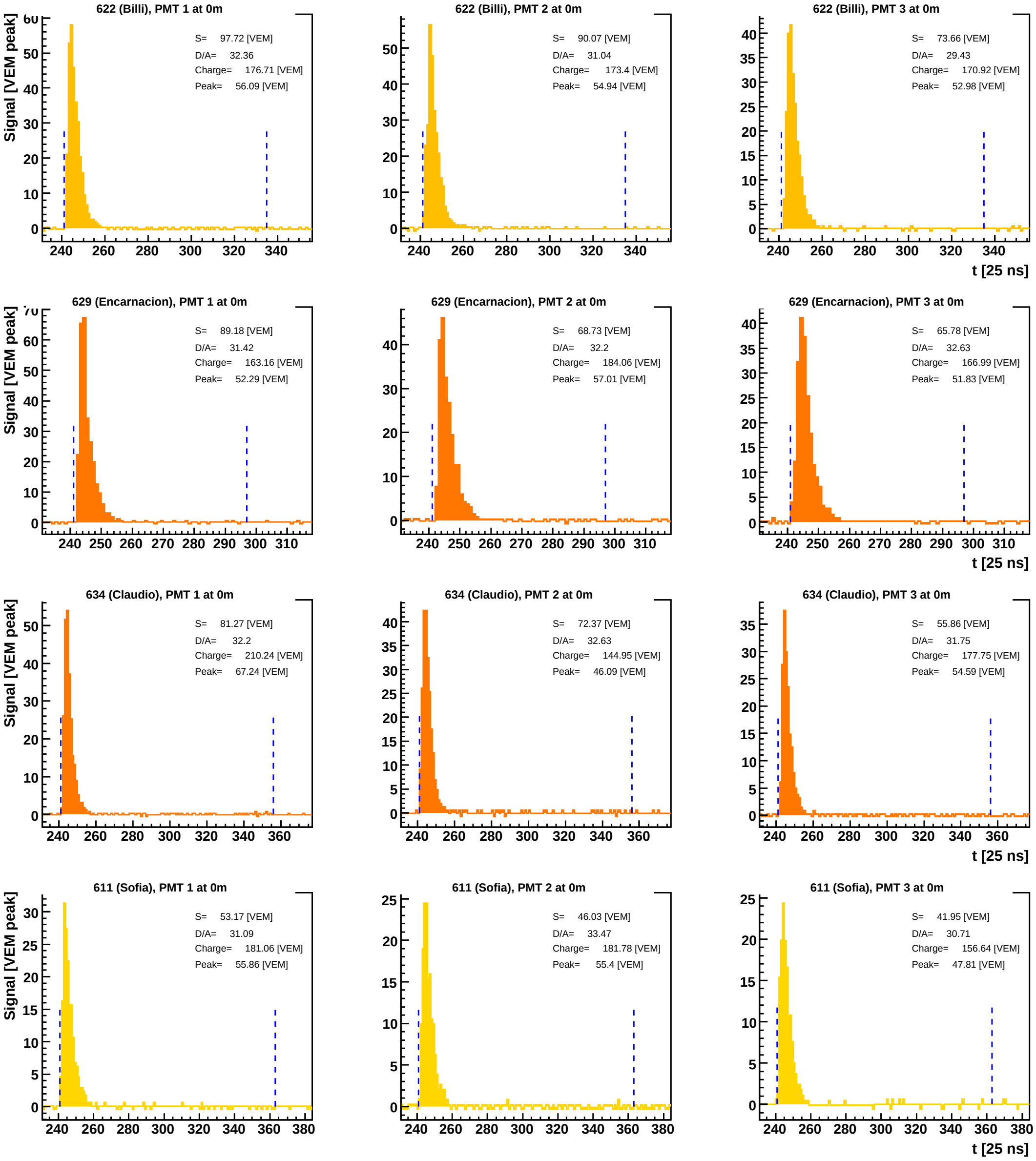

Figure E.1: *Traces of stations 622, 629, 634 and 611.*

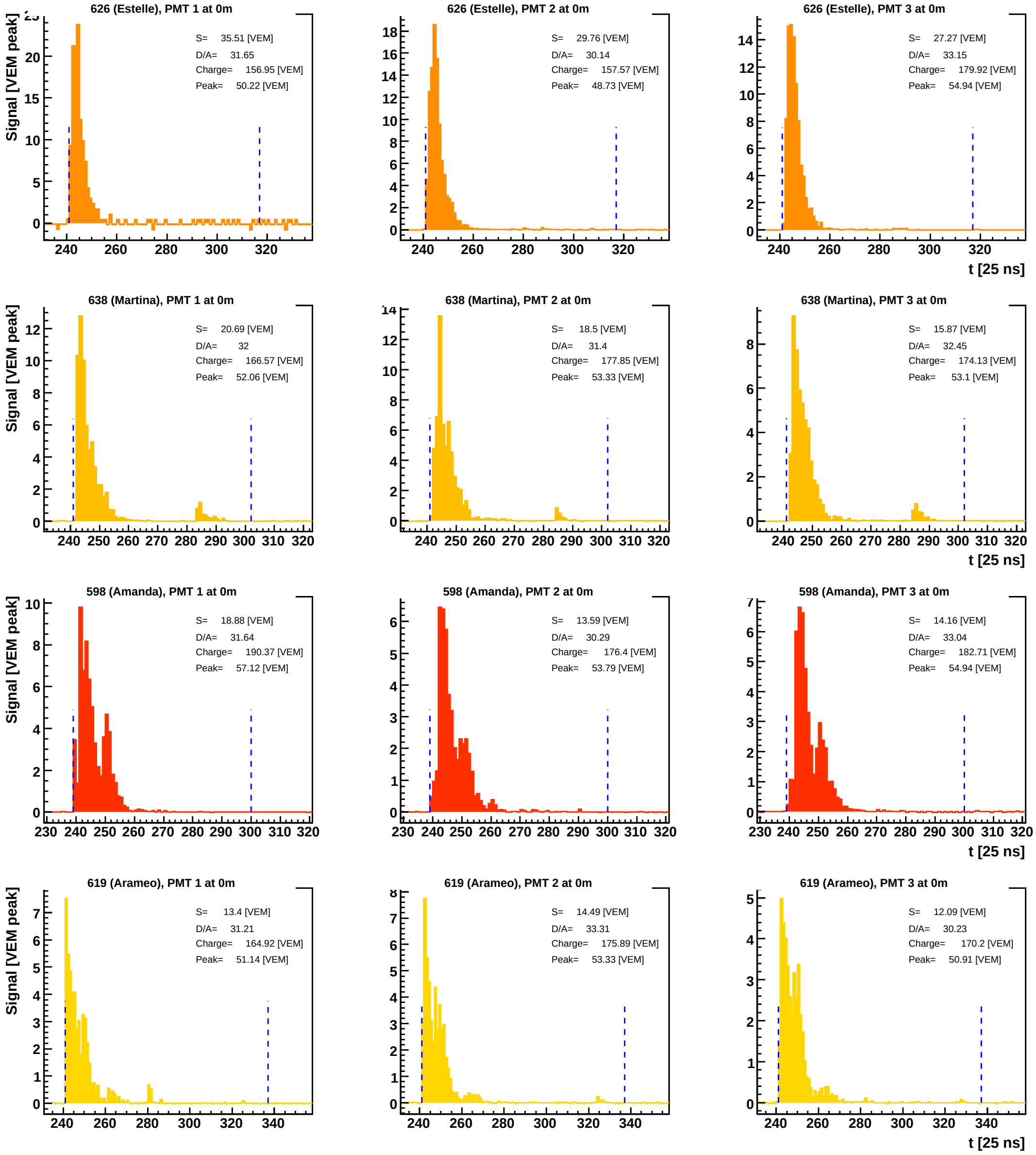

Figure E.2: *Traces of stations 626, 638, 598 and 619.*

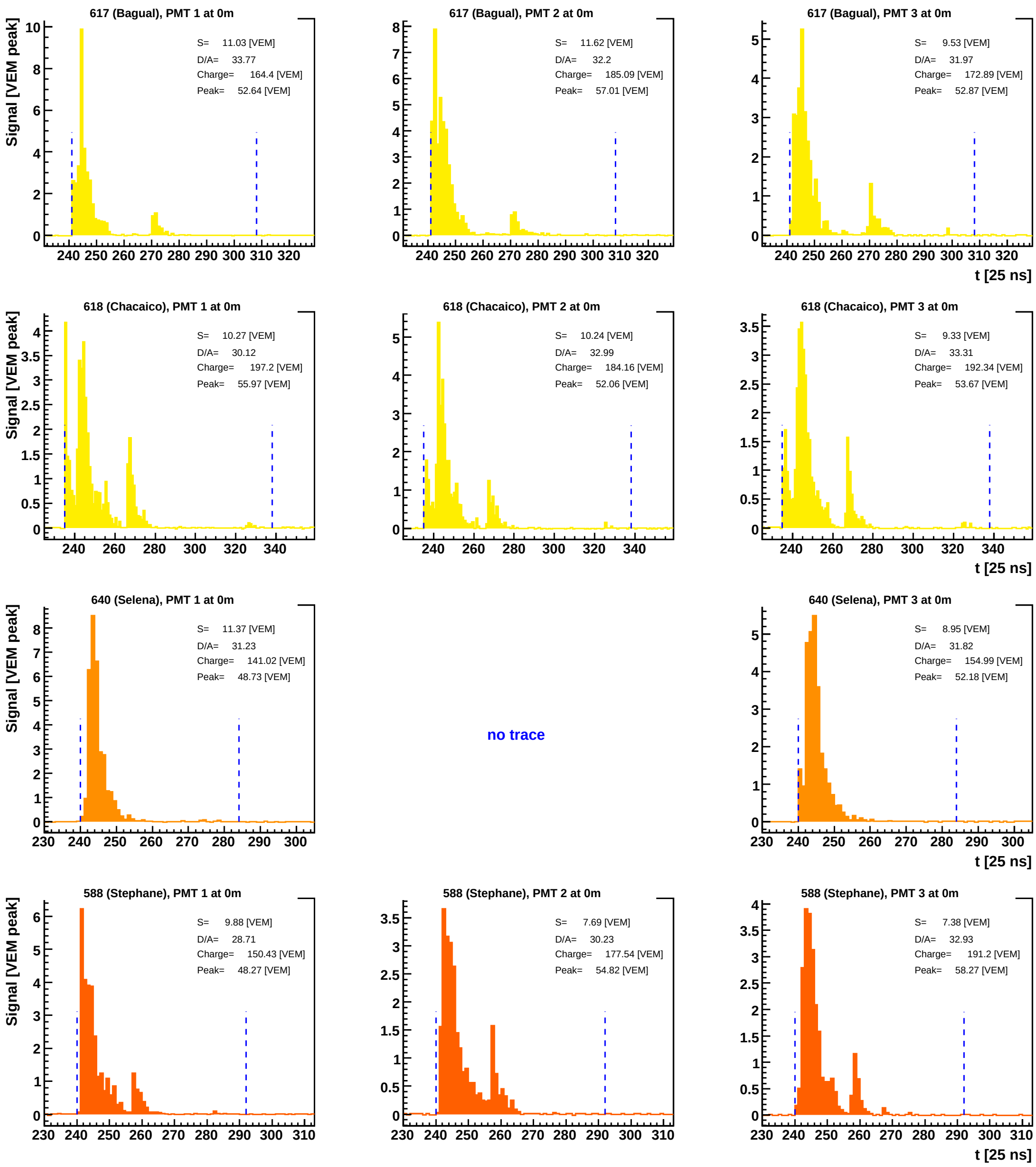

Figure E.3: *Traces of stations 617, 618, 640 and 588.*

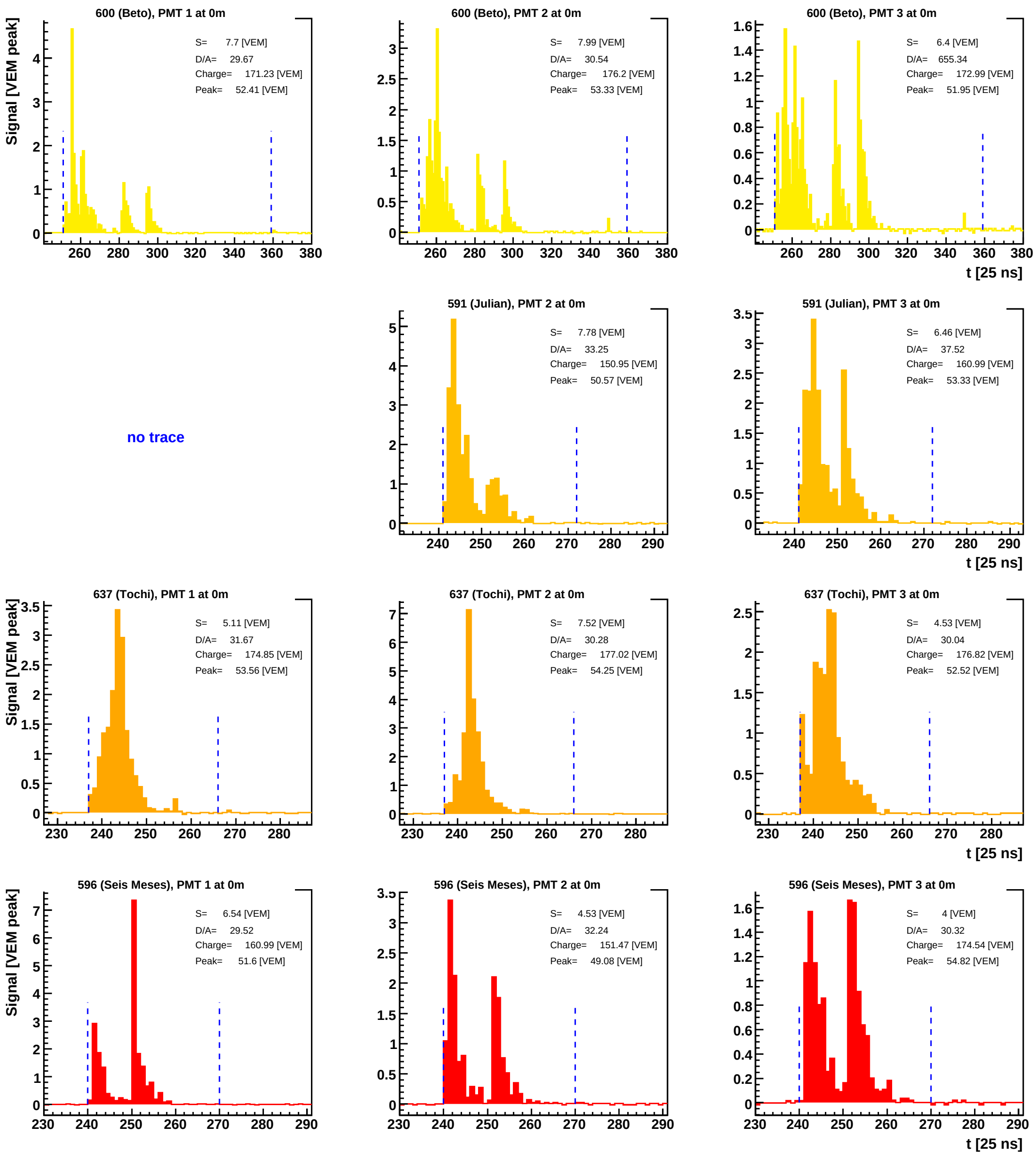

Figure E.4: *Traces of stations 600, 591. 637 and 596.*

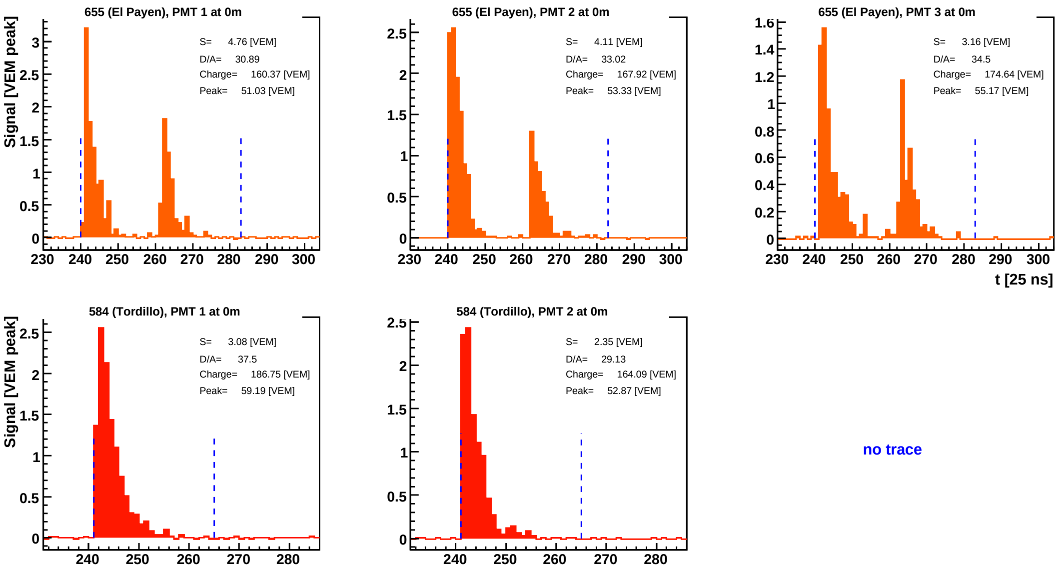

Figure E.5: *Traces of stations 655 and 584 .*

E.2 Event 2550163

In this section the traces for the candidate stations of event 2550163 are listed in decreasing order of signal.

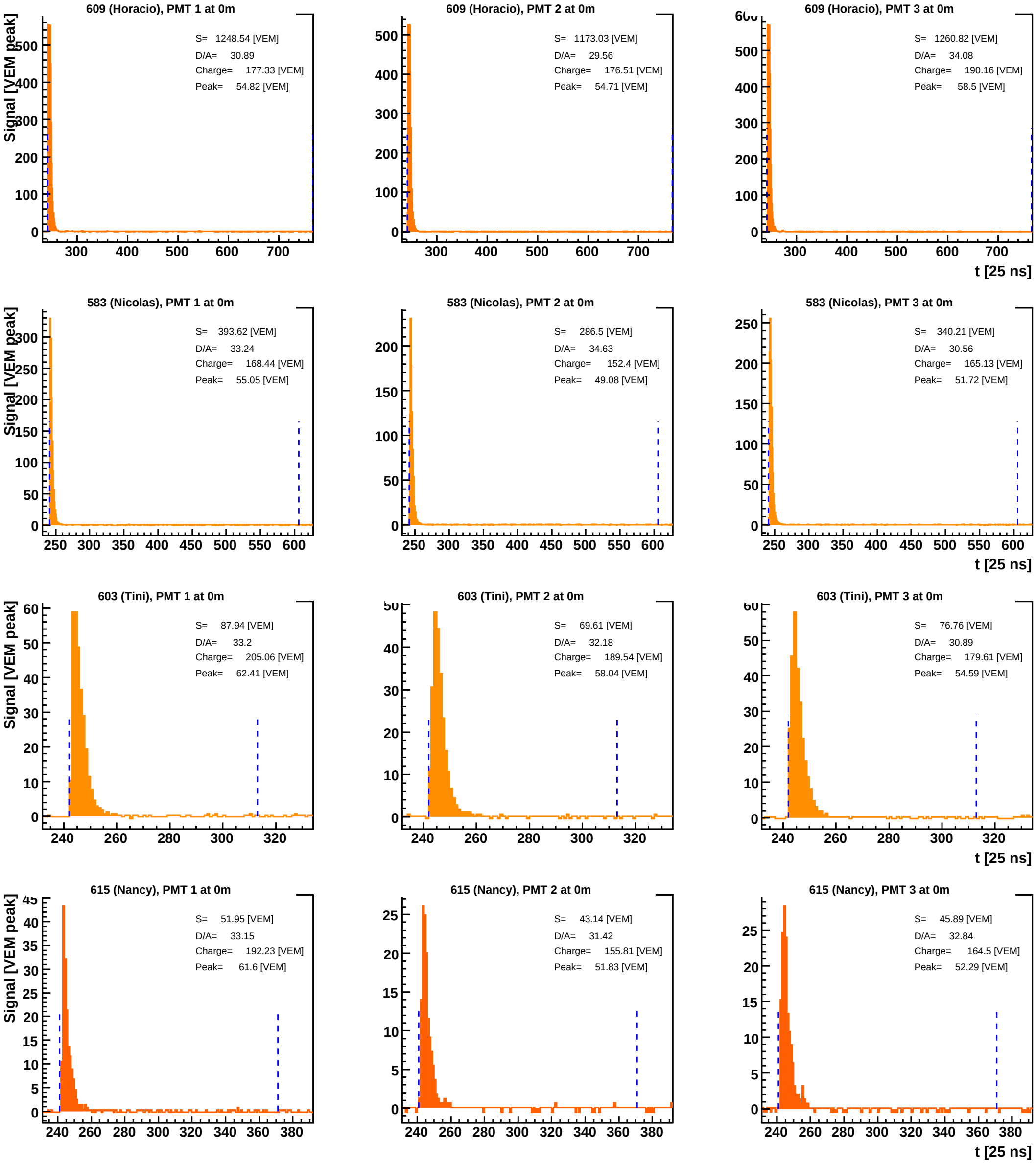

Figure E.6: *Traces of stations 609, 583, 603 and 615*

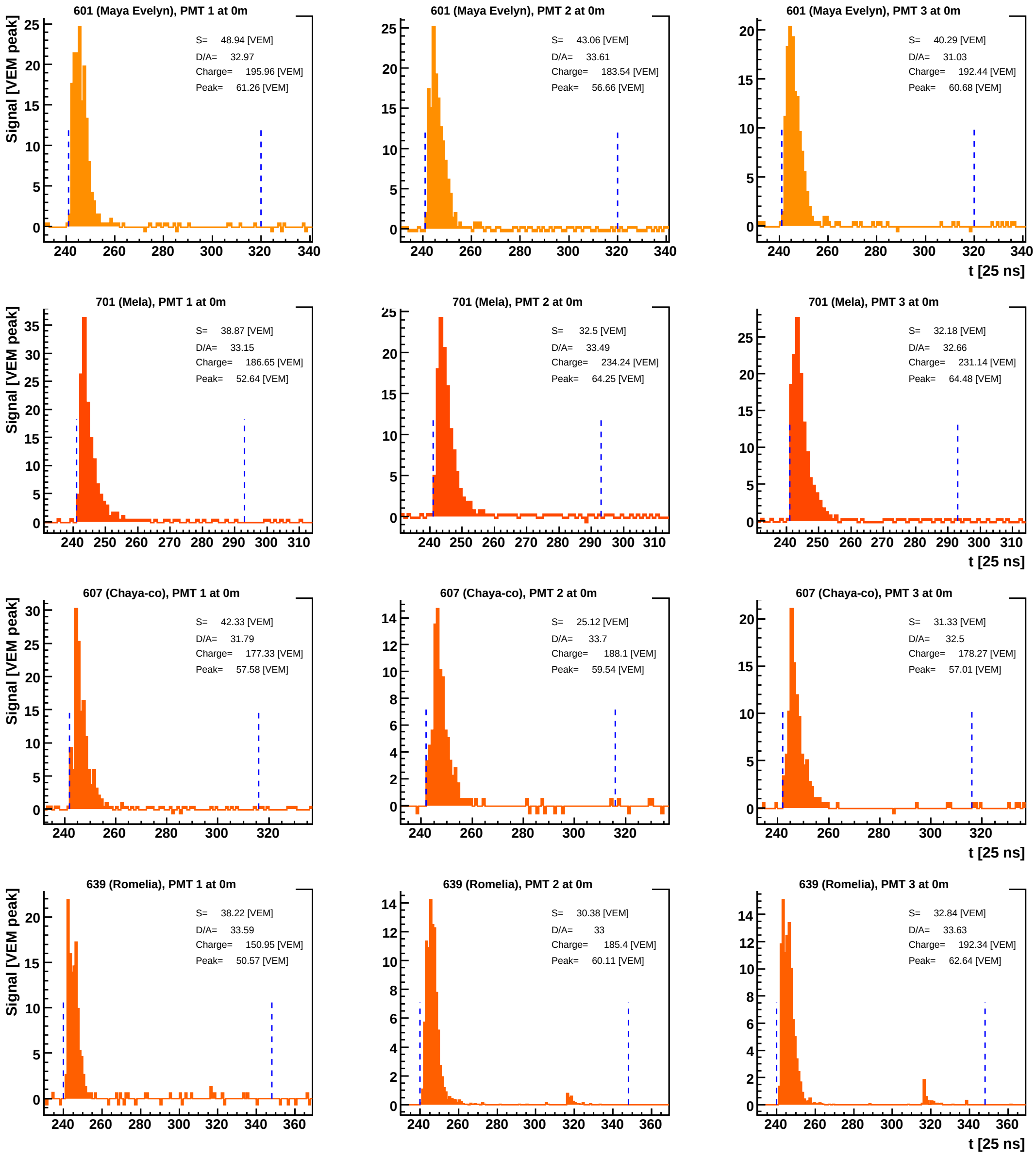

Figure E.7: *Traces of stations 601, 701, 607 and 639*

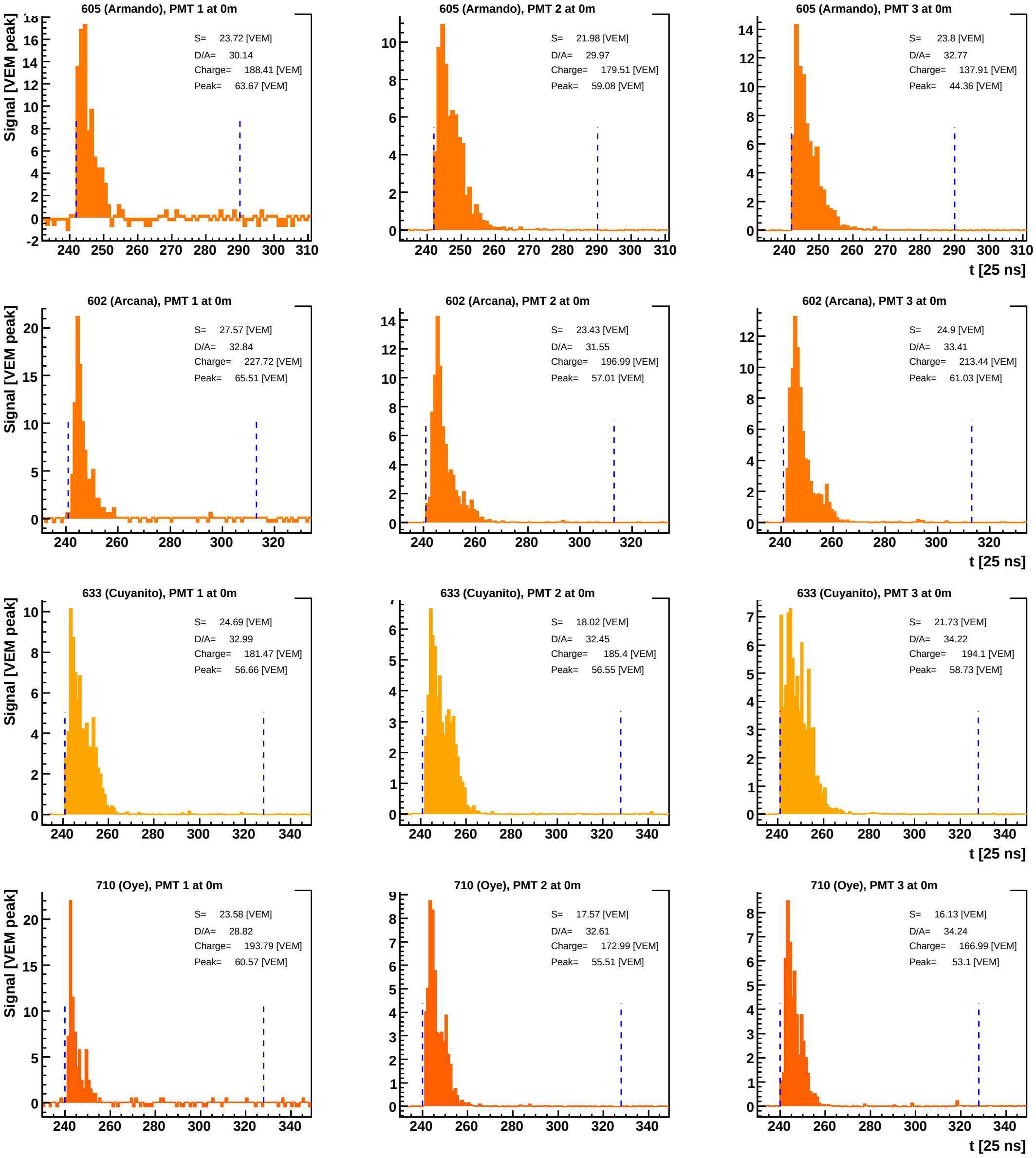

Figure E.8: *Traces of stations 605, 602, 633 and 710*

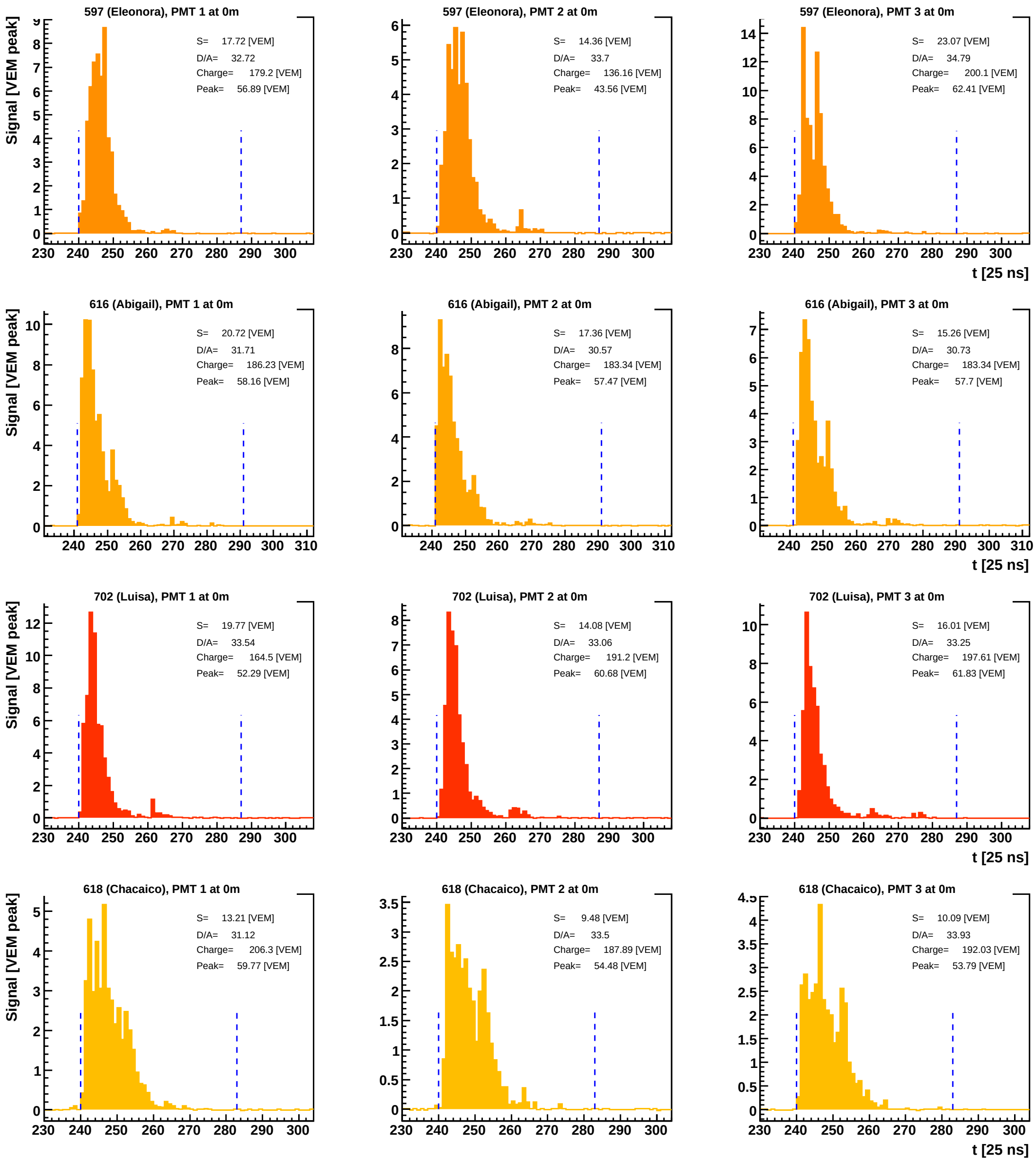

Figure E.9: *Traces of stations 597, 616, 702 and 618*

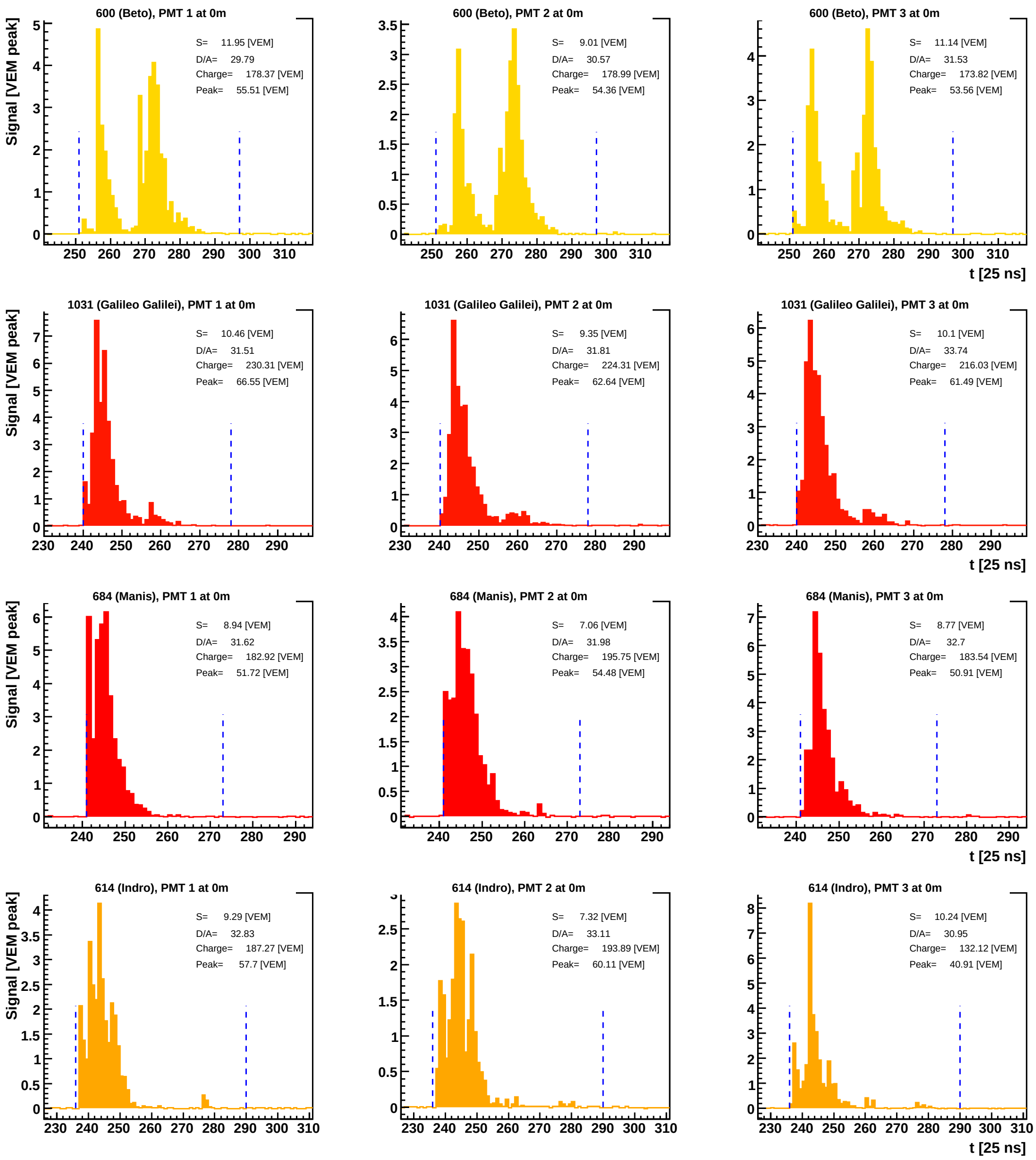

Figure E.10: *Traces of stations 600, 1031, 684 and 614*

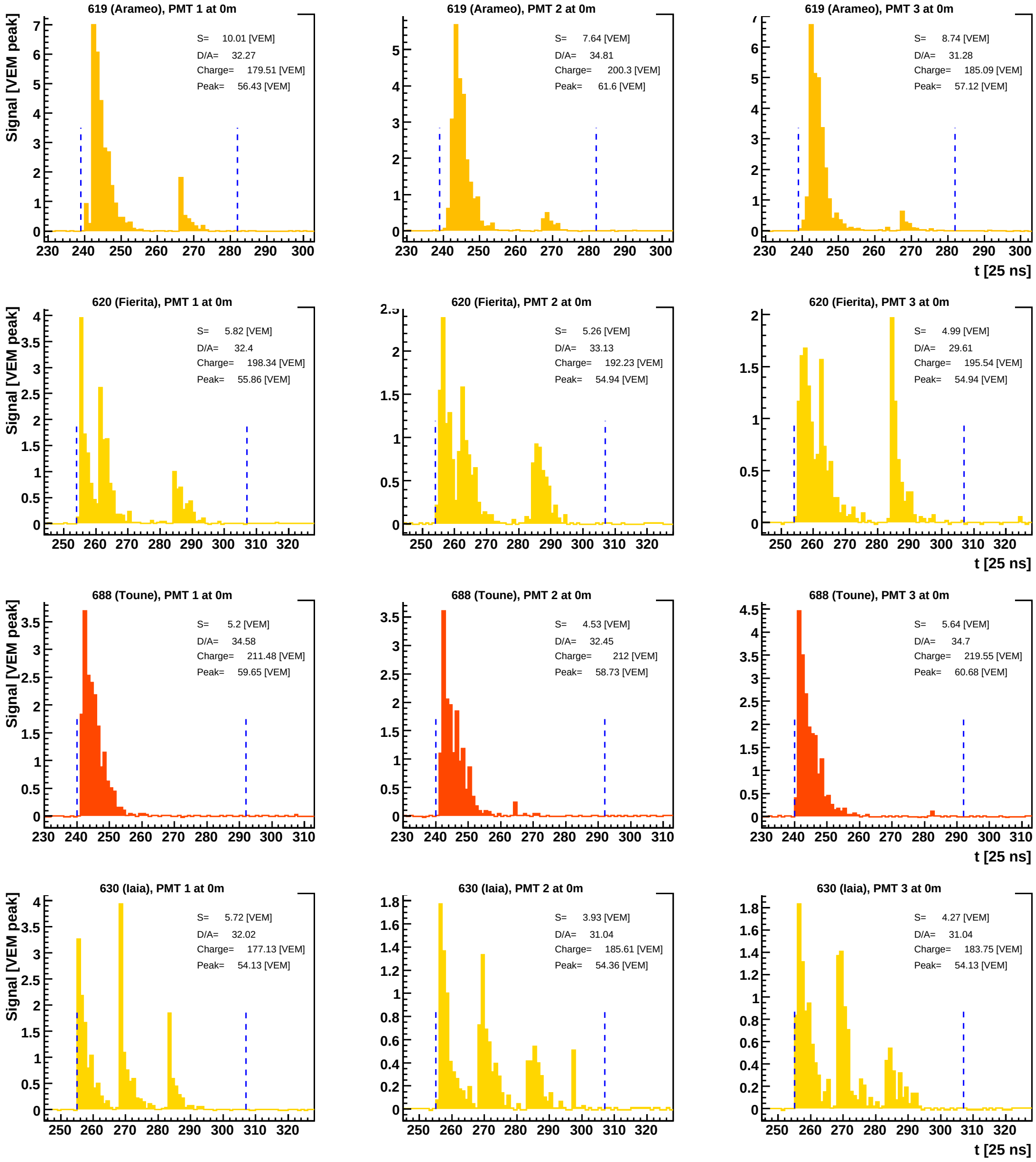

Figure E.11: *Traces of stations 619, 620, 688 and 630*

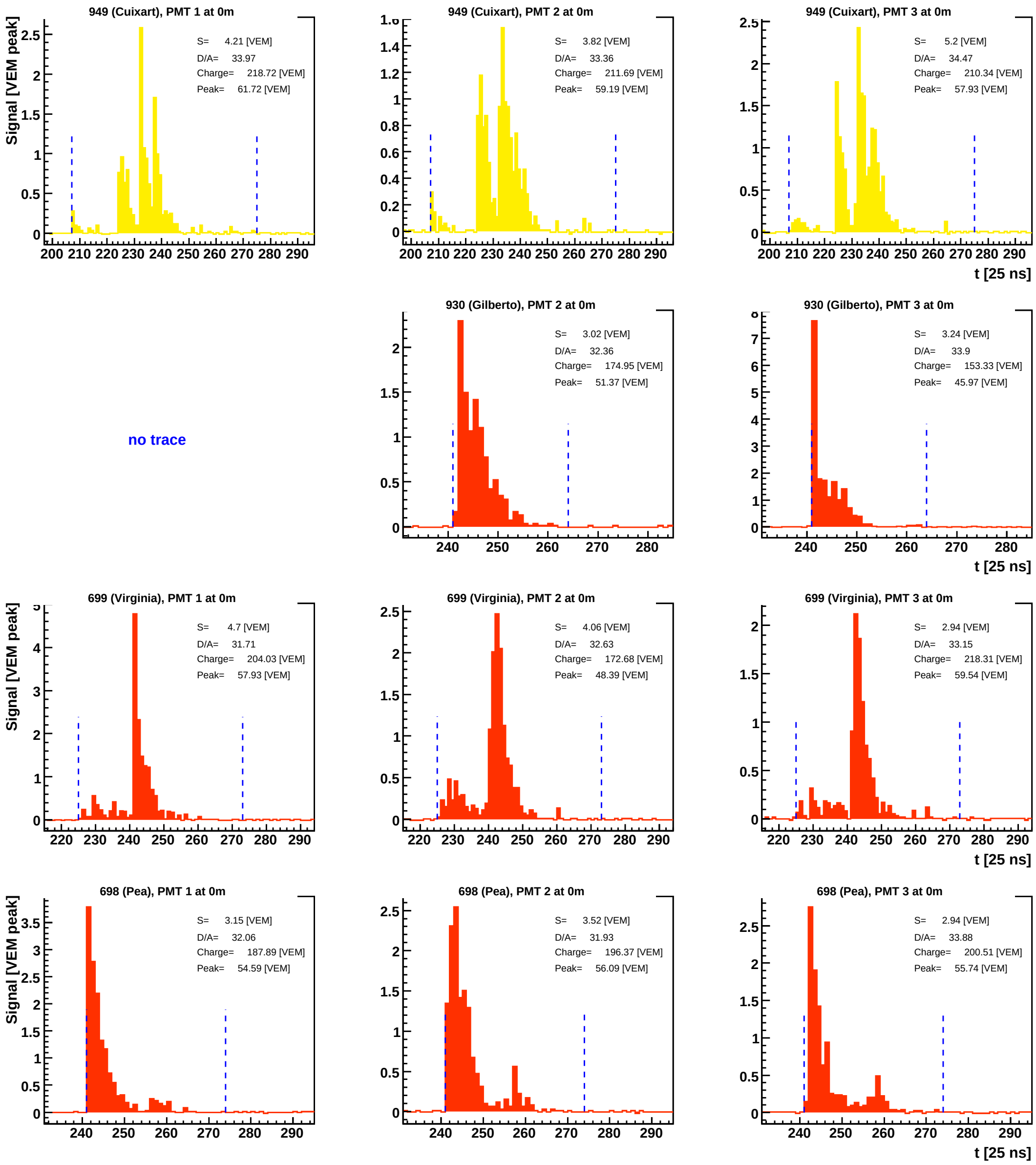

Figure E.12: *Traces of stations 949, 930, 699 and 698*

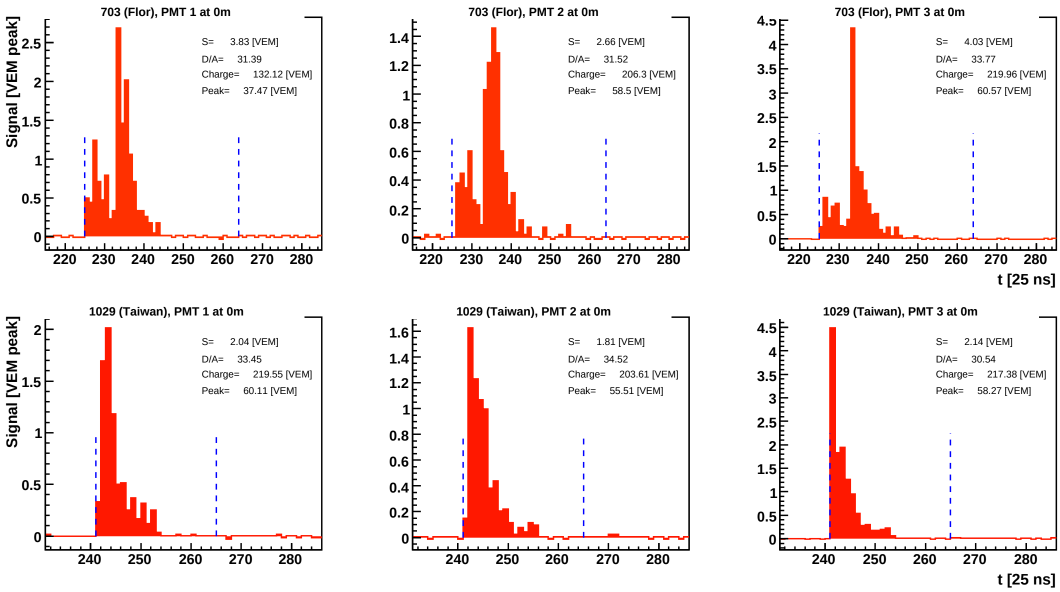

Figure E.13: *Traces of stations 703 and 1029*

E.3 Event 4617571

In this section the traces for the candidate stations of event 4617571 are listed in decreasing order of signal.

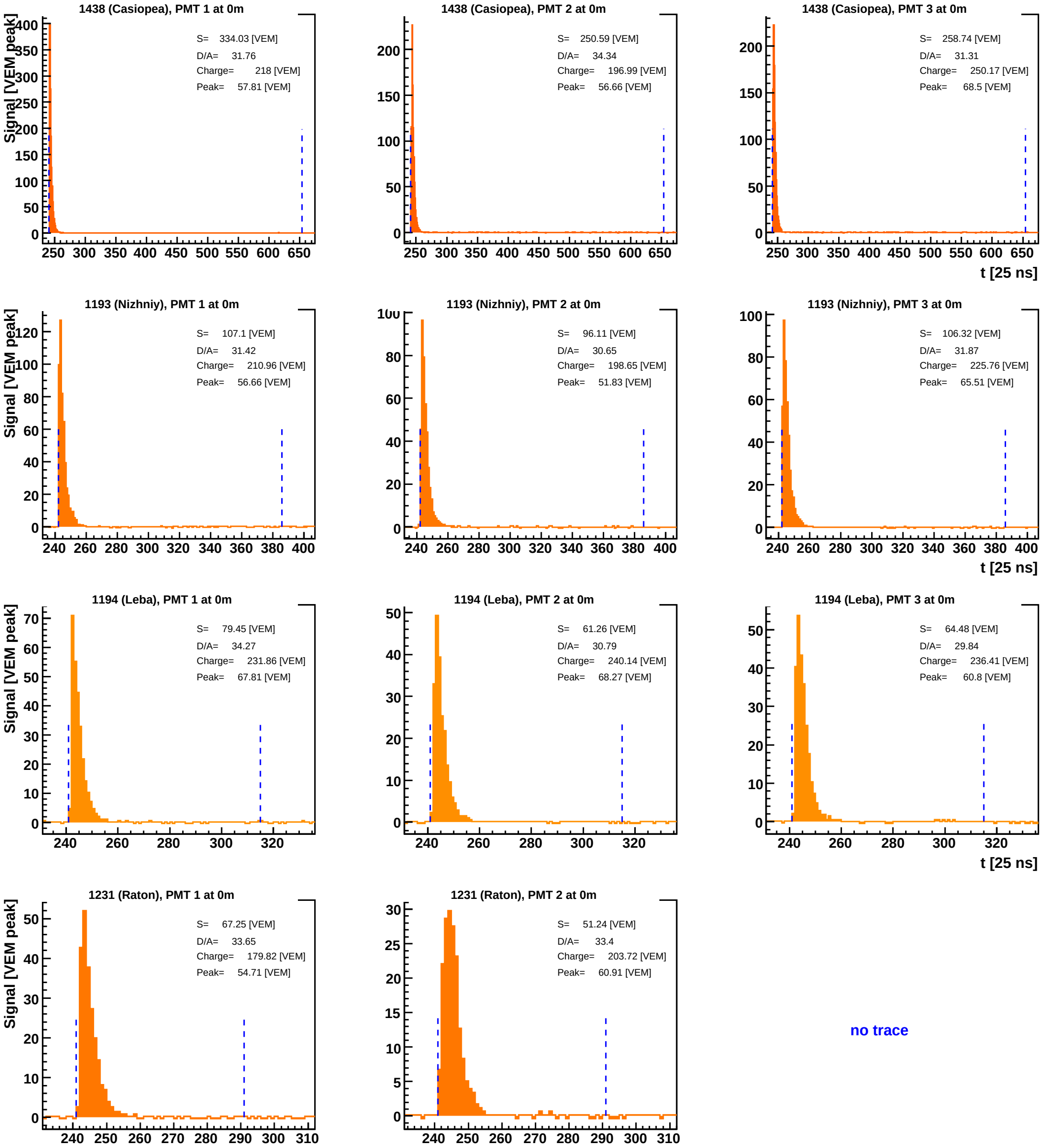

Figure E.14: *Traces of stations 1438, 1193, 1194 and 1231.*

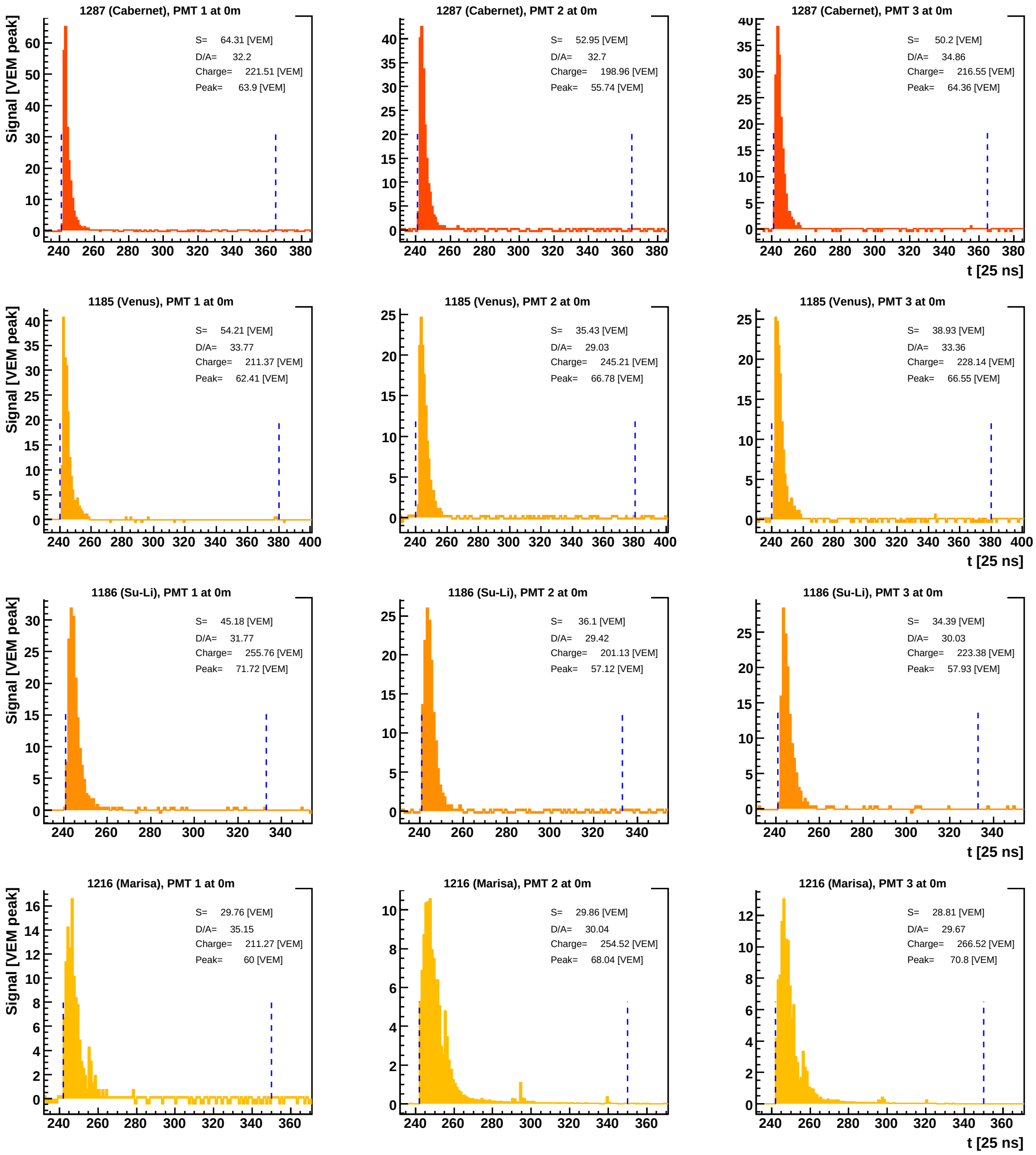

Figure E.15: *Traces of stations 1287, 1185, 1186 and 1216.*

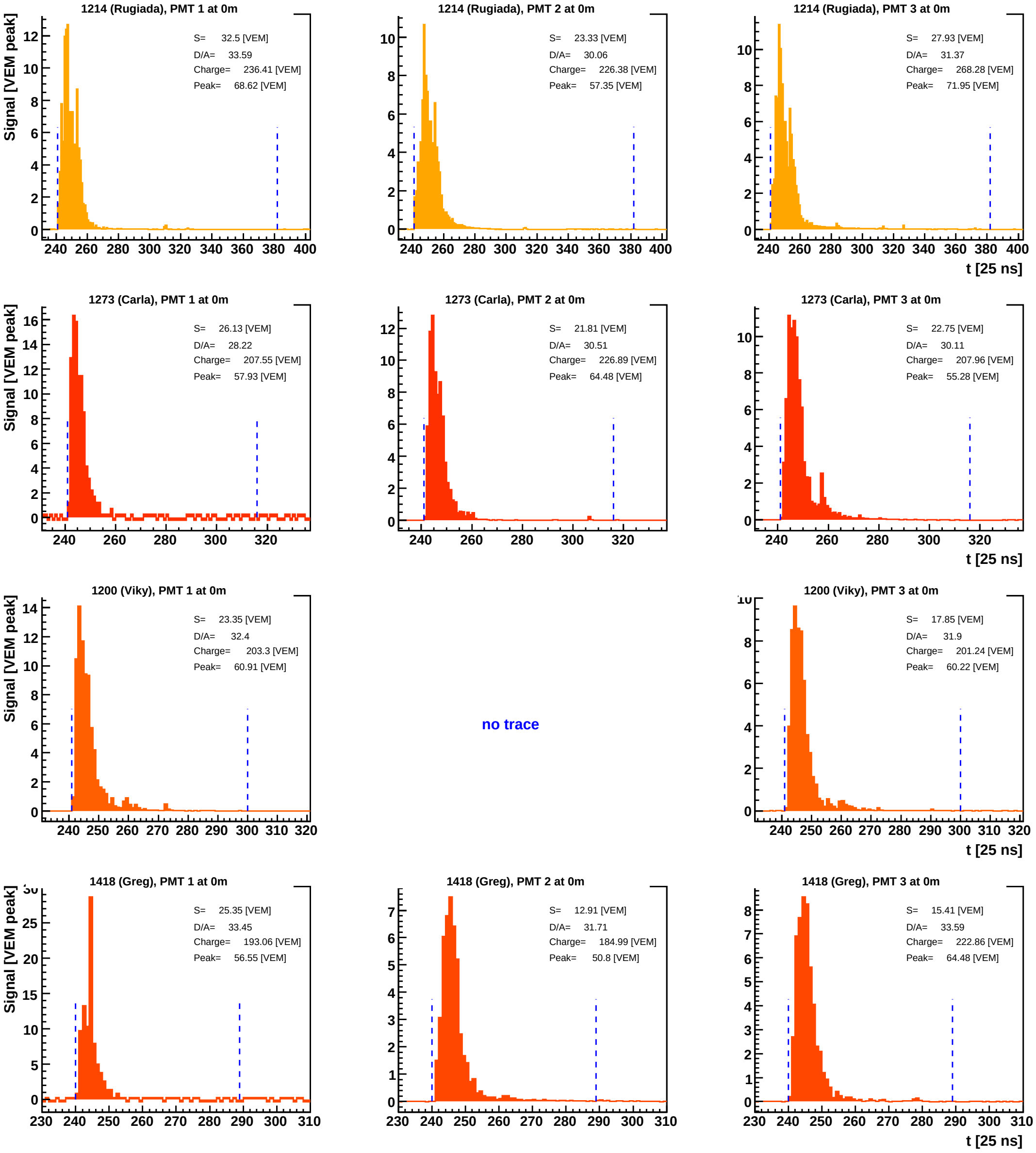

Figure E.16: *Traces of stations 1214, 1273, 1200 and 1418.*

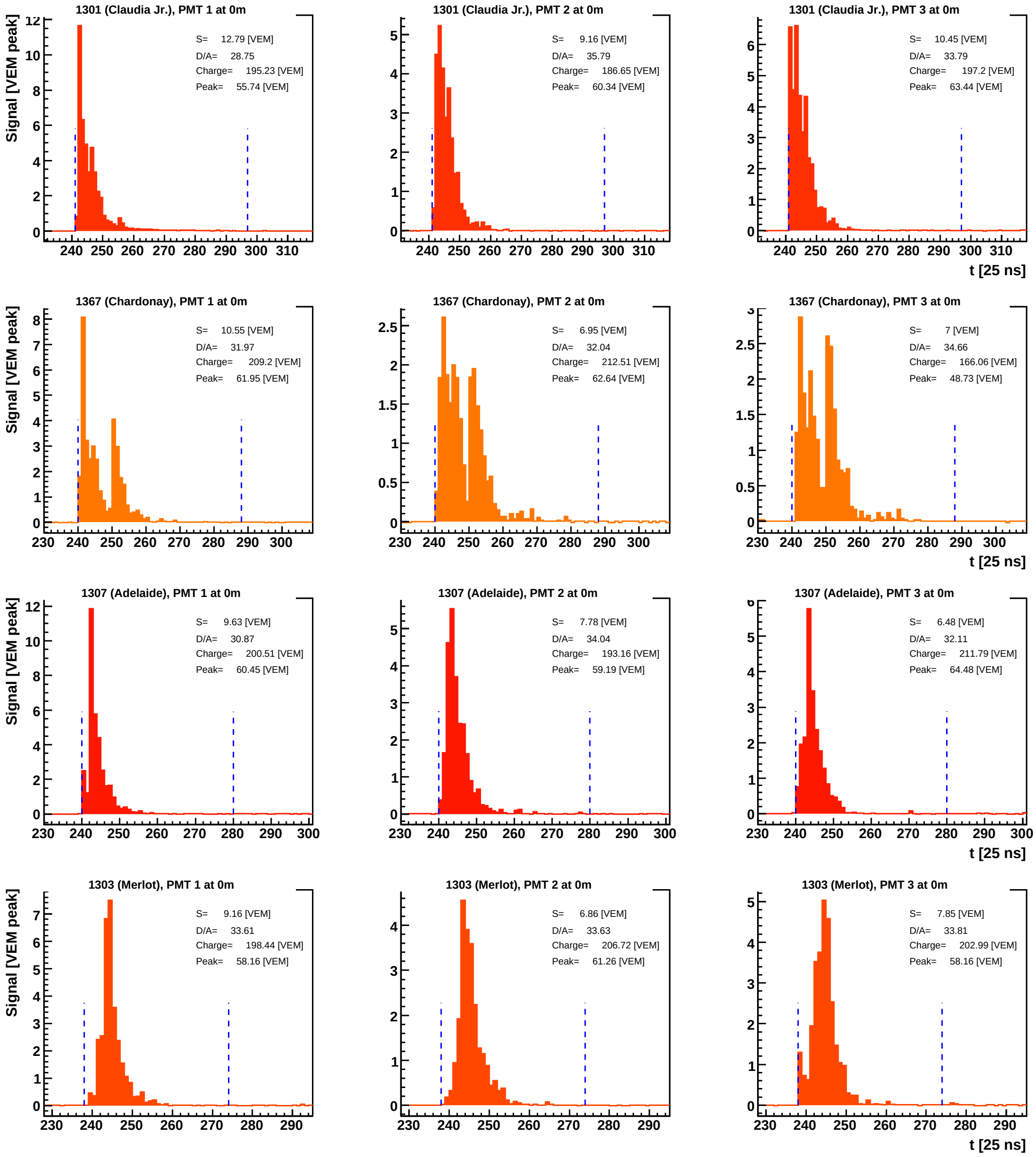

Figure E.17: *Traces of stations 1301, 1367, 1307 and 1303.*

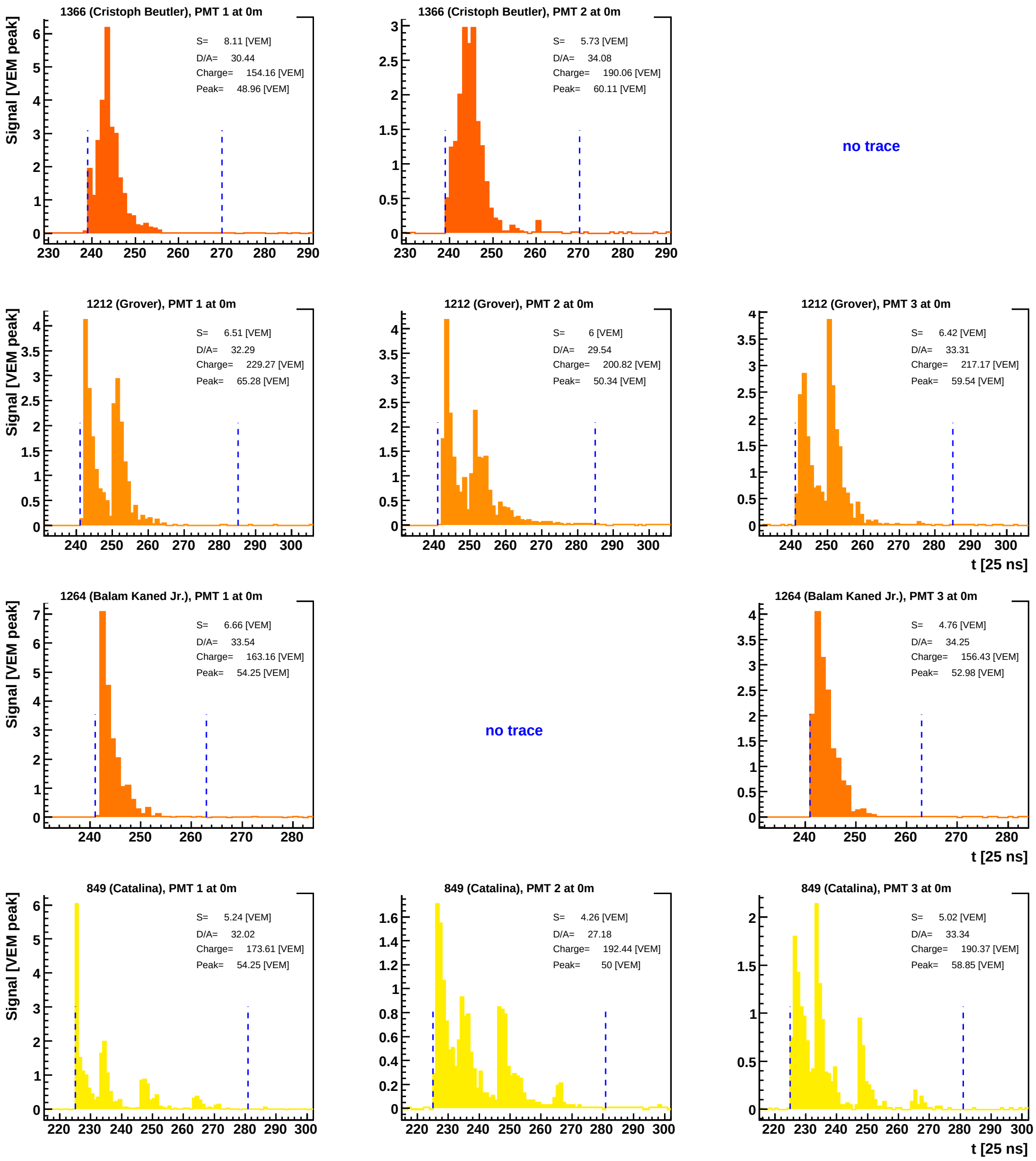

Figure E.18: *Traces of stations 1366, 1212, 1264 and 849.*

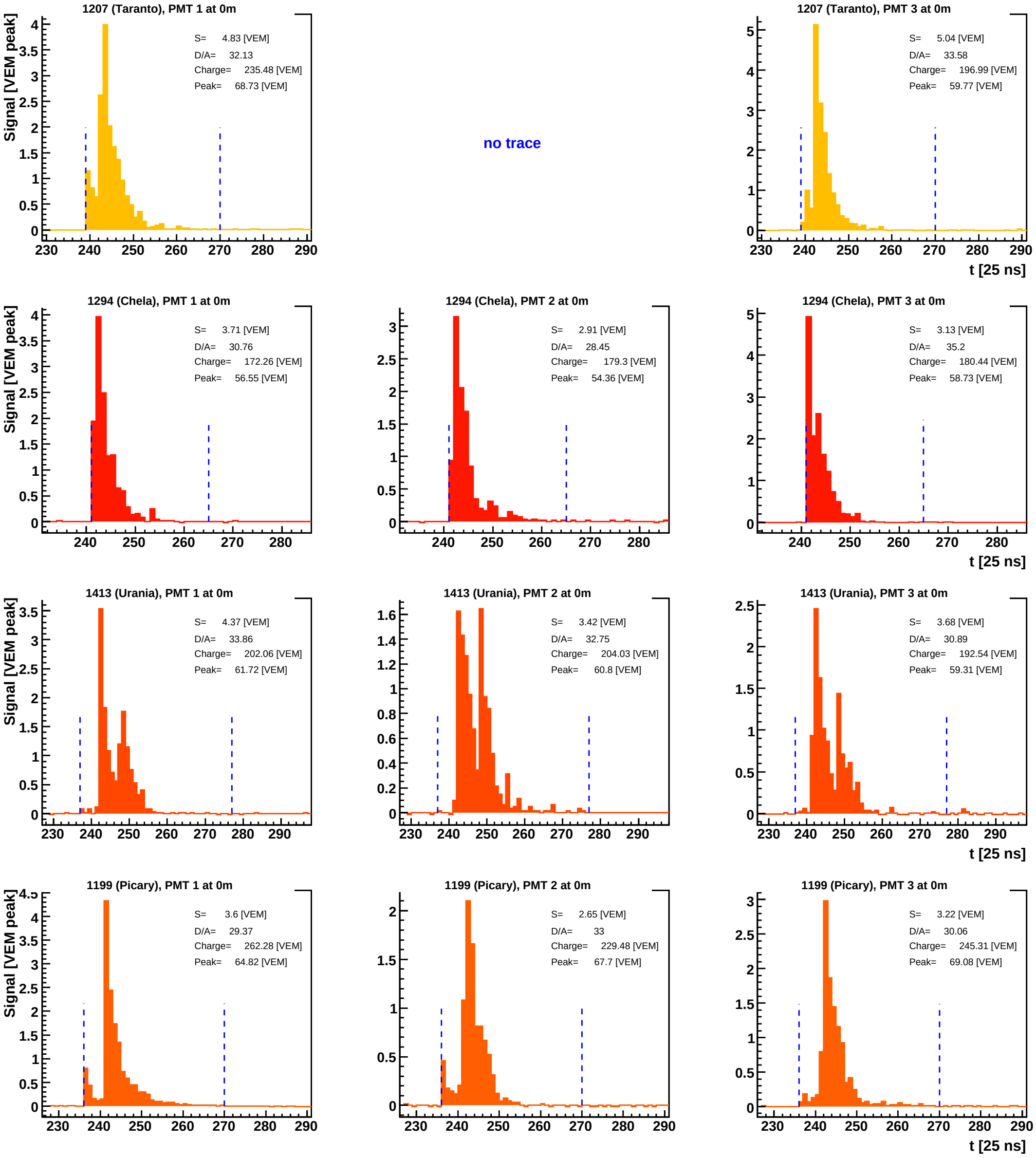

Figure E.19: *Traces of stations 1207, 1294, 1413 and 1199.*

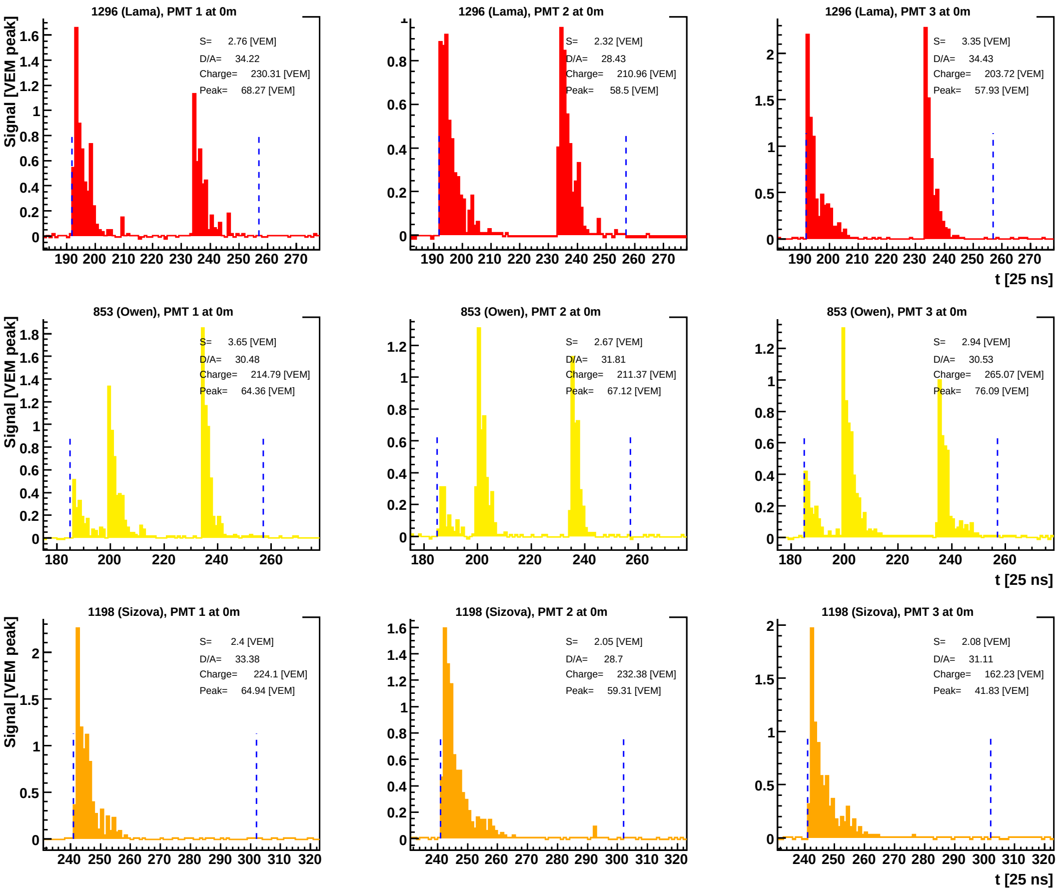

Figure E.20: *Traces of stations 1296. 853 and 1198.*

Acknowledgment

The last part of any hard work is usually one of the most pleasant chapter of someone's life and words of gratitude for assistance and collaboration come out very easily and, unfortunately, sometimes also without any particular feeling.

On my part, I can assure that the current statement stems from sincere feeling of gratitude and liking for many people who I knew during my doctorate.

To be honest, however, I have to say that in a large collaborative scientific group it is always possible to dislike some members but perhaps only because the natural and unavoidable competition of human being leads to develop distaste for something, even if without particular reasons.

It is not the case of my closest collaborators, Dr. Markus Roth and Dr. Dariusz Gora, who, after three year of work with them, I could consider almost friends. Although Dr. Markus Roth was also my supervisor, he did never make me feel shyness but rather will of catching his experienced suggestions as motivating drive to achieve the best of my possibilities. In a word a confortable working group. Of Dr. Dariusz Gora, I will always remember his patience and natural vocation for teamwork. Without his help, I do not think I could have solved many of my problems.

I should thank a long list of people who contributed to my scientific formation although did not collaborate directly with me. Among them I need to mention Dr. Ralph Ulrich and Dr. Michael Unger for their support in programming, Dr. Fabian Schlüssel for its advice, Ms. Talianna Schmidt and Ms. Karen Mora for their nice collaboration in understanding topics related to horizontal showers and composition studies, respectively. I can not forget the support of the Offline team, in particular Dr. Tom Paul and Dr. Javier Gonzales, and the support of the neutrino taskforce, in particular Dr. Jaime Alvarez-Muniz, for leading the fruitful comparison of works done in Santiago, Karlsruhe and Buenos Aires.

A special thank to Dr. Dieder Heck, Dr. Ioana Maris and Dr. Michael Unger for their opinion on this work, and Dr. Ralph Engel for its availability on fruitful physics discussions.

And finally, but just because they were more directly involved in the latest period of my work, I need to thank my first referee Prof. Dr. H. Johannes Blümer, who gave me the opportunity to be a member of the Pierre Auger Collaboration and to profit of the possibility of my position to gain valuable expertise by traveling to conferences and schools, and my second referee Prof. Dr. Michael Feindt, who made himself available to co-referee this work and whose helpfulness I only recently discovered.

This work was made possible with the financial support by the HHNG-128 grant of the Helmholtz association.

Bibliography

[1] K. S. Hirata, et al., *Observation of a small atmospheric ν_μ/ν_e ratio in Kamiokande*, Phys. Lett. **B280** (1992) 146–152.

[2] K. S. Hirata, et al., *Observation of a Neutrino Burst from the Supernova SN 1987a*, Phys. Rev. Lett. **58** (1987) 1490–1493.

[3] C. Spiering, *Status and Perspectives of Astroparticle Physics in Europe*, arXiv: astro-ph/0804.1500.

[4] Particle Data Group [W. M. Yao et al.], *Review of particle physics*, J. Phys. **G33** (2006) 1–1232.
URL `http://pdg.lbl.gov/`

[5] N. Chiba, et al., *Akeno giant air shower array (AGASA) covering 100-km**2 area*, Nucl. Instrum. Meth. **A311** (1992) 338–349.

[6] S. C. Corbato, et al., *HiRes: A High resolution Fly's Eye detector*, Nucl. Phys. Proc. Suppl. **28B** (1992) 36–39.

[7] Pierre Auger Collaboration [J. Abraham et al.], *Properties and performance of the prototype instrument for the Pierre Auger Observatory*, Nucl. Instrum. Meth. **A523** (2004) 50–95.

[8] J. A. Simpson, *Elemental and isotopic composition of the galactic cosmic rays*, Ann. Rev. Nucl. Part. Sci. **33** (1983) 323–382.

[9] Pierre Auger Collaboration [J. Abraham et al.], *Correlation of the highest energy cosmic rays with nearby extragalactic objects*, Science **318** (2007) 938–943, arXiv: astro-ph/0711.2256.

[10] K. Greisen, *End to the Cosmic-Ray Spectrum?*, Phys. Rev. Lett. **16** (1966) 748–750.

[11] G. T. Zatsepin, V. A. Kuzmin, *Upper limit of the spectrum of cosmic rays*, JETP Lett. **4** (1966) 78–80.

[12] L. A. Anchordoqui, M. T. Dova, L. N. Epele, J. D. Swain, *Effect of the 3-K background radiation on ultrahigh energy cosmic rays*, Phys. Rev. **D55** (1997) 7356–7360, arXiv: hep-ph/9704387.

[13] Pierre Auger Collaboration [J. Abraham et al.], *Upper limit on the cosmic-ray photon flux above* 10^{19} eV *using the surface detector of the Pierre Auger Observatory*, Astropart. Phys. **29** (2008) 243–256, arXiv: astro-ph/0712.1147.

[14] X. Bertou, P. Billoir, O. Deligny, C. Lachaud, A. Letessier-Selvon, *Tau neutrinos in the Auger observatory: A new window to UHECR sources*, Astropart. Phys. **17** (2002) 183–193, arXiv: astro-ph/0104452.

[15] Pierre Auger Collaboration [J. Abraham et al.], *Upper Limit on the Diffuse Flux of Ultrahigh Energy Tau Neutrinos from the Pierre Auger Observatory*, Phys. Rev. Lett. **100** (2008) 211101.

[16] A. M. Hillas, *Where do 10**19-eV cosmic rays come from?*, Nucl. Phys. Proc. Suppl. **136** (2004) 139–146.

[17] J. R. Hoerandel, *On the knee in the energy spectrum of cosmic rays*, Astropart. Phys. **19** (2003) 193–220, arXiv: astro-ph/0210453.

[18] V. S. Berezinsky, S. I. Grigorieva, B. I. Hnatyk, *Extragalactic UHE proton spectrum and prediction for iron- nuclei flux at 10**8-GeV to 10**9-GeV*, Astropart. Phys. **21** (2004) 617–625, arXiv: astro-ph/0403477.

[19] E. Fermi, *On the Origin of Cosmic Radiation*, Phys. Rev. **75** (1949) 1169–1174.

[20] R. D. Blandford, J. P. Ostriker, *Particle Acceleration by Astrophysical Shocks*, Astrophys. J. **221** (1978) L29–L32.

[21] A. R. Bell, *The Acceleration of cosmic rays in shock fronts. I*, Mon. Not. Roy. Astron. Soc. **182** (1978) 147–156.

[22] A. R. Bell, *The acceleration of cosmic rays in shock fronts. II*, Mon. Not. Roy. Astron. Soc. **182** (1978) 443–455.

[23] A. M. Hillas, *The Origin of Ultrahigh-Energy Cosmic Rays*, Ann. Rev. Astron. Astrophys. **22** (1984) 425–444.

[24] P. Bhattacharjee, G. Sigl, *Origin and Propagation of Extremely High Energy Cosmic Rays*, Phys. Rept. **327** (2000) 109–247, arXiv: astro-ph/9811011.

[25] G. Steigman, M. S. Turner, *Cosmological Constraints on the Properties of Weakly Interacting Massive Particles*, Nucl. Phys. **B253** (1985) 375.

[26] T. Vachaspati, *Lectures on cosmic topological defects*, arXiv: hep-ph/0101270 (2000).

[27] J. K. Becker, *High-energy neutrinos in the context of multimessenger physics*, Phys. Rept. **458** (2008) 173–246, 0710.1557.

[28] X. W. Xu, *Results achieved with AMANDA*, Nucl. Phys. Proc. Suppl. **175-176** (2008) 401–406.

[29] M. Walter, *The IceCube Neutrino Observatory: Design and performance*, Nucl. Phys. Proc. Suppl. **172** (2007) 13–16.

[30] M. Naumann-Godo, *Current status of the ANTARES neutrino telescope*, Nucl. Phys. Proc. Suppl. **172** (2007) 36–40.

[31] M. Spurio, *Status of the NEMO experiment*, Nucl. Instrum. Meth. **A572** (2007) 503–504.

[32] S. L. Glashow, *Resonant Scattering of Antineutrinos*, Phys. Rev. **118** (1960) 316–317.

[33] R. Gandhi, C. Quigg, M. H. Reno, I. Sarcevic, *Neutrino interactions at ultrahigh energies*, Phys. Rev. **D58** (1998) 093009, arXiv: hep-ph/9807264.

[34] M. Haag, *Exotische Neutrino-Wirkungsquerschnitte*, Diploma Thesis, Karlsruhe Institute of Technology, Universität Karlsruhe, Germany (2008).

[35] M. Gluck, E. Reya, A. Vogt, *Dynamical parton distributions revisited*, Eur. Phys. J. **C5** (1998) 461–470, arXiv: hep-ph/9806404.

[36] M. Gluck, S. Kretzer, E. Reya, *Dynamical QCD predictions for ultrahigh energy neutrino cross sections*, Astropart. Phys. **11** (1999) 327–334, arXiv: astro-ph/9809273.

[37] CTEQ Collaboration [H. L. Lai et al.], *Global QCD analysis of parton structure of the nucleon: CTEQ5 parton distributions*, Eur. Phys. J. **C12** (2000) 375–392, arXiv: hep-ph/9903282.

[38] A. Donnachie, P. V. Landshoff, *Small x: Two pomerons!*, Phys. Lett. **B437** (1998) 408–416, arXiv: hep-ph/9806344.

[39] A. Donnachie, P. V. Landshoff, *New data and the hard pomeron*, Phys. Lett. **B518** (2001) 63–71, arXiv: hep-ph/0105088.

[40] J. L. Albacete, N. Armesto, J. G. Milhano, C. A. Salgado, U. A. Wiedemann, *Nuclear size and rapidity dependence of the saturation scale from QCD evolution and experimental data*, Eur. Phys. J. **C43** (2005) 353–360, arXiv: hep-ph/0502167.

[41] D. Fargion, *Discovering ultra high energy neutrinos by horizontal and upward tau air-showers: First evidences in terrestrial gamma flashes*, Astrophys. J. **570** (2002) 909–925, arXiv: astro-ph/0002453.

[42] J. L. Feng, P. Fisher, F. Wilczek, T. M. Yu, *Observability of earth-skimming ultra-high energy neutrinos*, Phys. Rev. Lett. **88** (2002) 161102, arXiv: hep-ph/0105067.

[43] A. Letessier-Selvon, *Establishing the GZK cutoff with ultra high energy tau neutrinos*, AIP Conf. Proc. **566** (2001) 157–171, arXiv: astro-ph/0009444.

[44] M. M. Guzzo, C. A. Moura Jr., *Ultra high energy tau neutrinos and fluorescence detectors: A phenomenological approch*, Astropart. Phys. **25** (2006) 277–283, arXiv: hep-ph/0504270.

[45] C. Moura, *Detection of ultra-high energy tau-neutrino by double-bang event*, AIP Conf. Proc. **809** (2006) 190–192.

[46] T. K. Gaisser, *Cosmic rays and particle physics*, Cambridge University Press, 1990.

[47] SNO Collanoration [Q. R. Ahmad et al.], *Direct evidence for neutrino flavor transformation from neutral-current interactions in the Sudbury Neutrino Observatory*, Phys. Rev. Lett. **89** (2002) 011301, arXiv: nucl-ex/0204008.

[48] Super-Kamiokande Collaboration [Y. Fukuda et al.], *Evidence for oscillation of atmospheric neutrinos*, Phys. Rev. Lett. **81** (1998) 1562–1567, arXiv: hep-ex/9807003.

[49] H. Athar, M. Jezabek, O. Yasuda, *Effects of neutrino mixing on high-energy cosmic neutrino flux*, Phys. Rev. **D62** (2000) 103007, arXiv: hep-ph/0005104.

[50] CHOOZ Collaboration [M. Apollonio et al.], *Limits on neutrino oscillations from the CHOOZ experiment*, Phys. Lett. **B466** (1999) 415–430, arXiv: hep-ex/9907037.

[51] J. F. Beacom, N. F. Bell, D. Hooper, S. Pakvasa, T. J. Weiler, *Decay of high-energy astrophysical neutrinos*, Phys. Rev. Lett. **90** (2003) 181301, arXiv: hep-ph/0211305.

[52] Y. Farzan, A. Y. Smirnov, *Leptonic unitarity triangle and CP-violation*, Phys. Rev. **D65** (2002) 113001, arXiv: hep-ph/0201105.

[53] G. Jungman, M. Kamionkowski, K. Griest, *Supersymmetric dark matter*, Phys. Rept. **267** (1996) 195–373, arXiv: hep-ph/9506380.

[54] K. Mannheim, R. J. Protheroe, J. P. Rachen, *On the cosmic ray bound for models of extragalactic neutrino production*, Phys. Rev. **D63** (2001) 023003, arXiv: astro-ph/9812398.

[55] J. G. Learned, K. Mannheim, *High-energy neutrino astrophysics*, Ann. Rev. Nucl. Part. Sci. **50** (2000) 679–749.

[56] V. S. Berezinsky, G. T. Zatsepin, *Cosmic rays at ultrahigh-energies (neutrino?)*, Phys. Lett. B **28** (1969) 423.

[57] V. Hess, *Über Beobachtungen der durchdringenden Strahlung bei sieben Freiballonfahrten*, Phys. Zeitschr. **XIII** (1912) 1084–91.

[58] B. Rossi, *Moments in the life of a Scientist*, Cambridge University Press, New York, 1990.

[59] P. Auger, P. Ehrenfest, R. Maze, J. Daudin, A. F. Robley, *Extensive cosmic-ray showers*, Rev. Mod. Phys. **11** (1939) 288–291.

[60] L. D. Landau, I. Pomeranchuk, *Limits of applicability of the theory of bremsstrahlung electrons and pair production at high-energies*, Dokl. Akad. Nauk Ser. Fiz. **92** (1953) 535–536.

[61] L. D. Landau, I. Pomeranchuk, *Electron cascade process at very high-energies*, Dokl. Akad. Nauk Ser. Fiz. **92** (1953) 735–738.

[62] A. B. Migdal, *Bremsstrahlung and Pair Production in Condensed Media at High Energies*, Phys. Rev. **103** (6) (1956) 1811–1820.

[63] M. Roth, *The Lateral Distribution Function of Shower Signals in the Surface Detector of the Pierre Auger Observatory*, in: T. Kajita, Y. Asaoka, A. Kawachi, M. Matsubara, Y.and Sasaki (Eds.), Proc. 28th Intern. Cosmic Ray Conf., Tsukuba, Japan, Universal Academy Press Inc., Tokyo, Japan, 2003, pp. 333–336.

[64] M. Unger [Auger Collaboration], *Study of the Cosmic Ray Composition above 0.4 EeV using the Longitudinal Profiles of Showers observed at the Pierre Auger Observatory*, in: Proc. 30th Intern. Cosmic Ray Conf., Merida, Mexico, 2007, arXiv: astro-ph/0706.1495.

[65] Y. Fedorova, et al. [HiRes Collaboration], *Cosmic Rays Composition Measurements by the HiRes Stereo*, in: Proc. 30th Intern. Cosmic Ray Conf., Merida, Mexico, 2007.

[66] D. Allard, A. V. Olinto, E. Parizot, *Signatures of the extragalactic cosmic-ray source composition from spectrum and shower depth measurements*, arXiv: astro-ph/0703633.

[67] K.-H. Kampert, *Ultra High Energy Cosmic Ray Observations*, J. Phys. Conf. Ser. **120** (2008) 062002, arXiv: astro-ph/0801.1986.

[68] M. Ave, J. A. Hinton, R. A. Vazquez, A. A. Watson, E. Zas, *A new approach to inferring the mass composition of cosmic rays at energies above 10**18-eV*, Astropart. Phys. **18** (2003) 367–375, arXiv: astro-ph/0112071.

[69] A. A. Watson, *The mass composition of cosmic rays above 10**17-eV*, Nucl. Phys. Proc. Suppl. **151** (2006) 83–91, arXiv: astro-ph/0410514.

[70] J. Linsley, in: B. Betev (Ed.), Proc. of the 15th Intern. Cosmic Ray Conf., Plovdiv, Bulgaria, Vol. **12**, Bulgarian Acad. Sci., Inst. of Nuclear Research and Energy, Blvd. Lenin 72, Sofia 13, Bulgaria, 1977, p. 89.

[71] T. K. Gaisser, in: K. Kamata (Ed.), Proc. of the 16th Intern. Cosmic Ray Conf., Kyoto, Japan, Vol. **9**, Institute for Cosmic Ray Research, Inst. for Cosmic Ray Research, Univ. of Tokyo, Tanashi, Tokyo 188, Japan, 1979, p. 258.

[72] J. Linsley, *Are extensive air showers produced by relativistic dust grains?*, Astrophys. J. **235** (1980) L167–L169.

[73] J. Linsley, A. A. Watson, *Validity of scaling to 10**20-eV and high-energy cosmic ray composition*, Phys. Rev. Lett. **46** (1981) 459–463.

[74] D. Barnhill, *Composition Analysis of Ultrahigh Energy Cosmic Rays Using the Pierre Auger Observatory Surface Detector*, Ph.D. thesis, University of California, Los Angeles, Auger Collaboration Tech. Rep. 082 (2005).

[75] B. Smith, C. Wileman, A. A. Watson, *Can the risetime be used to infer the position of the shower maximum?*, Tech. Rep. 092, Pierre Auger Collaboration (2007).

[76] L. Cazón-Boado, *Modelling the Muon Time Distribution in Extensive Air Showers*, Ph.D. thesis, Departamento de Fisica de Particulas, Universidade de Santiago de Compostela, Spain (2004).
URL `www-fp.usc.es/~astro/lorenzo\_tesis.pdf`

[77] L. Cazon, R. A. Vazquez, A. A. Watson, E. Zas, *Time structure of muonic showers*, Astropart. Phys. **21** (2004) 71–86, arXiv: astro-ph/0311223.

[78] P. Kiraly, M. G. Thompson, A. W. Wolfendale, *Cosmic ray showers produced by muon bremsstrahlung*, J. Phys. **A4** (1971) 367–376.

[79] Auger Collaboration, *The Pierre Auger Project Design Report*, FERMILAB-PUB **96-024** (1996) 252pp.

[80] K. S. Capelle, J. W. Cronin, G. Parente, E. Zas, *On the detection of ultra high energy neutrinos with the Auger Observatory*, Astropart. Phys. **8** (1998) 321–328, arXiv: astro-ph/9801313.

[81] C. Aramo, et al., *Earth-skimming UHE Tau Neutrinos at the Fluorescence Detector of Pierre Auger Observatory*, Astropart. Phys. **23** (2005) 65–77, arXiv: astro-ph/0407638.

[82] P. Billoir, O. Blanch Bigas, *The Pierre Auger Observatory and neutrinos*, Nucl. Phys. Proc. Suppl. **168** (2007) 225–231.

[83] O. Blanch Bigas, *Limits to the diffuse flux of UHE tau neutrinos at EeV energies from the Pierre Auger Observatory*, arXiv: astro-ph/0706.1658 (2007).

[84] G. Miele, S. Pastor, O. Pisanti, *The aperture for UHE tau neutrinos of the Auger fluorescence detector using a Digital Elevation Map*, Phys. Lett. **B634** (2006) 137–142, arXiv: astro-ph/0508038.

[85] D. Gora, M. Roth, A. Tamburro, *A MC approach to simulate up- and down-going neutrino showers including local topographic conditions*, Astropart. Phys. **26** (2007) 402–413.

[86] M. Nagano, *Horizontal air showers of energies above 10-to-the-13 eV*, J. Phys. Soc. Japan **30** (1971) 33.

[87] M. Nagano, A. A. Watson, *Observations and implications of the ultra-high energy cosmic rays*, Rev. Mod. Phys. **72** (2000) 689–732.

[88] S. Mikamo, et al., *Observation of horizontal air showers with energies of 1- TeV to 100-TeV*, Nuovo Cim. Lett. **34** (1982) 273.

[89] T. Doi, et al., *Inclined giant air showers with energies above 10**19.5-eV observed by AGASA*, in: Proc. 24th Intern. Cosmic Ray Conf., Rome, Italy, 1996, ICRR-Report-353-96-04 (96/01,rec.Mar.) 25-28.
URL `http://preprints.cern.ch/cgi-bin/setlink?base=preprint&%categ=.&id=SCAN-9604076`

[90] N. Inoue, *Characteristics of inclined giant air showers observed by AGASA*, in: Proc. 26th Intern. Cosmic Ray Conf., Salt Lake City, Utah, USA, Vol. **1**, 1999, pp. 361–364.

[91] G. Navarra, *Study of horizontal air showers from EAS-TOP: A possible tool for UHE neutrino detection?*, Nucl. Phys. Proc. Suppl. **70** (1999) 509–511.

[92] M. Aglietta, et al., *Study of horizontal air showers at EAS-TOP*, in: Proc. 26th Intern. Cosmic Ray Conf., Salt Lake City, Utah, USA, 1999.

[93] M. Ave, R. A. Vazquez, E. Zas, J. A. Hinton, A. A. Watson, *The rate of cosmic ray showers at large zenith angles: A step towards the detection of ultra-high energy neutrinos by the Pierre Auger Observatory*, Astropart. Phys. **14** (2000) 109–120, arXiv: astro-ph/0003011.

[94] I. Valiño-Rielo, *Detection of Horizontal Air Shower and Neutrino Induced Showers with the Pierre Auger Observatory*, Ph.D. thesis, Departamento de Fisica de Particulas, Universidade de Santiago de Compostela, Spain (2007).

[95] E. Zas, *Neutrino detection with inclined air showers*, New Journal of Physics **7** (2005) 130.

[96] D. Bird, et al., *The Calibration of the absolute sensitivity of photomultiplier tubes in the High Resolution Fly's Eye Detector*, Nucl. Instrum. Meth. **A349** (1994) 592–599.

[97] J. V. Jelley, et al., *Radio pulses from extensive cosmic-ray air showers*, Nature **205** (1965) 327.

[98] H. R. Allan, J. K. Jones, *Radio pulses from extensive cosmic-ray air showers*, Nature **212** (1966) 129–131.

[99] T. Huege, H. Falcke, *Radio Emission from Cosmic Ray Air Showers: Coherent Geosynchrotron Radiation*, Astron. Astrophys. **412** (2003) 19–34, arXiv: astro-ph/0309622.

[100] A. A. Watson, *The role of Cherenkov radiation in the detection of ultra- high-energy cosmic rays*, Nucl. Instrum. Meth. **A553** (2005) 256–263.

[101] J. Linsley, *Primary cosmic rays of energy 10**17 to 10**20-eV: The energy spectrum and arrival directions*, in: Proc. 8th Intern. Cosmic Ray Conf., Jaipur, India, 1963.

[102] G. Cunningham, et al., *Catalog of Highest Energy Cosmic Ray*, World Data Center of Cosmic Rays, Institute of Physical and Chemical Research, Itabashi, Tokyo **1** (1980) 61.

[103] T. Waldenmaier, *Spectral resolved Measurement of the Nitrogen Fluorescence Yield in Air induced by Electrons*, Ph.D. thesis, Institute für Kernphysik, Universität Karlsruhe, Germany (2006).

[104] Auger web site.
URL `http://www.auger.org/`

[105] S. Y. BenZvi, et al., *The lidar system of the Pierre Auger observatory*, Nucl. Instrum. Meth. **A574** (2007) 171–184, arXiv: astro-ph/0609063.

[106] J. Rautenberg, *Online Monitoring of the Pierre Auger Observatory*, in: Proc. 30th Intern. Cosmic Ray Conf., Merida, Mexico, 2007.

[107] H. Salazar, L. Villasenor, *Separation of cosmic-ray components in a single water Cherenkov detector*, Nucl. Instrum. Meth. **A553** (2005) 295–298.

[108] M. A. Lawrence, R. J. O. Reid, A. A. Watson, *The Cosmic ray energy spectrum above 4x10**17-eV as measured by the Haverah Park array*, J. Phys. **G17** (1991) 733–757.

[109] C. L. Pryke, J. Lloyd-Evans, *A High performance GPS based autonomous event time tagging system with application in a next generation extensive air shower array*, Nucl. Instrum. Meth. **A354** (1995) 560–566.

[110] X. Bertou, et al., *Calibration of the surface array of the Pierre Auger Observatory*, Nucl. Instrum. Meth. **A568** (2006) 839–846.

[111] D. Allard, et al., *The trigger system of the Pierre Auger Surface Detector: operation, efficiency and stability*, in: Proc. 29th Intern. Cosmic Ray Conf., Pune, India, Vol. **00**, 2005, pp. 101–106.

[112] P. Ghia, *The compact 3ToT as SD physics trigger for vertical ($\theta < 60$ deg) showers*, Tech. Rep. 018, Pierre Auger Collaboration (2004).

[113] S. Dagoret-Campagne, *The Central Trigger, User Guide and Reference Manual*, Tech. Rep. 020, Pierre Auger Collaboration (2004).

[114] Event Selection Group, *The Official Event Selection as of March 2005*, Tech. Rep. 023, Pierre Auger Collaboration (2005).

[115] D. Veberic, M. Roth, *SD Reconstruction; Offline Reference Manual*, Tech. Rep. 035, Pierre Auger Collaboration (2005).

[116] F. James, M. Roos, *Minuit: A System for Function Minimization and Analysis of the Parameter Errors and Correlations*, Comput. Phys. Commun. **10** (1975) 343–367.

[117] H. Asorey, X. Bertou, E. Roulet, *How to Improve the SD Arrival Direction Reconstruction by Correcting the Start Time of Individual Detectors*, Tech. Rep. 052, Pierre Auger Collaboration (2006).

[118] C. Pryke, *Asymmetry of Air Showers at Ground Level*, Tech. Rep. 034, Pierre Auger Collaboration (1998).

[119] P. Billoir, X. Bertou, *On the Origin of the Asymmetry of Ground Densities in Inclined Showers*, Tech. Rep. 017, Pierre Auger Collaboration (2000).

[120] S. Argiro, et al., *The Offline Software Framework of the Pierre Auger Observatory*, Nucl. Instrum. Meth. **A580** (2007) 1485–1496, arXiv: astro-ph/0707.1652.

[121] S. J. Sciutto, *AIRES: A system for air shower simulations (version 2.2.0)*, arXiv: astro-ph/9911331 (1999).

[122] AIRES web-site.
URL `http://www.fisica.unlp.edu.ar/auger/aires/`

[123] D. Heck, J. Knapp, J. N. Capdevielle, G. Schatz, T. Thouw, *CORSIKA: A Monte Carlo code to simulate extensive air showers*, FZKA-6019, Forschungszentrum Karlsruhe.

[124] CORSIKA web-site.
URL `www-ik.fzk.de/corsika/`

[125] T. Pierog, et al., *First Results of Fast One-dimensional Hybrid Simulation of EAS Using CONEX*, Nucl. Phys. Proc. Suppl. **151** (2006) 159–162, arXiv: astro-ph/0411260.

[126] J. Alvarez-Muniz, E. Zas, *The flux of emerging taus induced by tau nus crossing the Earth: Analytical calculations vs MC sims*, Tech. Rep. 017, Pierre Auger Collaboration (2007).

[127] O. Blanch-Bigas, O. Deligny, V. Van Elewyck, *On the proper formulation and calculation of Earth skimming tau fluxes*, Tech. Rep. 008, Pierre Auger Collaboration (2007).

[128] R. Engel, D. Gora, M. Roth, A. Tamburro, *The topography of the Auger site as a systematic uncertainty for skimming neutrinos*, Tech. Rep. 045, Pierre Auger Collaboration (2007).

[129] D. Gora, M. Roth, A. Tamburro, *A MC simulation of neutrino showers and their detection with the Pierre Auger Observatory*, in: Proc. 30th Intern. Cosmic Ray Conf., Merida, Mexico, 2007.

[130] A. Gazizov, M. P. Kowalski, *ANIS: High energy neutrino generator for neutrino telescopes*, Comput. Phys. Commun. **172** (2005) 203–213, arXiv: astro-ph/0406439.

[131] Consortium for Spatial Information (CGIAR-CSI).
URL `http://srtm.csi.cgiar.org/`

[132] T. Sjostrand, S. Mrenna, P. Skands, *PYTHIA 6.4 physics and manual*, JHEP **05** (2006) 026, arXiv: hep-ph/0603175.

[133] S. Jadach, Z. Was, R. Decker, J. H. Kuhn, *The tau decay library TAUOLA: Version 2.4*, Comput. Phys. Commun. **76** (1993) 361–380.

[134] M. Ambrosio, et al., *Corsika + Herwig Monte Carlo Simulation of Neutrino Induced Atmospheric Air Showers*, arXiv: astro-ph/0302602 (2003).

[135] A. M. Hillas, *Shower simulation: Lessons from MOCCA*, Nucl. Phys. Proc. Suppl. **52B** (1997) 29–42.

[136] N. N. Kalmykov, S. S. Ostapchenko, A. I. Pavlov, *Quark-gluon string model and EAS simulation problems at ultra-high energies*, Nucl. Phys. Proc. Suppl. **52B** (1997) 17–28.

[137] P. Billoir, *A sampling procedure to regenerate particles in a ground detector from a "thinned" air shower simulation output*, Submitted to Astropart. Phys.

[138] P. Billoir, *Unthinning of ground particles from an atmospheric shower*, Presented at VIHKOS CORSIKA School 2005.
URL `www-ik.fzk.de/corsika`

[139] P. Billoir, *Reconstruction of showers with the Ground Array: status of the "prototype" program*, Tech. Rep. 025, Pierre Auger Collaboration (2000).

[140] J. Blümer, D. Gora, M. Haag, M. Roth, A. Tamburro, *A cached shower regenerator for inclined events*, Tech. Rep. 064, Pierre Auger Collaboration (2008).

[141] P. Lipari, Lepton spectra in the earth's atmosphere, Astropart. Phys. **1** (1993) 195–227.

[142] T. McCauley, T. Paul, *GEANT4 simulation of the surface detectors*, Tech. Rep. 055, Pierre Auger Collaboration (2000).

[143] O. Blanch-Bigas, O. Deligny, V. Van Elewyck, *A proposal for a new T3 to increase the rate of ν-induced showers*, Tech. Rep. 082, Pierre Auger Collaboration (2006).

[144] J. Alvarez-Muniz [Auger Collaboration], *The sensitivity of the surface detector of the Pierre Auger Observatory to UHE neutrinos*, in: Proc. 30th Intern. Cosmic Ray Conf., Merida, Mexico, 2007.

[145] I. T. Jolliffe, *Principal Component Analysis*, 2nd Edition, Vol. XXIX of Springer Series in Statistics, Springer, New York, 2002.

[146] GARCON web-page.
URL `http://drozdets.home.cern.ch/drozdets/home/genetic/`

[147] S. Abdullin, et al., *GARCON: Genetic algorithm for rectangular cuts optimization. User's manual for version 2.0*, arXiv: hep-ph/0605143.

[148] E. Waxman, J. N. Bahcall, *High energy neutrinos from astrophysical sources: An upper bound*, Phys. Rev. **D59** (1999) 023002, arXiv: hep-ph/9807282.

[149] T. Stanev, D. Seckel, R. Engel, *Propagation of ultra-high energy protons in regular extragalactic magnetic fields*, Phys. Rev. **D68** (2003) 103004, arXiv: astro-ph/0108338.

[150] P. Bhattacharjee, *Cosmic topological defects, highest energy cosmic rays, and the baryon asymmetry of the universe*, Phys. Rev. Lett. **81** (1998) 260–263, arXiv: hep-ph/9803223.

[151] S. I. Dutta, Y. Huang, M. H. Reno, *Tau neutrino propagation and tau energy loss*, Phys. Rev. **D72** (2005) 013005, arXiv: hep-ph/0504208.

[152] H. Abramowicz, A. Caldwell, *HERA collider physics*, Rev. Mod. Phys. **71** (1999) 1275–1410, arXiv: hep-ex/9903037.

[153] H. Abramowicz, A. Levy, *The ALLM parameterization of $\sigma_{tot}(\gamma * p)$: An update*, arXiv: hep-ph/9712415.

[154] E. V. Bugaev, Y. V. Shlepin, *Photonuclear interaction of high energy muons and tau leptons*, Phys. Rev. **D67** (3) (2003) 034027.

[155] A. Cappella, A. Kaidalov, C. Merino, J. Tran Thanh, *Structure function and low x physics*, Phys. Lett. **B337** (1994) 358.

[156] N. Armesto, C. Merino, G. Parente, E. Zas, *Charged Current Neutrino Cross Section and Tau Energy Loss at Ultra-High Energies*, Phys. Rev. **D77** (2008) 013001, arXiv: hep-ph/0709.4461.

[157] K. Hagiwara, K. Mawatari, H. Yokoya, *Polarization effects in tau production by neutrino*, arXiv: hep-ph/0408212.

[158] G. J. Feldman, R. D. Cousins, *A Unified approach to the classical statistical analysis of small signals*, Phys. Rev. **D57** (1998) 3873–3889, arXiv: physics/9711021.

[159] Pierre Auger Collaboration [J. Abraham et al.], Observation of the suppression of the flux of cosmic rays above 4×10^{19}eV, Phys. Rev. Lett. **101** (2008) 061101, 0806.4302.

[160] MACRO Collaboration [M. Ambrosio et al.], *Search for diffuse neutrino flux from astrophysical sources with MACRO*, Astropart. Phys. **19** (2003) 1–13, arXiv: astro-ph/0203181.

[161] Frejus Collaboration [W. Rhode et al.], *Limits on the flux of very high-energetic neutrinos with the Frejus detector*, Astropart. Phys. **4** (1996) 217–225.

[162] IceCube Collaboration [A. Achterberg et al.], *Multi-year search for a diffuse flux of muon neutrinos with AMANDA-II*, Phys. Rev. **D76** (2007) 042008, arXiv: astro-ph/0705.1315.

[163] K. Martens, *HiRes Estimates and Limits for Neutrino Fluxes at the Highest Energies*, arXiv: astro-ph/0707.4417.

[164] BAIKAL Collaboration [V. Aynutdinov et al.], *Search for a diffuse flux of high-energy extraterrestrial neutrinos with the NT200 neutrino telescope*, Astropart. Phys. **25** (2006) 140–150, arXiv: astro-ph/0508675.

[165] I. Kravchenko, et al., *RICE limits on the diffuse ultra-high energy neutrino flux*, Phys. Rev. **D73** (2006) 082002, arXiv: astro-ph/0601148.

[166] ANITA Collaboration [S. W. Barwick et al.], *Constraints on cosmic neutrino fluxes from the ANITA experiment*, Phys. Rev. Lett. **96** (2006) 171101, arXiv: astro-ph/0512265.

[167] P. W. Gorham, et al., *Experimental limit on the cosmic diffuse ultrahigh-energy neutrino flux*, Phys. Rev. Lett. **93** (2004) 041101, arXiv: astro-ph/0310232.

[168] N. G. Lehtinen, P. W. Gorham, A. R. Jacobson, R. A. Roussel-Dupre, *FORTE satellite constraints on ultra-high energy cosmic particle fluxes*, Phys. Rev. **D69** (2004) 013008, arXiv: astro-ph/0309656.

[169] S. Agostinelli, et al., *G4 – a simulation toolkit*, Nucl. Instr. and Meth. in Phys. Res. A **506** (2003) 250–303.

[170] R. Brun, F. Rademakers, *ROOT: An object oriented data analysis framework*, Nucl. Instrum. Meth. **A389** (1997) 81–86.

[171] ROOT web-page.
URL `http://root.cern.ch/`

[172] P. Billoir, *Does the resampling procedure induce distorsion in the FADC traces of the Surface Detector?*, Tech. Rep. 109, Pierre Auger Collaboration (2005).

[173] J. Blümer, D. Gora, M. Haag, M. Roth, A. Tamburro, *On the influence of accidental muons on air shower detection*, Tech. Rep. 110, Pierre Auger Collaboration (2008).

[174] P. S. Allison, *Origin of the Time over Threshold trigger rate dependence on water quality and Time over Threshold background*, Tech. Rep. 040, Pierre Auger Collaboration (2005).

Acronyms

AGN Active Galactic Nuclei

ALLM Abramowicz-Levy

AMANDA Antarctic Muon and Neutrino Detector Array

ANTARES Astronomy with a Neutrino Telescope and Abyss environmental RESearch

AIRES AIRshower Extended Simulations

AGASA Akeno Giant Air-Shower Array

ASW Armesto-Salgado-Wiedemann

ANIS All Neutrino Interaction Simulation

BBBS Bugaev-Shlepin

BH Black Hole

CC Charged Current

CDAS Central Data Aquisition System

CKMT Cappella-Kaidalov-Merino-Tran

CL Confidence Level

CMB Cosmic Microwave Background

CORSIKA COsmic Ray SImulations for KAscade

CT Central Trigger

CTEQ Coordinated Theoretical-Experimental project on QCD

DB Double Bang

DEM Digital Elevation Map

DIS Deep Inelastic Scattering

EAS Extensive Air Shower

FADC Flash Analog Digital Converter

FD Fluorescence Detector

GARCON Genetic Algorithm for Rectangular Cuts OptimizatioN

GVD Generalized Vector Dominance

GPS Global Positioning System

GR Glashow Resonance

GRB Gamma Ray Burst

GRV Gluck-Reya-Vogt

GZK Greisen-Zatsepin-Kuzmin

HERA Hadron Elektron Ring Anlage

HiRes High Resolution

HP Hard Pomeron

LPM Landau-Pomeranchuk-Migdal

LIDAR LIght Detection And Ranging

MC Monte Carlo

NC Neutral Current

NEMO NEutrino Mediterranean Observatory

PDF Parton Distribution Function

PMT Photo Multiplier Tube

p.e. photoelectron

QCD Quantum Chromo Dynamics

QGSJET Quark Gluon String JET

SD Surface Detector

SUGAR Sidney University Giant Air-Shower Recorder

ToT Time over Threshold

TOTF Time Over Threshold trigger Fraction

TD Topological Defect

UHE Ultra High Energy

UHECR Ultra High Energy Cosmic Ray

VCT Vertical and Central Throughgoing (muon)

VEM Vertical Equivalent Muon

WB Waxman-Bahcall

WIMP Weakly Interacting Massive Particle